

TWO CRETACEOUS TALES OF THE LAND AND THE SEA

by

PULOMA CHAKRABARTY

Presented to the Faculty of the Graduate School of
The University of Texas at Arlington in Partial Fulfillment
of the Requirements
for the Degree of

DOCTOR OF PHILOSOPHY

THE UNIVERSITY OF TEXAS AT ARLINGTON

May 2019

Copyright © by Puloma Chakrabarty 2019

All Rights Reserved



Dedicated to NumNum,

Ma & Juju

FOREWORD

The Cretaceous Period (145-66 Ma), with no magnetic reversal for ~ 79 Ma, is generally termed as the Cretaceous Normal Superchron or the Magnetic Quiet Zone. There is evidence of at least two major large scale, global volcanisms in this long period synchronous with mass extinctions, during the Late Cretaceous and at the end of the Cretaceous.

This study focusses on the effect of these two global volcanisms on

1. The Ocean: Eagle Ford, South Texas at the beginning of the Late Cretaceous, 93.9 Ma, probably caused by Cretaceous mafic volcanism from the Ontong Java Plateau and/or Caribbean Large Igneous Province volcanism (LIP), and
2. The Land: Deccan Traps, end-Cretaceous, 66 Ma, LIP volcanism.

ACKNOWLEDGEMENTS

*Two roads diverged in a wood, and I—
I took the one less traveled by,
And that has made all the difference.*

Robert Frost

To take a less travelled path and make a difference, is never an easy task. However, the presence of a wise voyager, makes the journey worthwhile, knowledgeable and delightful.

I would like to begin by extending my sincerest thanks to my supervisor, Prof. Asish R Basu for guiding me through the entirety of the research work, beginning from the phrasing of the title for the thesis to the finding of the results. More than his knowledge and in-depth appreciation for science from the littlest atom to the massive universe, what I will always be indebted to Dr. Basu, is his patience. More often than not, our discussions have resulted in a cease-fire but his immense patience with a novice like me has given me the courage, motivation and spirit to push through and try and reach for the skies (or from the crust to the mantle, in my case). He is my mentor, in all things related to Geology, human nature and theology, linking science to world affairs and religion has made this journey even more endearing.

I would also like to express my gratitude to my committee members: Prof. Andrew Hunt, Prof. Robert Gregory, Prof. Galina Nestell and Prof. Max Hu, for giving the encouragement and sharing insightful suggestions. They have played a major role in polishing my writing skills with valuable inputs to my dissertation.

I would like to express my thanks to the Department of Earth and Environmental Sciences and the College of Science at the University of Texas at Arlington for providing me with financial support.

In everyone's life, at some time, our inner fire goes out. It is then burst into flame by an encounter with another human being. We should all be thankful for those people who rekindle the inner spirit. - Albert Schweitzer

To me, these people are beacons of hope during my times of despair. During the different phases of my life, the people who have stood beside me and been my rocks, Somiddho Bosu, ds/dt, Ranita Bera, Tamara Adams, Jiayi Wang, Swapnendu Goon and Ohood Bader Al Salem. I have nagged all of you to death with my constant outbursts of self-pity, thank you for not turning your backs on me. Shariva Darmaoen, Soumyava Das, Souvik Das, Sinjinee Sardar, Jenny Rashall, Lu Zhu, Subharag Sarkar and Neeraj Gill, thank you for holding me at an invariant point when pressure and temperature started acting up. To Jordan Wright, thank you for helping me out with the analytical lab work from ion exchange chemistry to rock dissolution. My heartfelt thanks go out to Biplob Chatterjee, Dr. Bhabesh C. Sarkar, my uncles, Atanu Sen and Jayanta Acharya and aunties Avipsa Ghosh and Sumona Das, for their unerring support and belief in me.

Last but not the least, my everlasting gratitude to my mum and dad (Juju) who have never for a moment let me forget my purpose in life. They have listened to me vent my frustration out at 2am in the morning and 2pm in the afternoon, keeping in mind the 11.5 (-1) hours' time difference. They have never let me wallow in self-pity and have raised me up from the deepest pits of low self-esteem simply by listening to my rants. You are the reason why I am still a 10 on the Moh's scale.

This dissertation is dedicated to my late grandfather, Anil Kr Sen (NumNum), whose life long wish was to see my mum get her doctorate. This attempt is in your honor.

May, 2019

TABLE OF CONTENTS:

PROJECT 1	13
A MINERALOGICAL-GEOCHEMICAL EVIDENCE FOR THE ORIGIN OF THE LATE-CRETACEOUS EAGLE FORD SHALE OF SOUTH TEXAS	13
CHAPTER 1:	15
MINERALOGY AND GEOCHEMISTRY OF THE EAGLE FORD SHALE OF SOUTH TEXAS	15
1.1.1. INTRODUCTION	15
1.1.2. GEOLOGICAL SETTING	17
1.1.3. MINERALOGY	23
1.1.3.1. Methods	23
1.1.3.2. Results	24
1.1.3.3. Discussion of XRD and Petrology	27
1.1.3.4. Discussion of the source of Phosphorus in continental arc setting	31
1.1.3.5. Discussion of the source of Nitrogen (N ₂)	32
1.1.3.6. Results and discussion of sources of trace metal (nutrient elements)	33
1.1.4. U-PB AND LU-HF ANALYSIS OF ZIRCONS IN ASH BEDS	45
1.1.4.1. Methods	45
1.1.4.2. Results	48
1.1.4.3. Discussion	49
1.1.5. RE-OS ISOTOPE SYSTEMATICS	53
1.1.5.1. Methods	53
1.1.5.2. Results	54
1.1.5.3. Discussion	55
CHAPTER 2:	57
RAMAN MICROSCOPIC STUDY OF KEROGEN MATURITY	57
1.2.1. Introduction	57
1.2.2. Methods	59
1.2.3. Results	63
1.2.4. Discussion	64
CHAPTER 3:	67
HIGH PRECISION STRONTIUM (SR)-ISOTOPES AT THE OCEANIC ANOXIC EVENT 2 (OAE2)	67
1.3.1. Introduction	67
1.3.2. Methods	68
1.3.3. Results	69
1.3.4. Discussion	71
CONCLUSION	73
PROJECT 2	75
SYNCHRONOUS ACID VOLCANISM WITHIN THE DECCAN: PLUME HEAD-INDUCED ANATEXIS NEAR THE END-CRETACEOUS MASS EXTINCTION	75

CHAPTER 4:	77
SYNCHRONOUS ACID VOLCANISM WITHIN THE DECCAN: PLUME HEAD-INDUCED ANATEXIS NEAR THE END-CRETACEOUS MASS EXTINCTION	77
2.1. Introduction	77
2.2. Methods	81
2.3. Results	81
2.4. Discussion	84
2.5. Conclusion	94
REFERENCES	95
APPENDIX	113

LIST OF FIGURES

FIGURE 1: EAGLE FORD SHALE PLAY AND THE WELLS PERMITTED AND COMPLETED UNTIL DATE (TEXAS RAILROAD COMMISSION, 2019)	16
FIGURE 2: PALEOGEOGRAPHIC MAP OF THE LOCATION OF THE MID-CRETACEOUS EF BLACK SHALE DEPOSITS OF SOUTH TEXAS WITH RESPECT TO THE CRETACEOUS WESTERN INTERIOR SEAWAY OF NORTH AMERICA, MAP MODIFIED FROM BLAKEY, 2014.....	18
FIGURE 3: LOCATION OF SUBSURFACE WELLS OF EAGLE FORD SHALE USED IN THIS STUDY. MAP MODIFIED FROM TEXAS RAILROAD COMMISSION.....	19
FIGURE 4: GENERALIZED STRUCTURAL FEATURES NEAR LATE CRETACEOUS STRATA IN TEXAS OUTCROPS ARE OUTLINED IN DARK GREEN. MAP MODIFIED FROM WORKMAN AND GRAMMER, 2013.....	21
FIGURE 5: VOLCANOGENIC ASH BEDS (LIGHTER IN COLOR) AND CALCITE IN KEROGEN IN THE SUBSURFACE EAGLE FORD CORE WELL 8. NOTICE HOW THE THICKNESS OF VOLCANIC ASH BEDS VARIES RANGING FROM 1 CM TO 6 CM.	22
FIGURE 6: VOLCANOGENIC ASH BEDS (LIGHTER IN COLOR) AND CALCITE IN KEROGEN IN THE SUBSURFACE EAGLE FORD CORE WELL 8.....	22
FIGURE 7: MODAL MINERALOGY FROM XRD REPRESENTED IN A PIE DIAGRAM (A) FOR A SAMPLE FROM WELL 20 AND ITS SPECTRA (B) SHOWING THE VOLCANOGENIC SWELLING CLAYS	25
FIGURE 8: VOLCANOGENIC SWELLING CLAY WEIGHT PERCENTAGE IN FOUR SUBSURFACE CORES PLOTTED VERSUS THE DEPTHS IN EACH CORE.	26
FIGURE 9: TOTAL CLAY WEIGHT PERCENTAGE IN FOUR SUBSURFACE CORES PLOTTED VERSUS THE DEPTHS IN EACH CORE.....	27
FIGURE 10: PLAGIOCLASE WITH PLANKTONIC FORAMINIFERS IN A THIN SECTION OF THE WELL 8, AT A DEPTH OF 13094.3 FT.....	29
FIGURE 11: VOLCANIC (ANDESITIC) ROCK FRAGMENT IN A THIN SECTION OF THE WELL 8, AT A DEPTH OF 13087 FT..	29
FIGURE 12: KEROGEN WITH CALCISPHERES IN A THIN SECTION OF THE WELL 8, AT A DEPTH OF 13379.1 FT.	30
FIGURE 13: BIOTITE IN A THIN SECTION OF THE WELL 8, AT A DEPTH OF 13369.5 FT.....	30
FIGURE 14: ALKALI FELDSPAR FROM THE WELL 8, AT A DEPTH OF 13090.45 FT.	31
FIGURE 15: A-O: HISTOGRAMS OF THE CONCENTRATIONS OF NUTRIENT ELEMENTS (Cu, Co, Cr, Ni, Zn, U, Th, Pb, Sc, Hf, Ta, Mo, Zr, Y AND V) IN ~300 WHOLE ROCK SAMPLES OF SEVEN SUBSURFACE CORES OF EF (WELLS 3, 12, 16, 17, 19, 20 AND 24) IN SOUTH TEXAS. THE BLACK DOTTED LINES IN EACH FIGURE REPRESENT THE AVERAGE CONCENTRATION OF THE SAME NUTRIENT ELEMENT IN THE UPPER CRUST (TAYLOR AND MCLENNAN, 1984, AND MCLENNAN, 2001). THE NUTRIENT ELEMENTS ARE CALLED THE CHEMICAL PARTNERS OF PORPHYRINS FOUND IN THE CENTER OF THE MOLECULE (KEROGEN).	41
FIGURE 16: SUMMARY FIGURE OF THE 15 NUTRIENT ELEMENTS (FIGURE 14: A-O) FOUND IN AVERAGE OF 300 SAMPLES OF EF WHOLE ROCK BLACK SHALES PLOTTED AGAINST THE AVERAGE CONCENTRATION IN SEVEN VOLCANIC ASH BEDS. THE BLACK DOTTED LINE IS THE THEORETICAL BEST-FIT LINE BETWEEN THE TWO PARAMETERS. NOTICE HOW ALL THE ELEMENTS EXCEPT FOR Zr, Cr AND V FALL VERY CLOSE TO OR ON THE LINE ITSELF, INDICATING SIMILAR CONCENTRATION OF THE ELEMENTS IN VOLCANIC ASH AND WHOLE ROCK SAMPLE. THE RELATION BETWEEN THE TRACE ELEMENT CONCENTRATION BETWEEN ASH BEDS AND WHOLE ROCK EF SHALE SHOWS THAT THERE WAS CONTINUOUS VOLCANISM THROUGHOUT THE DEPOSITION OF THE EF SHALE. THE THREE ELEMENTS FALLING BEYOND THE DASH LINE ARE Cr, Zr AND V AND THERE COULD BE MULTIPLE REASONS FOR SUCH APPARENT DISCREPANCY. NOTICE THE TOTAL Fe CONCENTRATIONS IN BOTH THE ASH BEDS AND THE BLACK SHALES ARE REMARKABLY SIMILAR.	42
FIGURE 17: BENTONITE SAMPLES PLOT AS VARIOUS TYPES OF BASALT AND BASALTIC ANDESITE BASED ON THEIR SILICA, SODIUM, AND POTASSIUM CONTENT. A POSITIVE TREND IMPLIES AN INCREASE IN Na ₂ O+K ₂ O AS SiO ₂ INCREASES.	43
FIGURE 18: (A) AVERAGE RARE EARTH ELEMENT PATTERN OF SEVEN ASH BEDS OF EF SHALE ALONG WITH EAGLE FORD GROSS WHOLE ROCKS (B) (~298 SAMPLES) WITH ANDESITIC ARC VOLCANICS SUCH AS THE ANDEAN, ALEUTIAN AND CASCADES. ALSO PLOTTED ARE THE RANGE OF PLUME DERIVED MAFIC VOLCANISM FROM THE ONTONG JAVA PLATEAU. THE CALC-ALKALINE ROCKS ARE SIMILAR TO THE EF SHALE IN CONTRAST TO THE ONTONG JAVA PLATEAU.	44
FIGURE 19: A-D: SEPARATED ZIRCONS OF ASH BEDS IN SUBSURFACE CORES OF EF SHALE.	48
FIGURE 20: RELATIVE POSITIONS OF VOLCANIC ASH BEDS IN THE DIFFERENT DRILL CORES OF THE EF SUBSURFACE DEPOSITS AS SHOWN IN FIGURE 3. HEREIN THE LA-ICP-MS ZIRCON AGES OF THE ASH BEDS ARE SHOWN IN BLACK. THE EF SHALE IS BOUNDED BY AUSTIN CHALK IN THE TOP AND BY BUDA LIMESTONE IN THE BOTTOM. THE EF IS DIVIDED INTO LOWER, MIDDLE AND UPPER PARTS BASED ON NANNOFOSSILS, LITHOLOGY AND	

GAMMA-RAY DATA FROM PIONEER NATURAL RESOURCES PVT. LTD. THE EF DIPS AT A SHALLOW ANGLE FROM WEST TO EAST. FOR THE TOPS OF THE EF SHALE IN SUBSURFACE CORES, THE DEPTH VARIES FROM 13100FT TO 13950FT.....	50
FIGURE 21: RELATIVE POSITIONS OF ZIRCON U-Pb AGES FROM EF ASH BEDS WITH RESPECT TO THE OUTCROP SAMPLES OF THE DEL RIO AREA (BOQUILLAS FORMATION.). THIS NON-CORRESPONDENCE OF U-Pb AGES ARE SHOWN IN THIS FIGURE.	51
FIGURE 22: AN EXAMPLE OF Nd-Hf ISOTOPIC DATA SIMILAR TO OUR EF DATA OBTAINED FROM AN ANDESITIC VOLCANISM IN CENTRAL MEXICAN BELT. MAP MODIFIED AFTER CAI ET AL., 2014.....	52
FIGURE 23: ISOTOPE EVOLUTION OF THE CONTINENTAL CRUST AND MANTLE. THE MANTLE SLOPE CORRESPONDS TO A CHONDRITIC RE/OS RATIO AS SHOWN BY ALLEGRE AND LUCK (1980).	54
FIGURE 24: RE-OS ISOCHRON DIAGRAM. ONLY THREE OF THE WHOLE ROCK BLACK SHALE SAMPLES FALL ON AN ISOCHRON DIAGRAM SUGGESTING A PROBABLE AGE OF 76 MA FOR OIL GENERATION. THE NON-LINEAR RELATIONSHIP OF SEVEN WHOLE ROCK DATA POINTS MAY BE DUE TO MOBILITY OF THE KEROGEN RICH LAYER AND MIXING WITH THE KEROGEN POOR SEDIMENTS.	55
FIGURE 25: OIL SAMPLE FEATURES CAN BE DETERMINED USING VIDEO MOSAIC IMAGE. THE RED SQUARE IS THE AREA WHERE RAMAN IMAGING WAS PERFORMED.....	58
FIGURE 26: SUPERIMPOSED VIEW OF VIDEO AND RAMAN IMAGES WITH THE KEROGEN IN RED.	58
FIGURE 27: LOCATIONS OF THE G (GRAPHITIC) AND D (DISORDERED) BANDS IN THE RAMAN SHIFT IN TWO DIFFERENT SAMPLES OF VARYING KEROGEN MATURITY. DEPENDING ON CHANGE IN MATURITY, THESE PEAKS MOVE CLOSER OR FURTHER AWAY FROM EACH OTHER.	61
FIGURE 28: RAMAN IMAGING OF KEROGEN RICH FORAMINIFERAL TEST (RED SPOT) IN THE MARL (DULL BROWN COLOR, INDICATING PRESENCE OF KEROGEN, UNDER 10X, CONFOCAL LENS, IN REFLECTED LIGHT).	62
FIGURE 29: RAMAN SPECTRA OF THE SPOT IN FIGURE 28.....	62
FIGURE 30: PLOT OF THE TOTAL ORGANIC CARBON (TOC), T _{MAX} AND Ro% OF WELL 8 AGAINST THE DEPTHS SHOWS A CORRELATION BETWEEN THE THREE PARAMETERS. WITH DEPTH, IT IS SEEN THAT THE TOC, T _{MAX} AND Ro% BEAR A LINEAR CORRELATION WITH EACH OTHER. WITH INCREASE IN TOC, THE OTHER TWO INCREASE AND VICE VERSA, ALONG THE DEPTH. THERE IS A CHANGE IN THE VARIATION, NEAR THE C/T BOUNDARY AROUND 13200FT MARK.	64
FIGURE 31: G-D (RBS) IS MAPPED ALONG THE DEPTH OF THE 300 FT LONG WELL 8 CORE. THERE IS A VERY SMALL VARIATION IN THE RBS OVER THIS VERTICAL EXTENT. THE KEROGEN MATURITY SHOULD FALL WITHIN A SHORT BOUND DUE TO THIS SMALL RBS VARIATION, INDEPENDENT OF DEPTH.	65
FIGURE 32: RBS VS Ro% FOR BLACK SHALES ACROSS NORTH AMERICA AND SAUDI ARABIA, OF DIFFERENT AGES OF FORMATION, CREATE A CURVE THAT HELPS IN THE ESTIMATION OF THE RBS OR Ro% DEPENDING ON THE UNKNOWN. THE BEST-FIT CURVE IS A POLYNOMIAL WITH R ² =0.7735. THE EF BLACK SHALE KEROGEN MATURITY (Ro%) PLOTTED AGAINST ITS RBS FALLS ON THIS BEST-FIT CURVE INDICATING THAT THE METHOD APPLIED IN USING RAMAN AS AN INDICATOR OF THERMAL MATURITY WORKS.	66
FIGURE 33: ⁸⁷ Sr/ ⁸⁶ Sr SEA WATER CURVE FROM 28 CLOSE SPACED CARBONATES IN BLACK SHALES OF 300 FT EF SHALE SUBSURFACE CORE DISPLAYING A LESSER RADIOGENIC INPUT OF ⁸⁷ Sr/ ⁸⁶ Sr DURING C-T EVENT (OAE2) AND LEADING UP TO IT, IN COMPARISON TO THE MOST RECENT GLOBAL ⁸⁷ Sr/ ⁸⁶ Sr SEA WATER CURVE ESTABLISHED BY JENKYN ET AL. (2016) FROM PLATFORM CARBONATES IN ITALY. NOTICE HOW THE CURVE BY JENKYN ET AL. (2016) DO NOT TRACE THE ENTIRETY OF THE OAE2 DURING WHICH THE ENTIRE EF SHALE WAS DEPOSITED BUT DURING THE SHORT DURATION OF C-T BOUNDARY, THEIR SAMPLES SHOW A ZIGZAG VARIATION OF THE ⁸⁷ Sr/ ⁸⁶ Sr WITH MUCH LARGER ERRORS ESSENTIALLY OBLITERATING THE VARIATION OBSERVED IN THIS STUDY. THE LOWERING OF THE ⁸⁷ Sr/ ⁸⁶ Sr RATIOS BEFORE C-T BOUNDARY AND ITS GRADIENT INCREASE IN THE TURONIAN INDICATE ARC SOURCE, SOME CONSIDERING LARGE SCALE GLOBAL ARC VOLCANISM IN THE CRETACEOUS (LEE ET AL., 2018; FIGURE 34).....	70
FIGURE 34: WIDE SCALE GLOBAL VOLCANISM DURING THE CRETACEOUS LEADING TO CO ₂ FLUXES, SOURCED FROM THE VOLCANISMS (ISLAND AND CONTINENTAL ARC VOLCANISMS ESPECIALLY), LEE AND LACKAY, (2015). FROM OUR STUDY, WE CAN CONCLUDE THAT THERE WAS CONTINUOUS, ENORMOUS QUANTITIES OF CO ₂ RELEASED DURING VOLCANISM FROM 84 MA TO 95.5 MA ATLEAST.	72
FIGURE 35: SCHEMATIC REPRESENTATION OF THE ORIGIN OF KEROGEN FROM PHYTOPLANKTON AND VOLCANIC ASH.73	
FIGURE 36: MAP OF PART OF THE INDIAN PENINSULA SHOWING THE APPROXIMATE LOCATIONS OF MANY OF THE ACID IGNEOUS COMPLEXES ASSOCIATED WITH THE DECCAN TRAPS (DT) VOLCANISM AND ITS MAJOR STRUCTURAL TECTONIC FRAMEWORK. ALSO SHOWN, CORRESPONDING U-Pb AGES FROM A RECENT STUDY, SCHOENE ET AL. (2019) FROM REDBOLES, WEATHERING SURFACES BETWEEN THE LAVA FLOWS. THE DATES ARE REFINED FROM STRATIGRAPHIC BAYESIAN MODEL. VERTICAL GREY SHADED BAR REPRESENTS CHICXULUB IMPACT AGE (CLYDE ET AL., 2016), CRETACEOUS-PALEOGENE (K-Pg) 66.016±0.050 MA.	78

FIGURE 37: EW SECTION IN NORTH SAURASHTRA SHOWING 7 KM CRUSTAL THINNING (CHOPRA ET AL., 2014).	80
FIGURE 38: NS SECTION IN JUNAGADH, CENTRAL SAURASHTRA WITH 10 KM UP-WARPING OF MOHO (CHOPRA ET AL., 2014).	80
FIGURE 39: A: HIGH-PRECISION U-Pb AGES IN ZIRCONS OBTAINED BY CA-ID-TIMS METHOD OF TWO ACID GRANOPHYRE INTRUSIVES. B: THE WEIGHTED MEAN AVERAGE AGES OF THE TWO GRANOPHYRES, A7 (65.724 ± 0.017 MA) AND B6 (65.751 ± 0.020 MA), C: THE ACID GRANOPHYRES ARE ONLY ~ 265 KYR YOUNGER THAN THE K-PG BOUNDARY.	82
FIGURE 40: WEIGHTED MEAN LA-ICP-MS U-Pb AGES OF ZIRCONS FROM FIVE ACID INTRUSIVE COMPLEXES IN THE DT ARE SUMMARIZED IN THIS FIGURE ALONG WITH K-PG BOUNDARY AGE (SCHOENE ET AL., 2019). 'N' REPRESENTS THE NUMBERS OF ZIRCONS ANALYZED PER SAMPLE.	83
FIGURE 41: HIGH RESOLUTION RELIEF MAP OF THE PART OF THE INDIAN SUBCONTINENT CONTAINING THE DT INCLUDING THE SAURASHTRA PENINSULA. THE ASSUMED DECCAN PLUME CENTER (RED DOT) YIELDS A U-Pb K-PG AGE (SCHOENE ET AL., 2019). THE DISTANCE OF BARDA-ALECH IS 580KM TO THIS CENTER.	85
FIGURE 42: ALECH AND BARDA LACCOLITHIC ACID INTRUSIONS WITH RING DYKES SOURCED FROM GOOGLE EARTH () AND LITHOLOGIC OUTLINE PLOTTED BASED ON FIELD OBSERVATION (BASU, PERSONAL), GEOLOGICAL MAP OF DE AND BHATTACHARYYA (1971) AND FROM DAVE (1971).	86
FIGURE 43: GEOLOGICAL MAP OF THE PART OF THE RAJULA COMPLEX SHOWING FELSIC BASALTIC DIKES WITH SAMPLE LOCATIONS IN THIS STUDY. THE MAP IS MODIFIED FROM CHATTERJEE AND BHATTACHARJI (2004).	86
FIGURE 44: GEOLOGICAL MAP OF THE GIRNAR LACCOLITHIC-GRANOPHYRIC COMPLEX WITH THE LOCATIONS OF SAMPLES IN THIS STUDY. THIS MAP IS MODIFIED AFTER MATHUR ET AL., 1926.	87
FIGURE 45: PART OF THE PHENAI MATA (PM) GEOLOGICAL COMPLEX ~ 550 KM E OF ALECH AND BARDA HILLS, LYING IN THE NARMADA-SON LINEAMENT (PM IN FIGURE 41 AND 4, 15 IN FIGURE 36). LOCATIONS OF SAMPLES ANALYZED ARE SHOWN IN THE MAP. THE MAP IS MODIFIED AFTER HARI ET AL., 2011.	88
FIGURE 46: OLIVINE LIQUIDUS TEMPERATURES FOR BASALTS AND RHYOLITE-MELTS TEMPERATURES FOR ACIDIC ROCKS.	90
FIGURE 47: INITIAL Nd AND Sr ISOTOPIC COMPOSITIONS OF THE WHOLE ROCK LITHOLOGIES OF THE FIVE INTRUSIVE COMPLEXES IN THE DT ANALYZED IN THIS STUDY.	91
FIGURE 48: A SCHEMATIC DIAGRAM OF THE DECCAN PLUME-HEAD IMPACTING BENEATH THE INDIAN PENINSULA (MODIFIED FROM THE RECENT CROSS-SECTIONAL DIAGRAM PROPOSED BY RICHARDS ET AL., 2015). IN THE INSET, A(ALECH), B(BARDA), G(GIRNAR) AND R(RAJULA).....	93

LIST OF TABLES

TABLE 1: U-Pb ZIRCON DATA OF 14 VOLCANIC ASH BEDS FROM EAGLE FORD, SOUTH TEXAS AND DEL RIO, WEST TEXAS, DETERMINED FROM LA-ICP-MS	114
TABLE 2: LU-Hf ISOTOPE DATA OF ZIRCONS FROM 10 VOLCANIC ASH BEDS OF THE EAGLE FORD SHALE, SOUTH TEXAS AND DEL RIO, WEST TEXAS, DETERMINED BY LA-ICP-MS.	127
TABLE 3: HIGH PRECISION $^{87}\text{Sr}/^{86}\text{Sr}$ RATIOS FROM 300 FT OF THE EAGLE FORD SHALE.....	131
TABLE 4: SOME RARE EARTH ELEMENTS OF EF VOLCANIC ASH BEDS, CALC-ALKALINE (ANDESITIC) ARC EXAMPLES OF THE ALEUTIAN, ANDES AND CASCADES ALONG WITH MAFIC VOLCANISM FROM THE ONTONG JAVA PLATEAU PLUME.	132
TABLE 5: NUTRIENT RICH ELEMENTS FROM THROUGHOUT SEVEN EF CORES. THE VOLCANIC ASH BEDS AND WHOLE ROCK EF SAMPLES HAVE SIMILAR CONCENTRATIONS OF NUTRIENT ELEMENTS.	133
TABLE 6: TI/ZR RATIOS IN SEVEN VOLCANIC ASH BEDS AND ~300 WHOLE ROCK SAMPLES FROM SEVEN SUBSURFACE CORES OF EF BLACK SHALES.	141
TABLE 7: RE-Os ISOTOPE SYSTEMATICS OF EF SHALE. NOTICE THE HIGH RE CONCENTRATION. THE $^{187}\text{Os}/^{188}\text{Os}$ INDICATES CONTINENTAL CRUSTAL ORIGIN.....	142
TABLE 8: RAMAN BAND SEPARATION (RBS/G-D), TOTAL ORGANIC CARBON (TOC), ROCKEVAL PYROLYSIS (T_{MAX}) AND VITRINITE REFLECTANCE ($R_o\%$) PLOTTED AGAINST THE DEPTH OF THE 300 FT LONG WELL 8 CORE.	143
TABLE 9: RAMAN SHIFT SPECTRA ANALYSIS OF 34 BILLETS OF EF BLACK SHALE.	144
TABLE 10: U-Pb ZIRCON DATA OF 10 ACID VOLCANIC ROCKS FROM FIVE COMPLEXES WITHIN THE DT DETERMINED FROM LA-ICP-MS.	146
TABLE 11: U-Pb ZIRCON DATA OF SAMPLES A7 (ALECH) AND B6 (BARDA) DETERMINED USING CA-ID-TIMS.....	153
TABLE 12: LU-Hf ISOTOPE DATA OF ZIRCONS FROM SEVEN ACID VOLCANIC ROCKS FROM FOUR COMPLEXES WITHIN THE DT DETERMINED BY LA-ICP-MS.	154
TABLE 13: LU-Hf ISOTOPE DATA OF ZIRCONS FROM SAMPLES A7 (ALECH) AND B6 (BARDA) DETERMINED USING SOLUTION-MC-ICP-MS.....	157
TABLE 14: MAJOR OXIDES OF WHOLE ROCK SAMPLES AND THEIR CRYSTALLIZATION TEMPERATURES FROM RHYOLITE-MELTS AND OLIVINE LIQUIDUS TEMPERATURES FROM PRIMELT3 AT 2KBAR.	158
TABLE 15: SM-Nd AND Rb-Sr SYSTEMATICS OF ACIDIC ROCKS AND ASSOCIATED BASALTS OF THE FIVE COMPLEXES WITHIN DT.	160

PROJECT 1

A MINERALOGICAL-GEOCHEMICAL EVIDENCE FOR THE ORIGIN OF THE LATE-CRETACEOUS EAGLE FORD SHALE OF SOUTH TEXAS

Puloma Chakrabarty, Ph.D.

The University of Texas at Arlington, 2019

Supervising Professor: Asish R Basu

Abstract:

Petrography, major and trace elements and X-ray diffraction (XRD) analyses of whole rock black shales (marls), Re-Os isotope systematics in kerogen rich shales in a proprietary core of the Eagle Ford Shale in South Texas, LA-ICP-MS U-Pb ages and Hf isotopes of zircons from volcanic subsurface as well as surface exposure ash beds of the Eagle Ford Shale and Boquillas Formation in South Texas were analyzed. In addition, Thermal Maturity estimation of kerogens using Raman microscopic studies was carried out and a high-Precision $^{87}\text{Sr}/^{86}\text{Sr}$ global seawater curve during the Cenomanian-Turonian (C-T) boundary and Ocean Anoxic Event 2 (OAE2) was established.

The mineralogy, major and trace elements of the ash beds suggest their source from nearby arc-derived calc-alkaline volcanism. The $\epsilon_{\text{Hf}(T)}$ of the analyzed ash bed zircons range between 6.6 to -0.6 averaging at +2.68, indicating substantial crustal component in the magmatic arc volcanism in the host magmas of the zircons, similar to arc-volcanism signatures such as the Quaternary andesitic volcanism in Central Mexico. Phenocrysts of biotite, alkali feldspar and andesitic rock fragments are observed from petrographic analyses of marls. High concentration of nutrient metals (Co, Cu, Cr, Sc, Hf, U, Th, V, Zn, Ni, Pb, Mo, Y, Zr and Ta) in whole rock marls and volcanic

ashes indicate contemporaneous arc volcanic activity at the time of marl deposition. Volcanogenic clays, such as montmorillonite, vermiculite, dickite and halloysite 10\AA , ranging from 2 to 12% in modal abundance are determined from XRD of subsurface Eagle Ford bulk marl samples from different depths in 4 cores, indicating continuous volcanism throughout the Eagle Ford deposition. The initial $^{187}\text{Os}/^{188}\text{Os}$ at 93 Ma, the time of deposition of the Eagle Ford of the ten whole rock samples, range between 2.47 to 5.11 with a majority of the samples lying between 2.46 and 3.62. This indicates a continental crustal origin of the Os without taking into account the sea water Os-isotopic composition at 93 Ma.

Zircons from the middle part of the ~300 ft long Eagle Ford cores yield U-Pb ages of 93.2 ± 1.66 Ma, 94.13 ± 1.25 Ma and 93.7 ± 1.9 Ma, consistent with the Cenomanian-Turonian (C-T) age of deposition. An approximate 10 Ma duration of deposition of volcanic ash and marl, at 28 ft/Ma for the Eagle Ford is suggested from the 85.76 to 95.5 Ma ages. These ages are from the Eagle Ford ash beds, between the Austin Chalk and the Buda Limestone, covering the OAE2 at the C-T boundary (93-93.5 Ma).

Using Raman microscopic techniques and RockEval pyrolysis, the EF black shales of the entire Well 8 fall between 0.7-1.4 Ro% and G-D of 240-270 cm^{-1} . The $^{87}\text{Sr}/^{86}\text{Sr}$ values range from 0.707405 – 0.707566 for the 300 ft long EF core, Well 8. The lowering in $^{87}\text{Sr}/^{86}\text{Sr}$ ratios is interpreted as indicating input from less radiogenic arc volcanism.

The continuous arc volcanism during the Eagle Ford deposition of volcanic silicic sediments and carbonates was part of the global continental arc flare-ups in the Cretaceous, responsible for greenhouse conditions and subsequent anoxia during marl deposition.

CHAPTER 1: MINERALOGY AND GEOCHEMISTRY OF THE EAGLE FORD SHALE OF SOUTH TEXAS

1.1.1. INTRODUCTION

A major unconventional source of oil and gas (Harbor, 2011), the Eagle Ford Shale of South Texas was deposited between 84-96 Ma, overlapping the Cenomanian-Turonian (C-T) boundary and Global Boundary Stratotype Section Point (GSSP) in Pueblo, Colorado deposited during 93-93.5 Ma (Leckie et al., 2002; Pierce, 2014). The GSSP and C-T boundary are a part of the global Oceanic Anoxic Event 2 (OAE2) and thereby the Eagle Ford is also a part of OAE2. The OAE2 was suggested to have been triggered by a massive volcanic episode (Turgeon and Creaser, 2008; Vogt, 1989; Jones and Jenkyns, 1994) releasing huge quantities of carbon dioxide (CO₂) into the atmosphere. This sudden accumulation of CO₂ resulted in an increase of delivery of hydrothermally derived and weathered nutrients into the photic zone, consequently resulting in an increase in the primary production. Scholle and Arthur (1980) discovered that marine strata deposited during the C-T boundary were rich in black, pyritic, laminated shales.

The Cretaceous 'black shales' are characterized by contemporaneous episodic deposition of organic-rich, carbonaceous marine sediments, distributed globally (Jenkyns, 1980). These black shales (with CaCO₃ > 60%) are interlayered with volcanic ash beds. These laminated, black shales were extensively studied when they were recognized as potential source rock for both natural gas and petroleum (Schlanger and Jenkyns, 1976). Anoxic conditions were evident from the lack of bioturbation (from burrowing fauna) in the shales during the C-T boundary (Pierce et al., 2014).

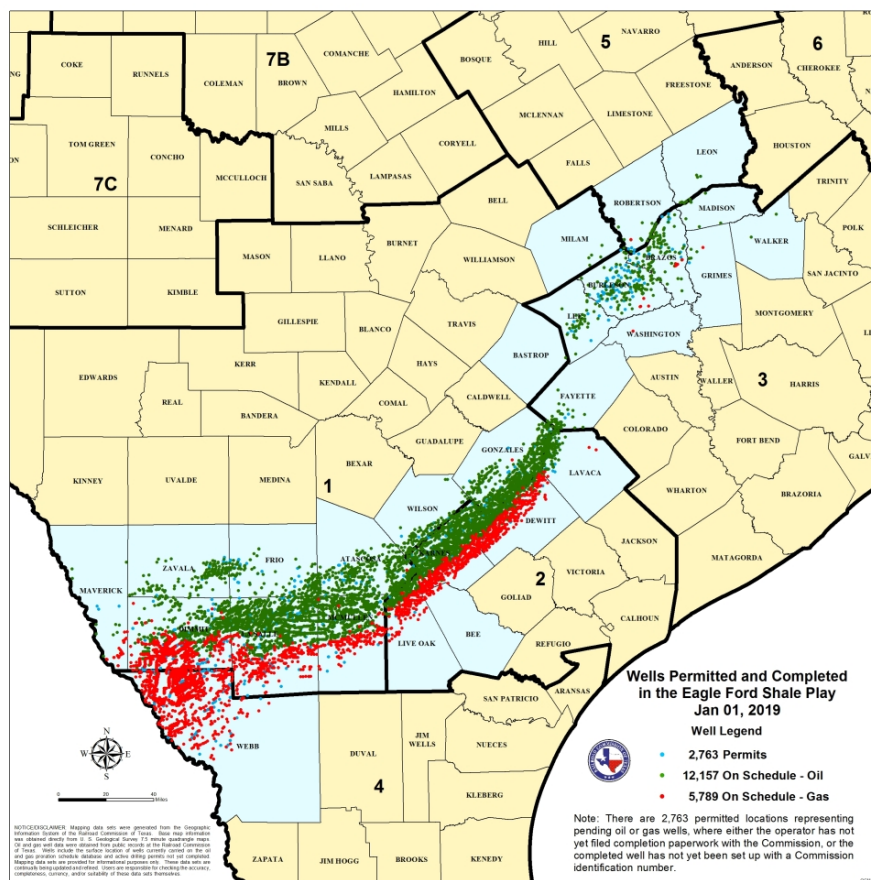


Figure 1: Eagle Ford Shale Play and the wells permitted and completed until date (Texas Railroad Commission, 2019)

In this study, we emphasize on the presence of abundant volcanic ash beds all throughout the subsurface cores of the Eagle Ford Shale from Karnes, Live Oak and DeWitt counties of South Texas (Figures 1, 3). We present a detailed study of these ash beds, including U-Pb geochronology and Lu-Hf isotope systematics of the zircons, separated from the whole rocks to yield their origin and depositional ages, in order to provide a better understanding of the facies architecture of the Eagle Ford Shale. Finally, based on trace element nutrients and rare earth elements (REE) studies of volcanic ash and correlating them with whole rock marls, we propose a novel hypothesis for the origin of petroleum under anoxic conditions. We also provide a high Precision $^{87}\text{Sr}/^{86}\text{Sr}$ analysis of the carbonates separated from the associated hosts of black shales and volcanic ashes and

establish a global $^{87}\text{Sr}/^{86}\text{Sr}$ seawater curve for the duration of the OAE2 event in South Texas. We also establish a volcanic history of the Eagle Ford (EF) Shale by characterization of the clay minerals as volcanogenic in origin using X-Ray diffraction (XRD) studies.

1.1.2. GEOLOGICAL SETTING

During the Late Cretaceous, the Western Interior Cretaceous Seaway split the North America into two land masses, Laramidia and Appalachia (Figure 2). Figure 2 shows a paleogeographic map of the location of the Eagle Ford black shale, marked in red rectangles, with respect to the Cretaceous Western Interior Seaway. From the Arctic Ocean in the north to the Gulf of Mexico in the south, the Western Interior Seaway spanned a length of 4800 km and a width of 1600 km (Kauffman, 1984). Based on lithofacies and faunal assemblages, the sea was approximated to have a maximum depth of 250-300 m during the Late Cretaceous (Kauffman, 1977). The Eagle Ford black shale was deposited during the transgression of the Cretaceous sea (Robinson, 1997) and has a trend around 80 km wide and 650 km long (Figure 3; McGarity, 2013).

The Eagle Ford study area is based on subsurface core samples taken in Karnes, Live Oak and DeWitt counties in South Texas and outcrop samples from Del Rio area of West Texas. The subsurface cores are separated on the surface by ~140 miles and found along the Lower Cretaceous shelf strike and between the Edwards/Stuart City (Albian) and Sligo (Aptian) shelf margins in South Texas (Figure 3). The Edwards/Stuart City and Sligo reef margins are separated on the ground by a distance of 30 miles and converge to the NE near Live Oak and Bee Counties, creating a deposition center and accumulation space for the Eagle Ford sediments (Phelps, 2011) (Figure 3).



Figure 2: Paleogeographic map of the location of the mid-Cretaceous EF black shale deposits of South Texas with respect to the Cretaceous Western Interior seaway of North America, map modified from Blakey, 2014

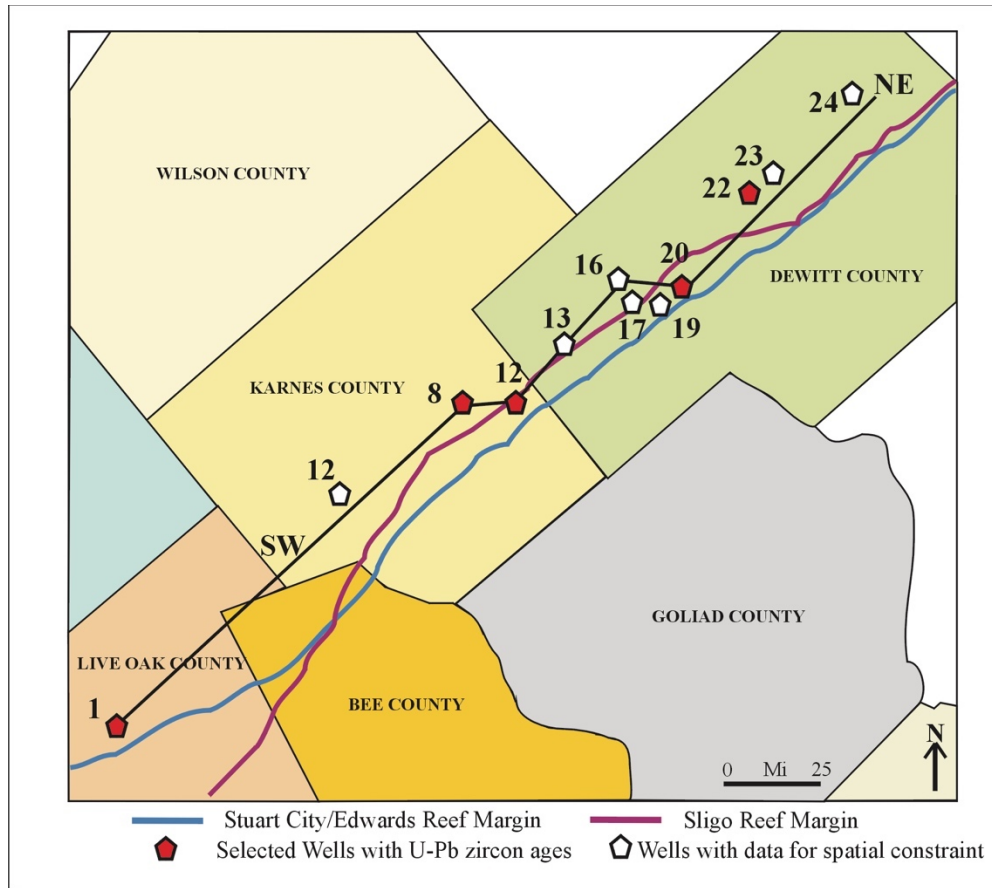


Figure 3: Location of subsurface wells of Eagle Ford Shale used in this study. Map modified from Texas Railroad Commission.

In the east, the Eagle Ford is a primarily a siliciclastic system with influence from the Woodbine Delta whereas in the west, it becomes carbonate-rich due to its distance from the delta system sediments. Increase in rate of subsidence resulted in regional thickening to the west (Hentz and Ruppel, 2010). The Eagle Ford is divided into upper and lower intervals, observed in a decrease in spectral gamma ray (U concentration) in outcrop (Pierce, 2014) and a sharp decrease in the Mo content from upper to lower EF shale in a subsurface core of Eagle Ford (Pierce, 2014). The organic-rich, argillaceous lower Eagle Ford Shale is separated from the more calcitic upper Eagle Ford (Romero et al., 2018).

The Eagle Ford Shale is overlain by the Austin Chalk and underlain by the Buda Limestone (Pierce, 2014). The Austin Chalk contains interbedded organic-rich shales and ash beds (Montgomery, 1990), planktonic foraminifers, calcispheres and coccoliths (Hentz and Ruppel, 2010). The contact between the Eagle Ford and Austin Chalk appears to be gradational in West Texas. In contrast, the Buda Limestone is mostly bioturbated, burrowed gray wackestone with variable clay content and interpreted to be a transgressive-regressive depositional cycle (Pierce, 2014). Addy and Buffler (1984) suggested that there is a widespread unconformity between Buda Limestone and Eagle Ford Shale, and called it, the mid-Cenomanian Unconformity. Figure 4 shows the generalized structural features near the Late Cretaceous strata in the EF West and South Texas outcrops, marked in dark green.

The 300ft long core from Karnes county (Figures 5 and 6) analyzed for the study of U-Pb ages in zircons of ash beds, Lu-Hf isotope systematics of these zircons, their trace elements and major element chemistry study and high Precision $^{87}\text{Sr}/^{86}\text{Sr}$ isotopes of separated carbonates is from a depth of ~13000 ft below the surface of core, Well 8, located southwest of the San Marcos Arch, on the Comanche Platform directly above the Edwards/Stuart City and Sligo Reef margins. Figures 5 and 6 show volcanogenic ash beds (lighter in color) and calcite in kerogen in the subsurface Eagle Ford core Well 8. Notice how the thickness of volcanic ash beds varies ranging from 1 cm to 6 cm.

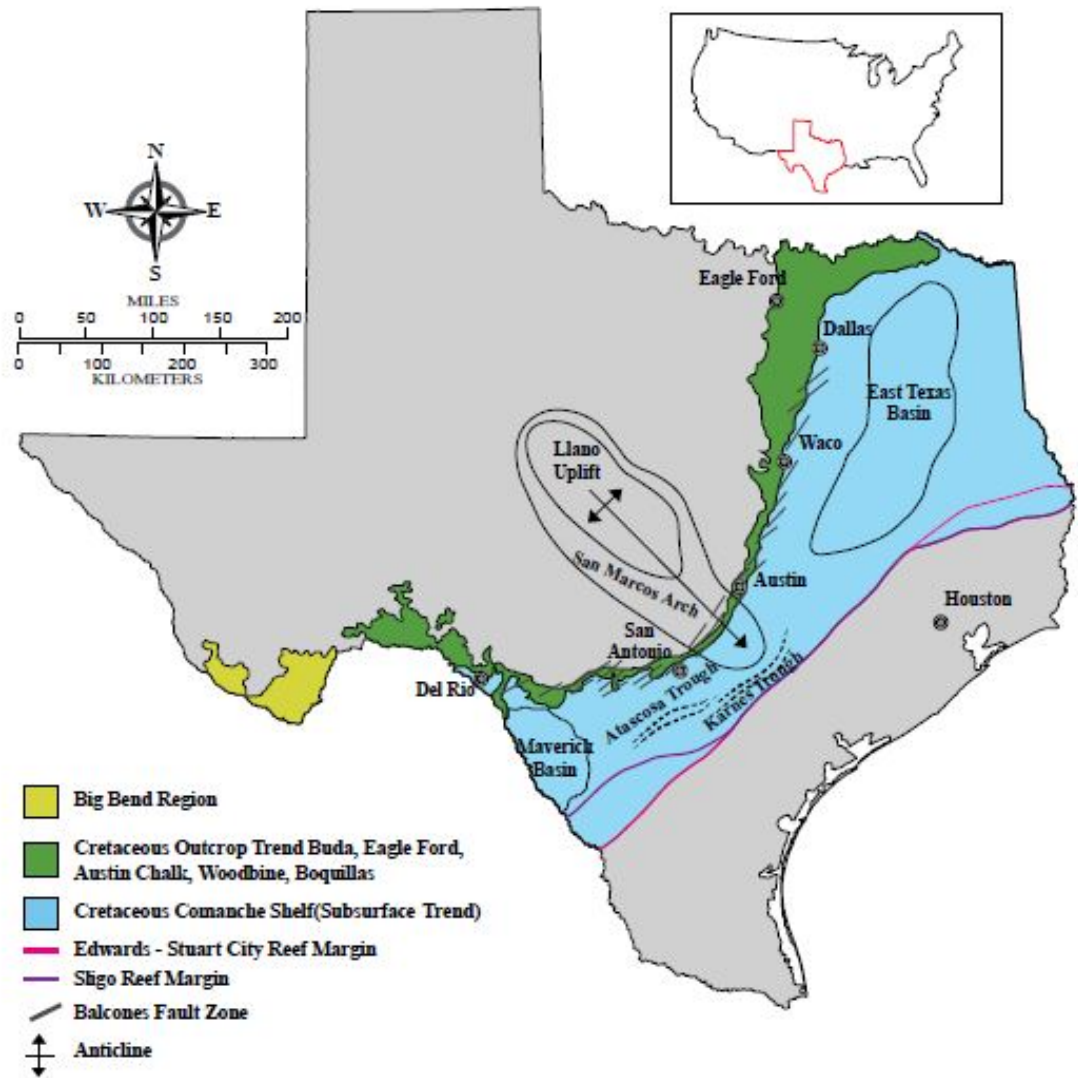


Figure 4: Generalized structural features near Late Cretaceous strata in Texas Outcrops are outlined in dark green. Map modified from Workman and Grammer, 2013.

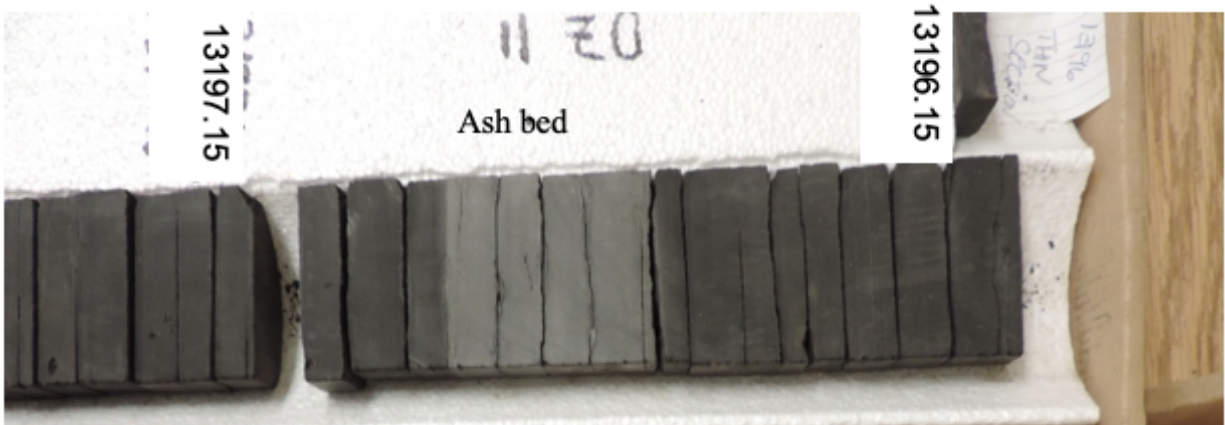


Figure 5: Volcanogenic ash beds (lighter in color) and calcite in kerogen in the subsurface Eagle Ford core Well 8. Notice how the thickness of volcanic ash beds varies ranging from 1 cm to 6 cm.



Figure 6: Volcanogenic ash beds (lighter in color) and calcite in kerogen in the subsurface Eagle Ford core Well 8.

1.1.3. MINERALOGY

1.1.3.1. Methods

X-ray Diffraction (XRD) is instrumental in characterizing mineralogically and modally the different minerals present in a given whole rock sample. Each mineral is characterized based on the diffraction displayed by the different planes of orientation of the crystals in the mineral.

The Bruker D8 Advance X-ray diffractometer in UT Arlington is used to analyze the whole rock samples of the Eagle Ford. At first the NBS standards for calcite, quartz, illite, kaolinite, pyrite and volcanogenic clay (smectites) montmorillonite are analyzed separately to obtain their spectra. These standards are run at a 2θ range of $3-65^\circ$ with a rate of 2° per minute increment and their spectra analyzed. The characteristic peaks are known from their Joint Committee on Powder Diffraction Standards (JCDPS) cards and are analyzed on the Jade 9.0 software. Each mineral present in the spectra is identified qualitatively and semi-quantitatively based on the counts per second (cps) and their 2θ angle. A synthetic composite standard of mixed clay/shale mineralogy was prepared and their XRD spectra were obtained for semi-qualitative model proportions of the black shale minerals.

Around 100 whole rock samples are crushed to a semi-fine powder and are mounted on the sample holder/stage. Usually for running the XRD on clay minerals, different laboratories use Ethylene glycol to spike the peaks of low 2θ angles. However, in the case of swelling clays whose 2θ angles for Montmorillonite are at 5.63° with the addition of ethylene glycol, the angle is reduced beyond the observable/detection limit of the XRD instrument (following Braggs law, $n\lambda=2d\sin\theta$). With increase in d-spacing (as used by the XRD) the 2θ angle drops below 3° , which cannot be detected by the XRD. Thereby we proceed with the analysis without adding ethylene glycol. The

scan range is set at 2θ from 3-65°, and scan rate of 2° per minute. The presence of a mineral is proven on the basis of the presence of three peaks in the XRD spectra based off the established JCPDS cards of the respective minerals, also validated by the standard spectra run for the composite minerals present. The quantitative analysis is based off the counts per second ratios of the different minerals using the software Jade 9.0 which provides us with the pie diagrams of the composition of the whole rock samples. To validate semi-qualitative analysis, the synthetic whole rock analyses spectra are compared to the EF Shale spectra and further validate the correct/accurate modal proportions (Figure 7). The synthetic test cases used varying proportions of calcite, quartz, clays and pyrite. The known samples compared to the EF Shale unknowns provided proof of the accuracy of the software used.

1.1.3.2. Results

XRD of 100 samples yielded modal mineralogy which are represented in Figure 7 (One example from Core 20) in a pie diagram along with its spectra from where the various volcanogenic swelling clays can be identified.

X-ray diffraction of subsurface Eagle Ford samples from different depths corresponding to the entire Eagle Ford Shale show volcanogenic swelling clays such as Montmorillonite, Halloysite 10Å, Vermiculite, Dickite and Nontronite ranging from 2 to 12% throughout the entire core (Figure 8). The amount of swelling clays in the subsurface Eagle Ford samples from different depths suggest continuous volcanism during the Eagle Ford deposition. The calcite composition varied on an average of 35-70% whereas the quartz varied from 15-30%, the pyrite amount is generally <3% of the total modal analysis. Figure 9 shows the total clay weight percentage varying

with depths for four different subsurface cores. These total clays including illite, kaolinite and volcanogenic swelling clays.

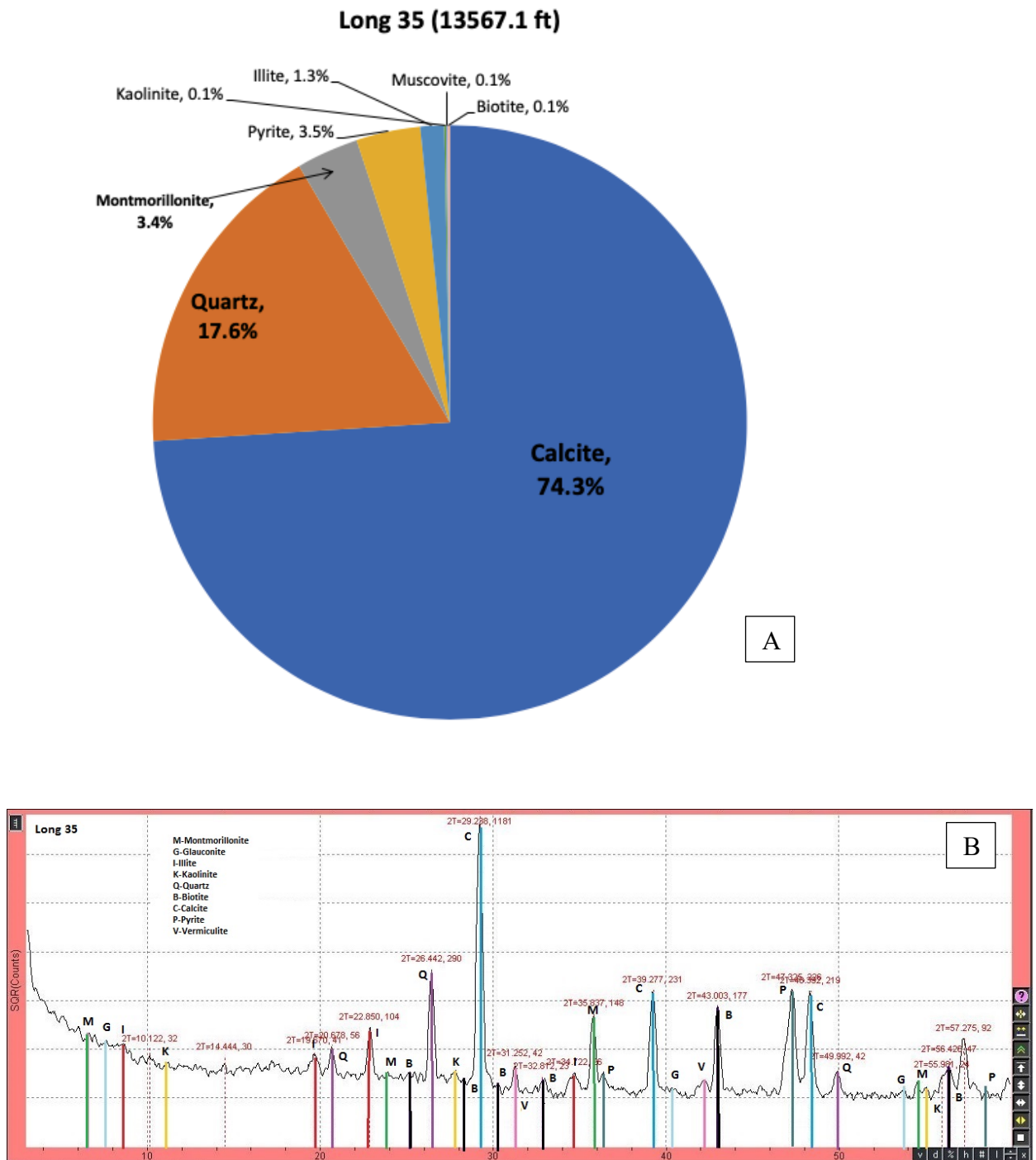


Figure 7: Modal mineralogy from XRD represented in a pie diagram (A) for a sample from Well 20 and its spectra (B) showing the volcanogenic swelling clays

Swelling clay percentage in bentonite beds vs depths in subsurface cores of Eagle Ford

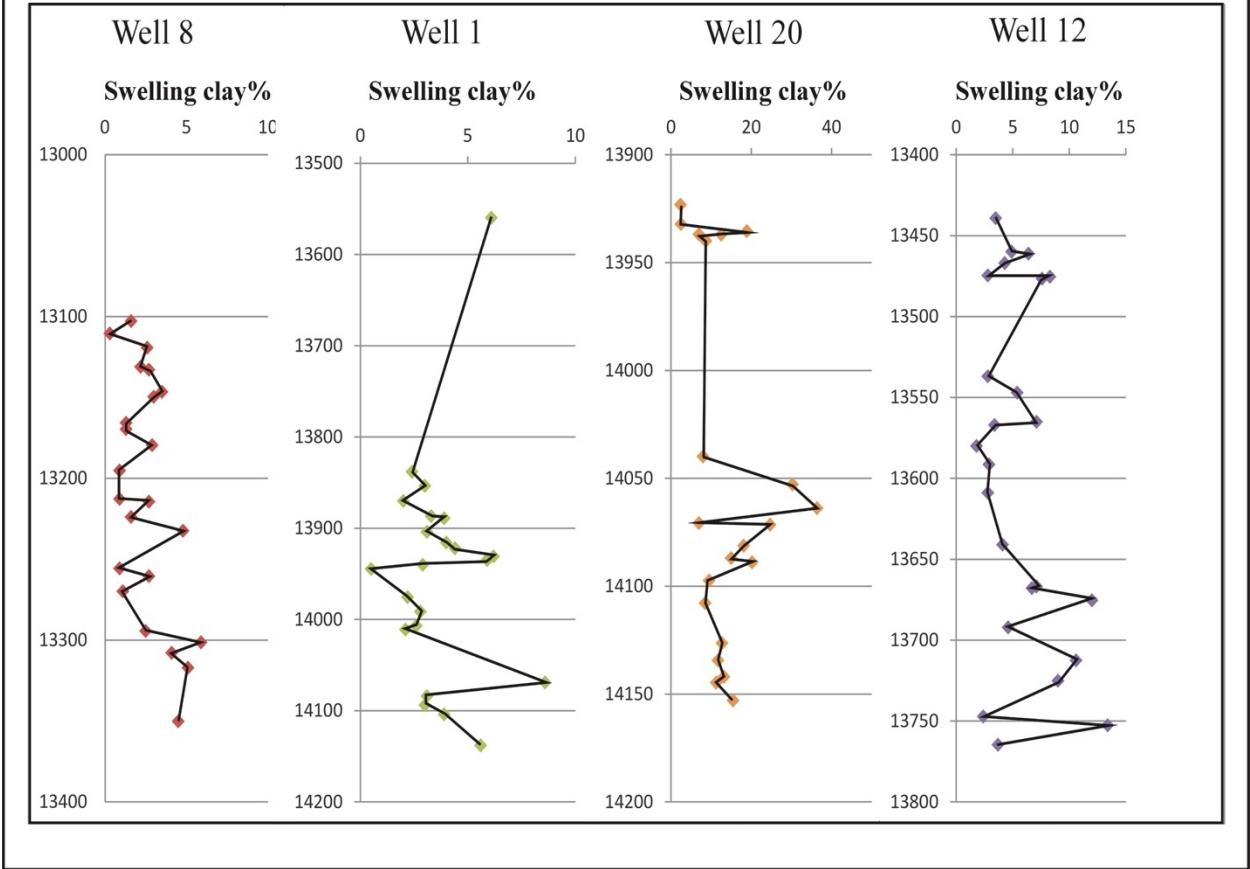


Figure 8: Volcanogenic swelling clay weight percentage in four subsurface cores plotted versus the depths in each core.

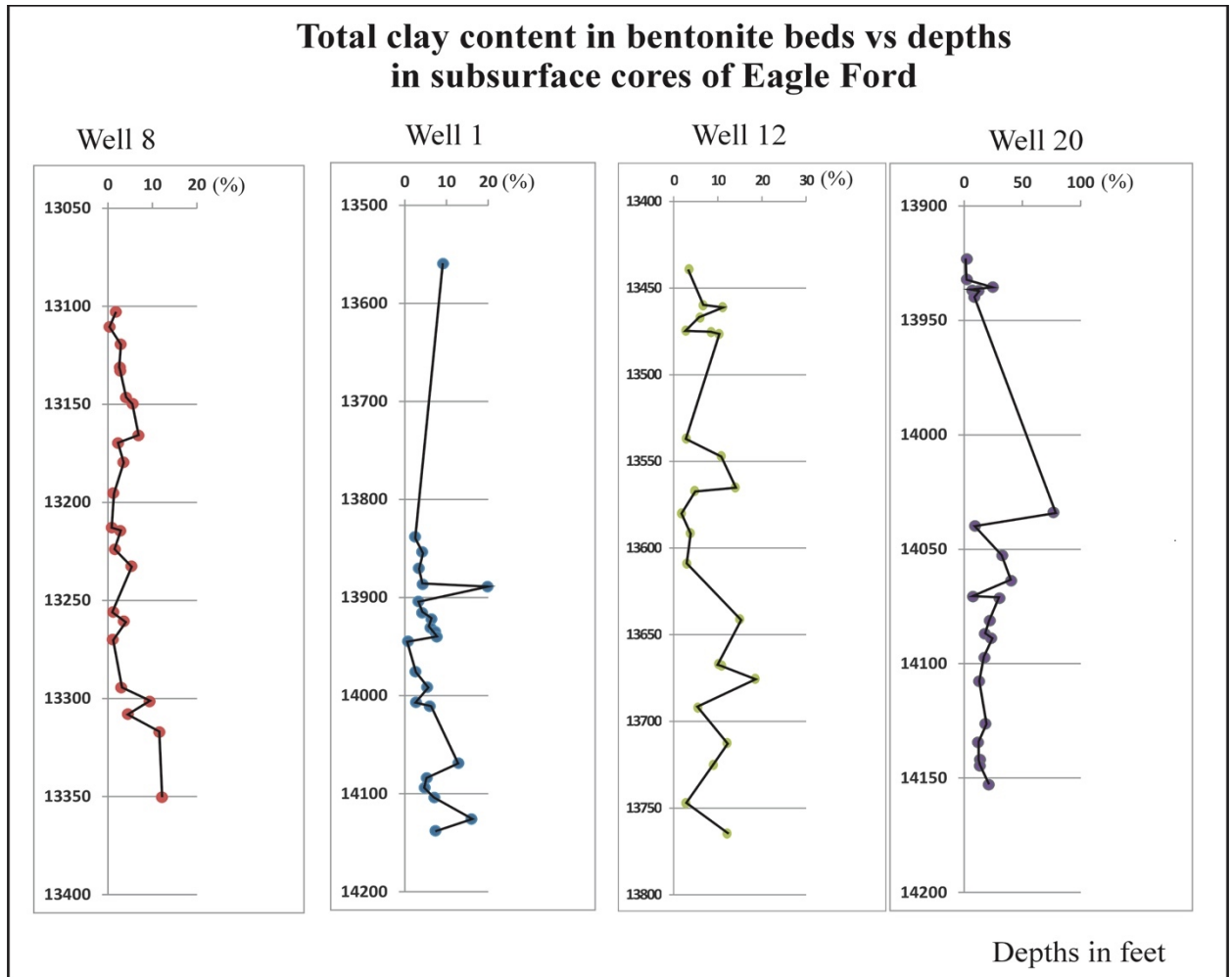


Figure 9: Total clay weight percentage in four subsurface cores plotted versus the depths in each core.

1.1.3.3. Discussion of XRD and Petrology

X-ray diffraction of subsurface Eagle Ford samples from different depths corresponding to the entire Eagle Ford Shale show volcanogenic swelling clays such as Montmorillonite, Halloysite 10Å, Vermiculite, Dickite and Nontronite ranging from 2 to 12% throughout the entire core (Figures 8 and 9). The consistent amount of swelling clays in the subsurface Eagle Ford samples from different depths suggest continuous volcanism during the Eagle Ford deposition.

Phenocrysts of plagioclase (Figure 10), biotite (Figure 13), alkali feldspar (Figure 14), kerogen interspersed with calcispheres (Figure 12) and andesitic rock fragments (Figure 11) are

observed from petrographic analyses of marls. Although the ash layers are mostly altered to clays, euhedral feldspar, quartz and zircons grains of volcanic origin are distinctly observable. We also observe that no detrital quartz or rare lithic fragments are present, not only in the ash, but throughout the EF whole rock samples (Figure 12). This observation strongly suggests that the ash beds or the host-rock marl were affected by clastic sedimentation.

The EF shales show nutrient enriching elements, Ni, Mo, V, Cr, Co, Cu, Zn, U and Pb that are identical to their ash beds sourced from arc volcanism (Figures 15 and 16 and Tables 4 and 5). High concentrations of trace elements in asphaltenes aids increased productivity of phytoplankton and hydrocarbon generation since the nutrient elements are termed as “chemical partners of porphyrins”.

Ti/Zr ratios of the seven volcanic ash beds range from 8.74-49.29 whereas in the case of the ~300 whole rock EF marls from seven subsurface cores, the range is from 23.83-45.16 (Table 6). These ratios are comparable indicating that both Ti and Zr in the whole rock EF shales are derived from the ash component.

250 mg of whole rock ash is dissolved for the ICP-MS analysis from 1 g of the whole rock. The average amount of calcite in the volcanic ash bed is around 10% so the total whole rock ash beds constitute 0.9 g from which 250mg is used for the analysis. On the other hand, 250 mg of whole rock core sample is dissolved for ICP-MS from 6 g of whole rock core. The average calcite is ~70% while quartz is ~15%, leaving the remaining volcanic part to be ~15%. So, the concentration of the nutrient elements present in the whole rock samples are almost equal to those in the volcanic ash beds. In Figure 16, the theoretical best fit line displays the almost equal concentration of the nutrient elements present in whole rock ash as well as whole rock marls of EF Shale.

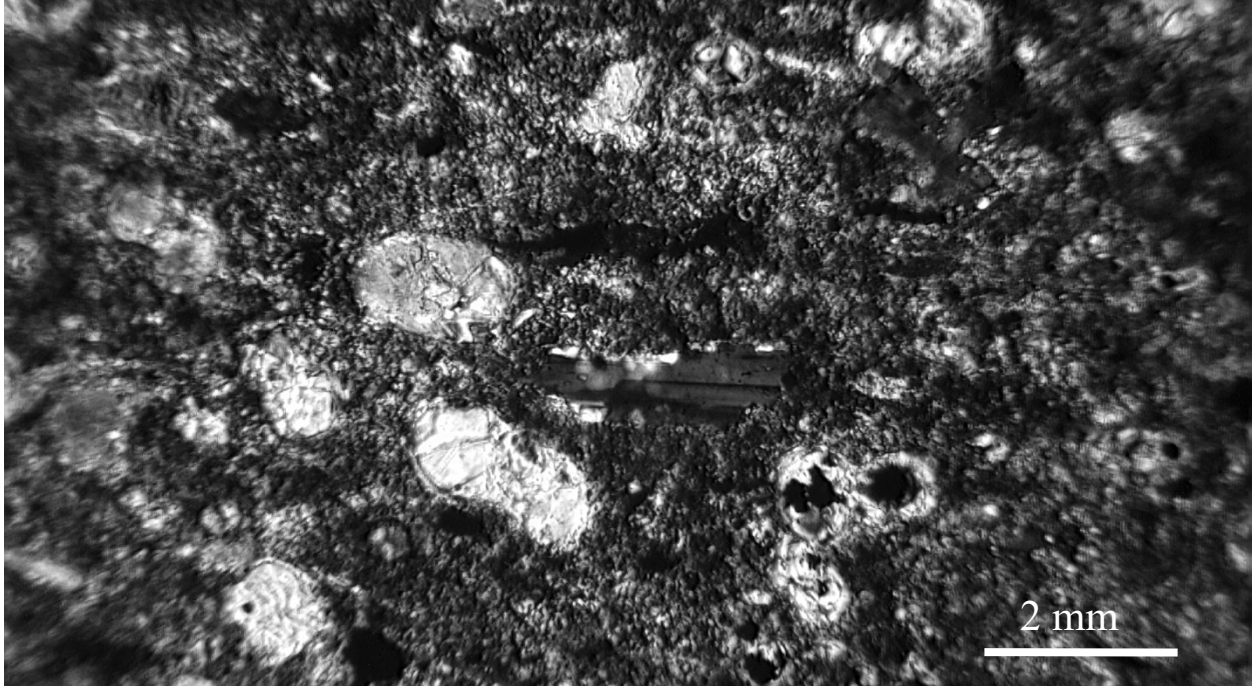


Figure 10: Plagioclase with planktonic foraminifers in a thin section of the Well 8, at a depth of 13094.3 ft.

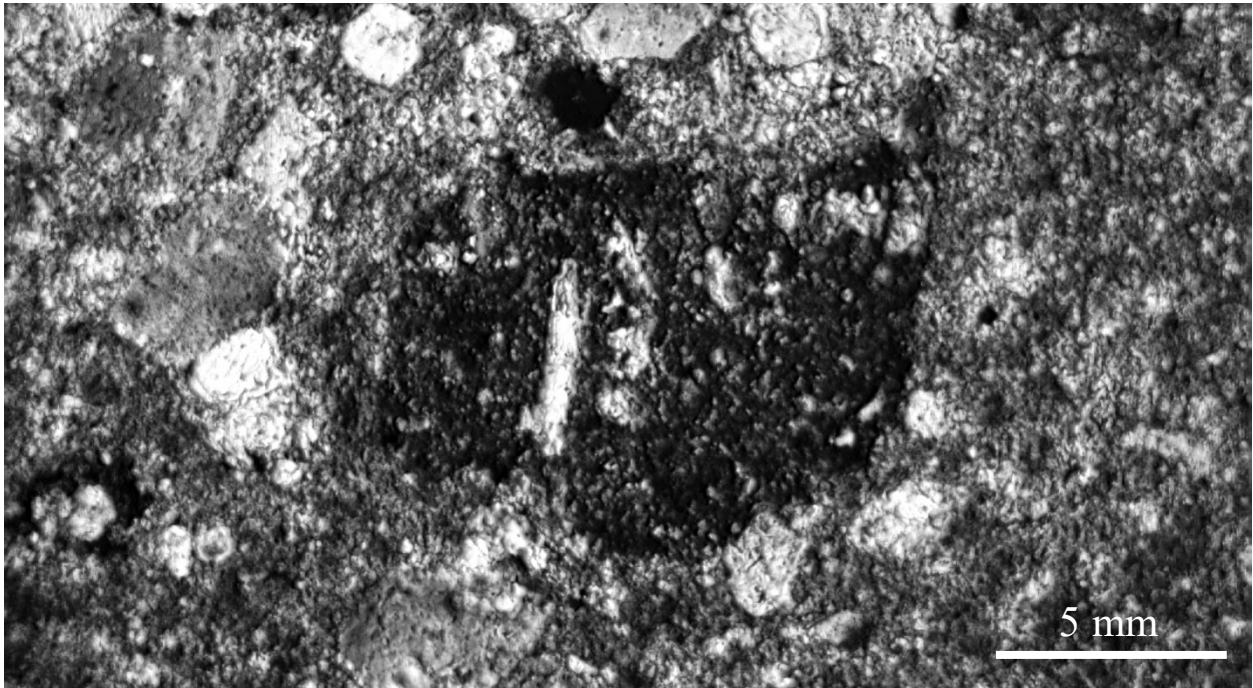


Figure 11: Volcanic (andesitic) rock fragment in a thin section of the Well 8, at a depth of 13087 ft.

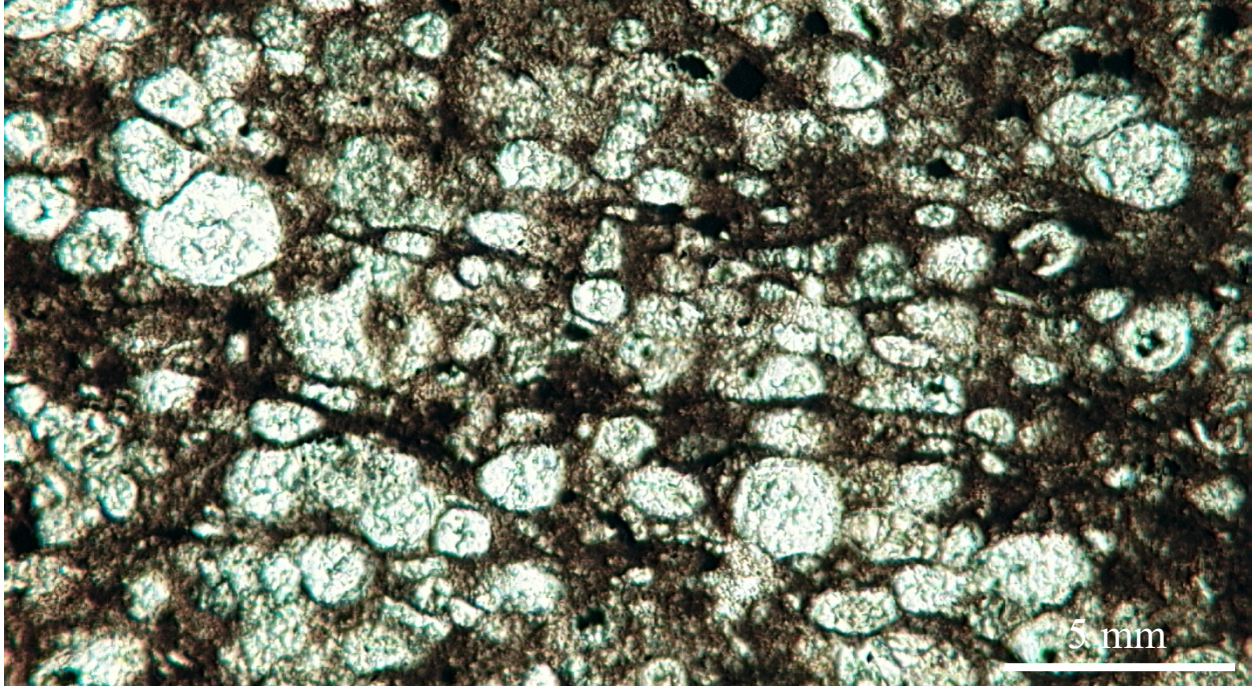


Figure 12: Kerogen with calcispheres in a thin section of the Well 8, at a depth of 13379.1 ft.

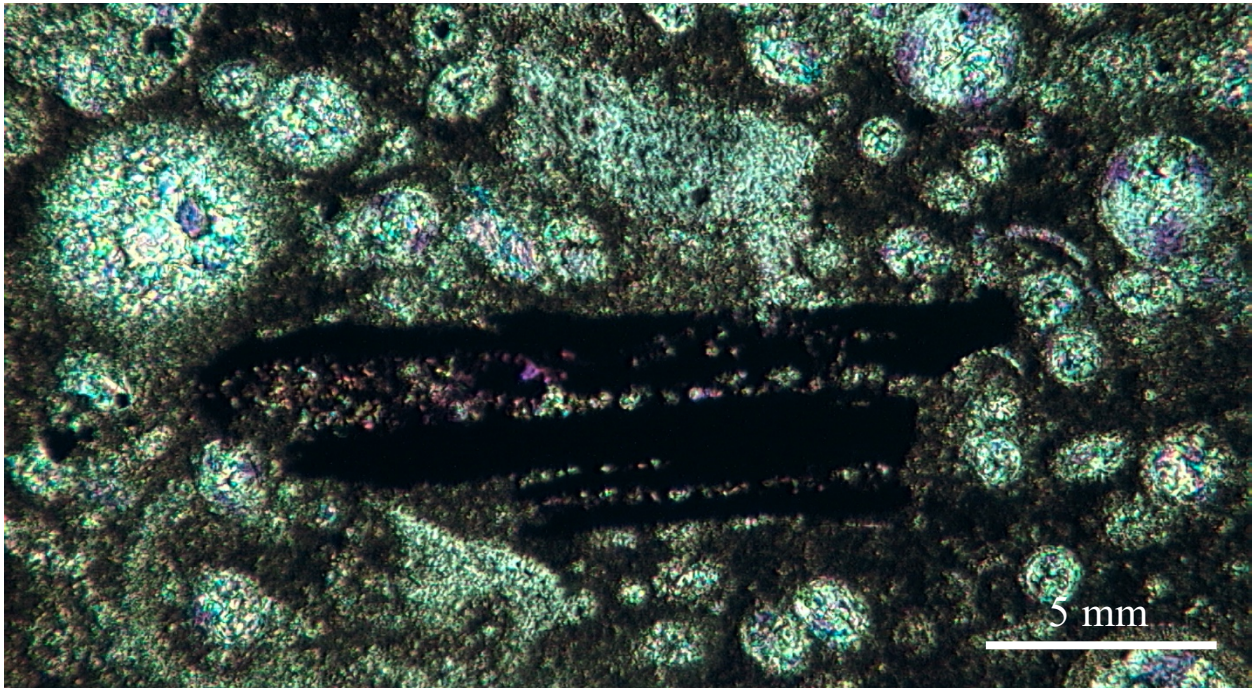


Figure 13: Biotite in a thin section of the Well 8, at a depth of 13369.5 ft.

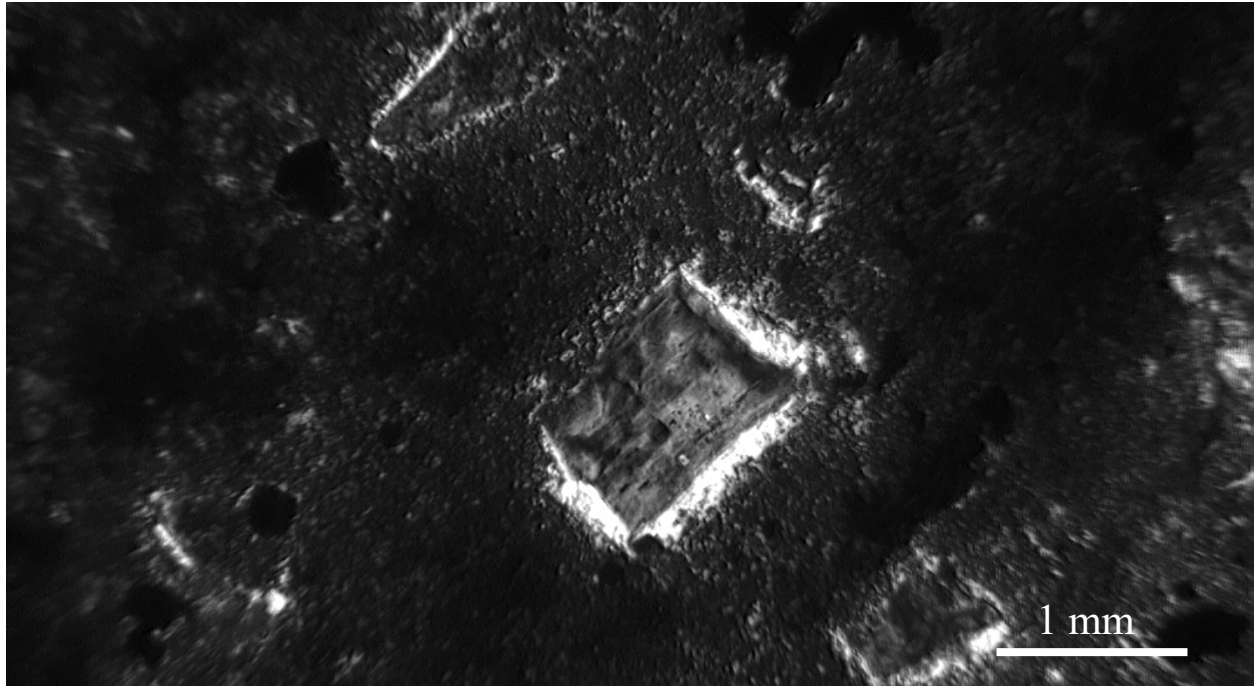


Figure 14: Alkali feldspar from the Well 8, at a depth of 13090.45 ft.

1.1.3.4. Discussion of the source of Phosphorus in continental arc setting

Andesite-dacite-rhyolite volcanism at convergent continental margins is considered the major source of tephra delivered to sedimentary basins (Sharpton and Ward, 1990). Thin volcanic ash beds have been found to be deposited thousands of kilometers from the source by modern studies (Felitsyn, 2004). P, Ca and Sr distributions are shown to be due to the intense weathering of the provenance. The arid weathering influences the mobility of P sourcing from basic volcanic rocks (Felitsyn, 2004). Zanin (1984) confined the P deposition to intense chemical weathering, suggesting that P deposition and weathering were synchronous. The synchronicity was due to the short residence time of P in the oceans ($\sim 10^4$ yr, Ruttenberg (1993) and Felitsyn (2004)) and the increased rate of burial of P and other organic and non-organic sediments during periods of global warming and aggravated continental weathering over the last 160 Ma (Fölmi, 1995). Hartmann et

al. (2014) document the construction of a global database describing weathering, CO₂ consumption and P release using empirical methods. The characteristics of P-release by chemical weathering helps in the prediction of response of ecosystem to changes in environment and identify feedbacks for carbon cycle globally (Porder et al., 2007). Volcanic rocks susceptible to weathering display higher content of P, along with islands with high mountains, arc areas or areas of active volcanism, contribute above average chemical weathering fluxes (Hartmann and Moonsdorf, 2011).

1.1.3.5. Discussion of the source of Nitrogen (N₂)

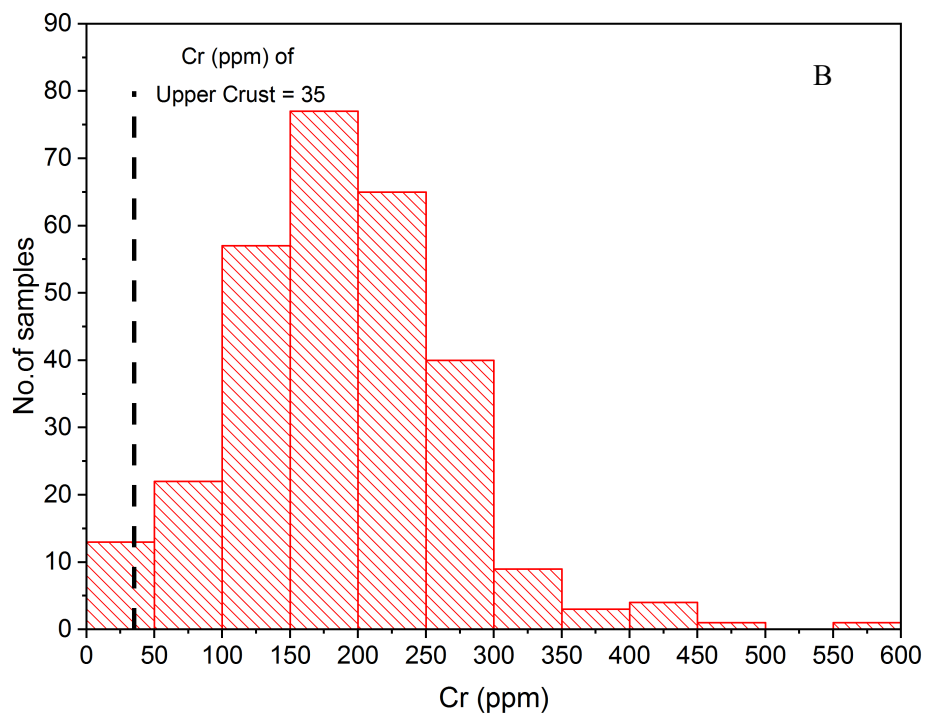
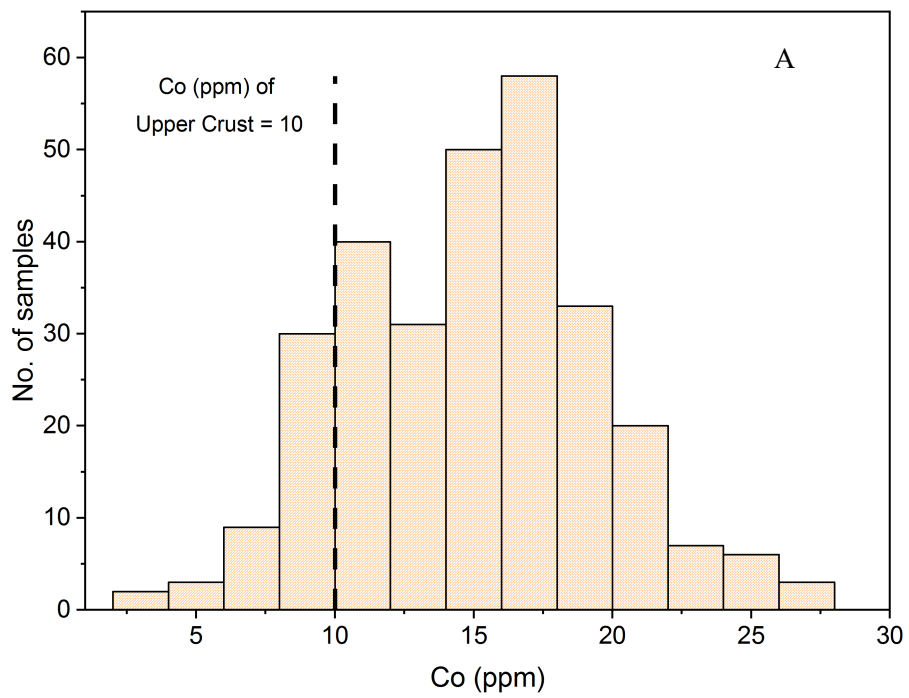
For the Nitrogen sources in subduction zones to be studied, contamination by air and crustal volatile sources have to be eliminated (Zimmer et al., 2004). Potential N₂ sources in subduction zones include mantle wedge, subducting crust and sediments (Sano et al., 2001). Isotopic analyses support the addition of sedimentary N₂ from subducted marine sediments (Marty and Zimmerman, 1999), that nitrogen emitted from arcs has higher ¹⁵N/¹⁴N than MORB (Fischer et al., 2002). Sano et al. (2001) estimates the nitrogen influx from island arc as 6.4x10⁸ mol/yr whereas that of 5.6x10⁸ mol/yr for back-arc basins. This estimate is ~30% of the nitrogen flux from mid-ocean ridges. Symonds et al. (2003) suggest that high N₂/Ar ratios, high non-meteoric N₂ concentrations and heavy δ¹⁵N values indicate sedimentary source of Nitrogen. Most sources of Nitrogen are from the MORBs but a significant amount of N₂ is released and re-released from the Arc volcanics.

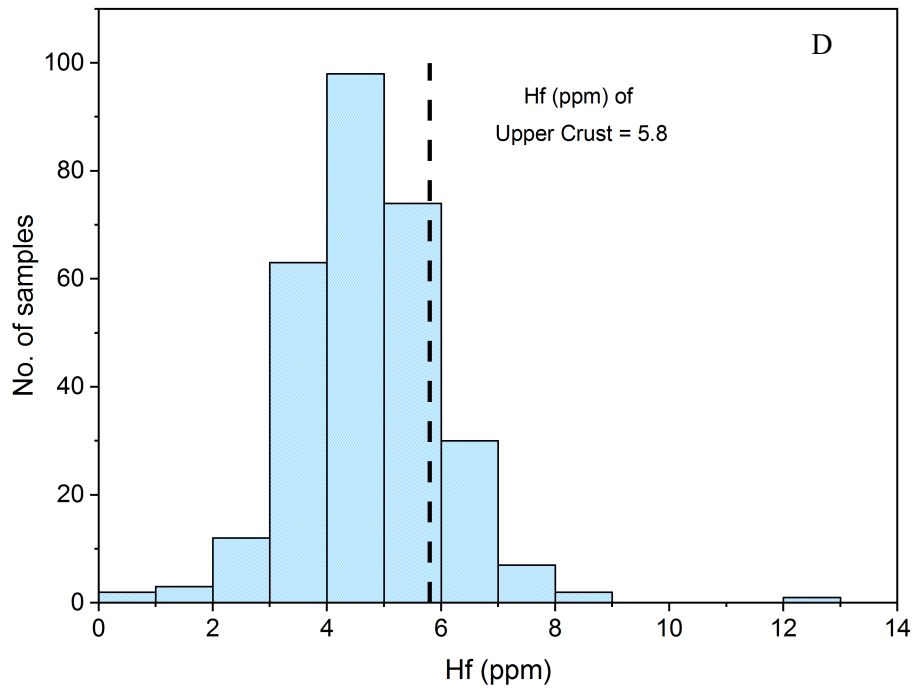
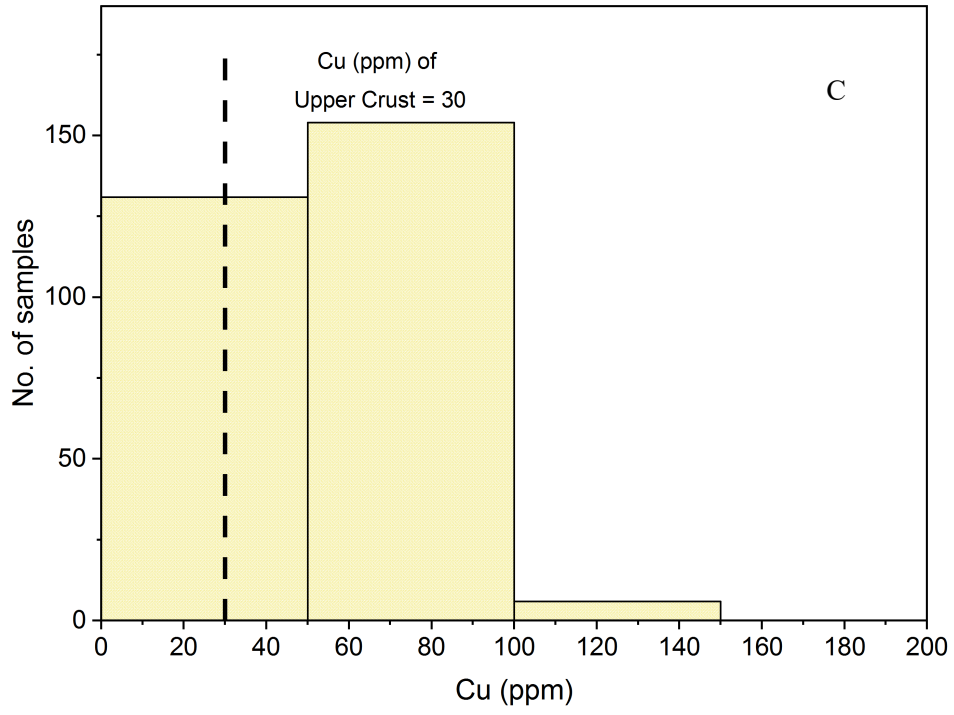
1.1.3.6. Results and discussion of sources of trace metal (nutrient elements)

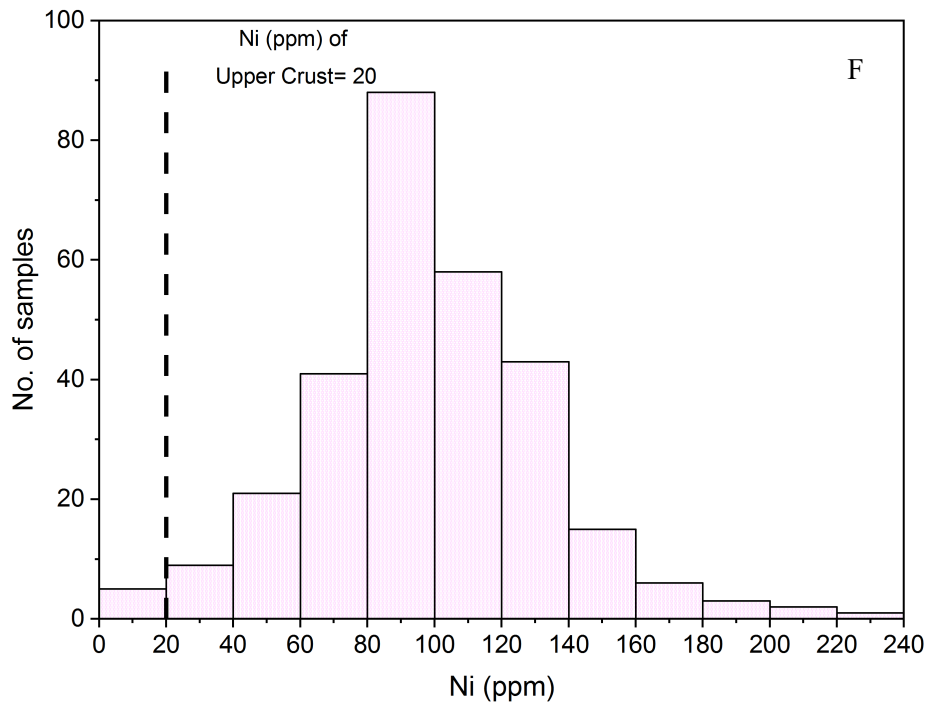
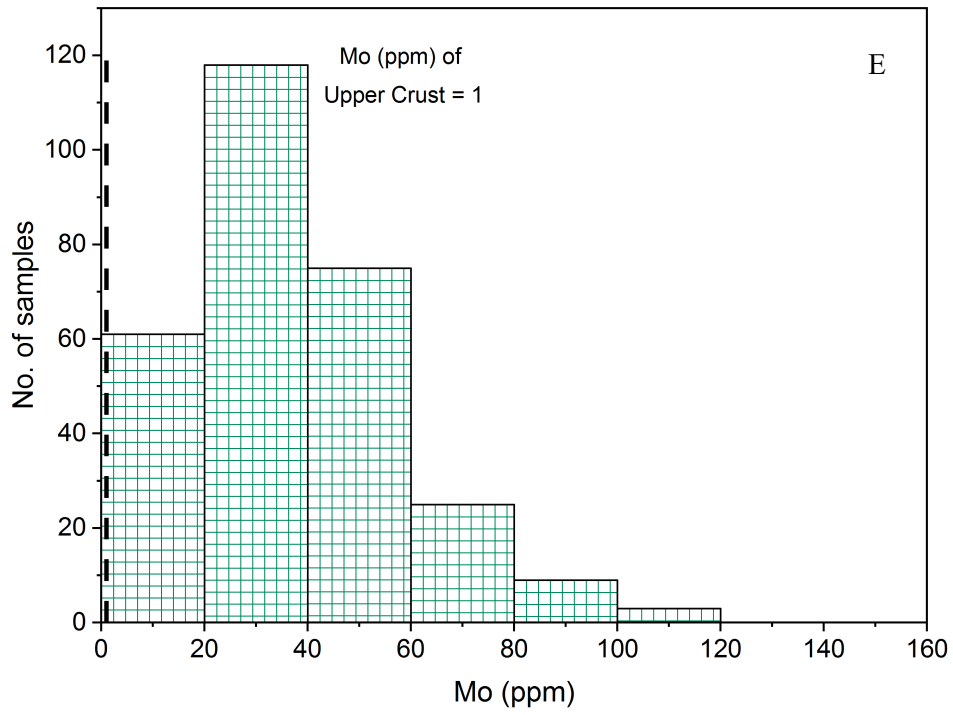
Aerosols contribute to the input mechanism of the trace (nutrient) elements and poorly soluble isotopes having a short residence time in the ocean. The elements Al, Fe and Ti occur in low dissolved concentrations in the ocean waters (Geibert, 2018). It has been established that nutrient trace elements such as Fe, Mn, Co, Cu, Ni and Zn have depleted concentrations in surface sea water, mostly due to biogenic uptake whereas it is found in increased concentrations with depth, due to remineralization of organic matter (Lohan and Tagliabue, 2018). Further studies suggest that the formation Fe-Mn sea floor ore deposits are most likely not from biological processes given their poor understanding (Zubkov et al., 2018) but from volcanic hydrothermal sources (Lusty and Murton, 2018; Murray and Renard, 1891). Zircon being a heavy mineral is immobile in the ash, showing more concentration in ash beds than the adjacent whole rock marls. Cr and V being organophilic, prefers affinity with the kerogen, thereby resulting in more concentration in whole rock marls than in volcanic ash.

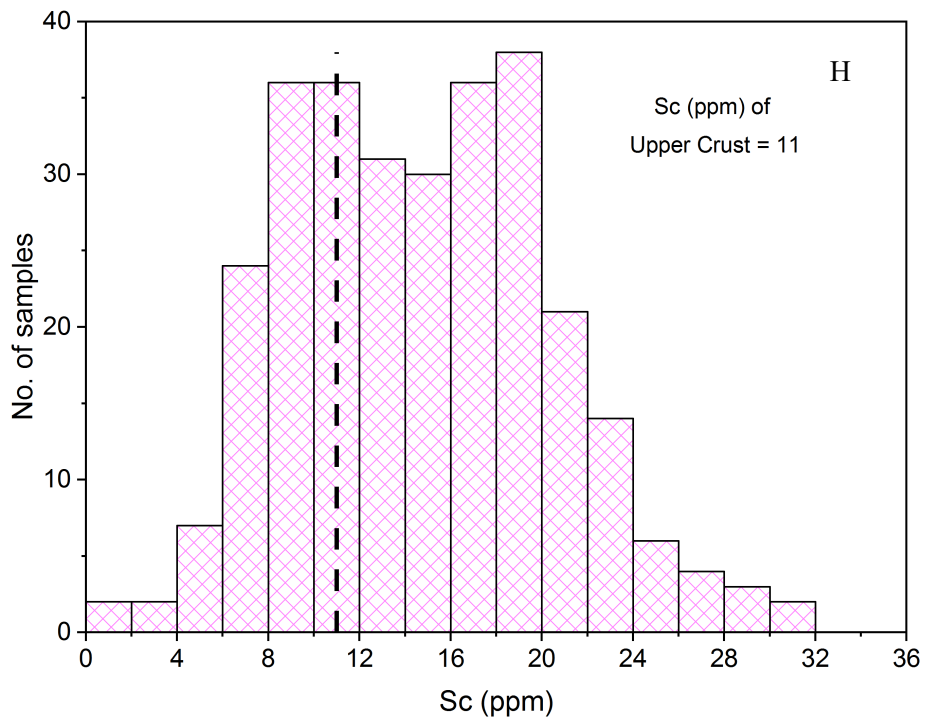
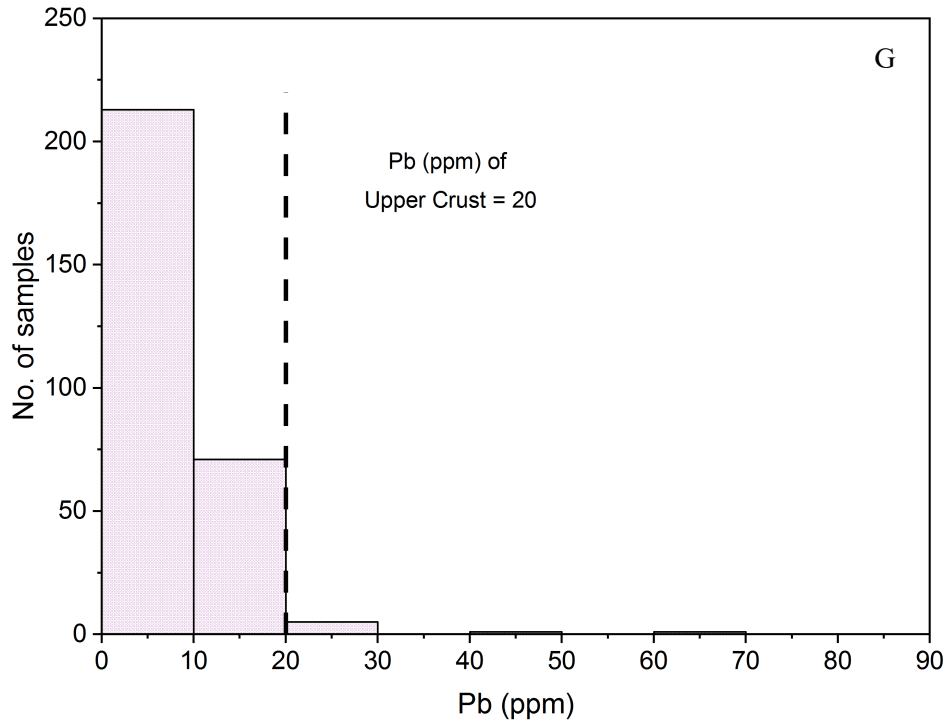
Figure 17 shows that the rare earth element patterns of seven ash beds of EF shale match with the andesitic arc volcanisms associated with the Aleutian, Andean and Cascades. The range of plume-derived mafic volcanism from the Ontong Java Plateau is also plotted alongside these andesitic volcanics. The EF shales are similar to the calc-alkaline rocks in contrast to the plume derived mafics from the Ontong Java Plateau.

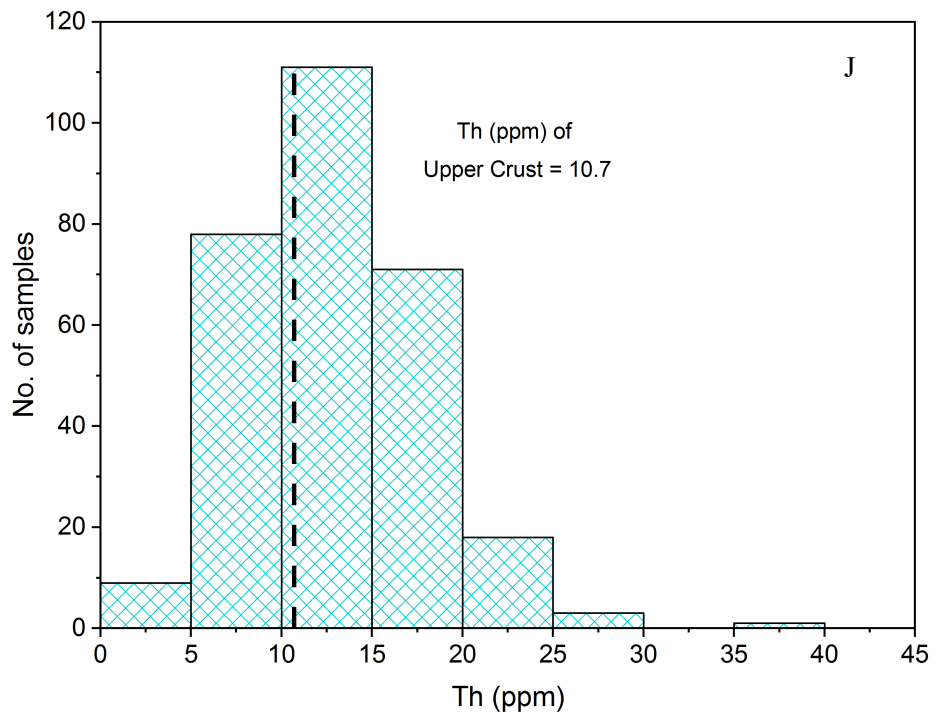
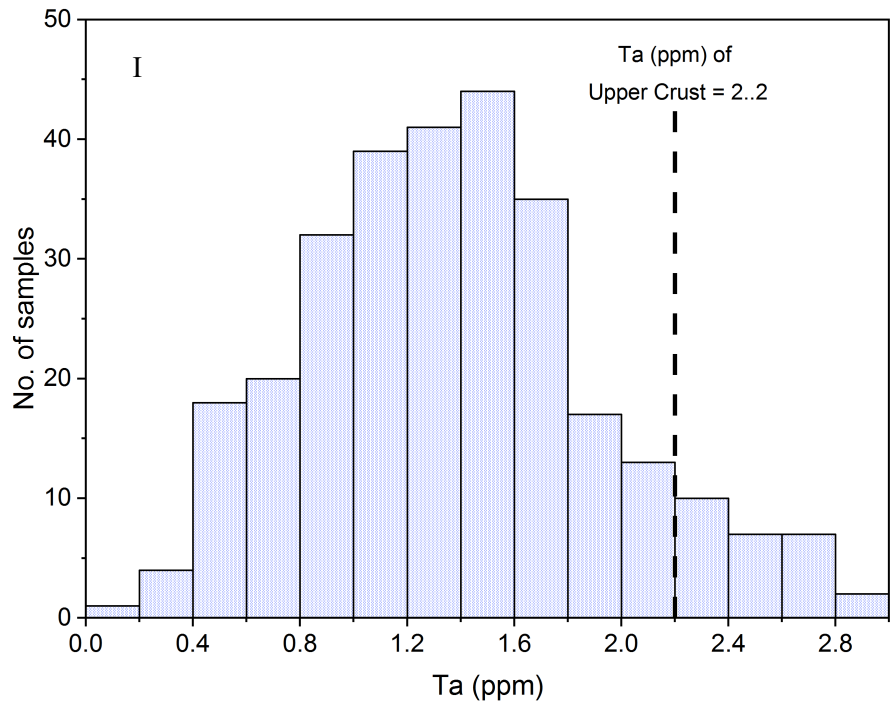
Figure 18 shows that the Bentonite samples plot as various types of basalt and basaltic andesite based on their silica, sodium, and potassium content. A positive trend implies an increase in $\text{Na}_2\text{O}+\text{K}_2\text{O}$ as SiO_2 increases.

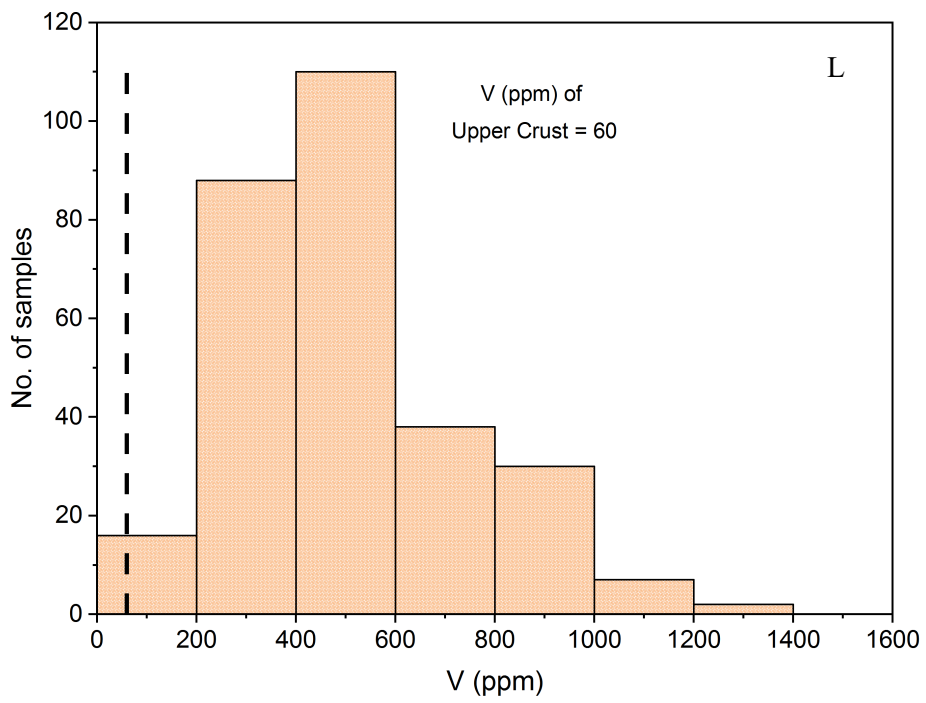
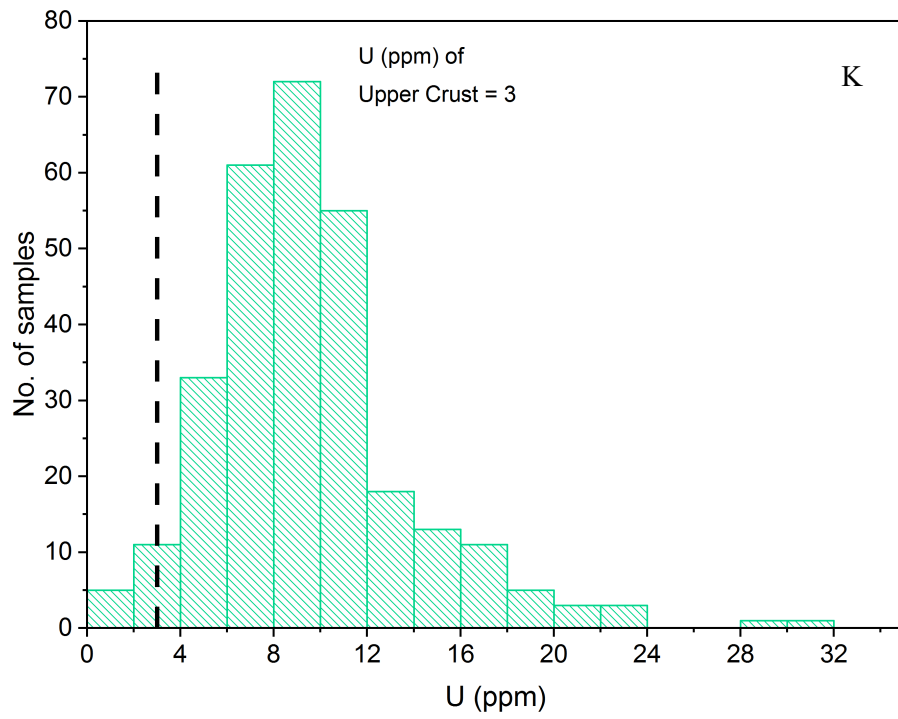


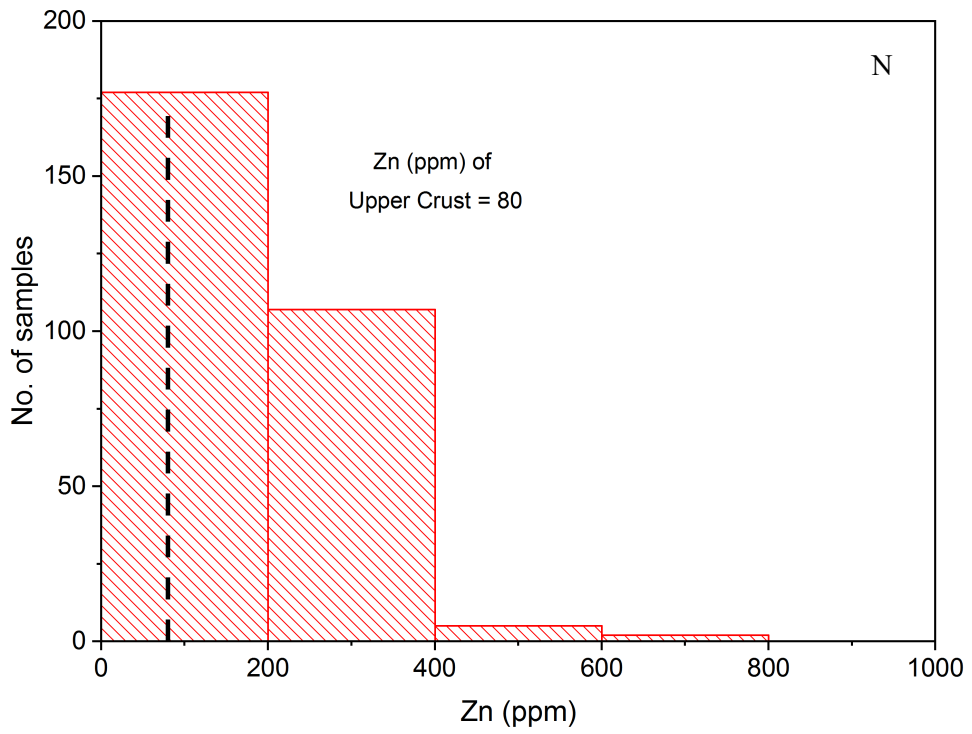
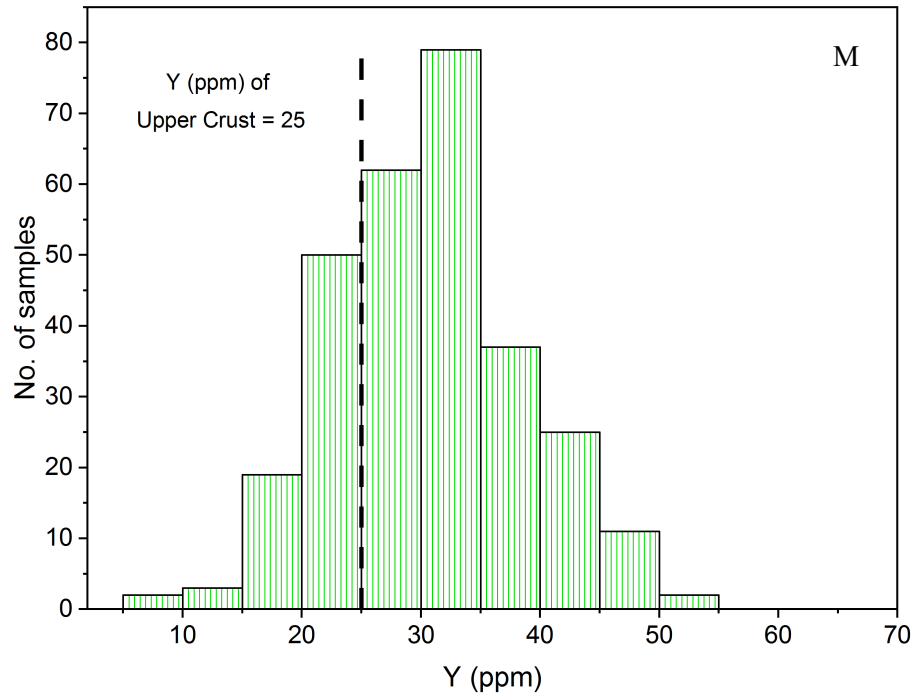












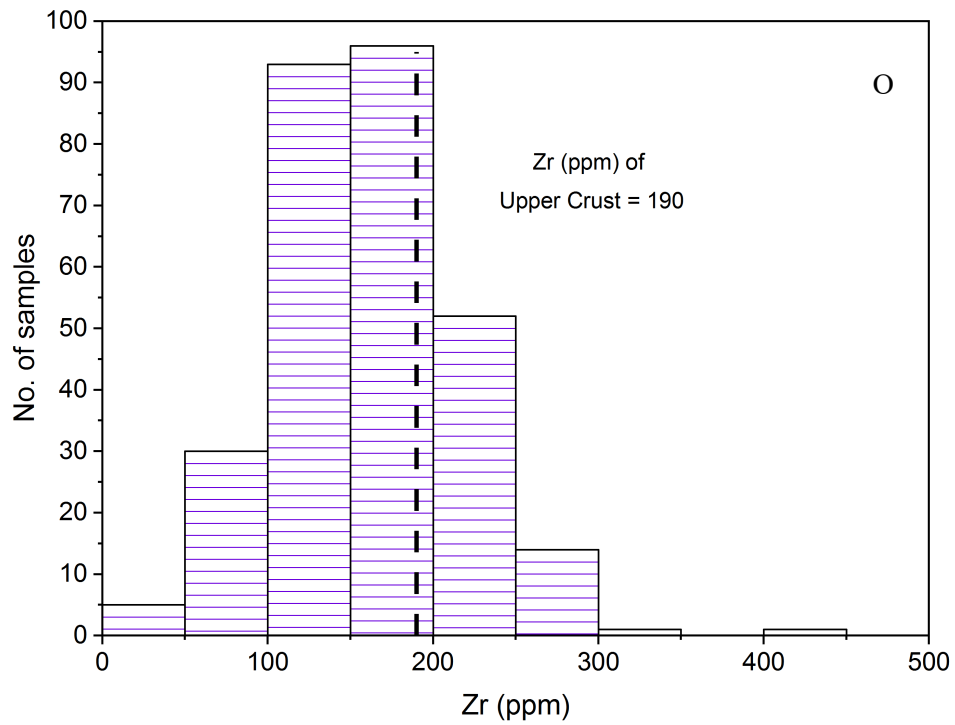


Figure 15: A-O: Histograms of the concentrations of nutrient elements (Cu, Co, Cr, Ni, Zn, U, Th, Pb, Sc, Hf, Ta, Mo, Zr, Y and V) in ~300 whole rock samples of seven subsurface cores of EF (Wells 3, 12, 16, 17, 19, 20 and 24) in South Texas. The black dotted lines in each figure represent the average concentration of the same nutrient element in the Upper Crust (Taylor and McLennan, 1984, and McLennan, 2001). The nutrient elements are called the chemical partners of porphyrins found in the center of the molecule (kerogen).

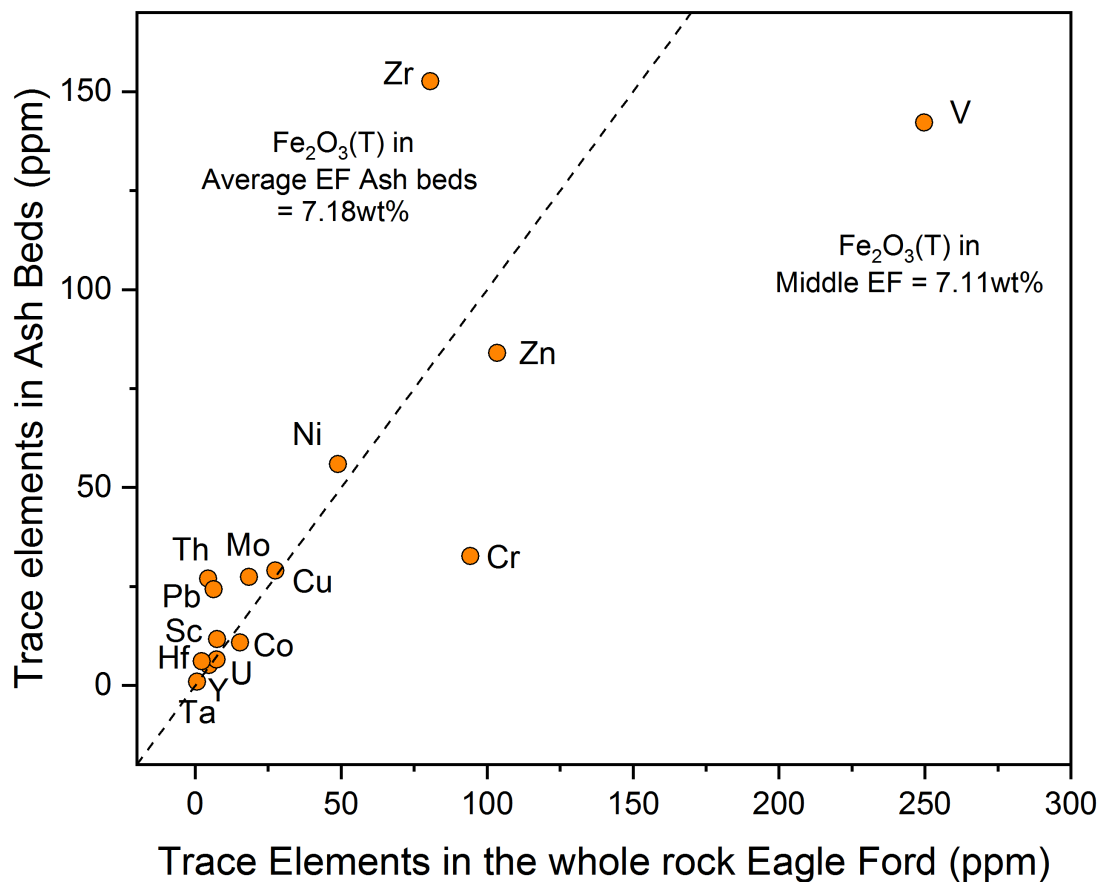


Figure 16: Summary figure of the 15 nutrient elements (Figure 14: A-O) found in average of 300 samples of EF whole rock black shales plotted against the average concentration in seven volcanic ash beds. The black dotted line is the theoretical best-fit line between the two parameters. Notice how all the elements except for Zr, Cr and V fall very close to or on the line itself, indicating similar concentration of the elements in volcanic ash and whole rock sample. The relation between the trace element concentration between ash beds and whole rock EF Shale shows that there was continuous volcanism throughout the deposition of the EF Shale. The three elements falling beyond the dash line are Cr, Zr and V and there could be multiple reasons for such apparent discrepancy. Notice the total Fe concentrations in both the ash beds and the black shales are remarkably similar.

Most of the trace metals and iron, shown in Figure 16 are important in global oceanic inventory for phytoplankton growth, a key in generating hydrocarbon potential. It is generally observed that in addition to the macronutrients such as nitrogen, phosphorous and iron that are depleted in the ocean, there are several trace elements such as Mn, Cu, Zn and Co that are deficient

in sea water for robust phytoplankton growth (Twining and Baines, 2013; Lohan and Tagliabue, 2018).

Our general thesis in documenting the general similarity of the trace metals and Fe in volcanic ash beds in the EF Shale and the whole rock black shales is that the ocean water cannot supply these nutrient elements for enriching a phytoplankton growth. Although iron oxide bearing aerosols in aeolian dust is also considered a source of iron for Fe-fertiization of oceans, in our case, the extraneous source of Fe, (Figure 16) (McTainsh and Strong, 2007) is demonstrably the calc-alkaline volcanic source. Thus, continuous volcanism during the entirety of the EF deposition enhanced the phytoplankton growth and hence the ultimate enrichment of the hydrocarbon deposit in the EF Shale.

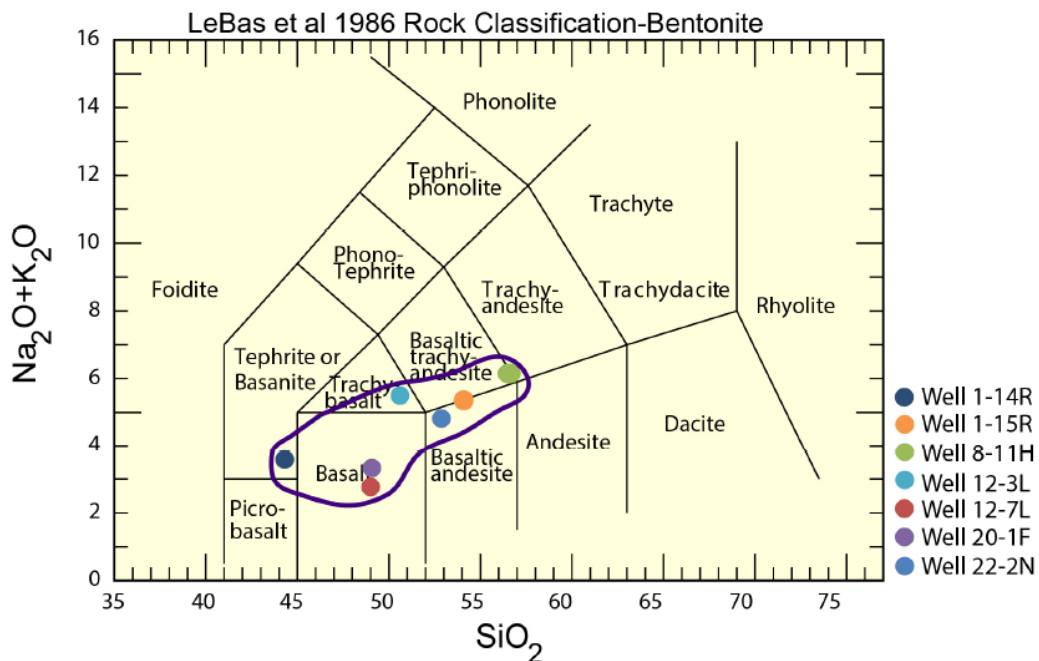


Figure 17: Bentonite samples plot as various types of basalt and basaltic andesite based on their silica, sodium, and potassium content. A positive trend implies an increase in Na₂O+K₂O as SiO₂ increases.

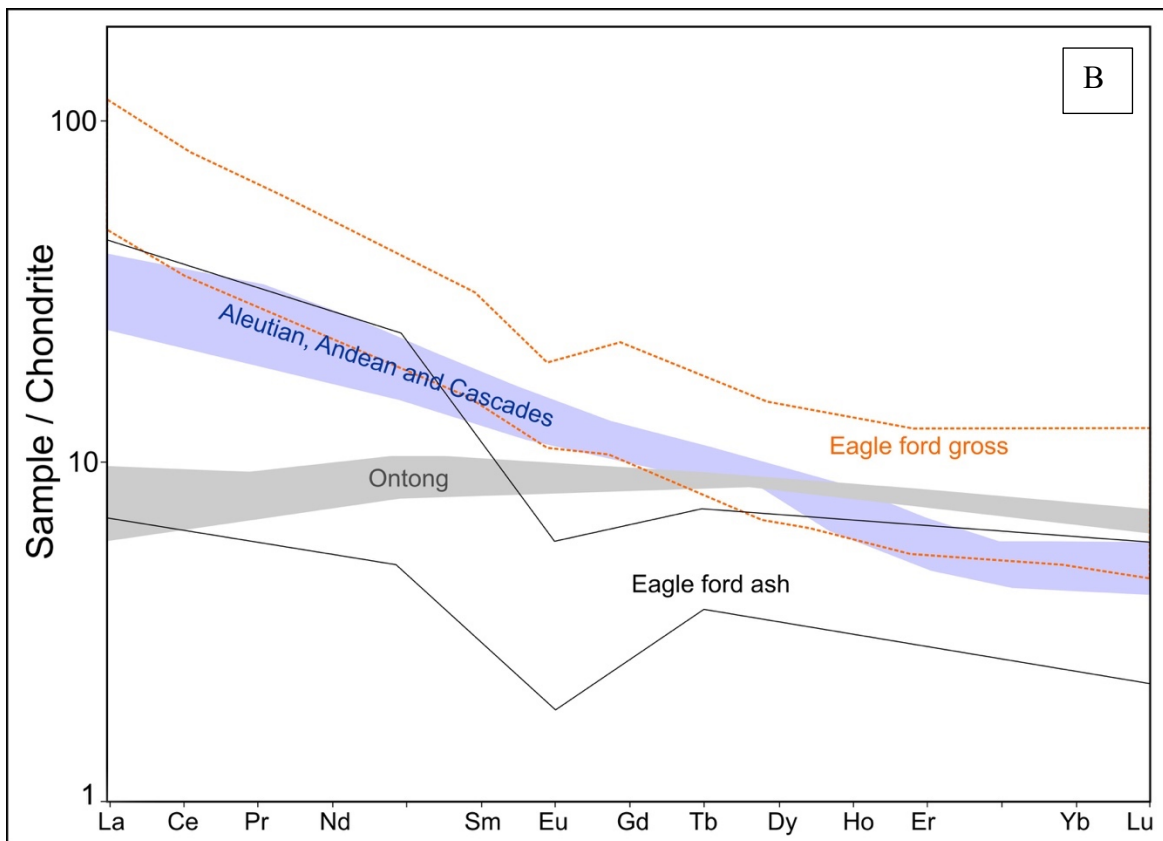
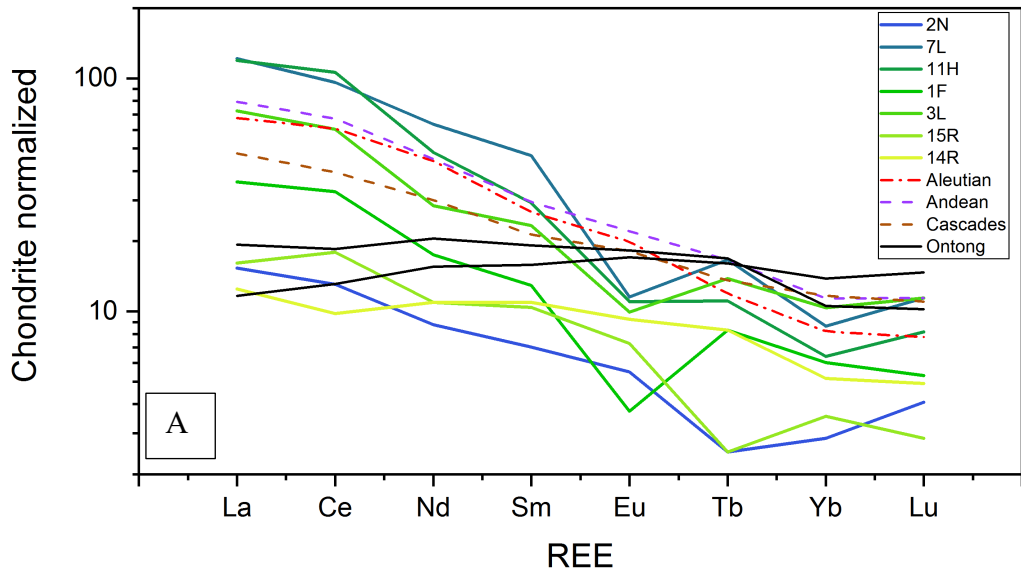


Figure 18: (A) Average Rare Earth Element pattern of seven ash beds of EF Shale along with Eagle Ford Gross whole rocks (B) (~298 samples) with andesitic arc volcanics such as the Andean, Aleutian and Cascades. Also plotted are the range of plume derived mafic volcanism from the Ontong Java Plateau. The calc-alkaline rocks are similar to the EF Shale in contrast to the Ontong Java Plateau.

1.1.4. U-PB AND LU-HF ANALYSIS OF ZIRCONS IN ASH BEDS

1.1.4.1. Methods

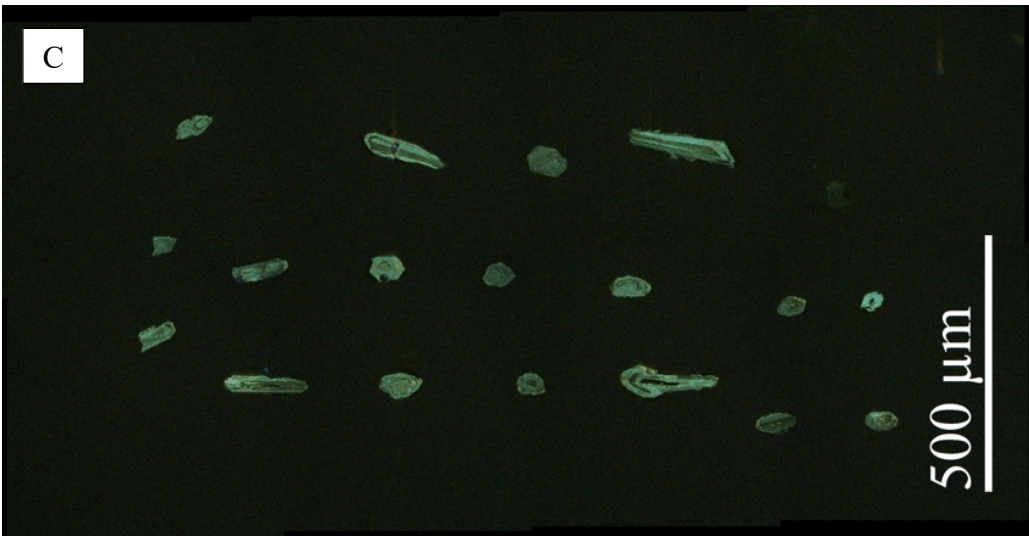
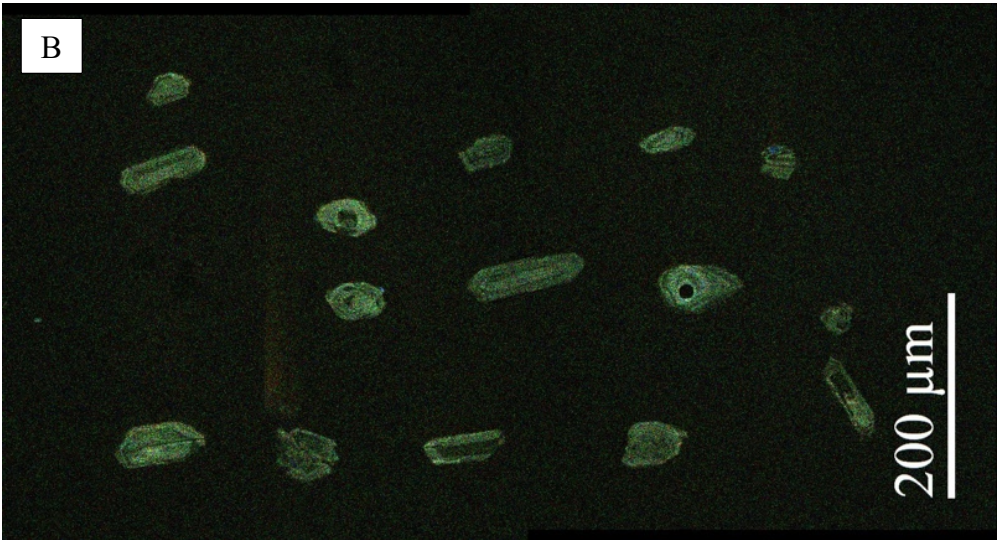
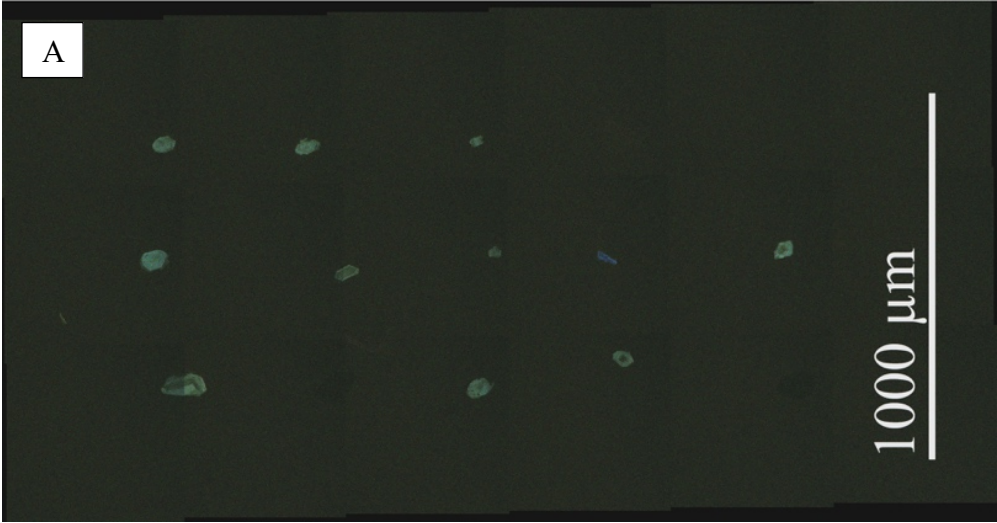
Zircon crystals were extracted from samples by crushing whole rock samples at first. Then the heavy minerals such as magnetite and zircons (density >2.98) are separated using heavy liquids separation method. Samples are processed such that all zircons are retained in the final heavy mineral fraction. The next step is picking out the zircons from the pile of heavy minerals left behind by the method of handpicking. A split of these grains (generally 20-25 grains per sample) are selected from the grains available and incorporated into a one inch epoxy mount together with fragments of Sri Lanka (SL) standard zircons. The mounts are then sanded down to a depth of ~20 microns, polished, imaged, and cleaned prior to isotopic analysis (Figure 19).

U-Pb geochronology of zircons was conducted by laser ablation multi-collector inductively coupled plasma mass spectrometry (LA-MC-ICPMS) at the Arizona LaserChron Center (Gehrels et al., 2006c, 2008). The analyses involve ablation of zircon with a New Wave DUV193 Excimer laser (operating at a wavelength of 193 nm) using a spot diameter of 20 microns. The ablation pit is ~12 microns in depth (Gehrels, 2011). The ablated material is carried in helium into the plasma source of a Nu HR ICPMS, which is equipped with a flight tube of sufficient width that U, Th, and Pb isotopes are measured simultaneously. All measurements are made in static mode, using Faraday detectors with 3×10^{11} ohm resistors for ^{238}U , ^{232}Th , ^{208}Pb - ^{206}Pb , and discrete dynode ion counters for ^{204}Pb and ^{202}Hg . Ion yields are ~0.8 mv per ppm. Each analysis consists of one 15-second integration on peaks with the laser off (for backgrounds), 15 one-second integrations with the laser firing, and 30 seconds delay to purge the previous sample and prepare for the next

analysis. The ablation pit is ~15 microns in depth. The U-Pb analyses were done following the lab-manual of the Arizona LaserChron Center.

The resulting ages are shown on Pb*/U concordia diagrams and weighted mean diagrams using Isoplot (Ludwig, 2008).

Hf isotopes are determined most accurately by measurement of isotopes of Hf, Yb, and Lu, at masses 171 through 180, with a multicollector mass spectrometer. For studies of zircon, Hf isotope ratios can be determined by dissolution followed by TIMS or ICPMS analysis, or by laser ablation using the same sample stages as for U-Pb by laser ablation. The same ablation spots are used to Lu-Hf isotope systematics determination at the Arizona LaserChron Center. Hf isotope data are acquired using a 40 μm diameter spot size and a laser pulse frequency of 7 Hz over the existing 20 μm diameter spot for U-Pb analyses. The zircon standards analyzed for the Lu-Hf isotope systematics include Mud Tank, Temora-2, FC-1, 91500, Plesovice, R33, and SL2, which have been analyzed by solution ICPMS by Woodhead and Hergt (2005), Slama et al. (2008), Bahlburg et al. (2010), and Vervoort (2010).



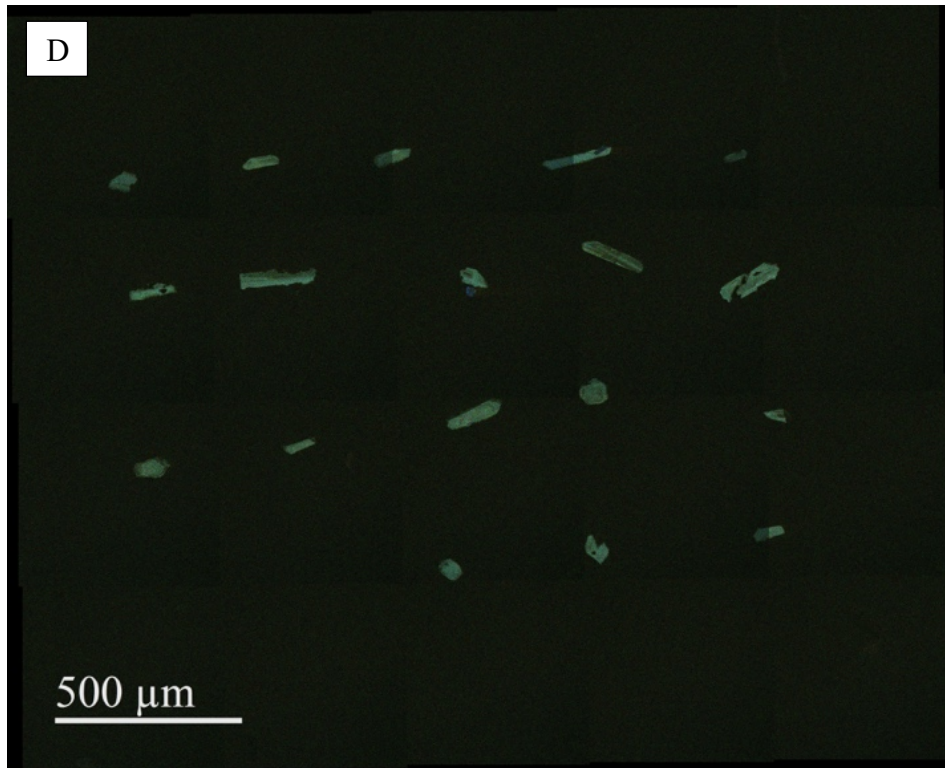


Figure 19: A-D: Separated zircons of ash beds in subsurface cores of EF Shale.

1.1.4.2. Results

U-Pb and Lu-Hf geochronological data in zircons are from ash beds from subsurface and surface samples of the Eagle Ford Shale, South Texas and the Del Rio area, West Texas respectively. Zircons from cores yield a consistently uniform Cenomanian-Turonian boundary age of deposition of the ash beds.

Around 150 zircons from eight ash beds (Figure 19, A-D) were collected from subsurface cores of Wells 8, 12, 20 and 22 in Karnes, Live Oak and DeWitt counties as well as from outcrop samples near Del Rio, West Texas. Results of the U-Pb LA-ICP-MS dating are shown in Figure 20 relative to a composite stratigraphic section. The zircons in four (8, 12, 20 and 22) of the contiguous cores, separated on the surface by ~140 miles, give ages 93.2 ± 1.66 Ma, 93.47 ± 0.8 Ma,

94.13±1.25 Ma and 93.7±1.9 Ma, from West to East (Figure 20). Zircons from Well 8 and 12 yield a consistently uniform Cenomanian-Turonian age of deposition of the ash beds. Well 8 shows three prominent ash beds (8-9, 8-11 and 8-13) yielding ages of 81.7±2.26-1.35 Ma, 85.76±1.20-0.58 Ma and 93.2±1.66 Ma respectively (Figure 20) in gradually increasing depths. Well 12 has three prominent ash beds (3L, 5L and 7L) with ages, 84.28±0.85-0.71 Ma, 93.47±0.8 Ma and 95.5±0.94 Ma respectively, gradually increasing in depth. Well 20 (2N) and Well 22 (1F) yield 94.13±1.25 Ma and 93.7±1.9 Ma respectively in ash bed zircons (Figure 20 and Table 1). The $\varepsilon_{\text{Hf}(T)}$ of the analyzed ash bed zircons range between +6.6 to -0.6 averaging at +2.68.

1.1.4.3. *Discussion*

The top and bottom of the Eagle Ford ash beds of the subsurface cores give ages from 85.76 to 95.5 Ma, suggesting duration of ~10 Ma for the Eagle Ford Shale with a deposition rate of 28 ft/Ma. The results are shown in Figures 20 and 21, correlating the five subsurface cores of the EF Shale in South Texas and outcrop samples in Del Rio, West Texas.

Figure 20 shows the relative positions of volcanic ash beds in the different drill cores of EF subsurface as shown in Figure 3. Herein, the LA-ICP-MS zircon ages of the ash beds are shown in black. Notice the boundary of the EF Shale below Austin Chalk and above Buda Limestone and the division of the EF Shale into lower, upper and middle EF based on nannofossils, lithology and gamma-ray data from Pioneer Natural Resources Pvt. Ltd.

Figure 21 shows the relative positions of zircon U-Pb ages from EF ash beds with respect to the outcrop samples of the Del Rio area (Boquillas Formation). A major conclusion of our geochronological data is that most of outcrop samples should belong to the Austin Chalk in age

although they look as EF Shale deposits in their lithology (marl-like). The non-correspondence of U-Pb ages are shown in figure 21.

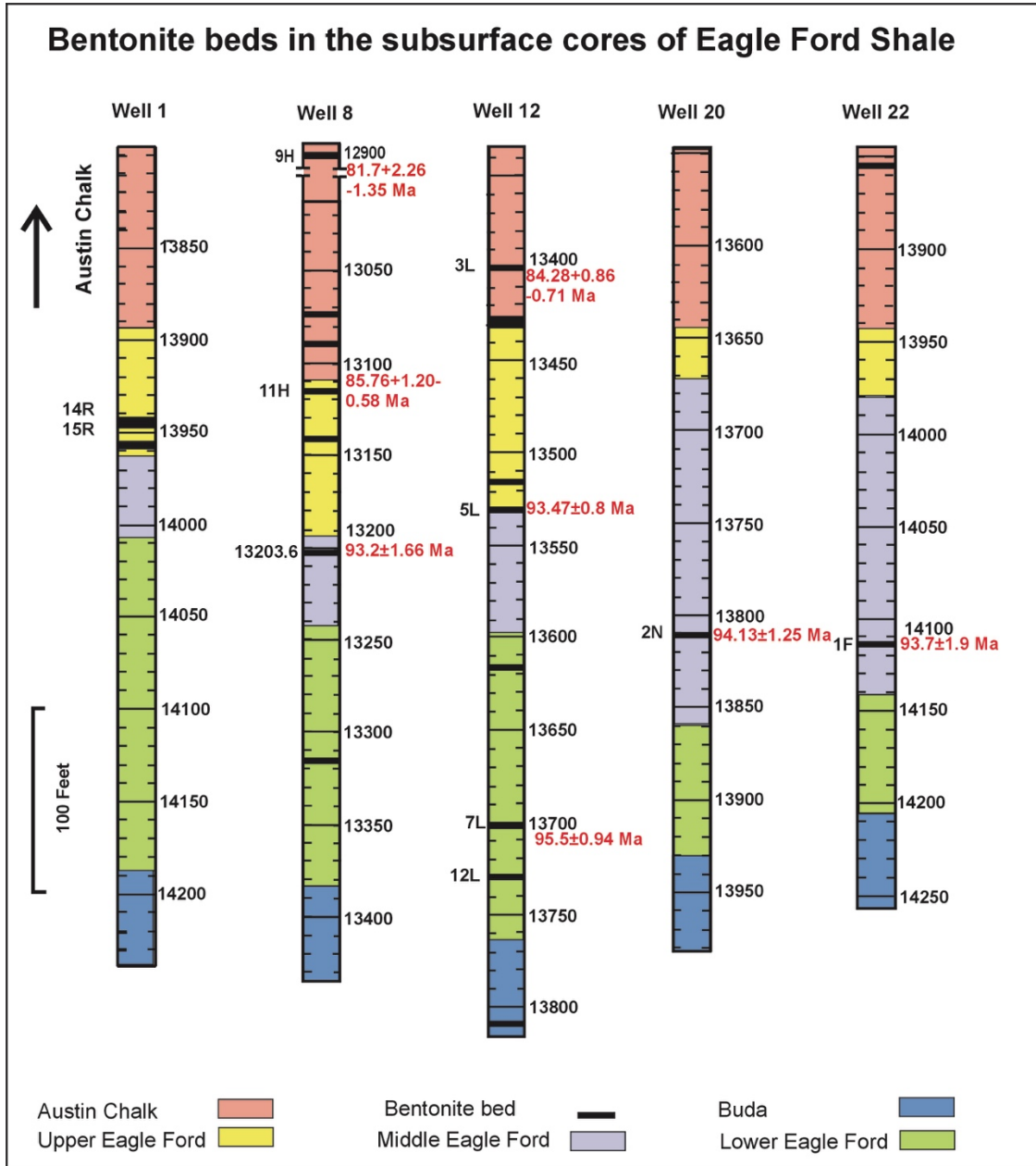


Figure 20: Relative positions of volcanic ash beds in the different drill cores of the EF subsurface deposits as shown in Figure 3. Herein the LA-ICP-MS zircon ages of the ash beds are shown in black. The EF Shale is bounded by Austin Chalk in the top and by Buda Limestone in the bottom. The EF is divided into lower, middle and upper parts based on nannofossils, lithology and gamma-ray data from Pioneer Natural Resources Pvt. Ltd. The EF dips at a shallow angle from West to East. For the tops of the EF Shale in subsurface cores, the depth varies from 13100ft to 13950ft

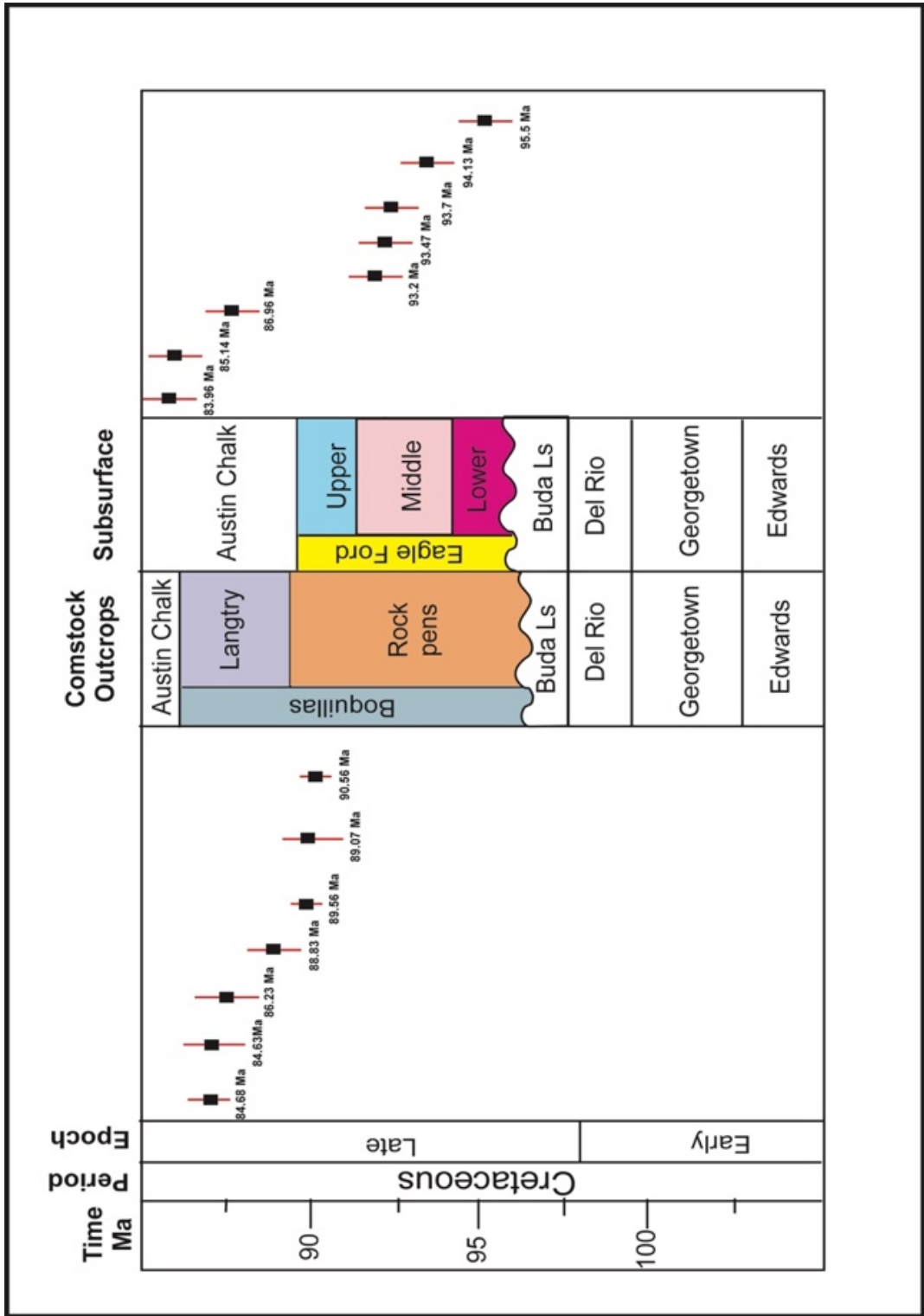


Figure 21: Relative positions of zircon U-Pb ages from EF ash beds with respect to the outcrop samples of the Del Rio area (Boquillas Formation.). This non-correspondence of U-Pb ages are shown in this figure.

In figure 21, one can see that the samples from the Boquillas Formation in West Texas are not correlatable with those in the EF Shale.

The average ϵ_{Hf} indicates a mantle component in the host magmas of the zircons, similar to arc-volcanism signatures such as the Quaternary andesitic volcanism in Central Mexico (Figure 22 and Table 2). The average ϵ_{Hf} is interpreted due to continental crustal contamination (from correlated ϵ_{Nd} and ϵ_{Hf} isotopic ratios).

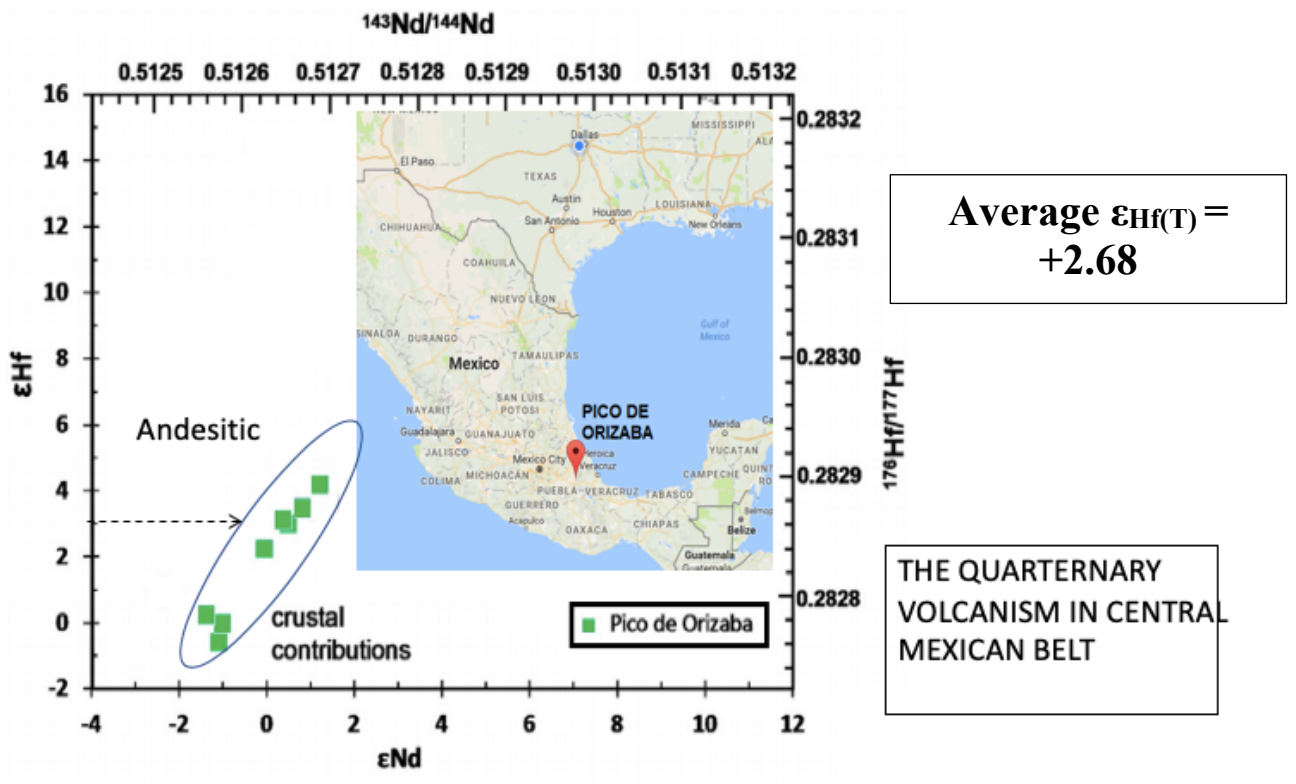


Figure 22: An example of Nd-Hf isotopic data similar to our EF data obtained from an andesitic volcanism in Central Mexican belt. Map modified after Cai et al., 2014.

1.1.5. RE-OS ISOTOPE SYSTEMATICS

1.1.5.1. *Methods*

Polycyclic aromatic hydrocarbons of heavy molecular masses known as porphyrins constitute a fraction of petroleum. Porphyrins are rings of pyrrole and pyrole groups (5-sided hydrocarbon rings that can complex a metal ion in the center. These porphyrins usually have high concentrations of transitional elements (nutrient elements) such as Ni, V, Mo, Cu, Co, Pb and Zn etc. (Figure 8). Re and Os are bound in porphyrins in the asphaltine fractions with Re concentration reaching as high as 50 ppb in petroleum, more concentrated than Os. With age, the $^{187}\text{Re}/^{188}\text{Os}$ ratio in petroleum can exceed 100.

Black shale powders were weighed and spiked with a mixed ^{185}Re - ^{190}Os spike. The digestion and oxidation were carried out in PFA pressure vials, which were heated at 120°C for at least 24 hours using $\text{Br}_2\text{-Cr}^{\text{VI}}\text{O}_3\text{-HNO}_3$ (Gannoun et al., 2015) and then Os was extracted into the liquid bromine, then dried and purified by microdistillation (Gannoun et al., 2015). The supernatant left after Os extraction was reduced with ethanol and Re was extracted and purified using iso-amyl alcohol and 2M HNO_3 prior to recovery in ultrapure water (Birck et al., 1997).

Os isotopic analyses were carried out by Negative Thermal Ionization Mass Spectrometry (NTIMS) on a Thermo Fisher Scientific Triton at Laboratoire Magmas et Volcans (LMV) at Observatoire de Physique du Globe de Clermont-Ferrand, France. The analyses were performed using the secondary electron multiplier in ion counting mode as detector. Os isotopic compositions for all samples were determined by peak-jumping of the OsO_3^- ion beam on masses 233, 235, 236, 238 and 240 (Gannoun et al., 2015). Osmium isotopic ratios were normalised to a $^{192}\text{Os}/^{188}\text{Os}$ ratio

of 3.08271 (Nier, 1937) and corrected off-line to remove spike and oxygen contributions using $^{18}\text{O}/^{16}\text{O}$ and $^{17}\text{O}/^{16}\text{O}$ ratios of 0.002047 and 0.0003708 respectively (Nier, 1950).

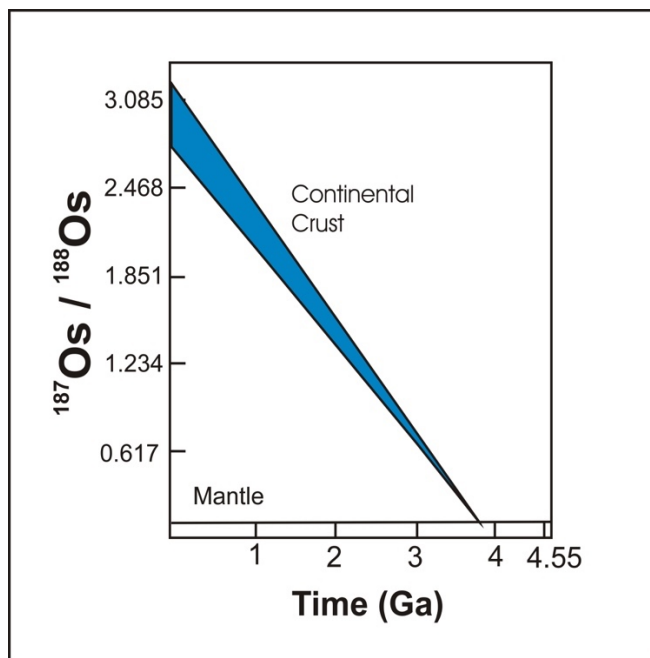


Figure 23: Isotope evolution of the continental crust and mantle. The mantle slope corresponds to a chondritic Re/Os ratio as shown by Allegre and Luck (1980).

Repeated analyses of the JM Os standard obtained on separate loads of 100 pg (n=12) yielded average $^{187}\text{Os}/^{188}\text{Os}$ ratios of 0.17391 ± 0.00026 , respectively. These values are in good agreement with published Faraday cup N-TIMS values of 0.17394 ± 14 (Birck et al., 1997) and 0.17398 ± 35 (Schaefer et al., 2000.)

1.1.5.2. Results

Six Lower Eagle Ford and four Middle Eagle Ford kerogen rich rocks show characteristic high Re-Os ratios. The initial $^{187}\text{Os}/^{188}\text{Os}$ at 93 Ma, the time of deposition of the Eagle Ford Shale of the ten whole rock samples, range between 2.466 to 5.111 (Table 7) with a majority of the samples lying between 2.46 and 3.62. In a Re-Os isochron diagram only three whole rock samples

yield a reasonable isochron of 76 ± 13 Ma with an initial $^{187}\text{Os}/^{188}\text{Os}$ ratio of 2.52 ± 0.22 . Other seven samples show scattering and do not define reasonable isochrons.

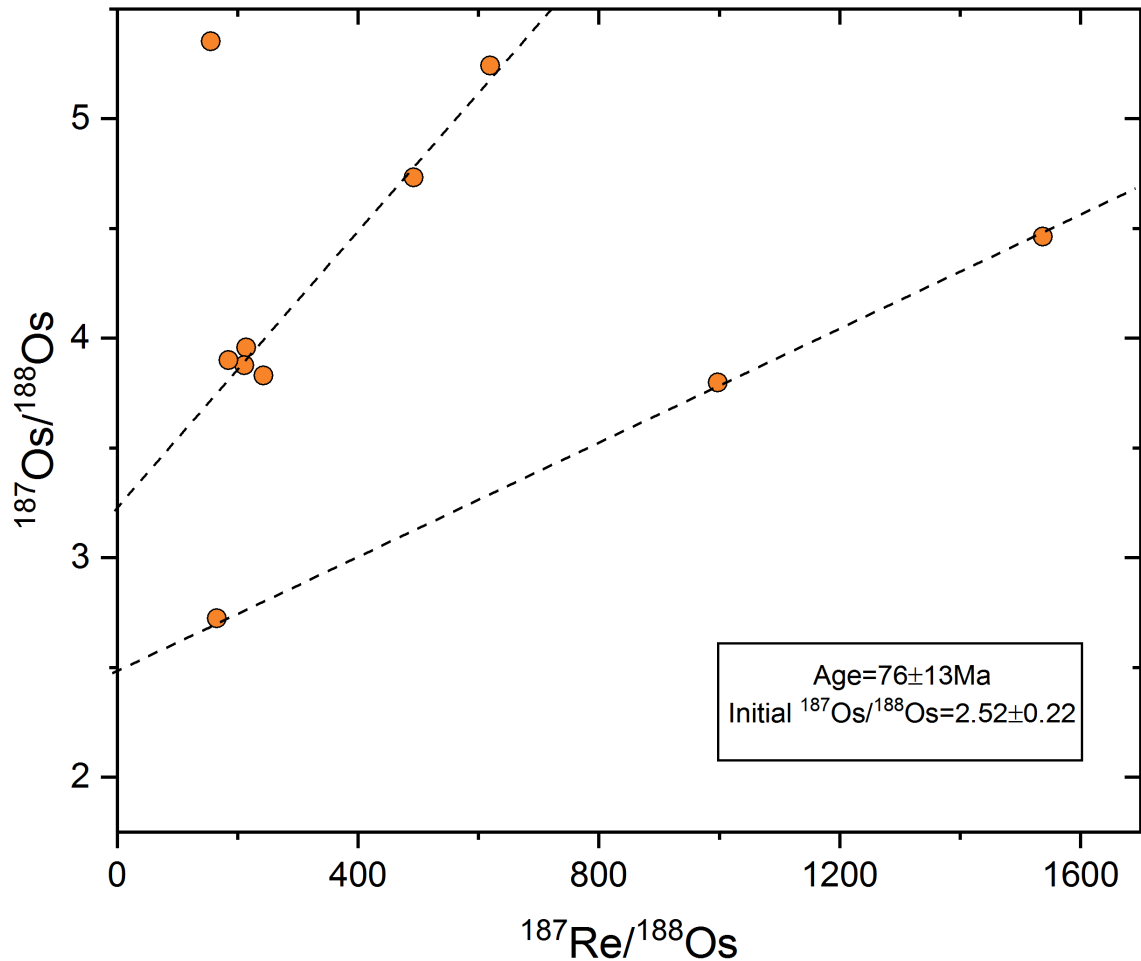


Figure 24: Re-Os isochron diagram. Only three of the whole rock black shale samples fall on an isochron diagram suggesting a probable age of 76 Ma for oil generation. The non-linear relationship of seven whole rock data points may be due to mobility of the kerogen rich layer and mixing with the kerogen poor sediments.

1.1.5.3. Discussion

The $^{187}\text{Os}/^{188}\text{Os}$ values at the time of deposition of the EF Shale indicate a continental crustal origin of the Os without taking into account the sea water Os-isotopic composition at 93

Ma. The continental crust fractionates Re from Os, the older continental crustal $^{187}\text{Os}/^{188}\text{Os}$ ratio (Figure 23) deviates strongly from the mantle ratio of around 0.124 at 93 Ma. The initial isotope ratio of the 76 Ma isochron in Figure 25 is 2.52 ± 0.22 , similar to ancient continental crust (Figure 23) whereas the other six falling on a separate isochron are far older than the 76 Ma rock.

Only three of the whole rock black shale samples fall on an isochron suggesting a probable age of 76 Ma for oil generation or kerogen maturation. The non-linear relationship of seven whole rock data points in the Table 7 and Figure 24 may be due to mobility of the kerogen rich layer and mixing with the kerogen poor sediments. Two different isochrons can be constructed from the set of data depending on the mobility of both the Re and Os (Figure 24).

Altogether, the results were inconclusive as the Re-Os data suggest mobility of both the Re and Os in the kerogen-rich layers within the analyzed 150 ft range of core 8. Perhaps, during the Chicxulub Impact at 66 Ma the kerogen layers were disturbed. It may not be surprising if we assume that the EF black shales were still soft sediments at the time of impact and the maturing kerogens were mixed vertically and horizontally, causing the disturbance in the Re-Os isotope systematics as observed in Figure 24 and its effect/impact on the Gulf of Mexico (Denne et al., 2013; Scott et al., 2014). In this context, a recent study by DePalma et al. (2019) on a seismically induced onshore surge deposit at the Cretaceous-Paleogene boundary in North Dakota may be plausible.

CHAPTER 2: RAMAN MICROSCOPIC STUDY OF KEROGEN MATURITY

1.2.1. Introduction

Optical inspection of vitrinite macerals (vitrinite reflectance) helps in the determination of thermal maturity of kerogen (Diesel et al., 1978). This technique may be applied to disperse organic matter (DOM) in shales to estimate the thermal maturity for petroleum exploration (Taylor et al., 1988). Laser micro-Raman spectroscopy allows us to get information on the short-range structural and chemical properties of different materials (Figures 25 and 26). It can be used to study small dispersed maceral grains as one can collect spectral data from a laser spot 2-10 μm diameter (50x-10x magnification) in the Thermo DXRxi Raman microscope (Figures 28 and 29). This technique enables analysis of data where the peaks of carbon are resolved into Gaussian bands (Wilkins et al., 2013). Raman Maturity Method (RaMM) has been developed for the determination of thermal maturity, avoiding the challenges of distinguishing the different macerals. Raman imaging also reveals, with high spatial resolution, the presence of several inorganic minerals (pyrite, marcasite, anatase and calcite). Raman thermal maturity images, plotted by Full Width and Half Maximum (FWHM) values of G-band by Thermo Scientific at UT Arlington on Eagle Ford black shales, showed that although relatively uniform overall, the areas close to minerals show lower maturity.

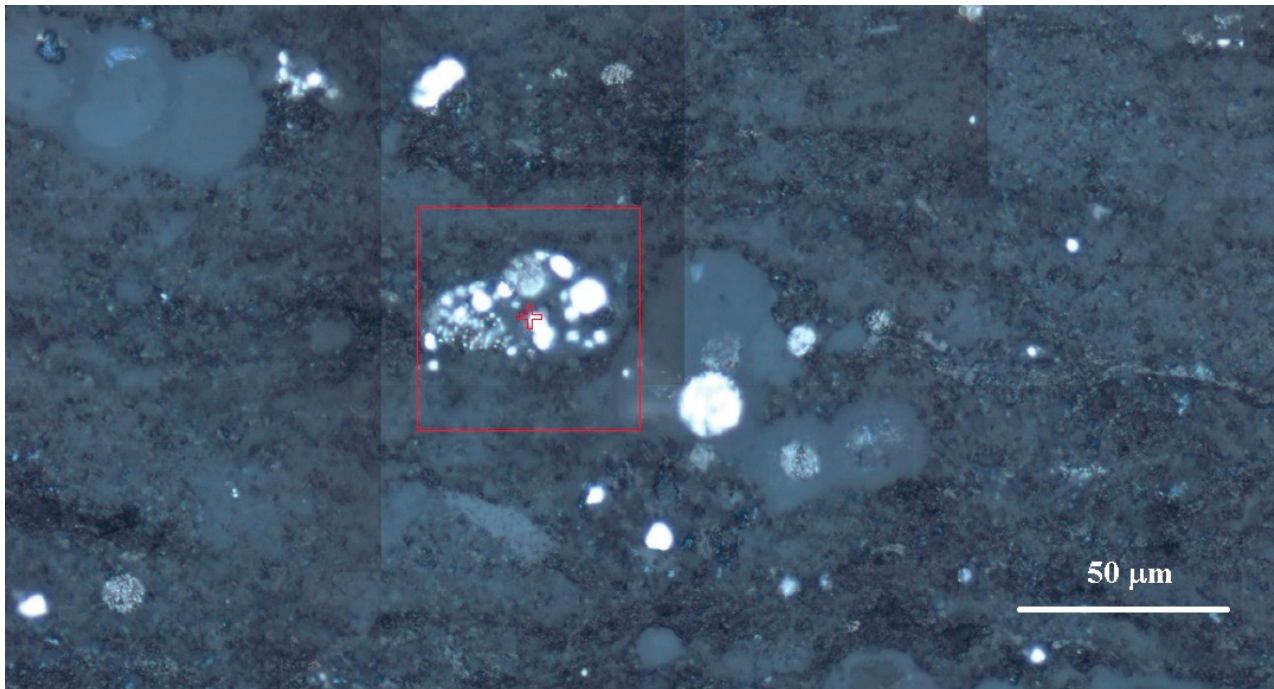


Figure 25: Oil sample features can be determined using video mosaic image. The red square is the area where Raman imaging was performed.

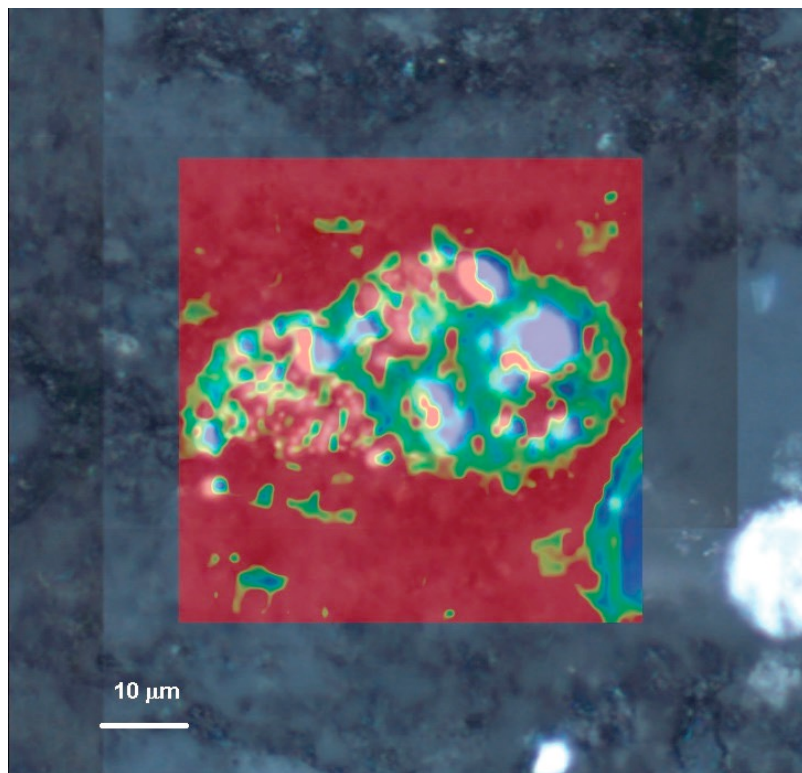


Figure 26: Superimposed view of video and Raman images with the kerogen in red.

Other methods, such as RockEval pyrolysis, X-Ray Diffraction (Nishimura et al., 2000) and high-resolution transmission electron microscopy (Beysac et al., 2002a), have also been used to estimate the graphitization of organic matter but these techniques are usually limited and destructive. Raman spectroscopy on the other hand is non-destructive, quicker, and easier and has been used to characterize the structure of the organic matter and the source rock. Raman scattering is a function of the molecular vibrations and symmetries of chemical bonds (Wilkins et al., 2014). Raman spectroscopy offers a high spatial resolution in the micrometer range (Marshall et al., 2012). The first-order Raman spectrum of kerogen consists of two main peaks (Cesare and Maineri, 1999; Marshall et al., 2010). The G band appears at $\sim 1600 \text{ cm}^{-1}$ and is indicative of well-ordered, graphite-like carbon structures in the kerogen (Wilkins et al., 2014). The D band appears at $\sim 1350 \text{ cm}^{-1}$. The G and D peaks shift towards higher and lower wavenumbers, respectively, as maturity of the kerogen increases. The Raman band separation (RBS), which is the wavenumber separation between the G and D peaks, has been proposed as a reliable maturity indicator (Kelemen and Fang, 2001). Kelemen and Fang (2001) also present that the most significant maturity-related change for fresh samples is a drop in the Raman intensity ratio from 3.2 to 2.4 and narrowing and shift to lower wavenumbers for the D band. The more the maturity, the greater is the Raman G-D band separation and the f_D/f_G intensity ratio decreases (Figure 27).

1.2.2. Methods

Thirty-four (34) billets of black shale distributed throughout the ~ 300 ft Well 8 core, from Lower to Upper Eagle Ford were used in this study. Twelve (12) thin sections were prepared and petrographic study was done at the University of Texas at Arlington. The thin sections were optically studied using a Leica DM750P polarizing microscope.

The Raman spectra on 34 billets subsequent analyses were carried out on a Thermo Scientific DXRxi Raman Imaging spectroscope in the Department of Earth and Environmental Sciences, UT Arlington. The instrument was calibrated based on an already mature kerogen fraction in the core, the ones that have been mobile and moved from the pores [of what?] to the foraminifers in the black shale. Thin sections or flattened/polished core sections were used selecting only the kerogen rich areas of the core throughout its depth. Spectra were generated using a 10X objective and 532 nm laser. The laser spot size at the time of analyses were $\sim 10 \mu\text{m}$ (Figures 28 and 29). The operating conditions were 1 – 5 sec acquisition time, 1 – 5 accumulations and 0.4-0.5 mW laser power. The Raman maps were made in standard 2D mode along the XY plane of a thin section. The accuracy of the Raman peak positions was generally considered to be $\pm 1 \text{ cm}^{-1}$.

The maps display the geometrical distribution of phases in detail, more importantly where mixed phases are concerned. The maps allow to search new phases in selected fluid inclusions (or selected area) if some phases were missed by single point analysis. Though the DXRxi Raman imaging microscope is calibrated through auto-alignment, Si (520.5 cm^{-1} peak) is used to recheck the calibration.

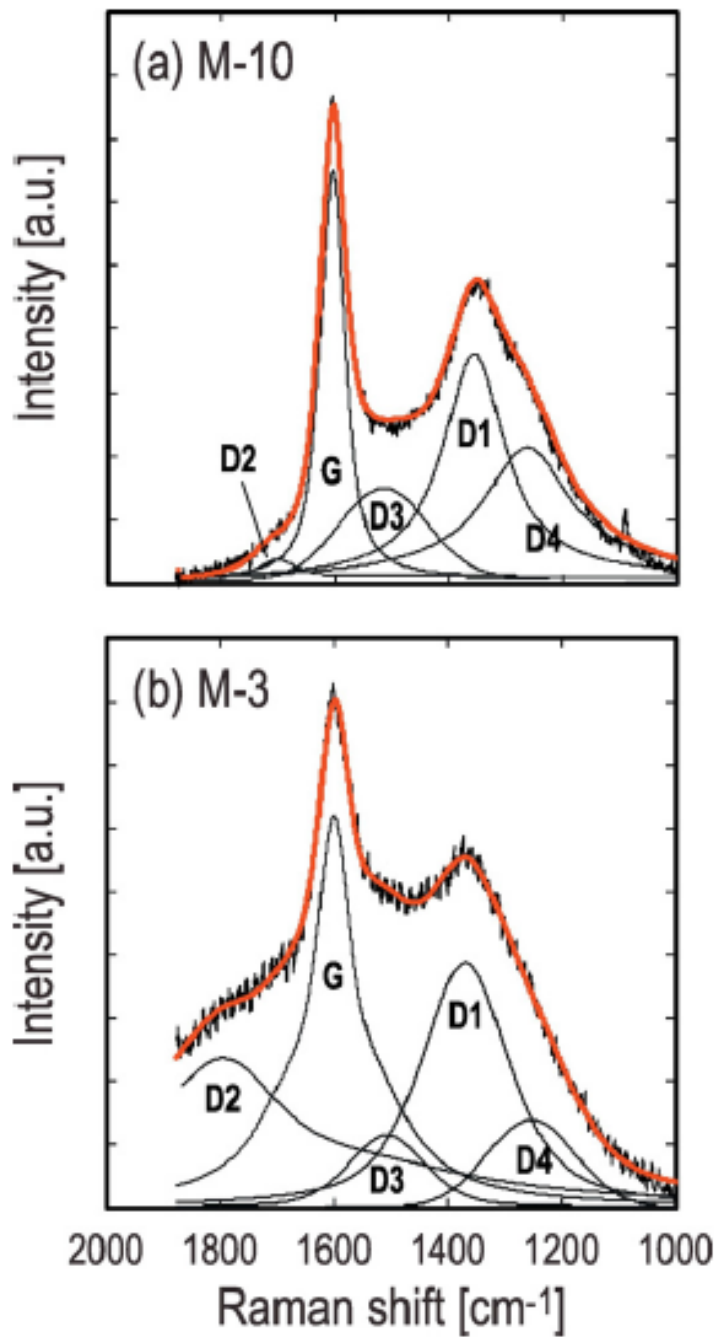


Figure 27: Locations of the G (graphitic) and D (disordered) bands in the Raman shift in two different samples of varying kerogen maturity. Depending on change in maturity, these peaks move closer or further away from each other.

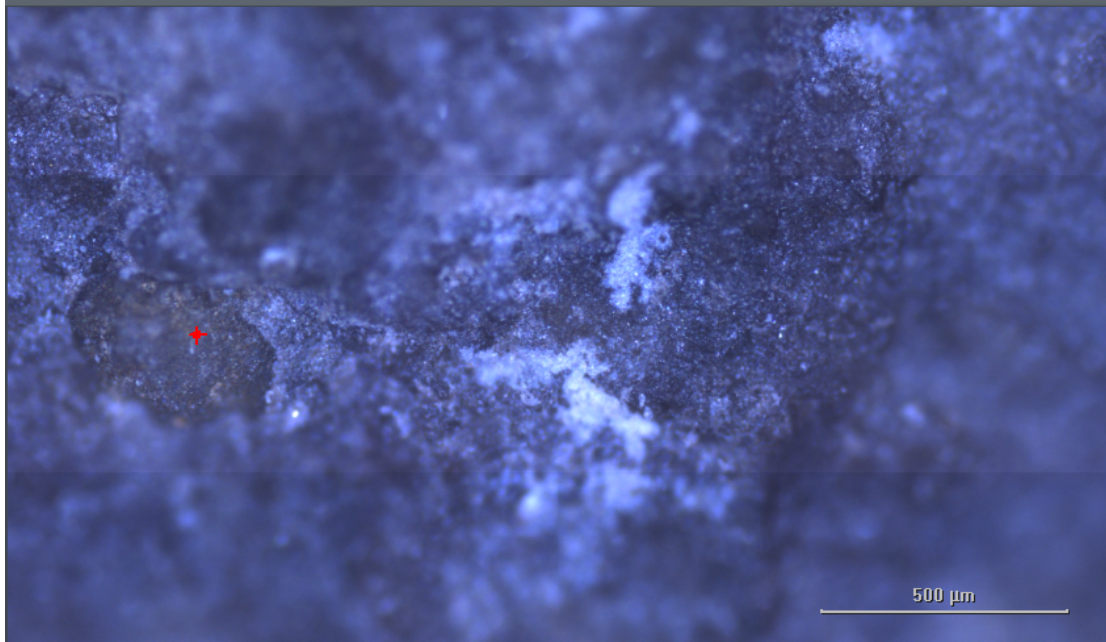


Figure 28: Raman imaging of kerogen rich foraminiferal test (red spot) in the marl (dull brown color, indicating presence of kerogen, under 10x, confocal lens, in reflected light).

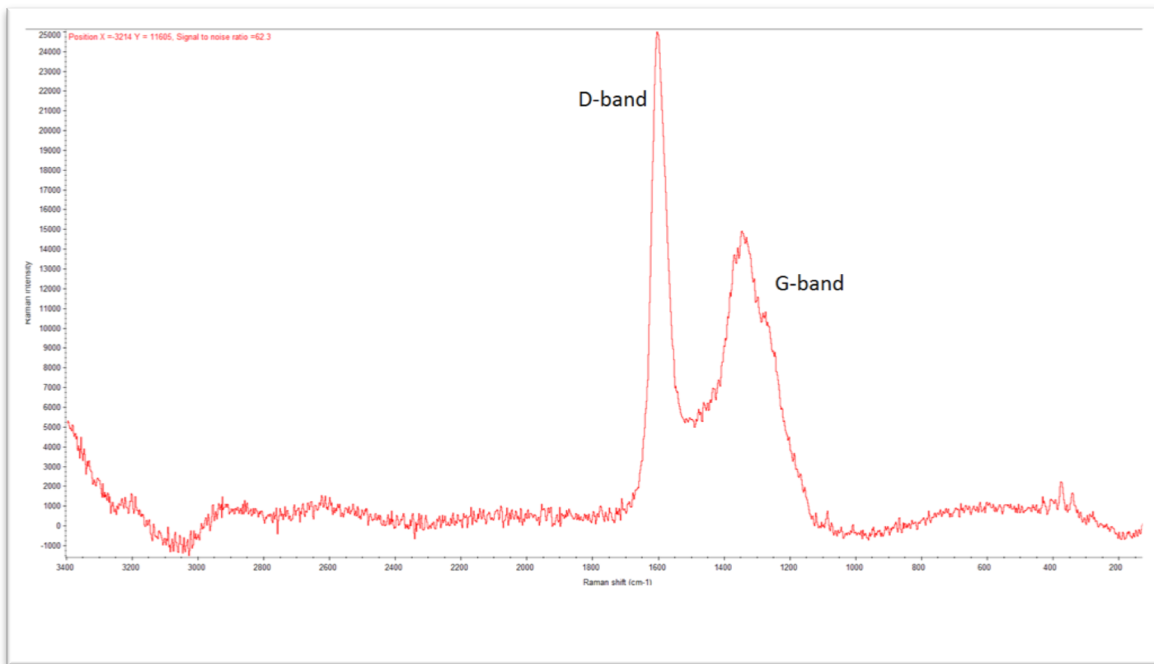


Figure 29: Raman spectra of the spot in Figure 28.

1.2.3. Results

The G and D peaks shift towards higher and lower wavelengths, respectively, as maturity of the kerogen increases (Kelemen and Fang, 2001). The Raman band separation (RBS), which is the wavelength separation between the G and D peaks, has been proposed by (Kelemen and Fang, 2001) as a reliable maturity indicator. Kelemen and Fang (2001) also present that the most significant maturity-related change for fresh samples is a drop in the Raman intensity ratio from 3.2 to 2.4 (G:D) and increase in D:G area ratio and narrowing and shift to lower frequencies for the D band. The more the maturity, the greater is the Raman G-D band separation and the f_D/f_G intensity ratio decreases. Raman thermal maturity images, plotted by Full Width and Half Maximum (FWHM) values of G-band by Thermo Scientific at UT Arlington on Eagle Ford black shales, showed that although relatively uniform overall but have a relatively higher thermal maturity towards the Lower Eagle Ford in comparison to the Upper Eagle Ford. FWHM, positions of the G and D bands and D/G area ratio are the most sensitive parameters to maturation (Guedes et al., 2010; Zhou et al., 2014; Lünsdorf, 2016; Schito et al., 2017).

The G-D vs Ro% of global black shales with different maturity shows a curvilinear relationship with $R^2=0.7735$. The EF black shales of the entire core #8 fall between 0.7-1.4 Ro% and G-D of 240-270 cm^{-1} , a narrow cluster in this plot. As we know the entire EF core #8 is thermally matured, the Ro% of the EF Shale samples fall in a narrow and restricted part of this curve (Figure 32).

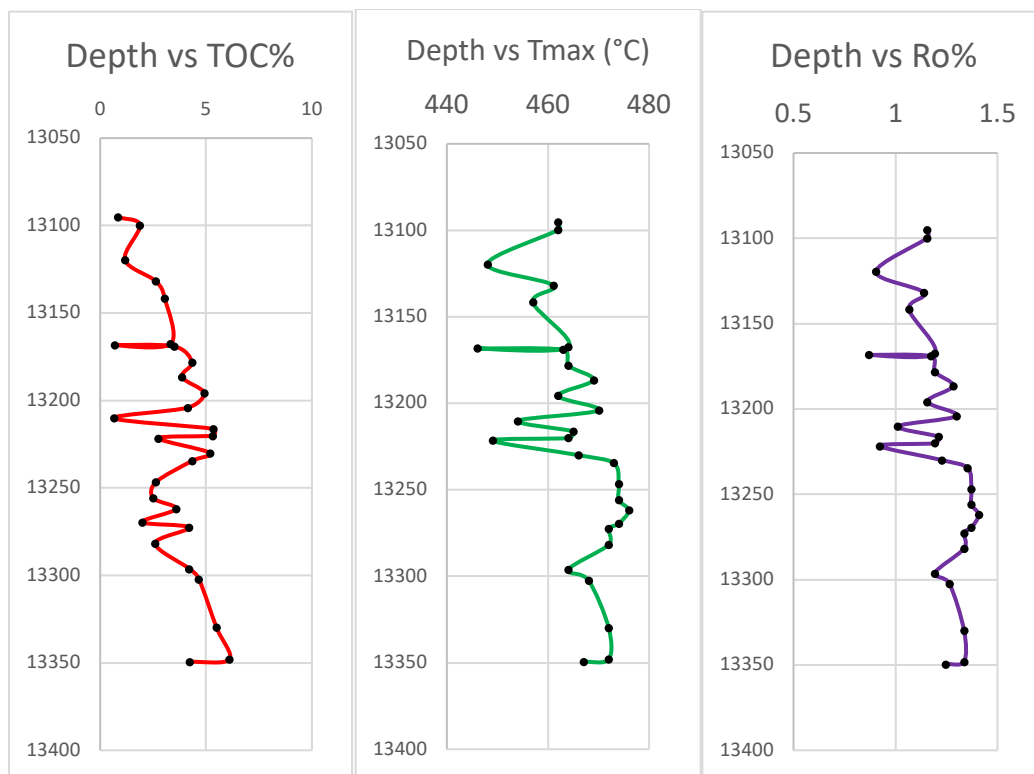


Figure 30: Plot of the Total Organic Carbon (TOC), T_{max} and Ro% of Well 8 against the depths shows a correlation between the three parameters. With depth, it is seen that the TOC, T_{max} and Ro% bear a linear correlation with each other. With increase in TOC, the other two increase and vice versa, along the depth. There is a change in the variation, near the C/T boundary around 13200ft mark.

1.2.4. Discussion

Total organic carbon (TOC), Rock-Eval Pyrolysis, Tmax and Thermal Maturity measurements, and vitrinite reflectance (VRe) are estimated of 34 billets of the EF core (Figure 30 and Table 8), Well 8 from Geomark Research Ltd. By plotting these parameters against depth Plot of the Total Organic Carbon (TOC), T_{max} and Ro% of Well 8 against the depths shows a correlation between the three parameters. With depth, it is seen that the TOC, T_{max} and Ro% bear a linear correlation with each other. With increase in TOC, the other two increase and vice versa, along the depth. Notice the change in the variation, near the C/T boundary around 13200ft mark.

In Figure 31, for the G-D (RBS) of the exact same 34 samples of the core plotted against the depth, one can see a negative correlation. The RBS varies inversely with the T_{max} and VRe

analysis as well as with the TOC. G-D (RBS) is mapped along the depth of the 300 ft long Well 8 core. There is a very small variation in the RBS over this vertical extent. The kerogen maturity should fall within a short bound due to this small RBS variation (Table 9).

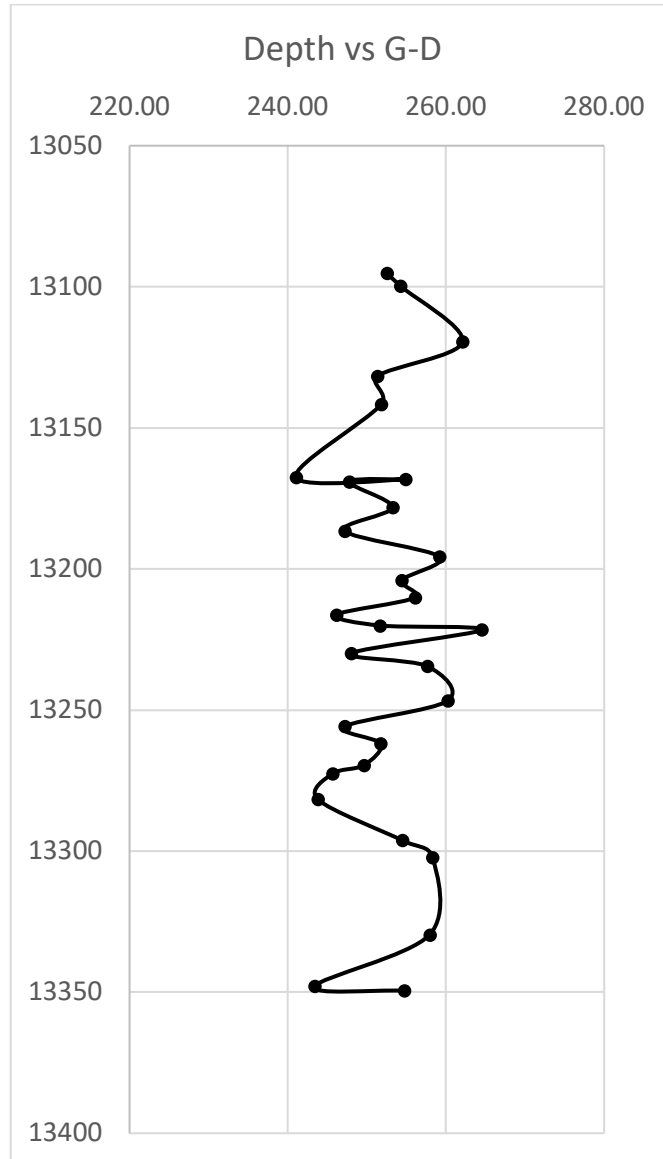


Figure 31: G-D (RBS) is mapped along the depth of the 300 ft long Well 8 core. There is a very small variation in the RBS over this vertical extent. The kerogen maturity should fall within a short bound due to this small RBS variation, independent of depth.

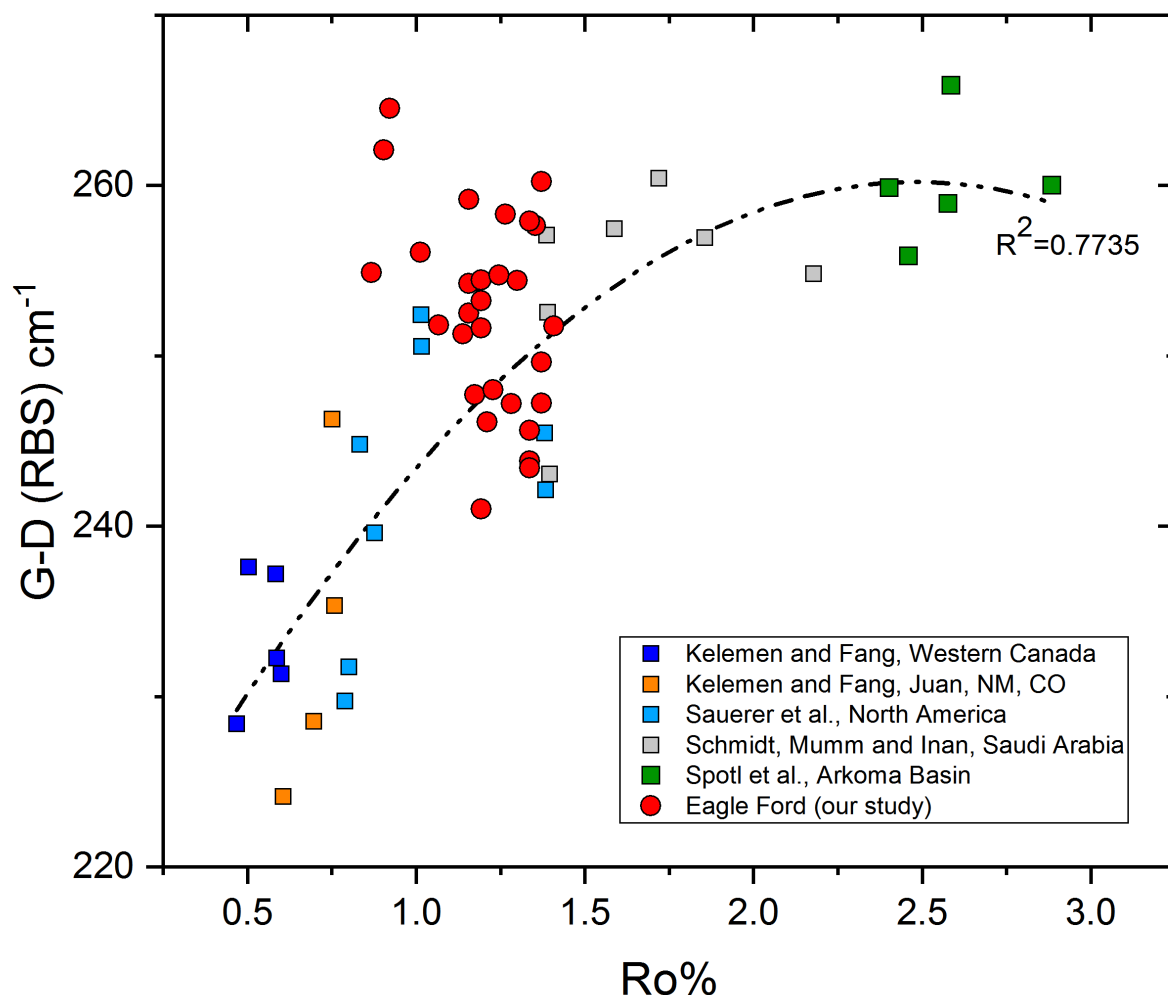


Figure 32: RBS vs Ro% for black shales across North America and Saudi Arabia, of different ages of formation, create a curve that helps in the estimation of the RBS or Ro% depending on the unknown. The best-fit curve is a polynomial with $R^2=0.7735$. The EF black shale kerogen maturity (Ro%) plotted against its RBS falls on this best-fit curve indicating that the method applied in using Raman as an indicator of thermal maturity works.

Interestingly, however, when the $VR_e/Ro\%$ of all 34 EF Shale samples are fitted on a curve from data from established literature, they fall on the best-fit line, where the Type II and Type III kerogens fall. EF Shale has both Types II and III kerogens indicating both oil and oil and gas forming compositions. The Ro% are plotted against the RBS (cm^{-1}) on the y-axis. The EF Shale samples fall in a narrow range of $VR_e/Ro\%$ (0.7-1.4) indicating a semi-constant value of the Ro% in a given G-D band range. The narrow range of Ro% indicates that the entire deposits of the EF Shale have the same thermal maturity, or it attained maturity in one shot.

CHAPTER 3:
HIGH PRECISION STRONTIUM (SR)-ISOTOPES AT THE OCEANIC ANOXIC
EVENT 2 (OAE2)

1.3.1. Introduction

The Cretaceous sea water Sr isotope composition at some Deep-Sea Drilling Projects (DSDP) sites has been studied (Bralower et al., 1997). The work documented lower $^{87}\text{Sr}/^{86}\text{Sr}$ values in the Aptian and early Albian stages, higher in the mid-Albian-Cenomanian stages, and then a decrease in the early Turonian stage (Figure 33).

The global strontium (Sr) isotopic ratios of sea water reflect a balance between the radiogenic $^{87}\text{Sr}/^{86}\text{Sr}$ values (~ 0.7045 to 0.943) of detrital input via rivers and aerial weathering from the continental crust (Faure et al, 1967; Veizer, 1989), and $^{87}\text{Sr}/^{86}\text{Sr}$ values (~ 0.703) (Veizer, 1989) from hydrothermal systems (water/rock interactions and basalt alterations), termed as mantle flux (Faure, 1986; Edmond, 1992). The Sr-isotopic composition of sea water changes over the geologic time scale (Wickman, 1948; Peterman et al, 1970). Sea water $^{87}\text{Sr}/^{86}\text{Sr}$ increases after an episode of orogenesis and continental suturing, which results in an increase in the rate of weathering and erosion and continental flux into ocean (Clauer, 1976; Richter et al., 1992). An increase in mantle flux induced by fast seafloor spreading and continental rifting (Larson, 1992), and plume volcanism (Jones and Jenkyns, 2001) decreases sea water $^{87}\text{Sr}/^{86}\text{Sr}$ values. High atmospheric pCO_2 also intensify chemical weathering of continental rocks, thus sea water $^{87}\text{Sr}/^{86}\text{Sr}$ water (Worsley and Kidder, 1991).

The residence time of strontium is long ($\sim 3\text{-}5 \times 10^6$ years), whereas the average mixing time of the ocean is $\sim 10^3$ years (Veizer, 1989; Goldberg, 1963). Therefore, the $^{87}\text{Sr}/^{86}\text{Sr}$ ratio of global ocean water is assumed to be homogeneous (Burke et al., 1982). Due to the large isotopic difference between the two main sources of Sr, the $^{87}\text{Sr}/^{86}\text{Sr}$ composition of sea water tracks long-

term changes in the weathering of the earth's surface (Halverson et al., 2007) and the importance of the hydrothermal flux (Richter et al., 1992).

Although the global $^{87}\text{Sr}/^{86}\text{Sr}$ sea water curve during the OAE2 of previous studies is broadly accepted, are samples are discontinuous and disparate, for which further close spaced high precision data is required, which forms the basis of our study. Previous work has been carried out at the DSDP sites 463 (Ando et al., 2009), 551 (Goban Spur, North Atlantic Ocean), 258 (Naturaliste Plateau, Indian Ocean) and platform carbonates of Italy (Jenkyns et al., 2016).

Lower sea water $^{87}\text{Sr}/^{86}\text{Sr}$ values and deposition of organic-rich sediments are co-incident with volcanism and change in sea level (Coccioni et al., 1987; Bralower et al., 1994). It has been shown that sea water Sr-isotope values were high below the organic-rich sedimentary rocks deposited during the OAE2 and were low above the black shale deposition (Bralower, 1988). It has been suggested that the change was due to a volcanic episode (Haq et al., 1987).

1.3.2. Methods

The strontium sample preparation and ion exchange column chemistry were carried out in the Clean Lab facility of UT Arlington. Between 10-20 mg of whole rock black shale samples were crushed and weighed out. 10-20 mg samples was adequate to collect at least 300 ng of Sr as the bulk rock EF shale shows an average a Sr concentration of 600 ppm. These samples were dissolved in 1.5 N Hydrochloric acid (HCl) for 1 minute in order to dissolve the calcite to form CaCl_2 in solution. The CaCl_2 solution was pipetted out carefully making sure that none of the silicates or kerogen are pipetted out. This solution was then dried on the hotplate overnight at 80°C in open Teflon beakers. Peroxide was then added to the sample to dissolve any remaining organic matter and dried at 180°C . 3.5N Nitric acid (HNO_3) was then used to dissolve the dried sample

and the solution pipetted out into centrifuge tubes. The solution was centrifuged for 30 minutes twice.

Strontium was separated in cation exchange columns using 0.2 ml Sr-Specific (50-100 mesh) columns, which were conditioned with 3.5N HNO₃. The sample is loaded in 500 µl of 3.5N HNO₃ and then washed with 25 µl of 3.5N HNO₃ three times to remove the rare earths. Afterwards the column is rinsed with 1160µl of 3.5N HNO₃ and in a fresh beaker, the Sr is collected with 560 µl of 3.5N HNO₃. Strontium analysis was carried out in the Thermal Ionization Mass Spectrometer (ThermoFinnigan TRITON) at Boston University, using SRM 987 Sr standard.

1.3.3. Results

High-Precision Sr-isotopic data were generated by analyzing 28 closely spaced samples from a sub-surface core of the Eagle Ford Shale. The core covers the Cenomanian- Turonian boundary at a depth of 4000 m from the surface. The core sample has well demarcated the Austin Chalk, the Eagle Ford Shale, and the Buda Limestone, ranging around 30-46 m.

The ⁸⁷Sr/⁸⁶Sr values range from 0.707405 – 0.707566 for the 300 ft long EF Shale core, Well 8 (Figure 33 and Table 3). The ⁸⁷Sr/⁸⁶Sr sea water curve from 28 close spaced carbonates in black shales of 300 ft EF Shale subsurface core displaying a lesser radiogenic input of ⁸⁷Sr/⁸⁶Sr during C-T event (OAE2) and leading up to it, in comparison to the most recent global ⁸⁷Sr/⁸⁶Sr sea water curve established by Jenkyns et al. (2016) from platform carbonates in Italy. Notice how the curve by Jenkyns et al. (2016) do not trace the entirety of the OAE2 during which the entire EF Shale was deposited but during the short duration of C-T boundary, their samples show a zigzag variation of the ⁸⁷Sr/⁸⁶Sr with much larger errors. The lowering of the

$^{87}\text{Sr}/^{86}\text{Sr}$ ratios before C-T boundary and its gradient increase in the Turonian indicate arc source, some considering large scale global arc volcanism in the Cretaceous (Lee et al., 2018; Figure 34).

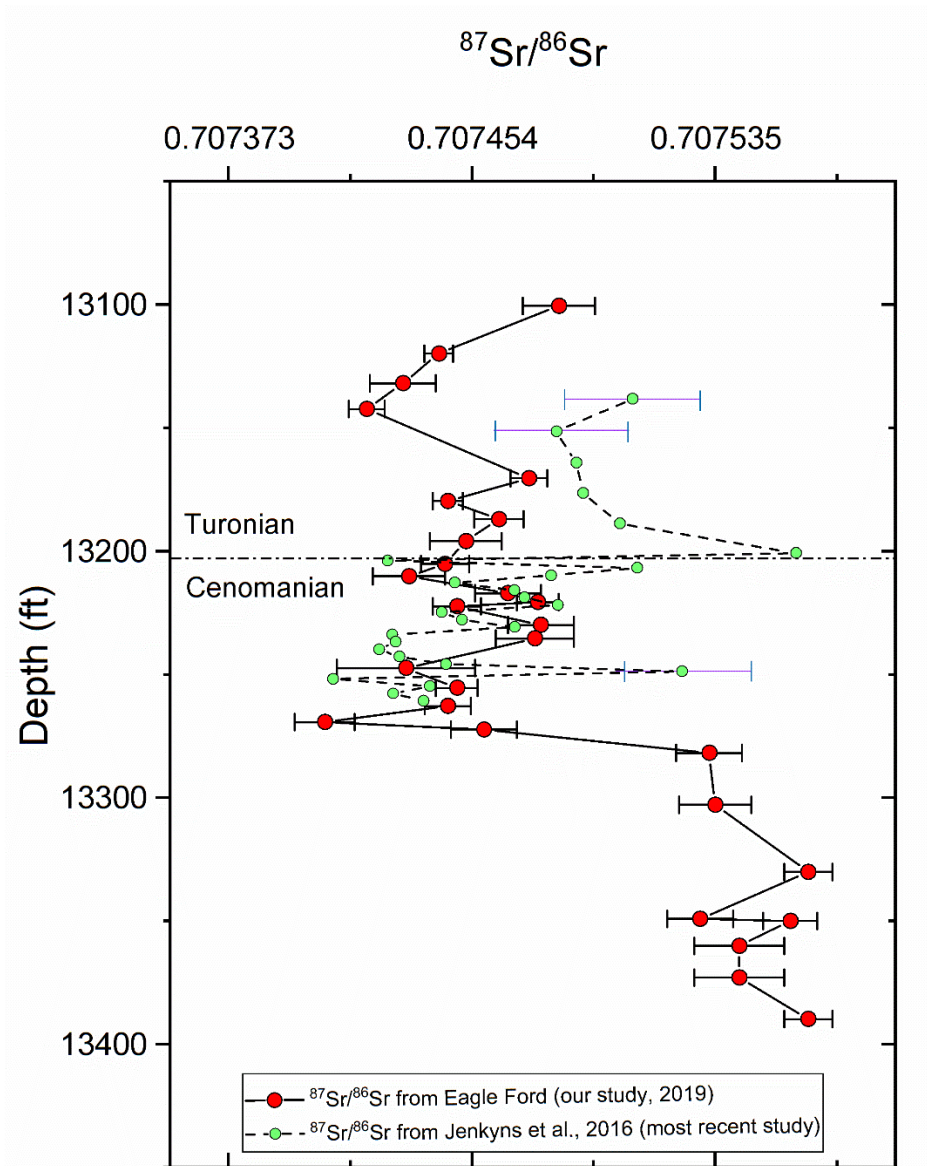


Figure 33: $^{87}\text{Sr}/^{86}\text{Sr}$ sea water curve from 28 close spaced carbonates in black shales of 300 ft EF Shale subsurface core displaying a lesser radiogenic input of $^{87}\text{Sr}/^{86}\text{Sr}$ during C-T event (OAE2) and leading up to it, in comparison to the most recent global $^{87}\text{Sr}/^{86}\text{Sr}$ sea water curve established by Jenkyns et al. (2016) from platform carbonates in Italy. Notice how the curve by Jenkyns et al. (2016) do not trace the entirety of the OAE2 during which the entire EF Shale was deposited but during the short duration of C-T boundary, their samples show a zigzag variation of the $^{87}\text{Sr}/^{86}\text{Sr}$ with much larger errors essentially obliterating the variation observed in this study. The lowering of the $^{87}\text{Sr}/^{86}\text{Sr}$ ratios before C-T boundary and its gradient increase in the Turonian indicate arc source, some considering large scale global arc volcanism in the Cretaceous (Lee et al., 2018; Figure 34).

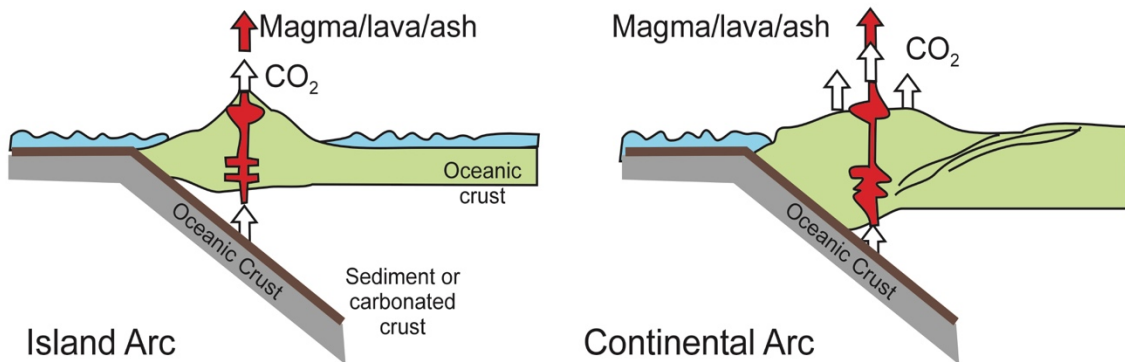
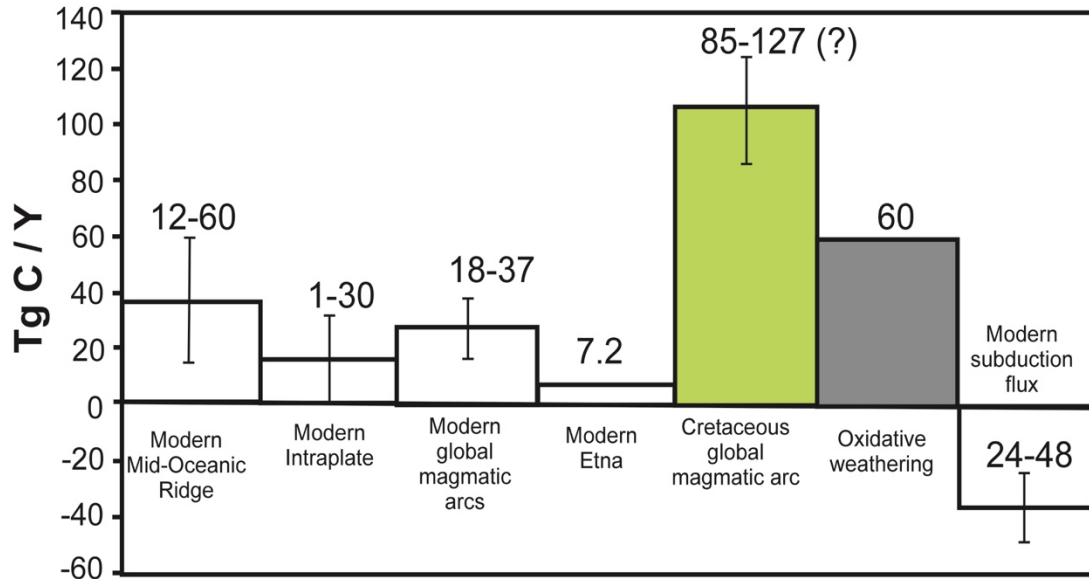
1.3.4. Discussion

The Sr isotopic ratios of global sea water, because Sr has a long enough residence time of 1-2 Ma in sea water, is well-mixed and generally believed to reflect continental weathering, MORB including hydrothermal strontium input and plume volcanism of ocean basins. A high-precision Sr isotopic ratio curve for the entire duration of deposition of the EF Shale including the C-T boundary is attempted herein. Figure 33 shows the data attained in separated carbonates of the EF Shale in the single core (Well #8 of Figures 3, 5, 6 and 20) covering a thickness of ~300 ft. The $^{87}\text{Sr}/^{86}\text{Sr}$ values range from 0.707405 – 0.707566 for the 300 ft long EF core, Well 8.

There is a sharp decrease in the isotopic ratio before the C-T boundary, in the Cenomanian? and then in the progressive increase in the Turonian. There is also a difference from the recently reported variation by Jenkyns et al. (2016). We interpret this lowering in the $^{87}\text{Sr}/^{86}\text{Sr}$ ratios as indicating input from less radiogenic arc volcanism, in contrast with mafic or plume volcanic sources considering the large scale global arc volcanism during Cretaceous (Lee et al., 2018).

Our high-precision Sr-isotopic analyses clearly shows considerable variation across the Cenomanian-Turonian boundary and into the Turonian. In contrast, the most recent $^{87}\text{Sr}/^{86}\text{Sr}$ variation by Jenkyns et al. (2016), with larger 2σ errors essentially obliterates the variation as observed by this study.

CO₂ sources and fluxes in terragrams Carbon per year



After Lee and Lackay (2015)

Figure 34: Wide scale global volcanism during the Cretaceous leading to CO₂ fluxes, sourced from the volcanisms (Island and Continental Arc volcanisms especially), Lee and Lackay, (2015). From our study, we can conclude that there was continuous, enormous quantities of CO₂ released during volcanism from 84 Ma to 95.5 Ma atleast.

CONCLUSION

We have demonstrated in Figure 16 that most of the micronutrients and Fe are equally sourced in the extraneous volcanic source and the host rock for the volcanic ash in the EF black shales. We have also documented above, the ubiquity of the ash beds throughout the EF deposition, not only obviously visible ash layers in cm scale to much greater in thickness (Figures 5 and 6) but also in fine lamellae-like thin layers that disappear in microscopic scale into micro-fragments of phenocrysts (Figures 10-14).

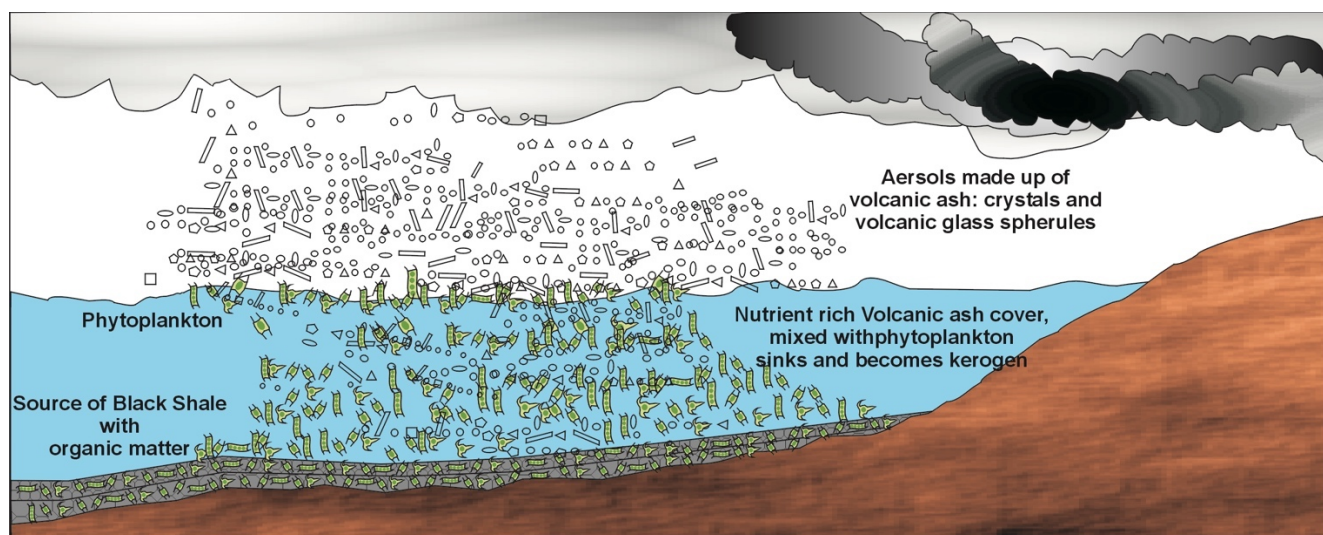


Figure 35: Schematic representation of the origin of kerogen from phytoplankton and volcanic ash.

Figure 35 is a visual representation of above-mentioned observation. Continuous andesitic volcanism creating aerosols cover the lush phytoplankton growing on the surface of the sea resulting from the high CO_2 in the atmosphere during the Cretaceous (from Barremian to Coniacian) (Figure 34). The phytoplankton get covered by the aerosol blanket and together submerge on the bottom of the shallow sea. The next phytoplankton bloom meets the same fate with the ash layer blanket, immersing below and covering the previous layer. These successive layers maintain an oxygen-deficient environment, preventing oxidation of the organic layer from

decomposition. Ultimately, preservation of these organic-rich layers results in kerogen-rich deposits of the EF Shale. This model of oil-generation is of course, suggested for the EF as we have documented the geology, petrography, geochemistry and geochronology of the entire EF Shale cores with a model of continuous volcanism as indicated by the volcanogenic clay (swelling clays/smectites) throughout the EF black shale succession (Figures 8 and 9).

PROJECT 2

SYNCHRONOUS ACID VOLCANISM WITHIN THE DECCAN: PLUME HEAD-INDUCED ANATEXIS NEAR THE END- CRETACEOUS MASS EXTINCTION

Puloma Chakrabarty, Ph.D.

The University of Texas at Arlington, 2019

Supervising Professor: Asish R Basu

Abstract

The Deccan Traps (DT) volcanism along with the Chicxulub bolide impact have been implicated in the Cretaceous-Paleogene (K-Pg) mass extinction. Recent studies used ‘redbole’ lava weathering surface U-Pb zircon geochronology to reconstruct a high-precision timeline of DT basaltic-volcanism suggesting a few high-volume eruptive periods. Relationship between acidic-carbonatitic-intrusives within DT and DT flood magmatism remain unknown. We present high-precision zircon U-Pb ages from two intrusive acid igneous complexes, Alech and Barda Hills in Saurashtra Peninsula, determined using chemical-abrasion isotope dilution thermal ionization mass spectrometry (CA-ID-TIMS). Crystallization ages for Barda (65.751 ± 0.020 Ma) and Alech (65.724 ± 0.017 Ma) granophyres indicate synchronicity with DT basaltic-volcanism, ~265 kyr

younger than K-Pg boundary. Located ~580 km NW of the most voluminous DT in western Ghats, near Mumbai, India these complexes were emplaced during a magmatic lull between Ambenali and Mahabaleshwar Formations. Lower precision U-Pb zircon ages of three other acid intrusives from the Girnar, Rajula and Phenaimata complexes, by laser ablation inductively-coupled plasma mass spectrometry (LA-ICP-MS), overlap the age of DT, also falling in the age gap between Ambenali and Mahabaleshwar Formations. The $\epsilon_{\text{Hf}}(\text{initial})$ of a few zircons (+6.4 to -8.9), whole-rock $^{87}\text{Sr}/^{86}\text{Sr}(\text{initial})$ (0.702439-0.760932) and $\epsilon_{\text{Nd}}(\text{initial})$ (+1.11 to -35.7) values for all five intrusives suggest significant reworking and anatexis of older continental crust, consistent with PRIMELT3 1341°C liquidus temperature estimates of associated basalts and Rhyolite-MELTS 958°C estimates for granophyres. We conclude that these felsic intrusive complexes, occurring over a wide region in the Deccan, originated by plume-induced catastrophic melting of continental crust, soon after the high-flux event of the DT that formed the Ambenali Formation following K-Pg mass extinction.

CHAPTER 4:

SYNCHRONOUS ACID VOLCANISM WITHIN THE DECCAN: PLUME HEAD-INDUCED ANATEXIS NEAR THE END-CRETACEOUS MASS EXTINCTION

2.1. Introduction

Deccan Traps (DT) continental flood basalt eruption in the Indian Peninsula have been proposed by Courtillot et al. (1988) and Courtillot and Renne (2003) as the cause of the K-Pg mass extinction, in contrast with an extra-terrestrial impact event (Alvarez et al., 1980). More than 25 years ago, it was also shown that the DT eruptions were in several pulses beginning at least several million years before the main volume tholeiitic pulse of the DT (Basu et al., 1993). Recent high-precision U-Pb ages in zircons from weathering surfaces (redbole-bearing) of the tholeiitic flows (Schoene et al., 2015, 2019) as well as Ar-Ar dating of the main sequence high-flux DT eruptions (Sprain et al., 2019) focused on small differences in relative timings of the impact, the K-Pg mass extinction and the major pulses of the lava eruptions in scales of only several thousands of years. Inherent in these small-scale differences of eruption ages is the consideration of the proposal of triggering the largest DT eruptions by the K-Pg boundary impact (Richards et al., 2015).

Although the DT dominantly comprise of tholeiitic flood basalts and basaltic andesites, there are well-documented examples of rhyolite, trachyte, basanite and carbonatites (Lightfoot et al., 1987; Basu et al., 1993; Sethna et al., 1999; Sheth et al., 2011; and others) found throughout the DT. Some of these studies, dealing mostly with trachytic and rhyolitic rocks within the DT were concerned with mixing, melting of mafic and felsic magmas. In this study, we focus on a few acid intrusives within the DT occurring as discrete, individual complexes and sometimes

associated with non-tholeiitic, alkalic-carbonatitic lithologies that appear to be of nearly same age as the main tholeiitic pulse of the DT. These intrusive complexes with heterogeneous lithologies, set within DT's major structural tectonic framework, lineaments and cratonic uplifts are shown in Figure 36: the acid complexes are shown in yellow triangles and the green stars are for the alkalic-carbonatitic complexes. We provide high precision CA-ID-TIMS U-Pb zircon ages of Alech and Barda acid complexes, marked as 11 and 12 (Figure 36), to the west aligned with the Narmada lineament. We also provide LA-ICP-MS U-Pb zircon ages for the Girnar, Rajula and Phenai Mata complexes, marked as 13, 16 and 15, respectively, in Figure 36.

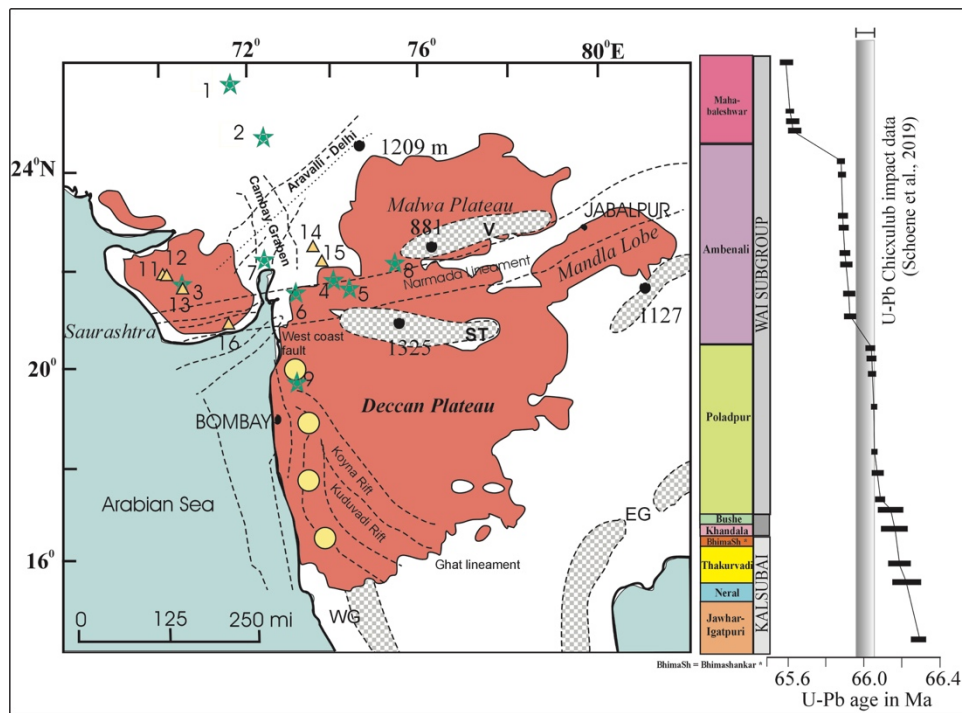


Figure 36: Map of part of the Indian Peninsula showing the approximate locations of many of the acid igneous complexes associated with the Deccan Traps (DT) volcanism and its major structural tectonic framework. Also shown, corresponding U-Pb ages from a recent study, Schoene et al. (2019) from redboles, weathering surfaces between the lava flows. The dates are refined from stratigraphic Bayesian model. Vertical grey shaded bar represents Chicxulub impact age (Clyde et al., 2016), Cretaceous-Paleogene (K-Pg) 66.016 ± 0.050 Ma.

Magneto-Tellurics (MT), Deep Resistivity Soundings (DRS) and Deep Seismic Soundings (DSS) have been able to give information about the high velocity traps (Deccan Traps) underlain

by low velocity Mesozoic sediments (Sarma et al., 2004; Reddy P.R., 2005). The Saurashtra Peninsula is a horst composed of Mesozoic and Cenozoic sediments, covered mostly by Deccan traps. There are three prevalent lineament trends, which are intersecting, NE-SW Delhi trend, ENE-WSW Narmada trend and NNW-SSE Dharwar trend (Chopra et al., 2014). The Mesozoic sediments underneath the Deccan Traps are thicker in the southern part of Saurashtra (2-3km) and insignificant in the NE part (few hundred of meters) (Figures 37 and 38).

The 1D shear wave velocity profile gives the top layer (Deccan Traps) a thickness between 0.8 and 1.4 km (Figure 37), underlying Mesozoic sediments (2.0-2.5 km thick) and the basement which is 1.2-5.0 km thick (Chopra et al., 2014). The crustal depth of Saurashtra Peninsula varies from 33 to 37 km (Tewari et al., 2009). In the northern part of Saurashtra, there is a crustal thinning of around 7 km whereas there is a 10 km up-warping of the Moho beneath Junagadh, in the central part (Figure 38). This might be due to mafic igneous intrusions that cause the under-plating (Tewari et al., 2009). The Moho depths and V_p/V_s ratios were measured by Chopra et al. (2014) using the methodology proposed by Zhu and Kanamori (2000). From the V_p/V_s ratios, Chopra et al. (2014) calculated the crustal elastic property, which is defined by Poisson's ratio (σ) using the equation

$$\sigma = ((V_p/V_s)^2 - 2)/2((V_p/V_s)^2 - 1)$$

The mafic/ultramafic rocks usually have high V_p/V_s and partial melt affects the V_p/V_s ratio (Watanabe, 1993). It has been documented that σ is sensitive to the composition of rocks, presence of fractures and partial melt (O'Connell and Budiansky, 1974; Mavko, 1980; Chopra et al., 2014). As the silica content goes up, the σ decreases whereas increase in mafic content causes an increase in the σ values (Zandt and Ammon, 1995). The ratio V_p/V_s in the Saurashtra region varies between 1.61 and 2.09, with an average of 1.81 and intermediate σ values (0.19-0.32, average 0.27). The intermediate σ values in Saurashtra show that the region has crust of intermediate composition and

some of the stations have $\sigma = 0.3$ which may be related to presence of local partial melt close by (Chopra et al., 2014) (Figures 37 and 38).

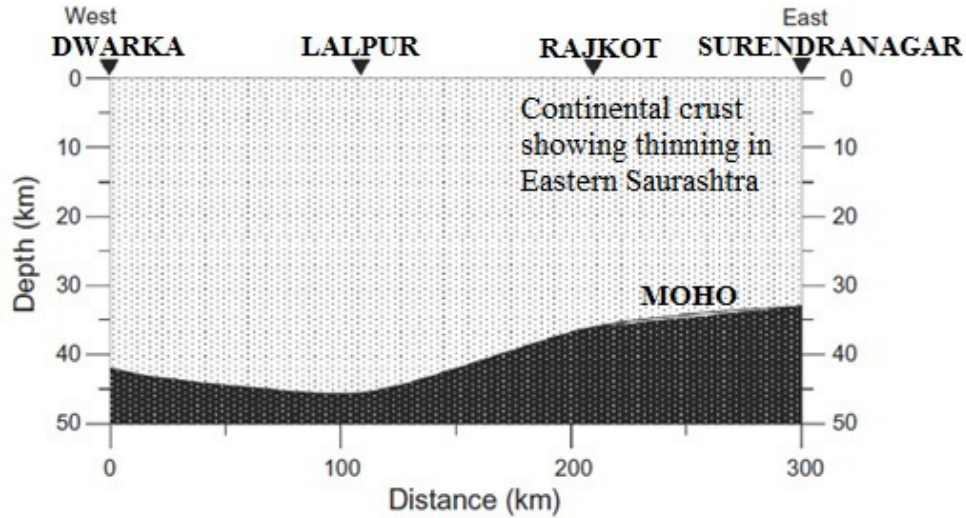


Figure 37: EW section in north Saurashtra showing 7 km crustal thinning (Chopra et al., 2014).

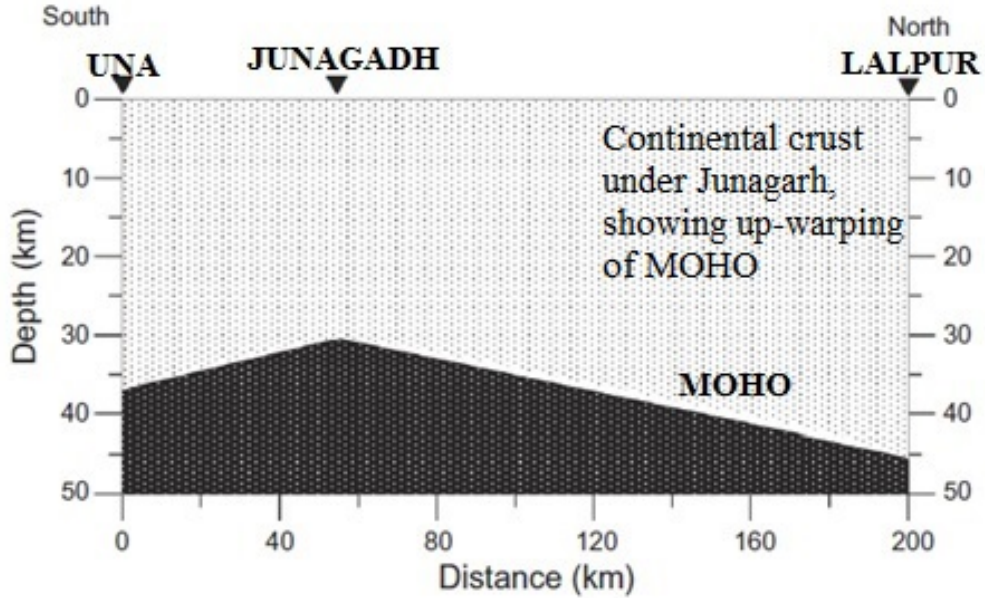


Figure 38: NS section in Junagadh, Central Saurashtra with 10 km up-warping of Moho (Chopra et al., 2014).

2.2. Methods

Ten whole rock samples of rhyolites and granophyres from the five acid complexes were crushed for zircon separation by heavy liquids and then by handpicking under binocular microscope in our laboratory in UT Arlington. 142 of these separated zircons were mounted and polished on plugs at the Arizona LaserChron Center and then analyzed for U-Pb geochronology by Element2 HR ICPMS with New Wave DUV193 Excimer laser, and for Lu-Hf isotopes by Nu HR ICPMS by New Wave UP193HE laser. Zircons from two of the samples, Alech 7 and Barda 6, were also analyzed for high precision U-Pb geochronology by CA-ID-TIMS method using EARTHTIME tracer in the MIT laboratory on a VG Sector 54 mass spectrometer. Thirty-six whole rock samples from the seven acid intrusive complexes were analyzed for major oxides by Jobin-Yvon Ultima-C ICP-OES at Boston University using the flux fusion method. Sr and Nd of twenty-five of these five acid intrusive samples and associated basalts were separated in the Ultra Clean Laboratory, UT Arlington following the ion-exchange chromatography techniques developed in-house and Boston University. These samples were analyzed using the ThermoFinnigan TRITON at Boston University for the Sr-isotopes and Nu Plasma 1700 MC-ICP-MS at the Water Quality Centre, Trent University for the Nd-isotopes.

2.3. Results

In this study, we report lower precision LA-ICP-MS along with high precision CA-ID-TIMS U-Pb zircon ages, the latter in two of the five complexes, most of them in the Saurashtra Peninsula (marked in yellow triangle, Figure 41) and falling along the E-W Narmada rift (Figures 36, 41). Our data also include (Figure 40) Lu-Hf isotopes in the same zircons analyzed for U-Pb

age by LA-ICPMS and by CA-ID-TIMS (Figure 39 and Table 11). The LA-ICPMS data of the zircons (Table 10) in the five acid complexes are summarized in a plot in Figure 40 along with the K-Pg boundary age. The Lu-Hf isotopes, ϵ_{Hf} initial values (+6.4 to -23.4) of the zircons analyzed in this LA-ICPMS study are reported in Table 12, along with two samples done by CA-ID-TIMS (Table 12).

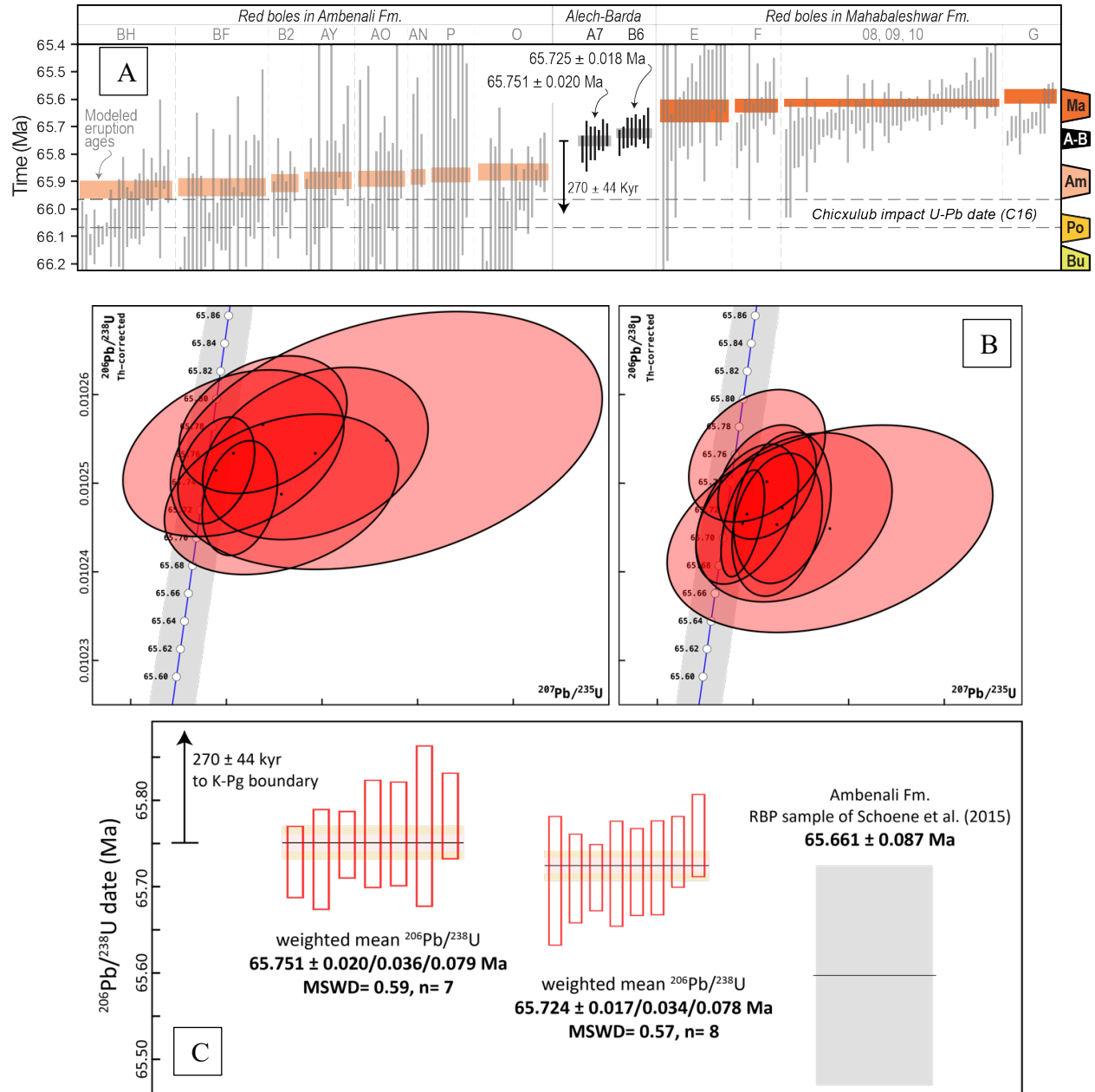


Figure 39: A: High-precision U-Pb ages in zircons obtained by CA-ID-TIMS method of two acid granophyre intrusives. B: The weighted mean average ages of the two granophyres, A7 (65.724 ± 0.017 Ma) and B6 (65.751 ± 0.020 Ma), C: the acid granophyres are only ~ 265 kyr younger than the K-Pg boundary.

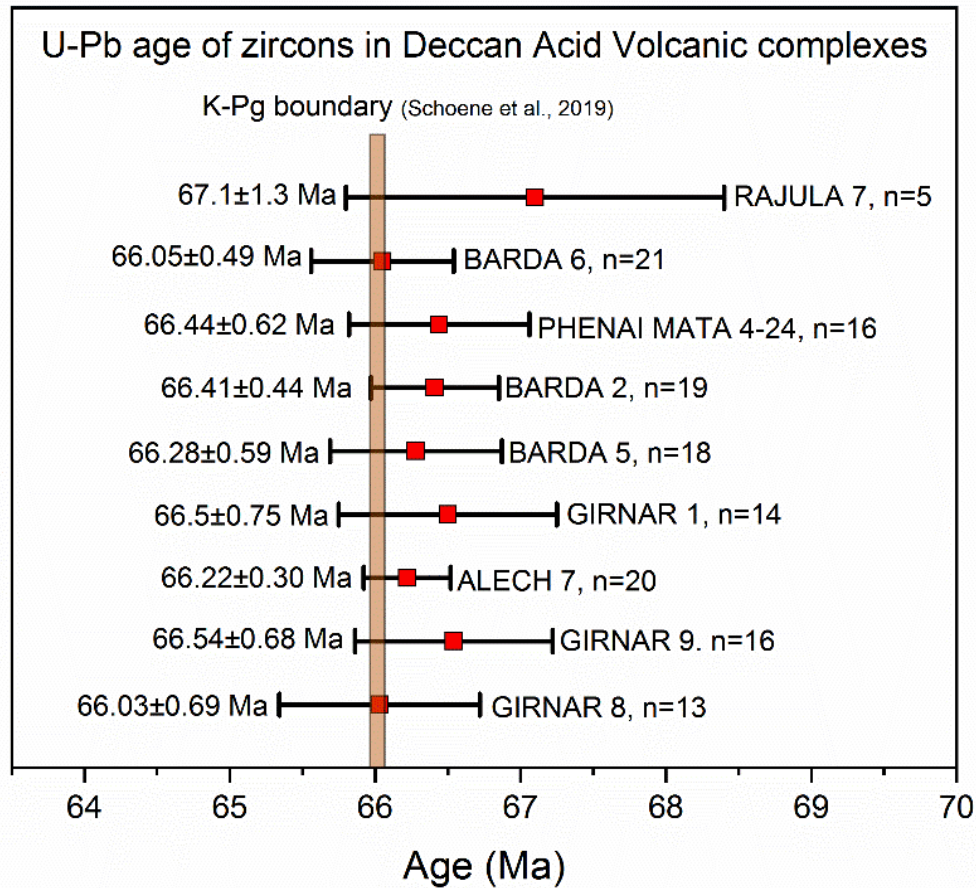


Figure 40: Weighted mean LA-ICP-MS U-Pb ages of zircons from five acid intrusive complexes in the DT are summarized in this figure along with K-Pg boundary age (Schoene et al., 2019). ‘n’ represents the numbers of zircons analyzed per sample.

Our high-precision U-Pb ages in zircons of two acid granophyre intrusives are shown in Figure 39 and compared with DT zircon ages in redboles weathering surface of the different DT lava formations (Schoene et al., 2019). These redbole zircon ages were refined from stratigraphic Bayesian model and Markov Chain Monte Carlo method (Schoene et al., 2019) and the data in two major formations of the DT, namely the Ambenali and Mahabaleshwar, are shown in Figure 39A as the two granophyre ages fall tightly between these two formations. The weighted mean average ages of the two granophyres, A7 (65.724 ± 0.017 Ma) and B6 (65.751 ± 0.020 Ma) are shown in Figure 39, that are only ~265 kyr younger than the K-Pg boundary.

Major element compositions of acid igneous rocks and associated basaltic rocks of seven igneous complexes including Pavagadh (marked 14 in Figure 36) and Osham complexes in Figure 41 are reported in Table 14. The olivine liquidus temperatures using PRIMELT3 of the basalt with MgO >7 wt% (Herzberg and Asimow, 2015) and the crystallization temperature of these acidic volcanics using Rhyolite-MELTS (Ghiorso and Gualda, 2015) were calculated (Table 14) and plotted in Figure 46. The estimated mantle potential temperature (1550°C) by Herzberg and Gazel (2009) of the DT using PRIMELT3 is also plotted in Figure 46, and of the basalts of this study are shown in Table 14.

Sm-Nd and Rb-Sr systematic data, the initial ϵ_{Nd} and initial $^{87}Sr/^{86}Sr$ isotopic composition of both mafic and acidic rocks of the five intrusive complexes (Figures 42 - 45) are shown in Table 15 and plotted in Figure 46. Initial ϵ_{Nd} values (1.1 to -35.7), initial $^{87}Sr/^{86}Sr$ values (0.702439-0.760932) are shown in this figure along with Sm-Nd model ages after DePaolo (1986). Also shown are the general range of the al DT lava flows in dotted outline; and in solid red, the isotopic ranges of the Poladpur, Ambenali and Mahabaleshwar formations are shown for comparison (Peng et al., 1994; Basu et al., in preparation 2019).

2.4. Discussion

Figure 36 shows part of the Indian Peninsula with approximate locations of igneous complexes of western and northwestern India that are associated with the DT. With the exception of the two alkalic intrusives, 1 and 2 in Figure 36, most of the rest are within the current exposures of the DT shown in red. The relationship of the intrusives with the major E-W trending Narmada-Son lineament, and some of the cratonic uplifts (Figure 36) are noteworthy. The high-precision U-Pb ages of zircons in granophyres of two acid laccolithic complexes, farthest to the west in the

Saurashtra Peninsula (11 and 12 in Figure 36) along the Narmada lineament were recently presented (Basu et al., 2018). Their more precise ages and petrogenetic relationship with the main tholeiitic pulses of the DT and the K-Pg boundary age are discussed herein. As the new age data presented herein are U-Pb ages in zircons of acidic complexes within the Deccan, a key feature of this discussion includes the high-precision U-Pb ages of zircons between the lava flows of the main DT Formations (Schoene et al., 2015, 2018), although new $^{40}\text{Ar}/^{39}\text{Ar}$ ages on DT Formations are also available (Sprain et al., 2019). It is worth noting that redbole aerosol zircons from Schoene et al. (2015, 2019) between the lava surfaces of the various formations of the DT were very likely sourced from the acid eruptive complexes of this study shown in Figure 36.

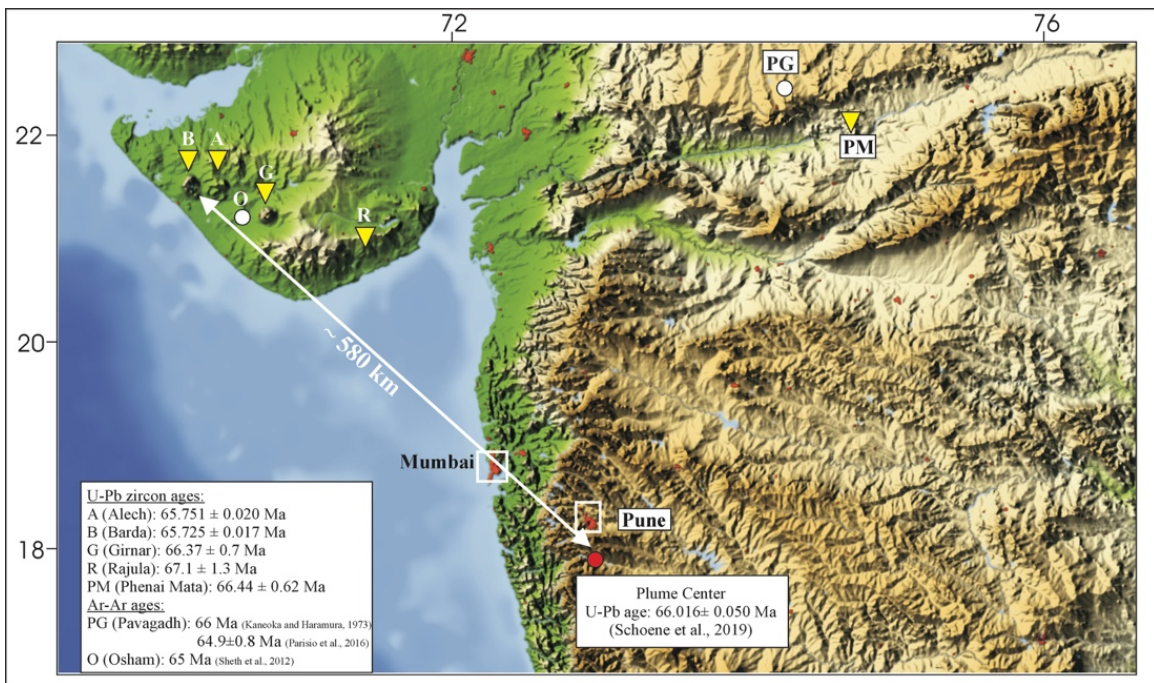


Figure 41: High resolution relief map of the part of the Indian subcontinent containing the DT including the Saurashtra Peninsula. The assumed Deccan plume center (red dot) yields a U-Pb K-Pg age (Schoene et al., 2019). The distance of Barda-Alech is 580km to this center.

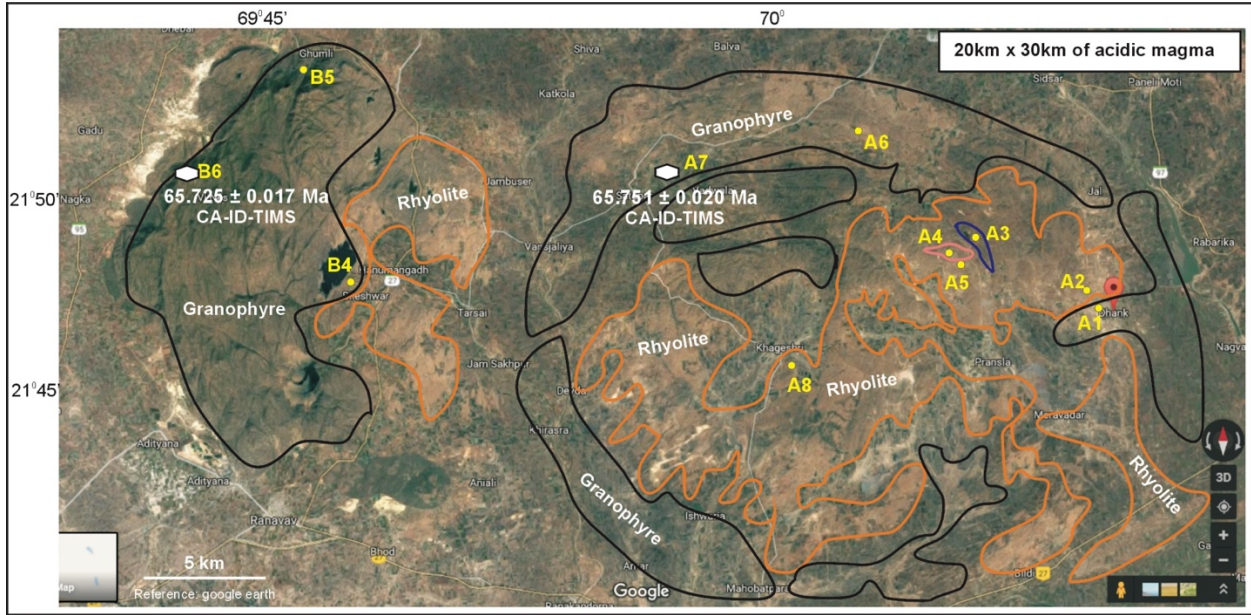


Figure 42: Alech and Barda laccolithic acid intrusions with ring dykes sourced from Google Earth () and lithologic outline plotted based on field observation (Basu, personal), geological map of De and Bhattacharyya (1971) and from Dave (1971).

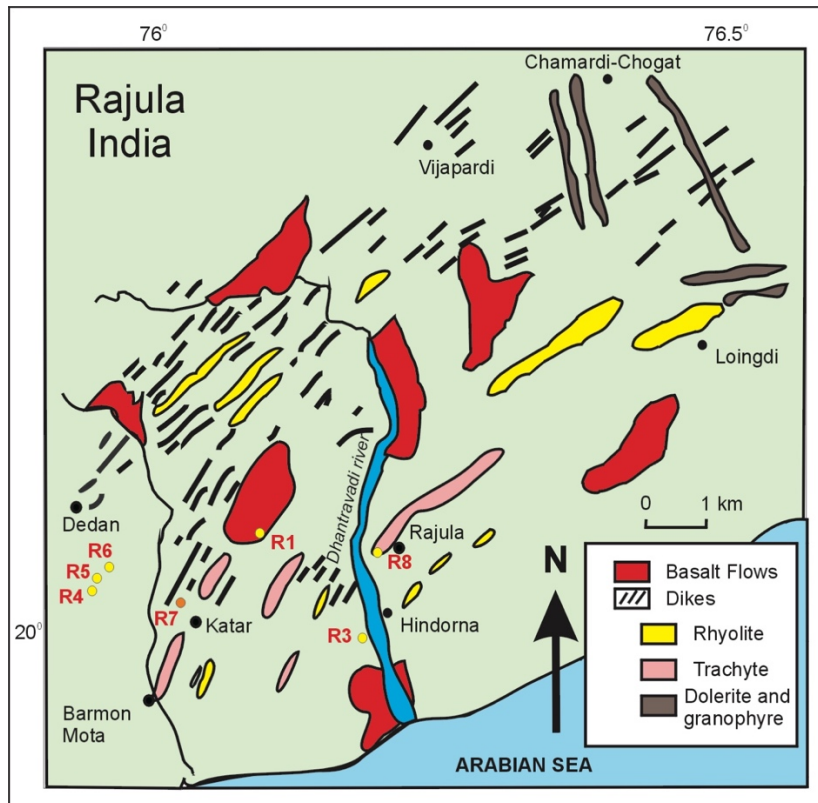


Figure 43: Geological map of the part of the Rajula complex showing felsic basaltic dikes with sample locations in this study. The map is modified from Chatterjee and Bhattacharji (2004).

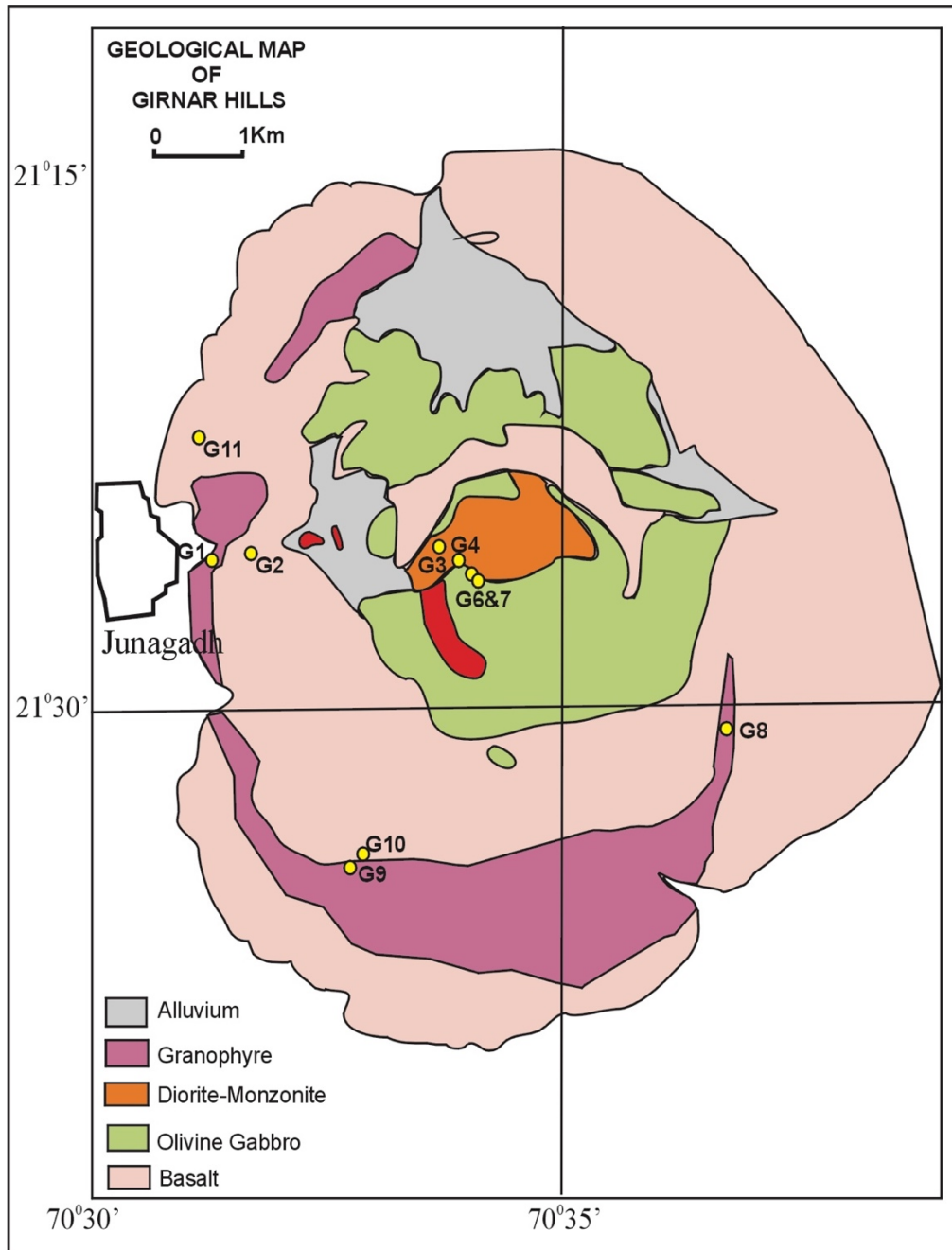


Figure 44: Geological map of the Girnar laccolithic-granophytic complex with the locations of samples in this study. This map is modified after Mathur et al., 1926.

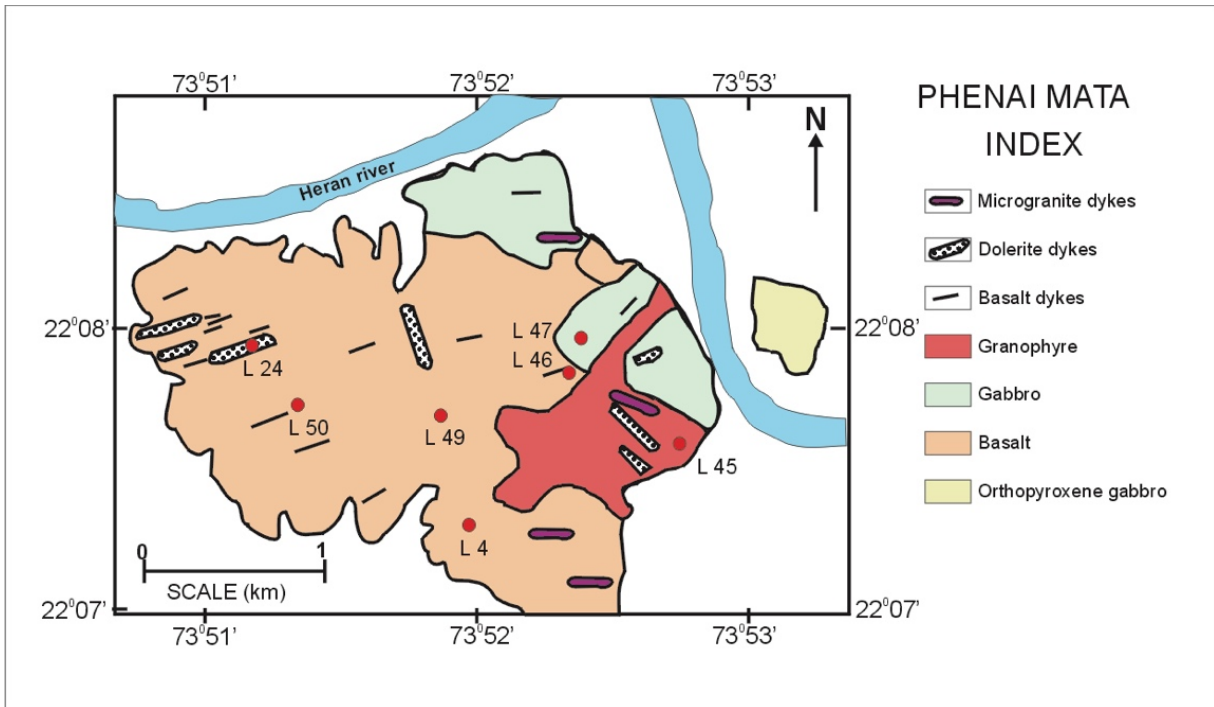


Figure 45: Part of the Phenai Mata (PM) geological complex ~550km E of Alech and Barda hills, lying in the Narmada-Son lineament (PM in Figure 41 and 4, 15 in Figure 36). Locations of samples analyzed are shown in the map. The map is modified after Hari et al., 2011.

The weighted mean zircon ages of Alech and Barda granophyres are 65.751 and 65.724 Ma, respectively, identical within error of each other. Interestingly, this age falls in a small gap between the Ambenali and Mahabaleshwar Formation ages, two of the most voluminous eruptions of the DT (Figure 39). This age is also approximately 265 kyr younger than the K-Pg boundary age. The U-Pb zircon ages of the three other complexes, Girnar and Rajula in Saurashtra, and Phenaimata, farther east in the Narmada lineament, although less precise, indicate approximately the same ages (Figures 40, 41). More interestingly, even if we do not take into account the less precise ages of these three complexes, the precise age of the Alech and Barda granophyres located approximately 580 km away from the main Deccan eruptive phases in the Western Ghats, the supposed plume Center, is of considerable interest for their petrogenesis. This is because these are fairly large shallow laccolithic acidic intrusives, synchronous with the main DT tholeiitic pulse without any evidence of being fractional crystallization residues of mafic magmas. Taking into

account the less precise zircon ages by LA-ICPMS (Figure 40) of three other acid complexes also fall between the eruptions of the Ambenali and Mahabaleshwar Formations. It is very likely that there was near-synchronous generation of these acidic magmas after a major tholeiitic pulse of the DT's Ambenali Formation over a large area of the DT (Figure 36).

Using PRIMELT3 software (Herzberg and Asimow, 2015), we estimated the olivine liquidus temperatures for the basaltic rocks (Figure 46) associated with the acidic rocks of the Alech, Barda, Girnar, Phenaimata and Rajula intrusive complexes, the primary focus of this study in terms of geochronology and Nd-Sr isotopes. We also include Osham and Pavagadh intrusive complexes in this estimate as their Ar-Ar ages and tectonic setting match the other five complexes (Parisio et al., 2016). The average liquidus temperature, estimated at 0.2-0.3 GPa, for the basalts is 1341°C, whereas the average crystallizing temperatures of the associated acidic rocks using Rhyolite-MELTS calibration of quartz and feldspar saturation surface software (Ghiorso and Gualda, 2011) for fluid-bearing silicic systems at 0.1-0.2 GPa pressures is 958°C. The three temperatures shown in Figure 46, including the mantle potential temperature of the DT at 1550°C (Herzberg and Gazel, 2009), the highest among global plume-related volcanisms, are all relatively high. We note these temperatures are higher than that normally found for lavas associated with plume-derived volcanic rocks.

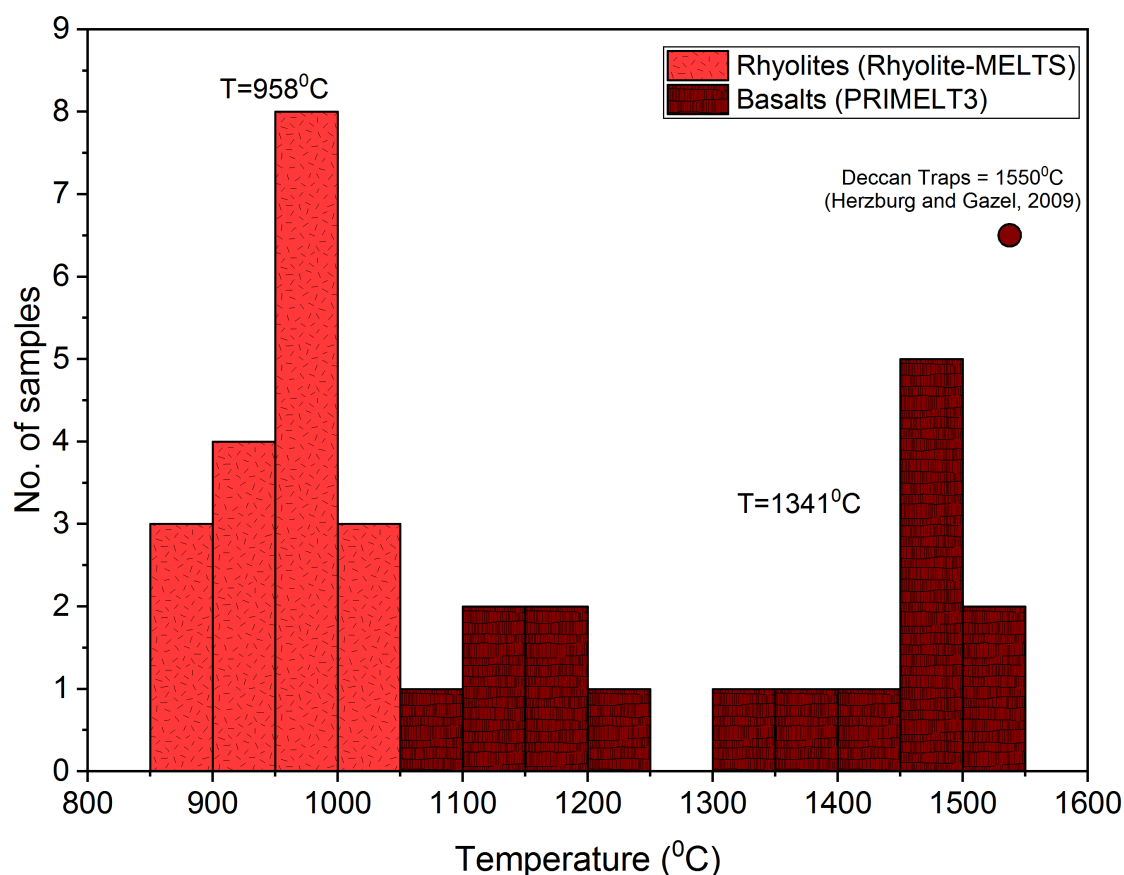


Figure 46: Olivine liquidus temperatures for basalts and Rhyolite-MELTS temperatures for acidic rocks.

The Nd-Sr isotopic correlations of the 25 whole rock samples of the five intrusive complexes in Figure 47 and listed in Table 15 indicate large variations in the initial Nd and Sr isotopic ratios, most of the samples falling outside the fields of the DT samplers of varying lithologies, outlined in Figure 47. The locations of the 25 samples with their rock-types in the various complexes are shown in the geological maps in Figures 41-44. The range of the Nd-Sr isotopic ratios of the samples fall within <1 Ga, 1 Ga and >2.8 Ga model ages of the basement that was intruded by the plume-derived DT lavas. The observed isotopic variations in the same complex of different lithologies are of special interest for their petrogenesis. The Girnar complex displays anomalous acid granophyre to undersaturated nepheline syenite in close proximity and their initial

ϵ_{Nd} values vary from -2.4 to -25.1. Similarly, undersaturated tinguaitite occurring in association with basalt and granophyre in the Phenaimata complex show initial ϵ_{Nd} isotopic ratios from -12.4 to -35.7 (Table 15 and Figure 47). Also, notably, acid granophyre-rich Alech laccolithic complex and its associated basalt show initial ϵ_{Nd} varying between -0.3 to -13.7. The samples plotting away from the DT field in Figure 47 are of special interest.

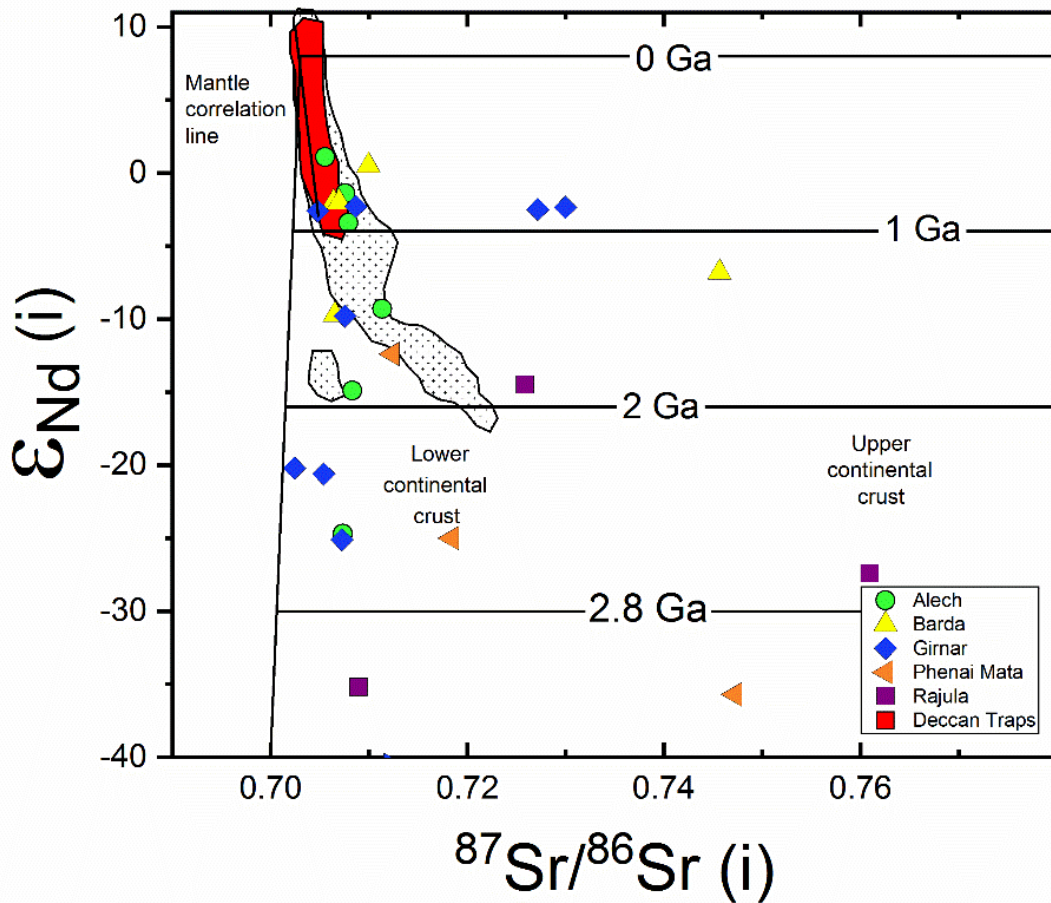


Figure 47: Initial Nd and Sr isotopic compositions of the whole rock lithologies of the five intrusive complexes in the DT analyzed in this study.

Several acid-mafic rocks on the eastern edge of the Saurashtra Peninsula about ~100km NE of Rajula (Figures 36 and 40) in Chogat-Chamardi area (Sheth et al. 2011) show some Nd-Sr isotopic variations plotting outside the main DT fields in Figure 47, but with a distinctly narrower range than shown by the five complexes of this study. It is usual practice among petrologists-

geochemists to interpret the relationship seen in Figure 47 by an assimilation fractional crystallization process including crustal material and mafic magma (e.g., Sheth et al., 2011). However, the occurrence of undersaturated and silica -saturated acidic rocks, side by side, in the same complex with wide isotopic variations indicate both these silicate melts (Table 15) have preserved their non-identical source variability faithfully. It is clear, considering the synchronous age relation, significant plume impact melting of superheated Saurashtra crust of heterogeneous lithology is required to explain such variability. The isotopic data of this study, in conjunction with the geochronological data, the relatively high olivine liquidus temperatures of the basalts and the temperatures of crystallization of the acidic rocks (Figure 46), would all be consistent with such a proposal of plume impact melting of local continental crust in Saurashtra. In other words, a large part of the continental crust of Saurashtra melted synchronously with the advent of the DT mafic melt. A similar anatectic reworking of the Saurashtra crust was suggested by Chatterjee and Bhattacharji (2004) for the Rajula Complex (marked as 16 in Figure 36).

A schematic diagram of the Deccan plume head impacting beneath the Indian Peninsula is shown in Figure 48, modified from Richards et al. (2015), based on our isotopic and geochronological data of the acidic intrusives of the Deccan, particularly in the western and northern part of the DT province. An important departure from the Richards et al. (2015) model is shown in the inset A in the NW corner of the Saurashtra Peninsula by near-contemporaneous, ~ 265 kyr after the K-Pg boundary, melting of lower crust by melts from the DT plume head. Shown in inset A are Barda (B), Alech (A), Girnar (G) and Rajula (R) complexes, ~ 580 km from probable plume center near Pune (Figure 41). Interestingly, this distance is within the 600 km radius of the “circular footprint area” around the Poladpur, Ambenali and Mahabaleshwar Formations (Richards et al., 2015).

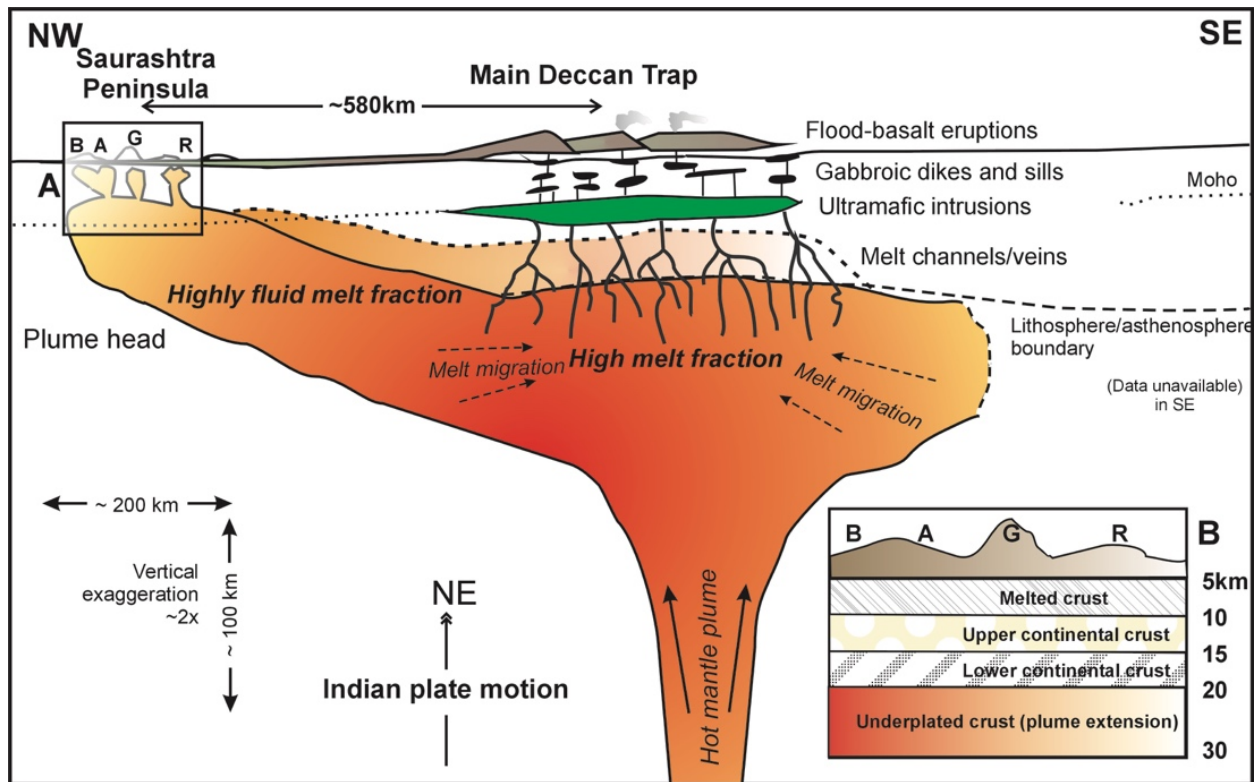


Figure 48: A schematic diagram of the Deccan plume-head impacting beneath the Indian Peninsula (modified from the recent cross-sectional diagram proposed by Richards et al., 2015). In the inset, A(Alech), B(Barda), G(Girnar) and R(Rajula)

The inset B in the lower right is a detailed version of A showing a geological section along B-A-G-R profile in Saurashtra based on seismic-gravity modeling (Rao and Tewari, 2004). The melted crust is inferred to be below 5 km depth in this model. We interpret the origin of B-A-G-R, based on geochronological and isotopic data presented above by catastrophic crustal melting, caused by the ingress of highly fluid melt fraction from the plume head that reaches continental crustal depths, generating B-A-G-R parent magmas. The central part of the plume head is shown in lighter shading suggesting its arrival at shallower depths.

2.5. Conclusion

Five coeval intrusive complexes, 500 km apart, of distinctly different lithologies formed over the Deccan plume head near the K-Pg age boundary. High precision CA-ID-TIMS in two of the acid complexes suggest emplacement age ~ 265 kyr after the K-Pg age of 66.04 Ma. Nd, Sr, and Hf isotopes in zircons indicate petrogenesis of these complexes by basement reworking including crustal anatexis. These results indicate a sudden increase in the effective permeability aided by the various lineaments, especially the E-W Narmada lineament (Figure 36) and the heat conducted and advected by the plume-derived mafic magma. We have shown in this study that the synchronous intrusive complexes over a wide region in the Deccan Province originated by plume-induced catastrophic melting of continental crust shortly after (~ 265 kyr) the K-Pg age boundary and between the DT extensive fluxes of the Ambenali and Mahabaleshwar Formations. Finally, modeling of plume head shape, flow and melting, in general, particularly beneath the Indian continent for the DT, would require further exploration.

REFERENCES

- Addy, S.K. and Buffler, R.T., 1984, Seismic stratigraphy of shelf and slope, northeastern Gulf of Mexico: AAPG Bulletin, v. 68, p. 1782-1789.
- Adepelumi, A.A., Alao, O.A., Ako, B.D., and Oseikpe, R.E., 2012, Modeling Of Hydrocarbon Potential And Thermal Maturity Of Gongila Shale, Chad Basin, Northeastern Nigeria: Oil Shale, v. 29, no. 2, p. 151, doi: 10.3176/oil.2012.2.05.
- Alalade, B., and Tyson, R.V., 2010, Hydrocarbon Potential Of The Late Cretaceous Gongila And Fika Formations, Bornu (Chad) Basin, Ne Nigeria: Journal of Petroleum Geology, v. 33, no. 4, p. 339–353, doi: 10.1111/j.1747-5457.2010.00483.x.
- Allègre, C. (2008). Isotope Geology (C. Sutcliffe, Trans.): Cambridge: Cambridge University Press, p. 512, doi:10.1017/CBO9780511809323
- Alvarez, L.W., Alvarez, W., Asaro, F., and Michel, H.V., 1980, Extraterrestrial cause for the Cretaceous-Tertiary extinction: Science, v. 208, p. 1095–1108, doi:10.1126/science.208.4448.1095.
- Aranovich, L.Y., Makhlof, A.R., Manning, C.E., and Newton, R.C., 2014, Dehydration melting and the relationship between granites and granulites: Precambrian Research, v. 253, p. 26–37, doi: 10.1016/j.precamres.2014.07.004.
- Assaad, F.A., 2009, Surface Geophysical Petroleum Exploration Methods: Field Methods for Petroleum Geologists, p. 21–23, doi: 10.1007/978-3-540-78837-9_3.
- Basu A, Chakrabarty P, Ibanez Mejia M, Georg B & Ghosh N, 2018, U-Pb Zircon Ages of Deccan Acid Igneous Complexes and their Temporal Relationship with the Cretaceous-Paleogene Boundary: Goldschmidt Abstracts2018, p. 145.

- Basu, A.R. and Chakrabarty P., 2017, U-Pb Ages and Hf-Isotopes of Zircons in Ash Beds and Re-Os Isotopes of the Eagle Ford Formation of South Texas: Geological Society of America, South Central Annual Meeting, San Antonio, TX, Abstract Volume, page?.
- Basu, A.R., and Chakrabarty, P., 2017, U-Pb Ages And Hf-Isotopes Of Zircons In Ash Beds And Re-Os Isotopes Of The Eagle Ford Formation Of South Texas: , doi: 10.1130/abs/2017sc-289602.
- Basu, A.R., Petaev, M.I., Poreda, R.J., Jacobsen, S.B., and Becker, L., 2003, Chondritic Meteorite Fragments Associated with the Permian-Triassic Boundary in Antarctica: *Science*, v. 302, no. 5649, p. 1388–1392, doi: 10.1126/science.1090852.
- Basu, A.R., Renne, P.R., Dasgupta, D.K., Teichmann, F., and Poreda, R.J., 1993, Early and Late Alkali Igneous Pulses and a High-³He Plume Origin for the Deccan Flood Basalts: *Science*, v. 261, no. 5123, p. 902–906, doi: 10.1126/science.261.5123.902.
- Beysac, O., Goffé, B., Chopin, C., and Rouzaud, J.N., 2002, Raman spectra of carbonaceous material in metasediments: a new geothermometer: *Journal of Metamorphic Geology*, v. 20, no. 9, p. 859–871, doi: 10.1046/j.1525-1314.2002.00408.x.
- Birck, J.L., Barman, M.R., and Capmas, F., 1997, Re-Os Isotopic Measurements at the Femtomole Level in Natural Samples: *Geostandards and Geoanalytical Research*, v. 21, no. 1, p. 19–27, doi: 10.1111/j.1751-908x.1997.tb00528.x.
- Birck, J.L., Barman, M.R., and Capmas, F., 1997, Re-Os Isotopic Measurements at the Femtomole Level in Natural Samples: *Geostandards and Geoanalytical Research*, v. 21, no. 1, p. 19–27, doi: 10.1111/j.1751-908x.1997.tb00528.x.
- Blakey, R.C., 2014, Paleogeography and Paleotectonics of the Western Interior Seaway, Jurassic–Cretaceous of North America: *American Association of Petroleum Geologists, Search and Discovery Article 30392*, p. 72.

- Bralower, T.J., Arthur, M.A., Leckie, R.M., Sliter, W.V., Allard, D.J., and Schlanger, S.O., 1994, Timing and Paleoceanography of Oceanic Dysoxia/Anoxia in the Late Barremian to Early Aptian (Early Cretaceous): *Palaios*, v. 9, no. 4, p. 335–369, doi: 10.2307/3515055.
- Bralower, T.J., Fullagar, P.D., Paull, C.K., Dwyer, G.S., and Leckie, R.M., 1997, Mid-Cretaceous strontium-isotope stratigraphy of deep-sea sections: *Geological Society of America Bulletin*, v. 109; no. 10; p. 1421–1442; 22
- Burke, W.H., Denison, R.E., Hetherington, E.A., Koepnick, R.B., Nelson, H.F., and Otto, J.B., 1982, Variation of seawater $^{87}\text{Sr}/^{86}\text{Sr}$ throughout Phanerozoic time: *Geology*, v. 10, no. 10, p. 516–519, doi: 10.1130/0091-7613(1982)10<516:vosstp>2.0.co;2.
- Cai, Y., Lagatta, A., Goldstein, S.L., Langmuir, C.H., Gómez-Tuena, A., Pozzo, A.L.M.-D., and Carrasco-Núñez, G., 2014, Hafnium isotope evidence for slab melt contributions in the Central Mexican Volcanic Belt and implications for slab melting in hot and cold slab arcs: *Chemical Geology*, v. 377, p. 45–55, doi: 10.1016/j.chemgeo.2014.04.002.
- Cardeneaux, A.P., 2014, Mapping of the oil window in the Eagle Ford Shale play of southwest Texas using thermal modeling and log overlay analysis: Master's Thesis, Louisiana State University, Louisiana. pages 84
- Carter, J.D., Barber, W., Tait, E. A, Jones, G. P., 1963, The geology of parts of Adamawa, Bauchi and Bornu provinces in Northeastern Nigeria. *Bulletin. Geological Survey. Nigeria*, v. 30; p. 1–108.
- Chakrabarty P., Basu A. R., and Freymuth B., 2017, Continuous Volcanism Throughout The Deposition Of The South Texan Eagle Ford Formation At The Cenomanian-Turonian (93-93.5 Ma) Boundary: Evidence From La-ICP-MS Zircon Age And XRD Analysis Of Expandable Clays, Abstract, GSA South Central Annual Meeting, San Antonio, TX Page?.

- Chatterjee, N., and Bhattacharji, S., 2004, A preliminary geochemical study of zircons and monazites from Deccan felsic dikes, Rajula, Gujarat, India: Implications for crustal melting: *Journal of Earth System Science*, v. 113, p. 533–542, doi: 10.1007/bf02704021.
- Chopra, S., Chang, T.-M., Saikia, S., Yadav, R., Choudhury, P., and Roy, K.S., 2014, Crustal structure of the Gujarat region, India: New constraints from the analysis of teleseismic receiver functions: *Journal of Asian Earth Sciences*, v. 96, p. 237–254, doi: 10.1016/j.jseaes.2014.09.023.
- Clauer, N. (1976) Géochimie isotopiques du strontium des milieu sédimentaires. Application à la géochronologie de la couverture du craton ouest-africain. *Sciences Géologiques, bulletins et mémoires*. Strasbourg; v. 45; p. 1–126.
- Coccioni, R., Nesci, O., Tramontana, M., Wezel, F.-C., and Moretti, E., 1987, Descrizione di un livello-guida “Radiolaritic-bituminoso-ittiolitico” alla base delle Marne a Fucoidi nell’Appennino Umbro-Marchigiano: *Bolletino della Società Geologica Italiana*, v. 106, p. 183–192.
- Courtillot, V.E., and Renne, P.R., 2003, On the ages of flood basalt events: *Comptes Rendus Geoscience*, v. 335, p. 113–140, doi: 10.1016/s1631-0713(03)00006-3.
- Courtillot, V.E., Feraud, G., Maluski, H., Vandamme, D., Moreau, M.G., and Besse, J., 1988, Deccan flood basalts and the Cretaceous/Tertiary boundary: *Nature*, v. 333, p. 843–846, doi:10.1038/333843a0.
- Dave, S.S., 1971, The geology of the igneous complex of the Barda hills, Saurashtra, Gujarat state (India): *Bulletin Volcanologique*, v. 35, p. 619–632, doi: 10.1007/bf02596832.
- De, A., and Bhattacharyya, D., 1971, Phase petrology with special reference to pyroxenes of the acid igneous complex of Barda hills, Western Saurashtra (Gujarat): *Bulletin Volcanologique*, v. 35, no. 4, p. 907–929, doi: 10.1007/bf02596854.

- Denne, R.A., Scott, E.D., Eickhoff, D.P., Kaiser, J.S., Hill, R.J., and Spaw, J.M., 2013, Massive Cretaceous-Paleogene boundary deposit, deep-water Gulf of Mexico: New evidence for widespread Chicxulub-induced slope failure: *Geology*, v. 41, no. 9, p. 983–986, doi: 10.1130/g34503.1.
- DePalma, R.A., Smit, J., Burnham, D.A., Kuiper, K., Manning, P.L., Oleinik, A., Larson, P., Maurrasse, F.J., Vellekoop, J., Richards, M.A., Gurche, L., and Alvarez, W., 2019, A seismically induced onshore surge deposit at the KPg boundary, North Dakota: *Proceedings of the National Academy of Sciences*, v. 116, no. 17, p. 8190–8199, doi: 10.1073/pnas.1817407116
- Edmond, J.M., 1992, Himalayan Tectonics, Weathering Processes, and the Strontium Isotope Record in Marine Limestones: *Science*, v. 258, no. 5088, p. 1594–1597, doi: 10.1126/science.258.5088.1594.
- Faure, G., 1986. *Principles of Isotope Geology*. Wiley, New York, no. 3, p. 928.
- Felitsyn, S.B., 2004, Vendian Volcanism, Weathering, and Phosphorus Cycle Variation in the East European Platform: *Lithology and Mineral Resources*, v. 39, no. 4, p. 322–332, doi: 10.1023/b:limi.0000033819.68327.aa.
- Fischer, T.P., Hilton, D.R., Zimmer, M.M., Shaw, A.M., Sharp, Z.D., and Walker, J.A., 2002, Subduction and Recycling of Nitrogen Along the Central American Margin: *Science*, v. 297, no. 5584, p. 1154–1157, doi: 10.1126/science.1073995.
- Fölmi, K.B., 160 M.y. Record of Marine Sedimentary Phosphorus Burial: Coupling of Climate and Continental Weathering under Greenhouse and Icehouse Conditions, *Geology*, 1995, vol. 23, pp. 859–862.

- Gaillardet, J., Dupré, B., Louvat, P., and Allègre, C., 1999, Global silicate weathering and CO₂ consumption rates deduced from the chemistry of large rivers: *Chemical Geology*, v. 159, no. 1-4, p. 3–30, doi: 10.1016/s0009-2541(99)00031-5.
- Gannoun, A., Vlastélic, I., and Schiano, P., 2015, Escape of unradiogenic osmium during sub-aerial lava degassing: Evidence from fumarolic deposits, Piton de la Fournaise, Réunion Island: *Geochimica et Cosmochimica Acta*, v. 166, p. 312–326, doi: 10.1016/j.gca.2015.06.039.
- Geibert, W., 2018, Processes that Regulate Trace Element Distribution in the Ocean: *Elements*, v. 14, no. 6, p. 391–396, doi: 10.2138/gselements.14.6.391.
- Ghiorso, M.S., and Gualda, G.A.R., 2015, An H₂O–CO₂ mixed fluid saturation model compatible with rhyolite-MELTS: *Contributions to Mineralogy and Petrology*, v. 169, no. 6, p. 1–30, doi: 10.1007/s00410-015-1141-8.
- Graciansky, P. C. de, Poag, C. W., Cunningham, R., Jr., Loubere, P., Masson, D. G., Mazzullo, J. M., Montadert, L., Muller, C., Otsuka, K., Reynolds, L., Sigal, J., Snyder, S., Townsend, H. A., Vaos, S. P., and Waples, D., 1985, Initial reports of the Deep Sea Drilling Project:: Washington, D.C., U.S. Government Printing Office;v. 80; no. 1; p. 679
- Halverson, G.P., Dudás, F.Ö., Maloof, A.C., and Bowring, S.A., 2007, Evolution of the ⁸⁷Sr/⁸⁶Sr composition of Neoproterozoic seawater: *Palaeogeography, Palaeoclimatology, Palaeoecology*, v. 256, no. 3-4, p. 103–129, doi: 10.1016/j.palaeo.2007.02.028.
- Haq, B.U., Hardenbol, J., and Vail, P.R., 1987, Chronology of Fluctuating Sea Levels Since the Triassic: *Science*, v. 235, no. 4793, p. 1156–1167, doi: 10.1126/science.235.4793.1156.
- Harbor, R., 2011. Facies Characterization and Stratigraphic Architecture of Organic-Rich Mudrocks, Upper Cretaceous Eagle Ford Formation, South Texas. Master's Thesis, University of Texas at Austin, Austin, TX, p. 195

- Hari, K.R., Rao, N.V.C., and Swarnkar, V., 2011, Petrogenesis of gabbro and orthopyroxene gabbro from the Phenai Mata Igneous Complex, Deccan volcanic province: Products of concurrent assimilation and fractional crystallization: *Journal of the Geological Society of India*, v. 78, p. 501–509, doi: 10.1007/s12594-011-0126-0.
- Hartmann, J., and Moosdorf, N., 2011, Chemical weathering rates of silicate-dominated lithological classes and associated liberation rates of phosphorus on the Japanese Archipelago—Implications for global scale analysis: *Chemical Geology*, v. 287, no. 3-4, p. 125–157, doi: 10.1016/j.chemgeo.2010.12.004.
- Hentz, T.F., and Ruppel, S.C., 2011, Regional Stratigraphic and Rock Characteristics of Eagle Ford Shale In Its Play Area: Maverick Basin to East Texas Basin. AAPG Annual Convention, Houston, Texas 2011. Search and Discovery Article #10325
- Herzberg, C., and Asimow, P.D., 2015, PRIMELT3 MEGA.XLSM software for primary magma calculation: Peridotite primary magma MgO contents from the liquidus to the solidus: *Geochemistry, Geophysics, Geosystems*, v. 16, no. 2, p. 563–578, doi: 10.1002/2014gc005631.
- Herzberg, C., and Gazel, E., 2009, Petrological evidence for secular cooling in mantle plumes: *Nature*, v. 458, p. 619–622, doi: 10.1038/nature07857.
- Hess, J., Bender, M.L., and Schilling, J.-G., 1986, Evolution of the Ratio of Strontium-87 to Strontium-86 in Seawater from Cretaceous to Present: *Science*, v. 231, no. 4741, p. 979–984, doi: 10.1126/science.231.4741.979.
- Ibrahim, M., Hellgeth, J., Smith, K., MacIsaac and Basu, A.R., 2016. Rapid Simultaneous Identification of Thermal Maturity and Mineral Contents in Oil Shale with High Speed Raman Imaging: Thermo Scientific Poster Note, PITTCON, PN52688

- Jenkyns, H.C., 1980, Cretaceous anoxic events: from continents to oceans: *Journal of the Geological Society*, v. 137, no. 2, p. 171–188, doi: 10.1144/gsjgs.137.2.0171.
- Jones, C.E. and Jenkyns, H.C., 2001, Seawater strontium isotopes, oceanic anoxic events, and seafloor hydrothermal activity in the Jurassic and Cretaceous: *American Journal of Science*, v. 301, no. 2, p. 112–149, doi: 10.2475/ajs.301.2.112.
- Jones, C.E., Jenkyns, H.C., Coe, A.L., and Stephen, H.P., 1994, Strontium isotopic variations in Jurassic and Cretaceous seawater: *Geochimica et Cosmochimica Acta*, v. 58, no. 14, p. 3061–3074, doi: 10.1016/0016-7037(94)90179-1.
- Kaneoka, I., and Haramura, H., 1973, K/Ar ages of successive lava flows from the Deccan Traps, India: *Earth and Planetary Science Letters*, v. 18, no. 2, p. 229–236, doi: 10.1016/0012-821x(73)90061-7.
- Kauffman, E.G., 1977, Upper Cretaceous cyclothems, biotas and environments, Rock Canyon, Anticline, Pueblo, Colorado, *Cretaceous Facies, Faunas and Paleoenvironments across the Western Interior Basin: Mountain Geologist*, v. 14; p. 129-152.
- Kauffman, E.G., 1984. Paleobiogeography and evolutionary response dynamic in the Cretaceous Western Interior Seaway of North America, *Jurassic-Cretaceous Biochronology and Biogeography of North America: Geological Association of Canada, Special Paper 27*, p. 273-306.
- Kholodov, V.N., 2014, Geochemical problems of the behavior of phosphorus: A basis for the biogenic hypothesis of phosphorite formation: *Lithology and Mineral Resources*, v. 49, no. 3, p. 228–249, doi: 10.1134/s0024490214030043.
- Leckie, R.M., Bralower, T.J., and Cashman, R., 2002, Oceanic anoxic events and plankton evolution: Biotic response to tectonic forcing during the mid-Cretaceous: *Paleoceanography*, v. 17, no. 3, p. 1–29, doi: 10.1029/2001pa000623.

- Lee, C.-T.A., and Lackey, J.S., 2015, Global Continental Arc Flare-ups and Their Relation to Long-Term Greenhouse Conditions: *Elements*, v. 11, no. 2, p. 125–130, doi:10.2113/gselements.11.2.125.
- Lee, C.-T.A., Jiang, H., Ronay, E., Minisini, D., Stiles, J., and Neal, M., 2018, Volcanic ash as a driver of enhanced organic carbon burial in the Cretaceous: *Scientific Reports*, v. 8, no. 1, p. 1–9, doi: 10.1038/s41598-018-22576-3.
- Lewan, M., 1997, Experiments on the role of water in petroleum formation: *Geochimica et Cosmochimica Acta*, v. 61, no. 17, p. 3691–3723, doi: 10.1016/s0016-7037(97)00176-2.
- Lightfoot, P.C., Hawkesworth, C.J., and Sethna, S.F., 1987, Petrogenesis of rhyolites and trachytes from the Deccan Trap: Sr, Nd and Pb isotope and trace element evidence: *Contributions to Mineralogy and Petrology*, v. 95, p. 44–54, doi: 10.1007/bf00518029.
- Lightfoot, P.C., Naldrett, A.J., Gorbachev, N.S., Doherty, W., and Fedorenko, V.A., Geochemistry of the Siberian Trap of the Norilsk Area, USSR, with Implication for the Relative Contributions of Crust and Mantle to Flood Basalt Magmatism, *Contrib. Mineral. Petrol.*, 1990, vol. 104, pp. 631–644.
- Lohan, M.C., and Tagliabue, A., 2018, Oceanic Micronutrients: Trace Metals that are Essential for Marine Life: *Elements*, v. 14, no. 6, p. 385–390, doi: 10.2138/gselements.14.6.385.
- Louis M. Liro, William C. Dawson, B, 1994, Sequence-Stratigraphic Elements and Geochemical Variability Within a Condensed Section: Eagle Ford Group, East-Central Texas: ABSTRACT": *American Association of Petroleum Geologists Bulletin*, v. 78, p. 393–402, doi: 10.1306/a25fef81-171b-11d7-8645000102c1865d.
- Lusty, P.A.J., and Murton, B.J., 2018, Deep-Ocean Mineral Deposits: Metal Resources and Windows into Earth Processes: *Elements*, v. 14, no. 5, p. 301–306, doi: 10.2138/gselements.14.5.301.

- Marty, B., and Zimmermann, L., 1999, Volatiles (He, C, N, Ar) in mid-ocean ridge basalts: assesment of shallow-level fractionation and characterization of source composition: *Geochimica et Cosmochimica Acta*, v. 63, no. 21, p. 3619–3633, doi: 10.1016/s0016-7037(99)00169-6.
- Mathur, K.K., Dubey, V.S., and Sharma, N.L., 1926, Magmatic Differentiation in Mount Girnar: *The Journal of Geology*, v. 34, p. 289–307, doi: 10.1086/623314.
- McGarity, H.A., 2013, Facies and Stratigraphic Framework of the Eagle Ford Shale in South Texas:Masters’ Thesis, University of Houston p. 105 <https://uh-ir.tdl.org/uh-ir/handle/10657/408>
- McLennan, S.M. and Taylor, S.R., Archean Sedimentary Rocks and Their Relation to the Composition of the Archean Continental Crust, *Archean Geochemistry*, Kröner, A., Hanson, G.N., and Goodwin, A.M., Eds., Berlin: Springer, 1984. Translated under the title *Geokhimiya arkheya*, Moscow: Mir, 1987, pp. 68–97.
- McLennan, S.M., 2001, Relationships between the trace element composition of sedimentary rocks and upper continental crust: *Geochemistry, Geophysics, Geosystems*, v. 2, no. 4, p. 1–24, doi: 10.1029/2000gc000109.
- McTainsh, G., and Strong, C., 2007, The role of aeolian dust in ecosystems: *Geomorphology*, v. 89, no. 1-2, p. 39–54, doi: 10.1016/j.geomorph.2006.07.028.
- Mundil, R., 2004, Age and Timing of the Permian Mass Extinctions: U/Pb Dating of Closed-System Zircons: *Science*, v. 305, no. 5691, p. 1760–1763, doi: 10.1126/science.1101012.
- Murray, J and Renard, A F., 1891, Manganese deposits from the HMS Challenger stations. PANGAEA, <https://doi.org/10.1594/PANGAEA.849073>, Supplement to: Murray, J; Renard, AF (1891): Deep-sea deposits (based on the specimens collected during the voyage of HMS Challenger in the years 1872 to 1876). Report on the scientific results of the voyage of H.M.S. Challenger during the years 1873-76; John Menzies and Co., Endinburgh, United Kingdom;

original link <http://www.vliz.be/nl/open-marien-archieff?module=ref&refid=41584>,
hdl:10013/epic.45942.d002, p. 688

Nier, A.O., 1937, A Mass-Spectrographic Study of the Isotopes of Hg, Xe, Kr, Be, I, As, and Cs: American Physical Society, v. 52, no. 9, p. 933-937, doi: 10.1103/PhysRev.52.933

Nier, A.O., 1950, A redetermination of the relative abundances of the isotopes of carbon, nitrogen, oxygen, argon, and potassium: American Physical Society, v. 77, no. 6, p. 789-793, doi: 10.1103/PhysRev.77.789

Oconnell, R.J., and Budiansky, B., 1974, Seismic velocities in dry and saturated cracked solids: Journal of Geophysical Research, v. 79, no. 35, p. 5412–5426, doi: 10.1029/jb079i035p05412.

Parisio, L., Jourdan, F., Marzoli, A., Melluso, L., Sethna, S.F., and Bellieni, G., 2016, $^{40}\text{Ar}/^{39}\text{Ar}$ ages of alkaline and tholeiitic rocks from the northern Deccan Traps: implications for magmatic processes and the K–Pg boundary: Journal of the Geological Society, v. 173, no. 4, p. 679–688, doi: 10.1144/jgs2015-133.

Peterman, Z.E., Hedge, C.E., and Tourtelot, H.A., 1970, Isotopic composition of strontium in sea water throughout Phanerozoic time: *Geochimica et Cosmochimica Acta*, v. 34, no. 1, p. 105–120, doi: 10.1016/0016-7037(70)90154-7.

Pierce, J. D., 2014, U-Pb geochronology of the Late Cretaceous Eagle Ford shale, Texas; defining chronostratigraphic boundaries and volcanic ash source: M.S. thesis, The University of Texas at Austin, Austin, Texas, p. 144.

Porder, S., Vitousek, P.M., Chadwick, O.A., Chamberlain, C.P., and Hilley, G.E., 2007, Uplift, Erosion, and Phosphorus Limitation in Terrestrial Ecosystems: *Ecosystems*, v. 10, no. 1, p. 159–171, doi: 10.1007/s10021-006-9011-x.

- Porder, S., Vitousek, P.M., Chadwick, O.A., Chamberlain, C.P., and Hilley, G.E., 2007, Uplift, Erosion, and Phosphorus Limitation in Terrestrial Ecosystems: *Ecosystems*, v. 10, no. 1, p. 159–171, doi: 10.1007/s10021-006-9011-x.
- Qing, H., Barnes, C.R., Buhl, D., and Veizer, J., 1998, The strontium isotopic composition of Ordovician and Silurian brachiopods and conodonts: relationships to geological events and implications for coeval seawater: *Geochimica et Cosmochimica Acta*, v. 62, no. 10, p. 1721–1733, doi: 10.1016/s0016-7037(98)00104-5.
- Railroad Commission of Texas, 2019, Eagle Ford Information, < <https://www.rrc.state.tx.us/oil-gas/major-oil-and-gas-formations/eagle-ford-shale-information/>>, accessed April 30, 2019
- Rao, G.S.P., and Tewari, H.C., 2004, The seismic structure of the Saurashtra crust in northwest India and its relationship with the Réunion Plume: *Geophysical Journal International*, v. 160, no. 1, p. 319–331, doi: 10.1111/j.1365-246x.2004.02448.x.
- Reddy, P.R., 2005, Crustal velocity structure of western India and its use in understanding intraplate seismicity: *Current Science*, v. 88, no. 10, p. 1652–1657.
- Renne, P.R., Black, M.T., Zichao, Z., Richards, M.A., and Basu, A.R., 1995, Synchrony and Causal Relations Between Permian-Triassic Boundary Crises and Siberian Flood Volcanism: *Science*, v. 269, no. 5229, p. 1413–1416, doi: 10.1126/science.269.5229.1413.
- Renne, P.R., Sprain, C.J., Richards, M.A., Self, S., Vanderkluyesen, L., and Pande, K., 2015, State shift in Deccan volcanism at the Cretaceous-Paleogene boundary, possibly induced by impact: *Science*, v. 350, no. 6256, p. 76–78, doi: 10.1126/science.aac7549.
- Richards, M.A., Alvarez, W., Self, S., Karlstrom, L., Renne, P.R., Manga, M., Sprain, C.J., Smit, J., Vanderkluyesen, L., and Gibson, S.A., 2016, Triggering of the largest Deccan eruptions by the

Chicxulub impact: Reply: Geological Society of America Bulletin, v. 129, no. 1-2, p. 256–256, doi: 10.1130/b31645.1.

Richards, M.A., Alvarez, W., Self, S., Karlstrom, L., Renne, P.R., Manga, M., Sprain, C.J., Smit, J., Vanderkluysen, L., and Gibson, S.A., 2016, Triggering of the largest Deccan eruptions by the Chicxulub impact: Reply: Geological Society of America Bulletin, v. 129, p. 256–256, doi: 10.1130/b31645.1.

Richter, F.M., Rowley, D.B., and DePaolo, D.J., 1992, Sr isotope evolution of seawater: the role of tectonics: Earth and Planetary Science Letters, v. 109, no. 1-2, p. 11–23, doi: 10.1016/0012-821x(92)90070-c.

Romero, A.A.M., Nguyen, T., and Philp, R.P., 2018, Organic geochemistry of the Eagle Ford Group in Texas: AAPG Bulletin, v. 102, no. 07, p. 1379–1412, doi: 10.1306/0828171614717055.

Ruttenberg, K.C., Reassessment of the Oceanic Residence Time of Phosphorus, Chem. Geol., 1993, vol. 107, pp. 405–409.

Sano, Y., Takahata, N., Nishio, Y., Fischer, T.P., and Williams, S.N., 2001, Volcanic flux of nitrogen from the Earth: Chemical Geology, v. 171, no. 3-4, p. 263–271, doi: 10.1016/s0009-2541(00)00252-7.

Sarma, S.V.S., Harinarayana, T., Rao, M.S., Virupakshi, G., Murty, D.N., Sastry, R.S., Nagarajan, N., Sastry, T.S., Sarma, M.V.C., Rao, M., Veeraswamy, K., Prabhakar E. Rao, S., Lingaiah, A., Srinivasulu, T., Patro, B.P.K., and Manoj, C., 2004. Delineation of electrical structure beneath Saurashtra Peninsula using MT studies: 5th Conference & Exposition on Petroleum Geophysics, Hyderabad-2004, India, p. 79–80.

- Schaefer, B.F., Turner, S., Parkinson, I., Rogers, N., and Hawkesworth, C., 2002, Evidence for recycled Archaean oceanic mantle lithosphere in the Azores plume: *Nature*, v. 420, no. 6913, p. 304–307, doi: 10.1038/nature01172.
- Schieber, J., 1994, Evidence for high-energy events and shallow-water deposition in the Chattanooga Shale, Devonian, central Tennessee, USA: *Sedimentary Geology*, v. 93, no. 3-4, p. 193–208, doi: 10.1016/0037-0738(94)90005-1.
- Schieber, J., 1999, Distribution and Deposition of Mudstone Facies in the Upper Devonian Sonyea Group of New York: *Society for Sedimentary Geology Journal of Sedimentary Research*, v. Vol. 69 (1999), doi: 10.1306/d4268ab8-2b26-11d7-8648000102c1865d.
- Schlanger, S.O., & Jenkyns, H.C., 1976, Cretaceous Oceanic Anoxic Events: Causes and Consequences: *Geologie En Mijnbouw*, v.55, no. 3-4, p. 179–184.
- Schoene, B., Eddy, M.P., Samperton, K.M., Keller, C.B., Keller, G., Adatte, T., and Khadri, S.F.R., 2019, U-Pb constraints on pulsed eruption of the Deccan Traps across the end-Cretaceous mass extinction: *Science*, v. 363, p. 862–866, doi: 10.1126/science.aau2422.
- Schoene, B., Samperton, K.M., Eddy, M.P., Keller, G., Adatte, T., Bowring, S.A., Khadri, S.F.R., and Gertsch, B., 2014, U-Pb geochronology of the Deccan Traps and relation to the end-Cretaceous mass extinction: *Science*, v. 347, no. 6218, p. 182–184, doi: 10.1126/science.aaa0118.
- Scholle P.A., Arthur M.A. (1980) Carbon isotope fluctuations in Cretaceous pelagic limestones: potential stratigraphic and petroleum exploration tool. *Am. Assoc. Pet. Geol. Bull.* 64, 67–87.
- Scott, E. D.; Denne R. A.; Kaiser, J.S.; and Eickhoff, D. P. ;2014, Impact on Sedimentation into the North-Central Deepwater Gulf of Mexico as Result of the Chicxulub Event: *Gulf Coast Association of Geological Societies Journal*, v. 3, p. 41-50.

- Selby, D., 2005, Direct Radiometric Dating of Hydrocarbon Deposits Using Rhenium-Osmium Isotopes: *Science*, v. 308, no. 5726, p. 1293–1295, doi: 10.1126/science.1111081.
- Sethna, S.F., 1999, Geology of Mumbai and surrounding areas and its position in the Deccan volcanic stratigraphy, India: *Journal of Geological Society of India*, v. 53, p. 359–365.
- Sharpton, V.L. and Ward, P.D., Global Catastrophes in Earth History, *Geol. Soc. Am. Spec. Papers*, 1990, vol. 247, pp. 1–631.
- Sheth, H.C., and Melluso, L., 2008, The Mount Pavagadh volcanic suite, Deccan Traps: Geochemical stratigraphy and magmatic evolution: *Journal of Asian Earth Sciences*, v. 32, p. 5–21, doi: 10.1016/j.jseaes.2007.10.001.
- Sheth, H.C., Choudhary, A.K., Bhattacharyya, S., Cucciniello, C., Laishram, R., and Gurav, T., 2011, The Chogat-Chamardi subvolcanic complex, Saurashtra, northwestern Deccan Traps: Geology, petrochemistry, and petrogenetic evolution: *Journal of Asian Earth Sciences*, v. 41, p. 307–324, doi: 10.1016/j.jseaes.2011.02.012.
- Simonetti, A., Goldstein, S.L., Schmidberger, S.S.; and Viladkar, S.G., 1998. Geochemical and Nd, Pb, and Sr isotope data from Deccan alkaline complexes —inferences for mantle sources and plume–lithosphere interaction. *Journal of Petrology*, v. 39, p. 1847–1864.
- Sinton, C.W., and Duncan, R.A., 1997, Potential links between ocean plateau volcanism and global ocean anoxia at the Cenomanian-Turonian boundary: *Economic Geology*, v. 92, no. 7-8, p. 836–842, doi: 10.2113/gsecongeo.92.7-8.836.
- Spears, D.A., 1980, Towards a classification of shales: *Journal of the Geological Society*, v. 137, p. 125-129.

- Sprain, C.J., Renne, P.R., Vanderkluyzen, L., Pande, K., Selief, S., and Mittal, T., 2019, The eruptive tempo of Deccan volcanism in relation to the Cretaceous-Paleogene boundary: *Science*, v. 363, p. 866–870, doi: 10.1126/science.aav1446.
- Symonds, R.B., Poreda, R.J., Evans, W.C., Janik, C.J., and Ritchie, B.E., 2003, Mantle and Crustal Sources of Carbon, Nitrogen, and Noble gases in Cascade-Range and Aleutian-Arc Volcanic gases: Open-File Report, p. 1–26, doi: 10.3133/ofr03436.
- Taylor, G.H., Teichmüller, M., Davis, A., Diessel, C.F.K., Littke, R., and Robert, P., 1998. *Organic Petrology*: Berlin, Gebrüder Borntraeger, p704..
- Taylor, S.R. and McLennan, S.M., 1984, *The Continental Crust: Its Composition and Evolution: An Examination of the Geochemical Record Preserved in Sedimentary Rocks*: Blackwell Scientific Publications, p. 312
- Turgeon, S.C., and Creaser, R.A., 2008, Cretaceous oceanic anoxic event 2 triggered by a massive magmatic episode: *Nature*, v. 454, no. 7202, p. 323–326, doi: 10.1038/nature07076.
- Tuttle, O.F and Bowen, N. L, 1958, Origin of granite in the light of experimental studies in the system NaAlSi₃O₈-KAlSi₃O₈-SiO₂-H₂O: *The Geological Society of America, Memoir 74*. p. 158
- Twining, B.S., and Baines, S.B., 2013, The Trace Metal Composition of Marine Phytoplankton: *Annual Review of Marine Science*, v. 5, p. 191–215, doi: 10.1146/annurev-marine-121211-172322.
- Veizer, J., 1989, Strontium Isotopes In Seawater Through Time: *Annual Review of Earth and Planetary Sciences*, v. 17, no. 1, p. 141–167, doi: 10.1146/annurev.earth.17.1.141.
- Vogt, P. R., 1989, Volcanogenic upwelling of anoxic nutrient-rich water: A possible factor in carbonate-bank/reef demise and benthic faunal extinctions: *Geological Society of America Bulletin*, v. 101, p. 1225–1245.

- Watanabe, T., 1993, Effects of water and melt on seismic velocities and their application to characterization of seismic reflectors: *Geophysical Research Letters*, v. 20, no. 24, p. 2933–2936, doi: 10.1029/93gl03170.
- Wickman, F., 1948. Isotope ratios: a clue to the age of certain marine sediments. *Journal of Geology*, v. 56, p. 61–66.
- Wilkins, R.W., Boudou, R., Sherwood, N., and Xiao, X., 2014, Thermal maturity evaluation from inertinites by Raman spectroscopy: The ‘RaMM’ technique: *International Journal of Coal Geology*, v. 128-129, p. 143–152, doi: 10.1016/j.coal.2014.03.006.
- Workman, S. J., and G. M. Grammer, 2013, Integrating depositional facies and sequence stratigraphy in characterizing unconventional reservoirs in the Cretaceous (Cenomanian-Turonian) Eagle Ford Shale, South Texas: *Gulf Coast Association of Geological Societies Transactions*, v. 63, p. 473–508.
- Worsley, T. R. and Kidder, D. L., 1991, First-order coupling of paleogeography and CO₂, with global surface temperature and its latitudinal contrast: *Geology*, v. 19, p. 1161–1164.
- Wyllie, P.J., 1988. Solidus curves, mantle plumes, and magma generation beneath Hawaii: *Journal of Geophysical Research*, v. 93, p. 4171–4181, doi: <https://doi.org/10.1029/JB093iB05p04171>
- Zandt, G., and Ammon, C.J., 1995, Continental crust composition constrained by measurements of crustal Poisson’s ratio: *Nature*, v. 374, p. 152–154. [http:// dx.doi.org/10.1038/374152a0](http://dx.doi.org/10.1038/374152a0).
- Zanin, Yu.N., *Problems of the Evolution of Phosphorite Formation in the Earth's History, Evolyutsiya osadochnogo rudoobrazovaniya v istorii Zemli (Evolution of Sedimentary Ore Formation in the Earth's History)*, Moscow: Nauka, 1984, pp. 79–86.
- Zhou, X., Jenkyns, H.C., Owens, J.D., Junium, C.K., Zheng, X.-Y., Sageman, B.B., Hardisty, D.S., Lyons, T.W., Ridgwell, A., and Lu, Z., 2015, Upper ocean oxygenation dynamics from I/Ca ratios

during the Cenomanian-Turonian OAE 2: *Paleoceanography*, v. 30, no. 5, p. 510–526, doi: 10.1002/2014pa002741.

Zhu, L., and Kanamori, H., 2000, Moho depth variation in southern California from teleseismic receiver functions: *Journal of Geophysical Research: Solid Earth*, v. 105, no. B2, p. 2969–2980, doi: 10.1029/1999jb900322.

Zimmer, M.M., Fischer, T.P., Hilton, D.R., Alvarado, G.E., Sharp, Z.D., and Walker, J.A., 2004, Nitrogen systematics and gas fluxes of subduction zones: Insights from Costa Rica arc volatiles: *Geochemistry, Geophysics, Geosystems*, v. 5, no. 5, p. 1–19, doi: 10.1029/2003gc000651.

Zubkov, M.V., Plucinski, P.K., Dartiguelongue, A.C.Y., and Lusty, P.A.J., 2018, Metal Extraction from Deep-Ocean Mineral Deposits: *Elements*, v. 14, no. 5, p. 319–324, doi: 10.2138/gselements.14.5.319.

Appendix

Table 1: U-Pb zircon data of 14 volcanic ash beds from Eagle Ford, South Texas and Del Rio, West Texas, determined from LA-ICP-MS

Analysis	Isotope ratios										Apparent ages (Ma)							
	U (ppm)	206Pb/ 204Pb	U/Th	206Pb*/ 207Pb*	± (%)	207Pb*/ 235U*	± (%)	206Pb*/ 238U	± (%)	error corr.	206Pb*/ 238U*	± (Ma)	207Pb*/ 235U	± (Ma)	206Pb*/ 207Pb*	± (Ma)	Best age (Ma)	± (Ma)
Spot 1	270	5978	3.1	20.2404	2.0	0.0796	4.5	0.0117	4.1	0.90	74.9	3.0	77.8	3.4	167.1	46.6	74.9	3.0
Spot 2	400	14740	2.9	20.3450	1.5	0.0857	3.4	0.0127	3.0	0.90	81.1	2.5	83.5	2.7	155.1	34.1	81.1	2.5
Spot 3	407	22676	2.7	20.1749	1.4	0.0931	2.7	0.0136	2.3	0.85	87.3	2.0	90.4	2.3	174.7	33.3	87.3	2.0
Spot 4	617	26516	1.4	18.8802	1.8	0.1014	3.1	0.0139	2.5	0.80	88.9	2.2	98.0	2.9	327.3	41.7	88.9	2.2
Spot 5	190	19112	2.7	19.8399	1.7	0.0970	3.5	0.0140	3.0	0.87	89.3	2.7	94.0	3.1	213.7	40.2	89.3	2.7
Spot 6	407	48673	2.4	19.1366	1.4	0.1023	4.2	0.0142	4.0	0.94	90.9	3.6	98.9	4.0	296.6	31.9	90.9	3.6
Spot 7	464	10086	2.5	19.6491	1.3	0.1002	2.7	0.0143	2.4	0.87	91.4	2.2	96.9	2.5	236.0	30.6	91.4	2.2
Spot 8	572	5560	2.2	19.3325	3.1	0.1021	4.4	0.0143	3.2	0.73	91.7	2.9	98.7	4.2	273.3	70.0	91.7	2.9
Spot 9	404	5504	2.4	21.5117	1.7	0.0923	3.9	0.0144	3.5	0.90	92.2	3.2	89.6	3.3	22.9	41.4	92.2	3.2
Spot 10	544	8024	2.2	21.4957	1.3	0.0925	2.6	0.0144	2.2	0.86	92.4	2.0	89.9	2.2	24.7	32.4	92.4	2.0
Spot 11	586	16604	1.0	20.9131	1.3	0.0954	2.4	0.0145	2.0	0.85	92.7	1.9	92.6	2.1	90.2	30.2	92.7	1.9
Spot 12	1264	32093	1.6	20.4133	1.0	0.0978	2.9	0.0145	2.7	0.94	92.8	2.5	94.8	2.6	147.2	23.0	92.8	2.5
Spot 13	280	4730	2.5	19.8006	2.3	0.1010	3.4	0.0145	2.6	0.75	92.8	2.4	97.7	3.2	218.2	52.6	92.8	2.4
Spot 14	339	8928	3.9	20.8760	1.8	0.0965	3.3	0.0146	2.8	0.84	93.5	2.6	93.5	3.0	94.4	43.3	93.5	2.6
Spot 15	514	40970	2.5	21.1058	1.3	0.0968	3.0	0.0148	2.7	0.91	94.9	2.6	93.9	2.7	68.4	30.4	94.9	2.6
Spot 16	281	12523	1.9	20.5170	1.4	0.0997	2.5	0.0148	2.0	0.82	95.0	1.9	96.5	2.3	135.3	33.0	95.0	1.9
Spot 17	351	12115	1.5	21.0517	1.5	0.0972	3.3	0.0148	3.0	0.89	95.0	2.8	94.2	3.0	74.5	36.2	95.0	2.8
Spot 18	193	12660	2.0	18.4009	1.6	0.1112	3.1	0.0149	2.7	0.85	95.0	2.5	107.1	3.2	385.4	37.0	95.0	2.5
Spot 19	310	139277	3.0	20.6601	1.3	0.0992	3.4	0.0149	3.1	0.92	95.2	2.9	96.0	3.1	119.0	31.7	95.2	2.9
Spot 20	286	8177	2.9	20.9481	1.1	0.0987	3.4	0.0150	3.2	0.94	95.9	3.0	95.5	3.1	86.3	27.2	95.9	3.0
Spot 21	186	7270	2.3	20.3806	1.2	0.1020	3.2	0.0151	3.0	0.93	96.5	2.8	98.6	3.0	151.0	28.1	96.5	2.8
Spot 22	304	3658	1.7	20.1427	4.2	0.1033	5.0	0.0151	2.6	0.53	96.6	2.5	99.8	4.7	178.4	98.8	96.6	2.5
Spot 23	487	37162	1.9	20.0551	1.4	0.1047	2.8	0.0152	2.4	0.87	97.5	2.4	101.1	2.7	188.6	32.5	97.5	2.4
Spot 24	238	2934	2.4	20.3673	5.5	0.1032	6.2	0.0152	3.0	0.48	97.6	2.9	99.7	5.9	152.6	128.4	97.6	2.9

Handy 13203

Contd.

Analysis	Isotope ratios										Apparent ages (Ma)							
	U	206Pb/	U/Th	206Pb*/	±	207Pb*/	±	206Pb*/	±	error	206Pb*/	±	207Pb*/	±	206Pb*/	±	Best	±
	(ppm)	204Pb		207Pb*	(%)	235U*	(%)	238U	(%)	corr.	238U*	(Ma)	235U	(Ma)	207Pb*	(Ma)	(Ma)	(Ma)
Spot 1	391	8898	1.7	21.2938	1.9	0.0901	4.7	0.0139	4.3	0.92	89.1	3.8	87.6	3.9	47.3	44.3	89.1	3.8
Spot 2	313	17223	1.5	20.5501	1.3	0.0949	2.8	0.0142	2.5	0.89	90.6	2.2	92.1	2.5	131.6	30.1	90.6	2.2
Spot 3	215	4267	1.6	21.0450	2.6	0.0951	4.0	0.0145	3.1	0.77	93.0	2.8	92.3	3.6	75.3	61.5	93.0	2.8
Spot 4	247	14668	1.5	20.2711	1.3	0.0993	2.7	0.0146	2.4	0.88	93.5	2.2	96.2	2.5	163.6	30.4	93.5	2.2
Spot 5	307	6460	1.5	21.2900	1.9	0.0947	3.3	0.0146	2.7	0.81	93.6	2.5	91.9	2.9	47.7	46.1	93.6	2.5
Spot 6	184	13634	1.9	20.6645	1.6	0.0976	3.2	0.0146	2.7	0.87	93.7	2.6	94.6	2.9	118.5	37.5	93.7	2.6
Spot 7	300	33503	1.1	20.4179	1.6	0.0989	2.6	0.0147	2.1	0.79	93.8	2.0	95.8	2.4	146.7	37.9	93.8	2.0
Spot 8	219	31965	1.3	20.4212	1.6	0.0991	3.0	0.0147	2.5	0.84	93.9	2.4	95.9	2.8	146.4	38.3	93.9	2.4
Spot 9	258	37329	1.7	19.4705	1.3	0.1041	2.8	0.0147	2.5	0.89	94.2	2.4	100.6	2.7	257.0	29.7	94.2	2.4
Spot 10	553	14988	1.0	20.6305	1.1	0.0983	2.6	0.0147	2.4	0.91	94.2	2.2	95.2	2.4	122.4	25.6	94.2	2.2
Spot 11	343	5373	0.6	21.3456	2.8	0.0952	3.6	0.0147	2.2	0.63	94.3	2.1	92.3	3.2	41.5	66.7	94.3	2.1
Spot 12	323	8241	1.4	20.9475	1.3	0.0970	2.6	0.0147	2.3	0.86	94.3	2.1	94.0	2.3	86.4	31.4	94.3	2.1
Spot 13	173	2419	1.4	22.9414	7.2	0.0887	7.6	0.0148	2.6	0.34	94.5	2.4	86.3	6.3	NA	NA	94.5	2.4
Spot 14	395	10807	1.0	20.3510	2.2	0.1000	3.6	0.0148	2.8	0.78	94.5	2.6	96.8	3.3	154.4	52.4	94.5	2.6
Spot 15	188	3441	2.4	21.9875	2.1	0.0925	2.9	0.0148	2.0	0.69	94.5	1.9	89.9	2.5	NA	NA	94.5	1.9
Spot 16	248	3381	1.2	21.9640	5.1	0.0929	5.6	0.0148	2.4	0.44	94.7	2.3	90.2	4.8	NA	NA	94.7	2.3
Spot 17	144	7836	1.9	20.6295	1.7	0.0997	3.2	0.0149	2.7	0.85	95.5	2.6	96.5	2.9	122.5	39.6	95.5	2.6
Spot 18	205	2232	1.3	23.3335	2.3	0.0881	3.4	0.0149	2.5	0.74	95.5	2.4	85.8	2.8	NA	NA	95.5	2.4
Spot 19	261	5799	1.6	19.8289	2.0	0.1038	3.2	0.0149	2.5	0.78	95.6	2.4	100.3	3.1	214.9	46.6	95.6	2.4
Spot 20	167	13460	2.0	20.4172	1.7	0.1014	2.7	0.0150	2.1	0.78	96.1	2.0	98.0	2.5	146.8	39.1	96.1	2.0
Spot 21	130	24979	1.5	19.7644	1.8	0.1049	3.0	0.0150	2.4	0.81	96.2	2.3	101.3	2.9	222.4	40.8	96.2	2.3
Spot 22	405	2572	0.9	14.4427	6.2	0.1436	6.8	0.0150	2.7	0.40	96.3	2.6	136.2	8.7	905.9	128.3	96.3	2.6
Spot 23	268	3861	1.9	20.5098	4.5	0.1016	5.3	0.0151	2.9	0.54	96.8	2.8	98.3	5.0	136.1	105.8	96.8	2.8
Spot 24	221	5121	1.0	21.1795	2.1	0.0985	3.3	0.0151	2.6	0.78	96.8	2.5	95.4	3.0	60.2	48.9	96.8	2.5
Spot 25	251	6769	1.9	21.2187	1.6	0.0984	2.9	0.0152	2.4	0.83	97.0	2.3	95.3	2.7	55.7	38.6	97.0	2.3

Long 7C

Contd.

Analysis	U (ppm)	206Pb/ 204Pb	U/Th	Isotope ratios							Apparent ages (Ma)						Best age (Ma)	±
				206Pb*/ 207Pb*	± (%)	207Pb*/ 235U*	± (%)	206Pb*/ 238U	± (%)	error corr.	206Pb*/ 238U*	± (Ma)	207Pb*/ 235U	± (Ma)	206Pb*/ 207Pb*	± (Ma)		
Spot 26	284	10511	1.5	20.6789	2.0	0.1018	3.3	0.0153	2.6	0.80	97.7	2.6	98.4	3.1	116.9	47.4	97.7	2.6
Spot 27	260	4528	1.1	21.4205	3.9	0.0984	4.5	0.0153	2.2	0.49	97.8	2.1	95.3	4.1	33.1	93.3	97.8	2.1
Spot 28	248	6695	1.6	20.9793	1.5	0.1010	3.4	0.0154	3.0	0.89	98.4	3.0	97.7	3.2	82.7	36.3	98.4	3.0
Spot 29	422	56003	1.8	19.9503	1.4	0.1063	2.6	0.0154	2.2	0.85	98.4	2.2	102.6	2.6	200.8	32.1	98.4	2.2
Spot 30	276	4793	1.4	18.9948	3.7	0.1119	5.1	0.0154	3.6	0.69	98.7	3.5	107.7	5.2	313.6	83.7	98.7	3.5
Spot 31	193	33155	1.0	20.4227	1.6	0.1050	2.7	0.0156	2.2	0.81	99.5	2.2	101.4	2.6	146.2	37.1	99.5	2.2
Spot 32	306	927	0.9	10.3284	15.6	0.2101	16.3	0.0157	4.7	0.29	100.7	4.7	193.7	28.7	1563.7	294.4	100.7	4.7
Spot 33	235	1397	1.1	15.1396	6.1	0.1501	7.2	0.0165	3.7	0.52	105.4	3.9	142.0	9.5	808.0	128.3	105.4	3.9
Spot 34	107	465	1.0	6.0563	9.6	0.4236	11.8	0.0186	6.9	0.58	118.9	8.1	358.6	35.8	2508.7	162.2	118.9	8.1
Spot 1	228	6613	2.2	20.5527	1.5	0.0882	3.5	0.0132	3.2	0.90	84.2	2.7	85.8	2.9	131.3	35.8	84.2	2.7
Spot 2	133	3195	2.1	23.4072	1.7	0.0845	3.2	0.0144	2.7	0.85	91.9	2.5	82.4	2.5	NA	NA	91.9	2.5
Spot 3	168	8949	2.4	21.8913	1.4	0.0905	2.8	0.0144	2.4	0.86	92.0	2.2	87.9	2.4	NA	NA	92.0	2.2
Spot 4	234	9628	2.0	20.7808	1.7	0.0956	4.1	0.0144	3.7	0.91	92.3	3.4	92.7	3.6	105.2	39.6	92.3	3.4
Spot 5	71	3347	3.0	22.0788	2.3	0.0902	4.2	0.0145	3.5	0.84	92.5	3.3	87.7	3.6	NA	NA	92.5	3.3
Spot 6	76	10081	3.0	20.7899	1.7	0.0959	3.9	0.0145	3.5	0.90	92.5	3.2	92.9	3.4	104.2	40.7	92.5	3.2
Spot 7	89	9238	3.1	21.3253	2.0	0.0936	3.9	0.0145	3.3	0.86	92.7	3.1	90.9	3.4	43.8	48.0	92.7	3.1
Friedrich's Spot 8	75	5153	2.6	22.4689	2.7	0.0889	3.8	0.0145	2.7	0.71	92.8	2.5	86.5	3.2	NA	NA	92.8	2.5
Spot 9	63	4333	2.9	22.2537	1.9	0.0905	3.9	0.0146	3.4	0.87	93.5	3.2	88.0	3.3	NA	NA	93.5	3.2
Spot 10	170	9275	3.1	20.7581	2.0	0.0971	3.8	0.0146	3.2	0.84	93.6	2.9	94.1	3.4	107.8	48.2	93.6	2.9
Spot 11	141	4446	2.1	22.5727	1.6	0.0895	3.1	0.0147	2.6	0.86	93.8	2.5	87.1	2.6	NA	NA	93.8	2.5
Spot 12	87	71033	3.2	20.5911	1.8	0.0982	3.7	0.0147	3.2	0.86	93.9	2.9	95.1	3.3	126.9	43.4	93.9	2.9
Spot 13	140	26256	2.4	19.9964	1.4	0.1027	3.5	0.0149	3.2	0.92	95.4	3.1	99.3	3.3	195.4	32.5	95.4	3.1
Spot 14	133	5524	2.3	22.1252	1.8	0.0930	3.7	0.0149	3.2	0.87	95.5	3.1	90.3	3.2	NA	NA	95.5	3.1
Spot 15	178	37127	2.4	20.9782	1.2	0.0987	2.9	0.0150	2.6	0.90	96.1	2.5	95.5	2.6	82.8	29.0	96.1	2.5

Contd.

Analysis	Isotope ratios										Apparent ages (Ma)							
	U (ppm)	206Pb/ 204Pb	U/Th	206Pb*/ 207Pb*	±	207Pb*/ 235U*	±	206Pb*/ 238U	±	error corr.	206Pb*/ 238U*	±	207Pb*/ 235U	±	206Pb*/ 207Pb*	±	Best age (Ma)	±
Spot 21	58	728	4.1	35.4241	3.0	0.0577	4.3	0.0148	3.0	0.71	94.8	2.9	56.9	2.4	NA	NA	94.8	2.9
Spot 22	75	49139	3.2	20.5207	2.1	0.0997	3.8	0.0148	3.2	0.84	95.0	3.0	96.5	3.5	134.9	48.5	95.0	3.0
Spot 23	98	7687	3.4	21.3595	1.7	0.0959	3.3	0.0149	2.9	0.87	95.1	2.7	93.0	2.9	40.0	39.7	95.1	2.7
Spot 24	75	1980	3.4	21.4145	3.4	0.0957	5.1	0.0149	3.8	0.74	95.1	3.6	92.8	4.5	33.8	81.9	95.1	3.6
Spot 25	104	1590	3.3	13.2456	4.4	0.1547	5.6	0.0149	3.4	0.60	95.2	3.2	146.1	7.6	1081.8	89.2	95.2	3.2
Spot 26	425	21829	1.1	21.2294	1.2	0.0965	2.5	0.0149	2.2	0.87	95.2	2.1	93.6	2.2	54.5	29.1	95.2	2.1
Spot 27	118	69402	3.3	21.0269	1.2	0.0979	3.1	0.0149	2.9	0.92	95.5	2.7	94.8	2.8	77.3	29.6	95.5	2.7
Spot 28	90	58268	2.6	20.3054	1.8	0.1019	3.8	0.0150	3.3	0.88	96.1	3.2	98.6	3.6	159.7	42.0	96.1	3.2
Spot 29	80	7242	3.0	20.8695	1.7	0.0998	3.4	0.0151	2.9	0.87	96.7	2.8	96.6	3.1	95.2	39.6	96.7	2.8
Spot 30	82	12472	3.3	20.8134	1.5	0.1003	2.8	0.0151	2.4	0.85	96.9	2.3	97.0	2.6	101.6	35.6	96.9	2.3
Spot 31	114	13417	3.1	19.6761	1.4	0.1063	3.1	0.0152	2.8	0.90	97.1	2.7	102.5	3.1	232.8	32.2	97.1	2.7
Spot 32	120	5959	3.2	21.5622	1.4	0.0971	3.2	0.0152	2.9	0.90	97.2	2.8	94.1	2.9	17.3	33.6	97.2	2.8
Spot 33	76	27152	2.4	20.7784	2.0	0.1013	3.8	0.0153	3.2	0.86	97.7	3.1	98.0	3.5	105.5	46.1	97.7	3.1
Spot 34	38	5356	4.1	22.3648	2.4	0.0942	3.3	0.0153	2.3	0.69	97.8	2.3	91.4	2.9	NA	NA	97.8	2.3
Spot 35	64	3402	3.4	21.5645	2.1	0.0981	3.2	0.0153	2.4	0.75	98.2	2.3	95.0	2.9	17.0	50.1	98.2	2.3
Long 5L																		
Spot 1	88	767	3.5	31.4140	3.3	0.0594	4.3	0.0135	2.8	0.64	86.8	2.4	58.6	2.5	NA	NA	86.8	2.4
Spot 2	100	911	2.2	27.8684	2.7	0.0679	4.1	0.0137	3.1	0.75	87.9	2.7	66.7	2.6	NA	NA	87.9	2.7
Spot 3	188	4296	3.3	21.1518	1.9	0.0923	2.7	0.0142	2.0	0.72	90.7	1.8	89.7	2.3	63.2	44.9	90.7	1.8
Spot 4	135	1992	2.2	23.1185	2.8	0.0847	3.9	0.0142	2.7	0.70	90.9	2.5	82.5	3.1	NA	NA	90.9	2.5
Spot 5	239	5163	2.6	21.1189	2.1	0.0930	3.4	0.0142	2.7	0.79	91.2	2.4	90.3	3.0	66.9	49.9	91.2	2.4
Spot 6	86	1555	2.9	22.3616	5.7	0.0883	6.2	0.0143	2.6	0.41	91.7	2.3	85.9	5.1	NA	NA	91.7	2.3
Spot 7	418	8102	2.0	21.0124	1.5	0.0947	2.8	0.0144	2.4	0.85	92.5	2.2	91.9	2.5	79.0	35.1	92.5	2.2

Contd.

Analysis	Isotope ratios										Apparent ages (Ma)							
	U (ppm)	²⁰⁶ Pb/ ²⁰⁴ Pb	U/Th	²⁰⁶ Pb*/ ²⁰⁷ Pb*	± (%)	²⁰⁷ Pb*/ ²³⁵ U*	± (%)	²⁰⁶ Pb*/ ²³⁸ U	± (%)	error corr.	²⁰⁶ Pb*/ ²³⁸ U*	± (Ma)	²⁰⁷ Pb*/ ²³⁵ U	± (Ma)	²⁰⁶ Pb*/ ²⁰⁷ Pb*	± (Ma)	Best age (Ma)	± (Ma)
Spot 8	140	70622	2.7	20.0989	1.5	0.0993	2.6	0.0145	2.0	0.80	92.6	1.9	96.1	2.3	183.5	36.0	92.6	1.9
Spot 9	96	1225	3.0	24.5490	3.2	0.0816	4.3	0.0145	2.9	0.67	93.0	2.6	79.6	3.3	NA	NA	93.0	2.6
Spot 10	93	1341	3.6	25.2205	3.4	0.0794	4.0	0.0145	2.2	0.54	93.0	2.0	77.6	3.0	NA	NA	93.0	2.0
Spot 11	91	3589	3.5	21.5026	2.9	0.0933	3.8	0.0146	2.5	0.65	93.1	2.3	90.5	3.3	23.9	69.6	93.1	2.3
Spot 12	88	710	2.8	33.2674	29.0	0.0603	29.1	0.0146	2.4	0.08	93.1	2.2	59.4	16.8	NA	NA	93.1	2.2
Spot 13	153	3348	2.8	21.9732	2.9	0.0914	3.6	0.0146	2.1	0.58	93.2	2.0	88.8	3.1	NA	NA	93.2	2.0
Spot 14	114	1223	1.9	24.5625	2.4	0.0818	3.8	0.0146	2.9	0.77	93.3	2.7	79.9	2.9	NA	NA	93.3	2.7
Spot 15	159	2625	3.4	21.0869	2.6	0.0955	3.5	0.0146	2.3	0.67	93.5	2.2	92.6	3.1	70.6	61.6	93.5	2.2
Spot 16	89	18005	3.5	20.7389	2.2	0.0972	4.0	0.0146	3.4	0.83	93.6	3.1	94.2	3.6	110.0	52.8	93.6	3.1
Spot 17	155	3666	2.0	21.1535	3.3	0.0954	4.3	0.0146	2.8	0.65	93.7	2.6	92.5	3.8	63.0	78.7	93.7	2.6
Spot 18	178	6382	2.9	21.5637	2.8	0.0936	4.0	0.0147	2.9	0.71	93.8	2.7	90.9	3.5	17.1	68.5	93.8	2.7
Spot 19	104	26432	2.9	17.6709	3.7	0.1145	4.7	0.0147	2.9	0.62	93.9	2.7	110.1	4.9	475.6	81.1	93.9	2.7
Spot 20	159	2959	2.1	21.5091	5.6	0.0942	6.4	0.0147	3.2	0.49	94.0	2.9	91.4	5.6	23.2	134.1	94.0	2.9
Spot 21	120	4253	2.3	19.6853	2.9	0.1030	3.7	0.0147	2.3	0.63	94.1	2.1	99.5	3.5	231.7	66.0	94.1	2.1
Spot 22	91	2288	2.6	21.5300	7.5	0.0944	7.8	0.0148	2.4	0.30	94.4	2.2	91.6	6.9	20.9	179.2	94.4	2.2
Spot 23	159	5786	2.0	21.3033	2.0	0.0958	3.2	0.0148	2.5	0.78	94.7	2.4	92.9	2.8	46.2	47.8	94.7	2.4
Spot 24	221	47904	2.8	19.9885	1.6	0.1021	3.6	0.0148	3.2	0.89	94.7	3.0	98.7	3.3	196.4	37.9	94.7	3.0
Spot 25	69	891250	2.8	20.4852	2.8	0.0997	4.1	0.0148	3.0	0.73	94.8	2.8	96.5	3.8	139.0	66.8	94.8	2.8
Spot 26	66	23683	3.2	21.1291	2.6	0.0967	3.9	0.0148	3.0	0.75	94.9	2.8	93.7	3.5	65.8	62.1	94.9	2.8
Spot 27	152	1562	2.0	25.0682	4.2	0.0816	5.0	0.0148	2.7	0.54	94.9	2.5	79.6	3.8	NA	NA	94.9	2.5
Spot 28	145	1300	2.4	25.7787	2.3	0.0796	3.1	0.0149	2.1	0.68	95.2	2.0	77.7	2.3	NA	NA	95.2	2.0
Spot 29	119	3173	3.1	22.8015	1.8	0.0900	2.7	0.0149	2.0	0.74	95.3	1.9	87.5	2.2	NA	NA	95.3	1.9
Spot 30	144	7864	3.1	21.0780	2.2	0.0979	3.3	0.0150	2.5	0.75	95.8	2.4	94.8	3.0	71.6	51.7	95.8	2.4
Spot 31	109	1746	2.0	13.7991	5.0	0.1501	6.2	0.0150	3.6	0.59	96.1	3.5	142.0	8.2	999.1	101.3	96.1	3.5

Contd.

Analysis	Isotope ratios										Apparent ages (Ma)								
	U (ppm)	206Pb/ 204Pb	U/Th	206Pb*/ 207Pb*	± (%)	207Pb*/ 235U*	± (%)	206Pb*/ 238U	± (%)	error corr.	206Pb*/ 238U*	± (Ma)	207Pb*/ 235U	± (Ma)	206Pb*/ 207Pb*	± (Ma)	Best age (Ma)	± (Ma)	
Spot 32	91	987	2.7	24.7110	13.3	0.0843	13.6	0.0151	2.7	0.20	96.8	2.6	82.2	10.7	NA	NA	96.8	2.6	
Spot 33	146	2013	2.5	23.1336	3.5	0.0906	4.2	0.0152	2.2	0.53	97.3	2.1	88.0	3.5	NA	NA	97.3	2.1	
Spot 34	150	12481	2.5	20.1768	1.9	0.1049	4.0	0.0154	3.5	0.87	98.2	3.4	101.3	3.8	174.5	45.0	98.2	3.4	
																	93.6		
24-10 OSW	Spot 1	327	2891	2.3	20.5949	0.7	0.0874	5.5	0.0131	5.4	0.99	83.6	4.5	85.1	4.5	126.5	15.7	83.6	4.5
	Spot 2	505	8641	1.6	20.4116	0.9	0.0900	4.4	0.0133	4.3	0.98	85.3	3.7	87.5	3.7	147.4	21.6	85.3	3.7
	Spot 3	423	5814	1.0	20.4304	1.2	0.0919	7.0	0.0136	6.9	0.99	87.2	6.0	89.3	6.0	145.2	27.9	87.2	6.0
	Spot 4	262	6137	3.2	20.0383	1.2	0.0939	2.2	0.0136	1.8	0.83	87.4	1.6	91.1	1.9	190.6	27.7	87.4	1.6
	Spot 5	255	1615	1.4	21.0645	0.5	0.0894	2.7	0.0137	2.7	0.98	87.5	2.3	87.0	2.3	73.1	12.8	87.5	2.3
	Spot 6	627	5643	2.1	20.5817	0.8	0.0916	2.9	0.0137	2.8	0.96	87.6	2.4	89.0	2.4	128.0	18.6	87.6	2.4
	Spot 7	228	6676	2.9	20.1593	0.9	0.0949	3.6	0.0139	3.5	0.97	88.9	3.1	92.1	3.2	176.5	21.5	88.9	3.1
	Spot 8	154	3391	1.6	20.2579	1.3	0.0949	5.0	0.0139	4.8	0.96	89.3	4.3	92.1	4.4	165.1	31.4	89.3	4.3
	Spot 9	161	3539	1.6	20.1708	1.6	0.0960	3.7	0.0140	3.3	0.90	89.9	2.9	93.0	3.3	175.2	37.9	89.9	2.9
	Spot 10	124	820	1.8	21.4622	1.5	0.0904	2.7	0.0141	2.2	0.83	90.1	2.0	87.9	2.3	28.4	36.0	90.1	2.0
	Spot 11	229	1537	3.9	20.6478	4.5	0.0941	4.6	0.0141	0.9	0.20	90.2	0.8	91.3	4.0	120.4	105.6	90.2	0.8
	Spot 12	99	1221	1.8	20.8527	1.8	0.0936	2.3	0.0142	1.4	0.62	90.6	1.3	90.9	2.0	97.1	42.4	90.6	1.3
	Spot 13	222	2150	1.6	20.8259	0.9	0.0939	2.4	0.0142	2.2	0.93	90.8	2.0	91.1	2.1	100.1	21.0	90.8	2.0
	Spot 14	172	2752	1.5	20.1332	1.8	0.0973	6.4	0.0142	6.2	0.96	90.9	5.6	94.2	5.8	179.5	42.5	90.9	5.6
	Spot 15	285	2848	1.5	20.5207	1.1	0.0961	1.8	0.0143	1.3	0.76	91.5	1.2	93.1	1.6	134.9	26.9	91.5	1.2
	Spot 16	376	4300	0.8	20.4711	1.0	0.0971	1.6	0.0144	1.3	0.78	92.3	1.2	94.1	1.5	140.6	24.0	92.3	1.2
	Spot 17	256	2914	2.5	20.5731	1.1	0.0968	4.7	0.0144	4.5	0.97	92.4	4.2	93.8	4.2	129.0	25.2	92.4	4.2
	Spot 18	248	14720	2.4	20.3172	1.1	0.0983	5.0	0.0145	4.9	0.97	92.7	4.5	95.2	4.6	158.3	26.8	92.7	4.5
	Spot 19	186	1954	2.2	20.7103	1.7	0.0971	1.8	0.0146	0.6	0.34	93.3	0.6	94.1	1.6	113.3	40.7	93.3	0.6
	Spot 20	184	2618	1.3	20.5217	1.5	0.0982	10.6	0.0146	10.5	0.99	93.5	9.8	95.1	9.6	134.8	34.8	93.5	9.8
	Spot 21	541	23251	5.3	20.3009	1.3	0.0998	4.8	0.0147	4.6	0.96	94.1	4.3	96.6	4.4	160.2	30.7	94.1	4.3
	Spot 22	122	3671	1.5	19.8249	1.3	0.1031	2.4	0.0148	2.0	0.83	94.9	1.8	99.7	2.2	215.4	30.7	94.9	1.8

Contd.

Analysis	Isotope ratios										Apparent ages (Ma)								
	U (ppm)	206Pb/ 204Pb	U/Th	206Pb*/ 207Pb*	±	207Pb*/ 235U*	±	206Pb*/ 238U	±	error corr.	206Pb*/ 238U*	±	207Pb*/ 235U	±	206Pb*/ 207Pb*	±	Best age (Ma)	± (Ma)	
Spot 1	170	1349	1.9	20.7638	1.7	0.0832	3.8	0.0125	3.4	0.89	80.3	2.7	81.2	3.0	107.2	40.9	80.3	2.7	
Spot 2	206	1963	1.2	20.7108	0.6	0.0858	1.4	0.0129	1.3	0.91	82.6	1.0	83.6	1.1	113.2	13.9	82.6	1.0	
Spot 3	335	4813	1.4	20.5503	1.1	0.0870	5.4	0.0130	5.3	0.98	83.1	4.3	84.7	4.4	131.5	24.7	83.1	4.3	
Spot 4	271	4818	1.4	19.9274	0.9	0.0905	1.7	0.0131	1.4	0.84	83.8	1.2	87.9	1.4	203.4	21.5	83.8	1.2	
Spot 5	388	1688	1.7	21.1093	1.1	0.0854	1.7	0.0131	1.3	0.77	83.8	1.1	83.2	1.4	68.1	25.9	83.8	1.1	
Spot 6	443	5944	1.1	20.3086	1.3	0.0889	2.6	0.0131	2.3	0.87	83.9	1.9	86.5	2.2	159.3	30.4	83.9	1.9	
Spot 7	179	1519	1.7	20.5709	2.0	0.0880	2.4	0.0131	1.2	0.51	84.1	1.0	85.7	1.9	129.2	47.9	84.1	1.0	
Spot 8	241	3467	1.0	20.3834	2.2	0.0900	2.5	0.0133	1.1	0.44	85.2	0.9	87.5	2.1	150.7	51.8	85.2	0.9	
Spot 9	414	4433	1.1	20.3890	1.4	0.0905	2.2	0.0134	1.7	0.76	85.7	1.4	88.0	1.8	150.0	32.9	85.7	1.4	
Spot 10	293	4883	1.6	20.2172	0.9	0.0918	2.3	0.0135	2.1	0.91	86.2	1.8	89.2	1.9	169.8	22.0	86.2	1.8	
HWY_90-72	Spot 11	317	2233	1.1	21.0906	1.3	0.0890	2.0	0.0136	1.5	0.75	87.2	1.3	86.6	1.6	70.1	31.0	87.2	1.3
Spot 12	342	4668	1.0	20.4863	1.3	0.0917	3.3	0.0136	3.0	0.92	87.2	2.6	89.1	2.8	138.8	30.4	87.2	2.6	
Spot 13	518	4352	0.7	20.6152	0.9	0.0913	3.4	0.0136	3.2	0.96	87.4	2.8	88.7	2.9	124.1	21.5	87.4	2.8	
Spot 14	167	1135	2.4	19.7913	1.6	0.0962	1.9	0.0138	1.0	0.54	88.4	0.9	93.3	1.7	219.3	37.6	88.4	0.9	
Spot 15	178	3808	1.6	20.2223	1.7	0.0945	1.9	0.0139	0.7	0.39	88.7	0.6	91.7	1.6	169.2	40.1	88.7	0.6	
Spot 16	246	2330	2.0	20.7821	1.4	0.0928	1.6	0.0140	0.7	0.45	89.5	0.6	90.1	1.4	105.1	34.1	89.5	0.6	
Spot 17	287	1219	1.8	21.0971	1.5	0.0915	2.3	0.0140	1.7	0.73	89.6	1.5	88.9	1.9	69.4	36.8	89.6	1.5	
Spot 18	180	3202	1.5	20.3666	1.4	0.0970	3.1	0.0143	2.8	0.89	91.7	2.5	94.0	2.8	152.6	32.7	91.7	2.5	
Spot 19	143	2467	2.5	20.2814	2.6	0.0979	3.5	0.0144	2.4	0.67	92.2	2.2	94.8	3.2	162.4	60.6	92.2	2.2	
Spot 20	277	3344	3.0	18.1879	1.6	0.1909	11.9	0.0252	11.8	0.99	160.3	18.7	177.4	19.4	411.5	35.3	160.3	18.7	
Spot 21	555	20612	2.9	12.4878	2.0	2.1069	4.2	0.1908	3.6	0.87	1125.8	37.7	1151.1	28.8	1198.9	40.0	1198.9	40.0	
Handy 11H	Spot 1	346	1694	1.5	20.3418	2.1	0.0884	2.9	0.0130	2.1	0.70	83.5	1.7	86.0	2.4	155.4	48.3	83.5	1.7
Spot 2	279	948	1.1	21.3850	1.2	0.0845	2.1	0.0131	1.8	0.84	84.0	1.5	82.4	1.7	37.1	27.8	84.0	1.5	
Spot 3	722	6146	1.4	20.0574	1.0	0.0902	4.5	0.0131	4.3	0.98	84.0	3.6	87.7	3.7	188.3	23.0	84.0	3.6	

Contd.

Analysis	Isotope ratios										Apparent ages (Ma)								
	U (ppm)	206Pb/ 204Pb	U/Th	206Pb*/ 207Pb*	± (%)	207Pb*/ 235U*	± (%)	206Pb*/ 238U	± (%)	error corr.	206Pb*/ 238U*	± (Ma)	207Pb*/ 235U	± (Ma)	206Pb*/ 207Pb*	± (Ma)	Best age (Ma)	± (Ma)	
Spot 4	364	2898	2.0	20.7968	1.2	0.0872	3.5	0.0132	3.3	0.94	84.2	2.8	84.9	2.9	103.4	28.0	84.2	2.8	
Spot 5	271	2129	1.5	20.5539	1.4	0.0887	2.1	0.0132	1.6	0.75	84.7	1.3	86.3	1.7	131.1	32.9	84.7	1.3	
Spot 6	302	3664	1.5	20.4299	1.1	0.0897	1.9	0.0133	1.5	0.81	85.1	1.3	87.2	1.6	145.3	26.1	85.1	1.3	
Spot 7	373	2579	1.2	20.5251	0.7	0.0894	4.2	0.0133	4.1	0.98	85.2	3.5	86.9	3.5	134.4	17.5	85.2	3.5	
Spot 8	338	1819	1.8	20.8364	1.0	0.0880	2.9	0.0133	2.7	0.94	85.2	2.3	85.7	2.4	98.9	23.2	85.2	2.3	
Spot 9	526	2229	1.5	20.7624	0.7	0.0884	2.9	0.0133	2.8	0.97	85.2	2.4	86.0	2.4	107.4	16.6	85.2	2.4	
Spot 10	331	2560	1.2	20.5178	1.1	0.0895	2.4	0.0133	2.1	0.88	85.3	1.8	87.1	2.0	135.2	26.5	85.3	1.8	
Spot 11	272	2900	2.1	20.6453	1.5	0.0890	3.5	0.0133	3.2	0.91	85.4	2.7	86.6	2.9	120.7	34.7	85.4	2.7	
Spot 12	1466	4849	1.4	20.7719	0.6	0.0889	1.5	0.0134	1.4	0.91	85.7	1.2	86.4	1.3	106.2	14.9	85.7	1.2	
Spot 13	208	1061	1.5	20.9642	1.4	0.0881	2.1	0.0134	1.6	0.75	85.8	1.3	85.8	1.7	84.4	33.5	85.8	1.3	
Spot 14	396	2779	1.6	20.2386	0.9	0.0914	1.8	0.0134	1.6	0.88	85.9	1.4	88.8	1.6	167.3	20.1	85.9	1.4	
Spot 15	233	1211	1.5	20.9271	1.2	0.0886	2.7	0.0135	2.4	0.88	86.1	2.0	86.2	2.2	88.7	29.3	86.1	2.0	
Spot 16	441	3209	1.5	20.6522	0.8	0.0899	3.9	0.0135	3.8	0.98	86.3	3.2	87.4	3.2	119.9	19.3	86.3	3.2	
Spot 17	305	1951	1.2	20.5754	1.5	0.0907	2.0	0.0135	1.4	0.68	86.7	1.2	88.2	1.7	128.7	34.2	86.7	1.2	
Spot 18	1072	7019	2.0	20.5722	1.0	0.0910	1.5	0.0136	1.1	0.73	87.0	0.9	88.5	1.2	129.0	23.7	87.0	0.9	
Spot 19	555	5718	1.8	20.1329	1.0	0.0932	1.7	0.0136	1.3	0.80	87.2	1.2	90.5	1.5	179.5	23.3	87.2	1.2	
Spot 20	464	10394	1.3	20.3703	1.3	0.0923	2.1	0.0136	1.6	0.79	87.3	1.4	89.6	1.8	152.2	29.7	87.3	1.4	
Spot 21	346	2205	1.4	20.7690	0.8	0.0912	1.9	0.0137	1.8	0.92	88.0	1.6	88.6	1.6	106.6	18.0	88.0	1.6	
Spot 22	815	8452	1.5	20.5208	1.2	0.0932	2.7	0.0139	2.4	0.89	88.8	2.1	90.5	2.3	134.9	28.2	88.8	2.1	
Spot 23	287	2347	1.9	20.5820	1.5	0.0945	4.8	0.0141	4.5	0.95	90.3	4.1	91.7	4.2	127.9	34.6	90.3	4.1	
Spot 24	1135	8531	1.3	20.4379	1.2	0.0957	1.8	0.0142	1.4	0.76	90.8	1.3	92.8	1.6	144.4	28.3	90.8	1.3	
Handy 9H	Spot 1	5427	845	2.5	12.3114	43.3	0.0940	43.5	0.0084	3.8	0.09	53.9	2.0	91.2	38.0	1226.9	894.7	53.9	2.0
	Spot 2	146	352	0.4	14.9408	6.2	0.0812	6.9	0.0088	2.9	0.42	56.4	1.6	79.2	5.2	835.6	129.7	56.4	1.6
	Spot 3	100	318	1.1	20.5169	3.3	0.0756	4.4	0.0112	3.0	0.67	72.1	2.1	74.0	3.2	135.4	77.9	72.1	2.1
	Spot 4	176	637	1.4	21.3943	1.8	0.0784	2.5	0.0122	1.8	0.72	77.9	1.4	76.6	1.9	36.0	42.2	77.9	1.4
	Spot 5	328	1167	2.1	20.8534	1.2	0.0823	3.2	0.0124	2.9	0.92	79.7	2.3	80.3	2.4	97.0	28.5	79.7	2.3

Contd.

Analysis	Isotope ratios										Apparent ages (Ma)							
	U (ppm)	206Pb/ 204Pb	U/Th	206Pb*/ 207Pb*	± (%)	207Pb*/ 235U*	± (%)	206Pb*/ 238U	± (%)	error corr.	206Pb*/ 238U*	± (Ma)	207Pb*/ 235U	± (Ma)	206Pb*/ 207Pb*	± (Ma)	Best age (Ma)	± (Ma)
Spot 6	170	614	1.4	22.0168	1.3	0.0783	2.1	0.0125	1.6	0.79	80.1	1.3	76.5	1.5	-33.1	30.6	80.1	1.3
Spot 7	2576	6720	2.9	20.5350	0.6	0.0842	1.8	0.0125	1.7	0.94	80.4	1.4	82.1	1.4	133.3	15.2	80.4	1.4
Spot 8	104	380	1.3	23.9209	2.2	0.0727	5.2	0.0126	4.7	0.90	80.8	3.8	71.3	3.6	-238.3	56.2	80.8	3.8
Spot 9	3907	6097	3.0	20.1888	0.6	0.0862	1.3	0.0126	1.1	0.88	80.8	0.9	83.9	1.0	173.1	14.5	80.8	0.9
Spot 10	172	571	1.0	22.7804	1.5	0.0769	2.7	0.0127	2.3	0.84	81.4	1.8	75.2	2.0	-116.4	36.2	81.4	1.8
Spot 11	184	766	1.0	22.0940	1.9	0.0796	2.1	0.0128	0.8	0.41	81.7	0.7	77.8	1.5	-41.5	45.7	81.7	0.7
Spot 12	456	1917	0.6	18.0125	18.3	0.0980	18.5	0.0128	2.4	0.13	82.0	2.0	94.9	16.7	433.1	410.7	82.0	2.0
Spot 13	248	1924	0.9	20.7002	1.6	0.0866	2.0	0.0130	1.3	0.62	83.3	1.0	84.4	1.6	114.4	37.3	83.3	1.0
Spot 14	250	1174	0.7	20.9280	1.1	0.0858	1.4	0.0130	0.9	0.63	83.4	0.8	83.5	1.2	88.6	26.7	83.4	0.8
Spot 15	213	835	1.4	21.1152	2.0	0.0856	2.6	0.0131	1.7	0.64	84.0	1.4	83.4	2.1	67.4	47.6	84.0	1.4
Spot 16	149	1006	1.0	20.9275	1.0	0.0867	2.5	0.0132	2.3	0.91	84.3	1.9	84.4	2.0	88.6	24.5	84.3	1.9
Spot 17	367	1366	1.2	21.2801	1.0	0.0858	2.8	0.0132	2.7	0.94	84.8	2.2	83.6	2.3	48.8	23.2	84.8	2.2
Spot 18	206	1597	1.1	20.5993	1.8	0.0887	4.4	0.0133	4.0	0.91	84.9	3.4	86.3	3.6	125.9	42.6	84.9	3.4
Spot 19	156	719	1.5	20.7096	1.9	0.0884	2.2	0.0133	1.0	0.46	85.0	0.8	86.0	1.8	113.3	45.5	85.0	0.8
Spot 20	2238	8382	3.0	20.3789	0.8	0.0902	1.5	0.0133	1.3	0.85	85.4	1.1	87.7	1.3	151.2	19.0	85.4	1.1
Spot 21	256	2412	0.8	19.8592	2.1	0.0930	3.1	0.0134	2.2	0.72	85.7	1.9	90.3	2.6	211.4	49.6	85.7	1.9
Spot 22	4373	14708	1.6	20.8061	1.2	0.0890	2.5	0.0134	2.2	0.88	86.0	1.9	86.6	2.1	102.4	27.5	86.0	1.9
Spot 23	129	1051	1.3	20.7748	1.7	0.0901	4.7	0.0136	4.3	0.93	87.0	3.7	87.6	3.9	105.9	40.5	87.0	3.7
Spot 24	816	7299	1.5	20.7969	0.5	0.0919	1.7	0.0139	1.7	0.95	88.7	1.5	89.2	1.5	103.4	12.5	88.7	1.5
Spot 25	475	614	0.4	17.0753	12.9	0.1172	16.4	0.0145	10.0	0.61	92.9	9.2	112.6	17.4	550.9	283.6	92.9	9.2
HWY 55-6B Spot 1	78	215	3.4	20.2671	6.1	0.0801	11.5	0.0118	9.7	0.84	75.4	7.3	78.2	8.6	164.0	143.6	75.4	7.3
Spot 2	368	2662	2.5	20.4216	4.6	0.0893	5.3	0.0132	2.7	0.51	84.7	2.3	86.8	4.4	146.3	107.0	84.7	2.3
Spot 3	121	388	1.7	23.6683	1.9	0.0771	3.0	0.0132	2.3	0.77	84.7	1.9	75.4	2.2	-211.6	47.7	84.7	1.9
Spot 4	231	1390	1.7	20.9039	1.3	0.0875	1.4	0.0133	0.4	0.31	84.9	0.4	85.2	1.2	91.3	31.8	84.9	0.4
Spot 5	481	2675	1.7	20.8021	0.8	0.0888	1.6	0.0134	1.4	0.86	85.8	1.2	86.4	1.3	102.8	19.2	85.8	1.2
Spot 6	330	1703	2.4	20.0787	1.6	0.0925	2.8	0.0135	2.3	0.83	86.2	2.0	89.8	2.4	185.8	36.6	86.2	2.0

Contd.

Analysis	Isotope ratios										Apparent ages (Ma)							
	U (ppm)	206Pb/ 204Pb	U/Th	206Pb*/ 207Pb*	±	207Pb*/ 235U*	±	206Pb*/ 238U	±	error corr.	206Pb*/ 238U*	±	207Pb*/ 235U	±	206Pb*/ 207Pb*	±	Best age (Ma)	±
Spot 6	330	1703	2.4	20.0787	1.6	0.0925	2.8	0.0135	2.3	0.83	86.2	2.0	89.8	2.4	185.8	36.6	86.2	2.0
Spot 7	719	3861	3.1	20.6362	0.7	0.0900	1.1	0.0135	0.8	0.75	86.2	0.7	87.5	0.9	121.7	16.7	86.2	0.7
Spot 8	332	1744	2.4	20.7890	1.1	0.0895	1.6	0.0135	1.1	0.69	86.4	0.9	87.0	1.3	104.3	27.1	86.4	0.9
Spot 9	365	1794	0.9	20.9263	1.0	0.0892	2.2	0.0135	2.0	0.90	86.7	1.7	86.7	1.8	88.7	22.7	86.7	1.7
Spot 10	455	1550	2.1	20.5693	1.9	0.0933	3.1	0.0139	2.4	0.79	89.1	2.2	90.6	2.7	129.4	45.1	89.1	2.2
Spot 11	222	950	3.2	21.4314	1.1	0.0896	1.9	0.0139	1.6	0.84	89.2	1.4	87.2	1.6	31.9	25.3	89.2	1.4
Spot 12	317	1811	1.3	20.8676	1.0	0.0921	1.1	0.0139	0.4	0.39	89.2	0.4	89.4	1.0	95.4	24.8	89.2	0.4
Spot 13	466	1270	4.8	20.8476	1.6	0.0927	2.4	0.0140	1.8	0.74	89.8	1.6	90.0	2.1	97.7	38.7	89.8	1.6
Spot 14	196	2094	3.2	20.4898	1.0	0.0944	2.5	0.0140	2.3	0.92	89.8	2.1	91.6	2.2	138.5	23.6	89.8	2.1
Spot 15	400	1310	2.7	21.1997	0.8	0.0913	1.7	0.0140	1.5	0.87	89.9	1.3	88.7	1.5	57.8	20.0	89.9	1.3
Spot 16	480	2184	1.9	20.7692	1.2	0.0934	3.1	0.0141	2.8	0.92	90.1	2.5	90.7	2.7	106.5	28.4	90.1	2.5
LONG 3L																		
Spot 1	236	1408	2.2	20.6177	1.9	0.0853	5.8	0.0128	5.5	0.95	81.7	4.4	83.2	4.6	123.8	43.8	81.7	4.4
Spot 2	208	1312	2.3	20.5792	1.5	0.0857	5.7	0.0128	5.5	0.96	81.9	4.4	83.5	4.5	128.3	35.1	81.9	4.4
Spot 3	214	796	2.4	21.6933	1.7	0.0816	3.2	0.0128	2.7	0.85	82.2	2.2	79.6	2.5	2.7	41.0	82.2	2.2
Spot 4	126	575	2.5	22.3965	1.8	0.0794	2.6	0.0129	1.9	0.72	82.6	1.6	77.5	2.0	-74.7	44.9	82.6	1.6
Spot 5	262	3048	1.8	20.5036	1.6	0.0872	4.2	0.0130	3.9	0.93	83.0	3.2	84.9	3.4	136.9	37.1	83.0	3.2
Spot 6	167	662	2.6	22.0448	2.2	0.0813	3.7	0.0130	2.9	0.79	83.3	2.4	79.4	2.8	-36.1	54.6	83.3	2.4
Spot 7	239	825	2.2	20.7353	1.6	0.0868	4.2	0.0130	3.9	0.93	83.6	3.3	84.5	3.4	110.4	37.7	83.6	3.3
Spot 8	557	2139	1.2	21.0854	1.3	0.0854	3.3	0.0131	3.0	0.92	83.7	2.5	83.2	2.6	70.7	29.9	83.7	2.5
Spot 9	236	816	2.2	21.3085	1.9	0.0847	3.1	0.0131	2.4	0.79	83.9	2.0	82.6	2.5	45.7	45.3	83.9	2.0
Spot 10	310	1199	1.7	21.4985	1.6	0.0842	3.2	0.0131	2.7	0.86	84.0	2.3	82.1	2.5	24.4	39.3	84.0	2.3
Spot 11	248	866	2.6	21.7679	1.3	0.0832	1.4	0.0131	0.5	0.37	84.1	0.4	81.2	1.1	-5.6	32.1	84.1	0.4
Spot 12	256	2053	1.8	20.7795	1.2	0.0873	4.6	0.0132	4.4	0.96	84.2	3.7	85.0	3.8	105.4	29.0	84.2	3.7
Spot 13	289	1503	1.0	20.8364	1.5	0.0871	3.8	0.0132	3.5	0.91	84.3	2.9	84.8	3.1	98.9	36.4	84.3	2.9
Spot 14	297	1893	1.6	20.6560	2.2	0.0881	2.6	0.0132	1.5	0.55	84.5	1.2	85.7	2.2	119.5	51.6	84.5	1.2

Contd.

Analysis	Isotope ratios										Apparent ages (Ma)				Best age	±		
	U (ppm)	206Pb/ 204Pb	U/Th	206Pb*/ 207Pb*	±	207Pb*/ 235U*	±	206Pb*/ 238U	±	error	206Pb*/ 238U*	±	207Pb*/ 235U	±			206Pb*/ 207Pb*	±
Spot 15	358	2535	1.5	20.7756	1.5	0.0881	1.7	0.0133	0.8	0.46	85.0	0.7	85.7	1.4	105.8	36.4	85.0	0.7
Spot 16	325	575	1.5	17.0244	3.4	0.1075	3.5	0.0133	0.8	0.22	85.0	0.6	103.7	3.5	557.4	75.2	85.0	0.6
Spot 17	361	1367	2.0	21.0951	1.2	0.0868	1.7	0.0133	1.1	0.66	85.1	0.9	84.5	1.3	69.6	29.5	85.1	0.9
Spot 18	234	1191	1.5	21.3696	2.2	0.0858	2.5	0.0133	1.2	0.49	85.1	1.0	83.6	2.0	38.8	51.8	85.1	1.0
Spot 19	253	1876	1.4	20.4285	1.3	0.0900	2.5	0.0133	2.1	0.84	85.4	1.8	87.5	2.1	145.5	31.2	85.4	1.8
Spot 20	333	1447	2.0	21.4636	1.0	0.0858	1.6	0.0134	1.2	0.76	85.6	1.0	83.6	1.3	28.3	24.7	85.6	1.0
Spot 21	616	4676	1.4	20.4347	0.9	0.0903	1.2	0.0134	0.7	0.61	85.7	0.6	87.8	1.0	144.8	22.0	85.7	0.6
Spot 22	255	1726	2.3	21.0680	1.9	0.0878	2.2	0.0134	1.1	0.48	85.9	0.9	85.5	1.8	72.7	45.9	85.9	0.9
Spot 23	772	2027	1.0	19.3503	1.0	0.0959	4.1	0.0135	4.0	0.97	86.2	3.4	93.0	3.7	271.2	23.9	86.2	3.4
Spot 24	293	1701	1.7	21.1634	1.5	0.0887	1.8	0.0136	0.9	0.52	87.2	0.8	86.3	1.5	62.0	36.7	87.2	0.8
Spot 25	835	8925	8.9	19.9557	1.1	0.1003	9.6	0.0145	9.5	0.99	92.9	8.8	97.0	8.8	200.1	24.8	92.9	8.8
Spot 1	337	1942	2.2	20.8399	1.0	0.0871	2.5	0.0132	2.3	0.92	84.3	1.9	84.8	2.0	98.5	23.5	84.3	1.9
Spot 2	166	1604	1.3	20.2066	2.2	0.0900	3.1	0.0132	2.3	0.72	84.4	1.9	87.5	2.6	171.0	50.2	84.4	1.9
Spot 3	233	3427	3.0	20.2942	1.5	0.0918	3.3	0.0135	2.9	0.89	86.5	2.5	89.1	2.8	160.9	34.4	86.5	2.5
Spot 4	358	8122	3.2	20.5694	1.1	0.0912	3.5	0.0136	3.3	0.95	87.1	2.8	88.6	3.0	129.4	26.7	87.1	2.8
Spot 5	546	6679	1.6	20.2849	0.8	0.0930	6.7	0.0137	6.7	0.99	87.6	5.8	90.3	5.8	162.0	18.7	87.6	5.8
Spot 6	236	1231	1.4	20.8244	3.1	0.0914	3.4	0.0138	1.2	0.35	88.4	1.0	88.8	2.9	100.3	74.4	88.4	1.0
Spot 7	357	4230	2.6	20.6348	1.5	0.0934	3.6	0.0140	3.3	0.91	89.5	2.9	90.6	3.1	121.9	35.5	89.5	2.9
Spot 8	402	1069	1.3	16.5464	5.6	0.1187	5.8	0.0142	1.7	0.29	91.2	1.5	113.9	6.3	619.2	120.0	91.2	1.5
Spot 9	346	2862	3.0	20.4743	1.3	0.0962	2.7	0.0143	2.3	0.87	91.4	2.1	93.3	2.4	140.3	30.5	91.4	2.1
Spot 10	276	2669	3.6	20.7013	1.1	0.0952	3.3	0.0143	3.1	0.94	91.5	2.8	92.3	2.9	114.3	25.9	91.5	2.8
Spot 11	433	3636	2.2	20.5756	1.3	0.0970	5.1	0.0145	4.9	0.97	92.6	4.6	94.0	4.6	128.7	30.5	92.6	4.6
Spot 12	485	9511	2.4	13.5486	0.9	0.8177	7.9	0.0804	7.9	0.99	498.2	37.9	606.8	36.3	1036.2	18.0	498.2	37.9

HWY_90_55

Contd.

Analysis	Isotope ratios										Apparent ages (Ma)							
	U (ppm)	206Pb/ 204Pb	U/Th	206Pb*/ 207Pb*	± (%)	207Pb*/ 235U*	± (%)	206Pb*/ 238U	± (%)	error corr.	206Pb*/ 238U*	± (Ma)	207Pb*/ 235U	± (Ma)	206Pb*/ 207Pb*	± (Ma)	Best age (Ma)	± (Ma)
Spot 1	70	95	1.4	8.4855	31.3	0.2056	31.6	0.0127	4.4	0.14	81.0	3.6	189.8	54.8	1923.8	576.4	81.0	3.6
Spot 2	252	648	1.3	22.4901	1.8	0.0780	7.5	0.0127	7.3	0.97	81.5	5.9	76.3	5.5	-84.9	43.5	81.5	5.9
Spot 3	87	416	1.2	23.5638	3.7	0.0775	4.5	0.0132	2.5	0.57	84.8	2.1	75.8	3.3	-200.5	92.9	84.8	2.1
Spot 4	568	2953	1.0	20.6901	0.8	0.0883	6.9	0.0132	6.9	0.99	84.9	5.8	85.9	5.7	115.6	18.6	84.9	5.8
Spot 5	230	702	1.4	20.7802	4.0	0.0882	5.2	0.0133	3.4	0.65	85.1	2.9	85.8	4.3	105.3	93.8	85.1	2.9
Spot 6	262	614	1.1	18.8683	20.5	0.0977	21.4	0.0134	6.2	0.29	85.6	5.2	94.7	19.4	328.7	470.2	85.6	5.2
Spot 7	362	1217	1.3	21.3258	1.1	0.0870	2.2	0.0135	1.9	0.85	86.2	1.6	84.7	1.8	43.7	27.3	86.2	1.6
Spot 8	225	1169	1.1	20.9847	1.7	0.0886	13.1	0.0135	12.9	0.99	86.3	11.1	86.2	10.8	82.1	41.0	86.3	11.1
Spot 9	474	1982	1.1	20.7551	1.1	0.0909	2.4	0.0137	2.1	0.88	87.6	1.8	88.3	2.0	108.2	26.1	87.6	1.8
Spot 10	286	1742	1.7	20.8309	1.8	0.0907	2.9	0.0137	2.3	0.79	87.7	2.0	88.2	2.5	99.6	41.7	87.7	2.0
Spot 11	906	3651	1.4	20.5526	0.7	0.0927	4.7	0.0138	4.6	0.99	88.5	4.1	90.0	4.0	131.3	16.8	88.5	4.1
Spot 12	250	1297	1.0	20.7346	1.5	0.0920	2.7	0.0138	2.3	0.83	88.6	2.0	89.4	2.3	110.5	36.2	88.6	2.0
HWY_90-80 Spot 13	188	630	1.0	20.5197	7.6	0.0932	7.7	0.0139	1.5	0.20	88.8	1.3	90.5	6.7	135.0	178.4	88.8	1.3
Spot 14	267	1177	1.3	21.0907	1.5	0.0908	2.2	0.0139	1.7	0.75	88.9	1.5	88.3	1.9	70.1	35.1	88.9	1.5
Spot 15	198	1284	1.8	20.9458	2.0	0.0915	4.7	0.0139	4.3	0.90	89.0	3.8	88.9	4.0	86.5	48.3	89.0	3.8
Spot 16	161	786	1.1	22.0194	1.0	0.0875	1.4	0.0140	1.0	0.74	89.4	0.9	85.2	1.2	-33.3	23.3	89.4	0.9
Spot 17	384	1046	1.6	21.2978	0.5	0.0912	2.7	0.0141	2.6	0.98	90.2	2.3	88.6	2.3	46.8	12.4	90.2	2.3
Spot 18	487	1983	1.0	21.0836	0.9	0.0925	3.6	0.0141	3.5	0.97	90.6	3.2	89.8	3.1	70.9	20.6	90.6	3.2
Spot 19	120	670	2.5	21.6390	1.4	0.0904	3.0	0.0142	2.6	0.88	90.8	2.3	87.9	2.5	8.8	34.6	90.8	2.3
Spot 20	648	5226	1.7	20.4859	1.0	0.0961	2.6	0.0143	2.4	0.92	91.4	2.1	93.2	2.3	138.9	23.0	91.4	2.1
Spot 21	328	1258	1.2	21.3273	0.9	0.0926	3.0	0.0143	2.8	0.95	91.7	2.6	89.9	2.6	43.5	22.6	91.7	2.6
Spot 22	374	1856	1.5	20.9261	0.5	0.0948	2.0	0.0144	2.0	0.96	92.0	1.8	91.9	1.8	88.8	12.7	92.0	1.8
Spot 23	175	713	1.8	21.9688	1.8	0.0904	2.8	0.0144	2.2	0.77	92.2	2.0	87.9	2.4	-27.8	43.4	92.2	2.0
Spot 24	277	1545	1.7	20.8444	1.5	0.0970	4.6	0.0147	4.3	0.94	93.8	4.0	94.0	4.1	98.0	35.6	93.8	4.0
Spot 25	461	2127	0.8	19.0655	12.5	0.1081	12.5	0.0149	0.9	0.07	95.6	0.9	104.2	12.4	305.1	285.4	95.6	0.9

Contd.

Analysis	U (ppm)	206Pb/ 204Pb	U/Th	Isotope ratios							Apparent ages (Ma)						Best age (Ma)	± (Ma)	
				206Pb*/ 207Pb*	± (%)	207Pb*/ 235U*	± (%)	206Pb*/ 238U	± (%)	error corr.	206Pb*/ 238U*	± (Ma)	207Pb*/ 235U	± (Ma)	206Pb*/ 207Pb*	± (Ma)			
OH_90-80	Spot 1	229	2036	1.3	20.6430	2.0	0.0901	3.5	0.0135	2.9	0.82	86.4	2.5	87.6	3.0	120.9	47.1	86.4	2.5
	Spot 2	130	1742	2.4	20.3472	1.9	0.0915	2.3	0.0135	1.2	0.52	86.4	1.0	88.9	1.9	154.9	45.2	86.4	1.0
	Spot 3	256	2271	1.4	20.9319	0.6	0.0909	2.5	0.0138	2.5	0.98	88.4	2.2	88.4	2.2	88.1	13.1	88.4	2.2
	Spot 4	178	2208	1.6	20.5395	1.1	0.0930	2.7	0.0139	2.4	0.91	88.7	2.1	90.3	2.3	132.7	26.6	88.7	2.1
	Spot 5	241	2208	1.2	20.6736	0.9	0.0932	2.4	0.0140	2.2	0.92	89.5	2.0	90.5	2.1	117.5	22.2	89.5	2.0
	Spot 6	400	5517	1.2	20.3695	1.2	0.0947	3.6	0.0140	3.4	0.94	89.6	3.0	91.9	3.1	152.3	27.7	89.6	3.0
	Spot 7	225	1916	1.6	20.9294	1.2	0.0932	2.4	0.0141	2.1	0.88	90.6	1.9	90.5	2.1	88.4	27.4	90.6	1.9
	Spot 8	270	2034	1.1	20.7350	1.0	0.0942	1.7	0.0142	1.4	0.80	90.7	1.3	91.4	1.5	110.5	24.3	90.7	1.3
	Spot 9	552	4002	1.3	20.5549	1.2	0.0952	1.7	0.0142	1.2	0.71	90.8	1.1	92.3	1.5	131.0	28.1	90.8	1.1
	Spot 10	128	1582	1.6	20.5551	2.7	0.0957	3.1	0.0143	1.6	0.51	91.3	1.5	92.8	2.8	131.0	63.0	91.3	1.5
	Spot 11	66	561	2.0	21.7434	2.1	0.0933	3.2	0.0147	2.4	0.75	94.1	2.2	90.5	2.8	-2.8	50.3	94.1	2.2
	Spot 12	308	2770	1.2	20.6454	0.7	0.0989	2.2	0.0148	2.1	0.95	94.8	2.0	95.8	2.1	120.7	16.6	94.8	2.0
13-5_OSE	Spot 1	185	1175	1.2	20.0798	2.0	0.0860	3.4	0.0125	2.8	0.82	80.3	2.2	83.8	2.7	185.7	45.5	80.3	2.2
	Spot 2	74	556	1.2	20.9907	0.9	0.0830	2.4	0.0126	2.2	0.93	81.0	1.8	81.0	1.8	81.4	20.3	81.0	1.8
	Spot 3	82	794	1.3	20.6544	2.7	0.0846	3.2	0.0127	1.6	0.52	81.2	1.3	82.4	2.5	119.6	63.7	81.2	1.3
	Spot 4	78	706	1.2	21.1580	1.1	0.0830	2.6	0.0127	2.3	0.90	81.6	1.9	81.0	2.0	62.5	26.7	81.6	1.9
	Spot 5	177	911	1.2	20.9974	1.0	0.0859	1.8	0.0131	1.5	0.84	83.8	1.3	83.7	1.5	80.7	23.8	83.8	1.3
	Spot 6	173	1425	2.0	20.6811	1.8	0.0877	3.6	0.0132	3.1	0.87	84.3	2.6	85.4	2.9	116.6	42.2	84.3	2.6
	Spot 7	100	1246	2.2	20.5214	1.4	0.0884	2.1	0.0132	1.6	0.75	84.3	1.4	86.0	1.8	134.8	33.3	84.3	1.4
	Spot 8	927	8399	0.8	20.2101	1.2	0.0902	2.4	0.0132	2.1	0.88	84.7	1.8	87.7	2.1	170.6	27.5	84.7	1.8
	Spot 9	270	1813	1.2	20.8045	1.1	0.0881	1.4	0.0133	0.9	0.65	85.1	0.8	85.7	1.1	102.5	25.2	85.1	0.8
	Spot 10	661	3593	0.5	20.4534	1.1	0.0901	2.9	0.0134	2.7	0.93	85.6	2.3	87.6	2.4	142.7	25.6	85.6	2.3
	Spot 11	77	1206	1.4	20.4870	2.9	0.0903	4.0	0.0134	2.8	0.70	85.9	2.4	87.7	3.4	138.8	66.9	85.9	2.4
	Spot 12	271	1789	1.6	20.7829	1.2	0.0904	1.8	0.0136	1.3	0.72	87.2	1.1	87.9	1.5	105.0	29.1	87.2	1.1
	Spot 13	212	2215	1.1	20.1187	1.8	0.0939	2.2	0.0137	1.3	0.58	87.7	1.1	91.1	1.9	181.2	42.6	87.7	1.1

*Note attached at the end of Table 10

Table 2: Lu-Hf isotope data of zircons from 10 volcanic ash beds of the Eagle Ford Shale, South Texas and Del Rio, West Texas, determined by LA-ICP-MS.

Sample	$\frac{(^{176}\text{Yb} + ^{176}\text{Lu})}{^{176}\text{Hf}} (\%)$	Volts Hf	$^{176}\text{Hf}/^{177}\text{Hf}$	$\pm (1\sigma)$	$^{176}\text{Lu}/^{177}\text{Hf}$	$^{176}\text{Hf}/^{177}\text{Hf}$ (T)	E-Hf (0)	E-Hf (0) \pm (1 σ)	E-Hf (T)	Age (Ma)	
Handy 13203	Spot 1	11.4	2.0	0.282852	0.000023	0.000687	0.282851	2.4	0.8	4.0	75
	Spot 2	20.1	2.9	0.282872	0.000026	0.001637	0.282869	3.1	0.9	4.9	89
	Spot 3	13.5	2.4	0.282846	0.000020	0.000669	0.282845	2.1	0.7	4.1	91
	Spot 4	19.7	2.6	0.282875	0.000017	0.001047	0.282873	3.2	0.6	5.1	92
	Spot 5	25.5	2.3	0.282976	0.000027	0.001964	0.282972	6.7	0.9	8.7	92
	Spot 6	16.9	1.8	0.282864	0.000025	0.001344	0.282862	2.8	0.9	4.8	93
	Spot 7	15.4	3.3	0.282831	0.000020	0.000863	0.282830	1.6	0.7	3.7	95
	Spot 8	14.5	3.2	0.282797	0.000020	0.000823	0.282796	0.4	0.7	2.5	95
	Spot 9	24.2	1.9	0.282753	0.000023	0.001357	0.282751	-1.1	0.8	0.9	95
	Spot 10	16.0	2.6	0.282918	0.000028	0.001302	0.282916	4.7	1.0	6.8	97
Long 7C	Spot 1	15.4	3.1	0.282892	0.000025	0.001337	0.282890	3.8	0.9	5.7	91
	Spot 2	31.5	2.3	0.282883	0.000020	0.002397	0.282879	3.5	0.7	5.4	94
	Spot 3	15.1	2.3	0.282934	0.000028	0.000921	0.282932	5.3	1.0	7.3	94
	Spot 4	28.2	2.8	0.282954	0.000020	0.002184	0.282950	6.0	0.7	7.9	94
	Spot 5	36.7	2.3	0.282949	0.000023	0.002733	0.282944	5.8	0.8	7.7	94
	Spot 6	32.4	1.9	0.283057	0.000024	0.002340	0.283053	9.6	0.8	11.6	94
	Spot 7	22.1	1.9	0.282920	0.000039	0.001840	0.282916	4.8	1.4	6.7	95
	Spot 8	42.2	1.8	0.282846	0.000023	0.002290	0.282842	2.2	0.8	4.1	95
	Spot 9	16.6	2.1	0.282875	0.000028	0.001011	0.282873	3.2	1.0	5.2	96
	Spot 10	21.1	2.2	0.282891	0.000024	0.001363	0.282889	3.7	0.9	5.8	98
	Spot 11	24.4	2.6	0.282858	0.000024	0.001563	0.282855	2.6	0.8	4.7	99

Contd.

Sample		$\frac{^{176}\text{Yb} + ^{176}\text{Lu}}{^{176}\text{Hf}} (\%)$	Volts Hf	$^{176}\text{Hf}/^{177}\text{Hf}$	$\pm (1\sigma)$	$^{176}\text{Lu}/^{177}\text{Hf}$	$^{176}\text{Hf}/^{177}\text{Hf}$ (T)	E-Hf (0)	E-Hf (0) $\pm (1\sigma)$	E-Hf (T)	Age (Ma)
NG2N	Spot 1	12.6	2.0	0.282764	0.000025	0.000784	0.282763	-0.8	0.9	0.8	74
	Spot 2	13.7	2.6	0.282895	0.000021	0.000832	0.282893	3.9	0.7	5.8	87
	Spot 3	11.2	2.2	0.282944	0.000025	0.000646	0.282943	5.6	0.9	7.6	91
	Spot 4	24.5	2.3	0.282877	0.000020	0.002061	0.282874	3.3	0.7	5.2	92
	Spot 5	15.0	2.3	0.282806	0.000018	0.000994	0.282804	0.7	0.7	2.7	92
	Spot 6	16.3	2.2	0.282892	0.000027	0.000982	0.282890	3.8	0.9	5.8	92
	Spot 7	18.6	2.0	0.282910	0.000020	0.001290	0.282908	4.4	0.7	6.4	93
	Spot 8	29.7	2.0	0.282922	0.000026	0.001647	0.282919	4.9	0.9	6.8	94
	Spot 9	15.6	2.3	0.282856	0.000019	0.000977	0.282855	2.5	0.7	4.6	95
	Spot 10	12.9	2.6	0.282781	0.000027	0.000781	0.282780	-0.1	0.9	1.9	95
FRIEDRICHS	Spot 1	28.3	2.1	0.282768	0.000032	0.001243	0.282765	-0.6	1.1	1.4	92
	Spot 2	18.8	2.3	0.282792	0.000027	0.001197	0.282789	0.2	0.9	2.2	93
	Spot 3	15.7	2.5	0.282827	0.000017	0.001017	0.282826	1.5	0.6	3.5	94
	Spot 4	13.1	2.4	0.282895	0.000026	0.000792	0.282893	3.9	0.9	5.9	93
	Spot 5	16.7	2.1	0.282836	0.000028	0.001005	0.282835	1.8	1.0	3.6	84
	Spot 6	15.1	2.6	0.282776	0.000027	0.000859	0.282775	-0.3	1.0	1.7	92
	Spot 7	13.1	2.2	0.282857	0.000023	0.000806	0.282856	2.6	0.8	4.6	93
HANDY_11H	Spot 1	15.0	2.5	0.282818	0.000044	0.000896	0.282817	1.2	1.6	3.0	84.7
	Spot 2	18.2	2.6	0.282920	0.000044	0.001059	0.282918	4.8	1.6	6.6	85.8

Contd.

Sample	$\frac{^{176}\text{Yb} + ^{176}\text{Lu}}{^{176}\text{Hf}} (\%)$	Volts Hf	$^{176}\text{Hf}/^{177}\text{Hf}$	$\pm (1\sigma)$	$^{176}\text{Lu}/^{177}\text{Hf}$	$^{176}\text{Hf}/^{177}\text{Hf}$ (T)	E-Hf (0)	E-Hf (0) \pm (1 σ)	E-Hf (T)	Age (Ma)	
	Spot 3	17.8	2.6	0.282880	0.000042	0.001071	0.282878	3.3	1.5	5.2	84.0
	Spot 4	20.4	2.6	0.282828	0.000035	0.001242	0.282826	1.5	1.2	3.4	88.0
	Spot 5	38.2	2.3	0.282878	0.000046	0.002196	0.282875	3.3	1.6	5.1	85.3
	Spot 6	21.1	2.7	0.282859	0.000039	0.001276	0.282857	2.6	1.4	4.5	86.7
	Spot 1	55.7	2.6	0.282620	0.000040	0.003229	0.282615	-5.8	1.4	-4.4	72.1
	Spot 2	30.7	2.6	0.282731	0.000040	0.001587	0.282729	-1.9	1.4	-0.2	77.9
	Spot 3	16.4	2.0	0.282721	0.000049	0.001118	0.282719	-2.3	1.7	-0.5	81.4
HANDY_9	Spot 4	53.9	2.1	0.282762	0.000066	0.003055	0.282758	-0.8	2.3	0.9	85.7
	Spot 5	52.3	2.8	0.282805	0.000035	0.003006	0.282800	0.7	1.2	2.5	87.0
	Spot 6	52.9	2.6	0.282847	0.000045	0.004392	0.282840	2.2	1.6	3.8	84.3
	Spot 7	50.7	1.8	0.282794	0.000036	0.002867	0.282789	0.3	1.3	2.0	83.3
	Spot 1	29.0	1.8	0.282754	0.000049	0.001779	0.282752	-1.1	1.7	0.7	84.9
	Spot 2	14.7	2.6	0.282827	0.000045	0.000817	0.282826	1.5	1.6	3.4	89.2
HWY_55-6B	Spot 3	22.7	2.3	0.282816	0.000038	0.001935	0.282813	1.1	1.3	2.9	84.7
	Spot 4	24.5	1.9	0.282799	0.000046	0.001524	0.282796	0.5	1.6	2.4	89.2
	Spot 5	8.9	3.0	0.282738	0.000040	0.000570	0.282737	-1.7	1.4	0.2	86.2
	Spot 1	11.8	2.6	0.282719	0.000035	0.000723	0.282718	-2.3	1.2	-0.4	89.6
	Spot 2	28.2	2.3	0.282702	0.000040	0.001811	0.282699	-2.9	1.4	-0.9	94.8
OH_90-80	Spot 3	11.0	2.5	0.282654	0.000030	0.000684	0.282653	-4.6	1.1	-2.7	91.3

Contd.

Sample		$\frac{(^{176}\text{Yb} + ^{176}\text{Lu})}{^{176}\text{Hf}} (\%)$	Volts Hf	$^{176}\text{Hf}/^{177}\text{Hf}$	$\pm (1\sigma)$	$^{176}\text{Lu}/^{177}\text{Hf}$	$^{176}\text{Hf}/^{177}\text{Hf}$ (T)	E-Hf (0)	E-Hf (0) \pm (1 σ)	E-Hf (T)	Age (Ma)
	Spot 4	20.9	2.7	0.282751	0.000034	0.001211	0.282749	-1.2	1.2	0.7	88.4
	Spot 5	15.8	2.5	0.282710	0.000036	0.000964	0.282708	-2.7	1.3	-0.7	90.7
	Spot 6	13.9	2.6	0.282750	0.000032	0.000861	0.282748	-1.2	1.1	0.7	88.7
	Spot 1	14.3	2.3	0.282686	0.000038	0.000901	0.282685	-3.5	1.3	-1.6	85.6
	Spot 2	27.2	2.2	0.282771	0.000041	0.002021	0.282768	-0.5	1.5	1.4	88.8
HWY_90- 80	Spot 3	22.9	2.6	0.282718	0.000038	0.001420	0.282716	-2.4	1.3	-0.4	91.7
	Spot 4	12.6	2.3	0.282678	0.000039	0.000799	0.282676	-3.8	1.4	-1.8	92.2
	Spot 5	27.3	2.3	0.282730	0.000038	0.002031	0.282727	-1.9	1.3	0.0	90.6
	Spot 6	12.3	2.4	0.282781	0.000045	0.000741	0.282779	-0.2	1.6	1.7	86.3
	Spot 1	9.2	2.4	0.282809	0.000037	0.000593	0.282808	0.8	1.3	2.8	88.4
	Spot 2	16.8	2.5	0.282722	0.000030	0.001001	0.282721	-2.2	1.1	-0.4	82.6
HWY_90- 72	Spot 3	16.8	2.5	0.282721	0.000030	0.001064	0.282719	-2.3	1.1	-0.4	85.7
	Spot 4	11.9	2.7	0.282787	0.000022	0.000761	0.282786	0.1	0.8	2.0	88.7
	Spot 5	21.8	2.6	0.282658	0.000031	0.001291	0.282656	-4.5	1.1	-2.6	87.2
	Spot 6	17.4	2.6	0.282882	0.000023	0.001131	0.282880	3.4	0.8	5.4	89.6

Table 3: High Precision $^{87}\text{Sr}/^{86}\text{Sr}$ ratios from 300 ft of the Eagle Ford Shale.

Depth	Sr	2sigma	Depth	Sr	2sigma
13100.65	0.707483	0.000012	13235.5	0.707475	0.000013
13120	0.707443	0.000005	13247.5	0.707432	0.000023
13132	0.707431	0.000011	13255.5	0.707449	0.000007
13142.5	0.707419	0.000006	13263	0.707446	0.000008
13170.5	0.707473	0.000006	13269.5	0.707405	0.000010
13179.75	0.707446	0.000005	13272.5	0.707458	0.000011
13187.1	0.707463	0.000008	13282	0.707533	0.000011
13196	0.707452	0.000012	13303	0.707535	0.000012
13205.25	0.707445	0.000008	13330.17	0.707566	0.000008
13210.25	0.707433	0.000012	13349.17	0.707530	0.000011
13217.2	0.707466	0.000011	13350.1	0.707560	0.000009
13220.75	0.707476	0.000007	13360.17	0.707543	0.000015
13222.5	0.707449	0.000008	13373	0.707543	0.000015
13230	0.707477	0.000011	13389.9	0.707566	0.000008

Standards		
SRM 987	0.710264	0.000008
SRM 987	0.710293	0.000006
SRM 987	0.710310	0.000009

Table 4: Some Rare Earth elements of EF volcanic ash beds, calc-alkaline (andesitic) arc examples of the Aleutian, Andes and Cascades along with mafic volcanism from the Ontong Java Plateau plume.

	La	Ce	Nd	Sm	Eu	Tb	Yb	Lu
2N	15.316	13.051	8.753	7.027	5.5062	2.4931	2.857	4.0816
7L	121.519	96.248	63.457	46.689	11.5453	16.6205	8.634	11.4286
11H	119.409	106.036	48.140	29.189	11.0124	11.0803	6.398	8.1633
1F	35.992	32.626	17.505	12.905	3.7300	8.3102	6.025	5.3061
3L	72.574	60.359	28.446	23.378	9.9467	13.8504	10.373	11.4286
15R	16.118	17.945	10.941	10.405	7.2824	2.4931	3.540	2.8571
14R	12.489	9.788	10.941	10.946	9.2362	8.3102	5.155	4.8980
Aleutian	67.595	60.799	44.201	26.689	19.8934	11.9114	8.199	7.7551
Andean	79.283	67.259	45.077	29.527	22.0249	16.6205	11.366	11.4286
Cascades	47.637	39.511	30.066	21.351	18.1172	13.5734	11.677	11.0204
Ontong	19.367	18.499	20.525	19.189	18.2948	16.8975	10.559	10.2041
	11.646	13.116	15.536	15.811	17.0515	16.0665	13.851	14.6939

	Average whole rock	Ash Beds		Average whole rock	Ash Beds
Cr	94.31993	32.71	Pb	4.3945636	27
Zn	103.4434	84	Th	6.4151438	24.29
V	249.7987	142.14	U	4.7362329	5.14
Co	7.505938	11.74	Sc	7.3456199	6.59
Ni	48.95989	55.86	Zr	80.612914	152.57
Cu	27.54599	29	Y	15.418267	10.857
Mo	18.41792	27.43	Hf	2.3445788	6.0715
Ta	0.691606	0.943			

Table 5: Nutrient rich elements from throughout seven EF cores. The volcanic ash beds and whole rock EF samples have similar concentrations of nutrient elements.

Well no.	Cr	Zn	V	Co	Ni	Cu	Mo	Pb	Th	U	Sc	Zr	Y	Hf	Ta
	(ppm)	(ppm)	(ppm)	(ppm)	(ppm)	(ppm)	(ppm)	(ppm)	(ppm)	(ppm)	(ppm)	(ppm)	(ppm)	(ppm)	(ppm)
	25.14	32.69	43.64	3.87	11.27	9.36	0.82	3.90	3.26	3.05	2.04	33.41	11.20	1.53	0.25
	17.81	37.07	43.50	3.38	10.55	9.01	1.40	3.24	3.00	1.96	2.43	39.41	8.75	1.76	0.29
Well 3	58.02	88.09	165.44	3.90	30.09	14.03	5.69	2.75	2.00	2.43	3.23	33.72	10.38	1.60	0.21
	37.44	117.50	207.41	3.42	31.53	16.45	8.47	3.72	5.42	4.08	2.68	49.47	10.40	2.03	0.31
	54.95	63.21	151.79	3.85	28.12	17.12	4.10	2.22	3.17	2.73	3.91	43.86	9.55	1.77	0.26
	53.89	58.37	147.54	3.70	26.19	16.02	3.50	1.78	2.71	2.66	3.59	44.07	9.29	1.78	0.23
	50.26	66.63	153.51	3.66	25.54	18.49	3.91	2.21	2.45	2.26	3.64	38.78	8.45	1.73	0.22
	41.66	59.18	114.98	4.04	21.89	14.68	2.59	2.13	2.70	1.85	4.37	45.40	9.18	1.83	0.24
	42.42	61.05	123.68	4.08	23.99	16.10	3.24	2.05	2.67	1.85	4.19	43.37	8.93	1.80	0.25
	46.31	78.88	148.55	4.44	28.38	15.43	4.26	1.73	3.54	2.45	4.43	47.31	10.70	1.83	0.32
	44.97	77.53	140.87	4.47	25.42	17.45	4.16	2.50	3.50	2.56	4.42	52.48	10.55	2.03	0.32
	42.74	77.43	116.09	4.68	20.88	18.78	3.51	8.70	3.02	2.48	3.73	50.42	9.85	2.04	0.29
	44.23	65.36	349.99	4.70	34.03	19.69	24.01	2.14	2.75	4.39	3.46	41.46	8.00	1.66	0.28
	56.04	87.22	382.86	5.48	38.24	15.97	28.85	2.02	3.30	4.75	4.13	48.87	9.72	1.83	0.31
	17.55	35.21	150.27	2.52	18.07	14.57	11.43	2.81	1.24	2.32	1.45	21.08	5.14	1.10	0.12
	53.42	98.56	432.61	6.47	49.07	19.05	37.84	7.63	3.34	5.68	3.88	54.69	10.89	1.95	0.38
	39.13	73.06	252.00	4.78	31.98	18.09	20.11	4.56	2.82	3.34	3.12	44.65	8.21	1.71	0.30
	52.04	134.77	513.72	7.46	58.52	18.14	45.86	1.81	4.03	7.29	4.28	59.54	11.43	2.08	0.49
	33.11	77.82	327.04	5.06	43.17	16.19	32.53	1.78	2.37	4.85	2.80	39.74	8.46	1.53	0.26
	39.69	92.63	357.48	5.35	47.96	18.36	35.86	1.58	2.57	5.20	3.01	42.26	8.94	1.57	0.31
	52.35	73.53	189.91	4.74	35.31	16.18	25.36	1.09	3.10	3.77	3.43	45.02	10.00	1.69	0.34
	47.43	96.40	353.94	6.53	48.09	20.82	38.45	1.35	3.75	5.87	3.98	54.96	11.30	1.93	0.40
	53.70	62.83	155.53	4.45	34.04	18.76	21.47	1.72	3.87	4.88	3.70	55.26	13.72	2.04	0.38
	49.48	72.10	159.37	4.51	32.31	19.09	22.77	1.47	4.22	5.21	3.85	56.01	14.49	1.99	0.40
	59.68	89.56	216.21	5.25	36.28	16.31	30.88	1.36	3.76	5.26	4.05	56.97	13.22	1.98	0.40
	38.54	57.86	163.72	3.93	24.63	18.68	18.57	3.78	4.22	4.53	3.08	47.72	11.88	1.84	0.33
	46.06	72.30	214.08	4.70	28.77	18.53	23.60	3.68	4.46	5.16	3.89	54.26	13.45	1.93	0.37
	53.54	78.63	231.17	5.06	32.45	18.99	28.27	2.13	5.11	5.30	4.05	57.48	13.04	2.06	0.45
	50.57	81.21	222.88	5.13	35.13	16.65	25.90	2.00	4.75	5.11	3.79	56.49	13.28	1.97	0.38
	50.96	102.55	379.42	6.69	47.29	20.40	37.91	1.95	4.09	6.53	4.37	54.78	12.14	1.99	0.43
	48.49	99.35	369.21	6.79	46.52	20.11	38.02	1.63	4.14	6.48	4.49	54.32	11.81	2.01	0.44
	66.88	88.81	173.43	5.39	34.09	19.09	27.25	3.39	5.75	5.54	4.88	62.36	15.09	2.26	0.52
	64.28	90.83	216.61	4.91	36.65	19.99	30.06	3.01	9.69	5.75	4.00	64.09	12.43	2.61	0.65
	67.51	92.36	210.44	4.85	37.40	19.38	29.85	2.27	8.89	5.71	4.36	68.92	12.74	2.67	0.62
	80.07	93.99	217.52	5.62	44.57	21.90	34.85	1.90	4.98	4.34	4.61	62.13	12.55	2.13	0.56
	77.72	98.91	225.71	5.17	38.72	19.01	34.07	1.85	5.72	4.76	4.42	62.84	12.98	2.25	0.60
	56.47	118.33	425.23	5.64	48.25	20.14	35.25	2.13	3.49	4.86	3.71	47.42	10.22	1.76	0.38

Well no.	Contd.														
	Cr (ppm)	Zn (ppm)	V (ppm)	Co (ppm)	Ni (ppm)	Cu (ppm)	Mo (ppm)	Pb (ppm)	Th (ppm)	U (ppm)	Sc (ppm)	Zr (ppm)	Y (ppm)	Hf (ppm)	Ta (ppm)
	77.51	93.66	218.94	5.34	42.46	19.43	25.38	2.03	4.14	3.90	4.66	52.69	11.79	1.97	0.45
	80.83	91.57	173.53	5.57	36.25	20.03	21.29	2.26	4.62	3.91	4.70	56.54	12.83	2.10	0.50
	83.20	99.96	196.08	5.98	31.41	15.39	18.72	1.59	5.53	4.37	5.63	74.62	16.29	2.51	0.55
	117.15	138.29	474.28	6.41	37.67	17.91	24.87	2.09	7.39	11.83	6.61	98.18	24.29	3.33	0.72
	118.91	148.73	403.19	5.87	30.37	13.36	19.56	2.49	6.67	10.25	6.36	90.43	21.91	2.98	0.67
Well 12	11.55	21.30	40.44	1.60	8.15	8.86	1.61	2.97	0.54	0.94	0.77	10.65	3.08	0.26	0.07
	16.47	37.49	84.69	1.96	10.45	11.39	2.92	5.12	0.82	1.07	0.92	13.37	3.37	0.34	0.10
	93.77	211.54	170.58	4.82	39.90	20.23	3.10	2.93	3.14	2.75	5.03	50.20	11.02	1.43	0.35
	93.14	52.02	200.99	4.62	34.67	20.47	2.77	3.35	3.35	2.36	5.20	54.97	10.84	1.59	0.39
	88.45	71.21	190.44	4.86	34.52	21.29	3.20	3.48	3.65	2.94	5.14	56.08	10.99	1.68	0.39
	91.94	48.66	138.82	5.66	35.14	28.04	2.14	3.90	3.94	2.26	6.15	67.13	12.82	2.00	0.53
	68.43	93.91	396.71	6.89	39.37	24.15	21.50	4.67	5.67	4.18	6.91	68.10	11.93	2.02	0.62
	69.03	76.13	345.41	7.05	40.68	23.36	21.03	3.70	5.99	4.28	6.68	73.53	13.14	2.07	0.69
	79.88	270.34	310.54	6.60	42.06	21.17	16.34	3.27	5.30	3.93	6.56	72.54	12.19	1.98	0.60
	79.88	114.60	476.58	8.14	45.52	25.59	22.28	3.82	7.04	4.51	7.94	88.03	13.22	2.34	0.87
	82.58	104.79	431.89	8.16	43.41	22.65	24.19	4.64	7.51	4.63	8.20	97.91	13.95	2.50	0.93
	79.62	109.36	463.33	8.49	49.09	22.67	28.95	2.77	6.57	6.04	7.77	85.84	13.80	2.27	0.76
	71.31	97.42	488.89	7.30	57.00	28.95	33.26	73.44	5.32	7.64	5.70	77.38	12.71	2.06	0.58
	75.43	128.31	486.40	8.61	64.33	27.84	44.80	2.56	5.09	8.01	5.81	69.42	13.34	1.89	0.60
	64.02	92.69	358.13	6.57	50.96	21.15	30.24	2.77	4.37	5.39	4.57	63.59	10.94	1.63	0.48
	45.94	67.87	212.99	4.57	42.45	22.04	18.44	3.06	2.69	3.72	2.81	41.25	8.40	1.06	0.30
	72.00	159.70	495.71	9.80	84.97	30.53	47.52	2.80	4.56	8.74	4.74	70.23	12.71	1.84	0.56
	67.46	107.75	405.71	7.91	68.93	27.96	37.49	1.80	4.27	7.08	4.81	59.96	11.23	1.57	0.49
	83.95	80.84	111.10	5.68	49.51	26.73	20.18	2.29	4.64	4.06	4.82	57.59	13.71	1.57	0.48
	83.84	83.75	116.48	5.55	50.08	25.81	20.81	2.77	4.72	4.08	4.86	56.53	13.69	1.55	0.50
	91.55	84.45	105.20	5.38	39.86	17.43	15.66	2.34	5.20	5.02	5.45	68.31	15.04	1.88	0.53
	91.03	88.53	100.59	5.49	41.45	18.74	15.94	2.94	5.07	4.99	5.41	65.78	15.09	1.79	0.50
	104.78	87.76	110.58	5.16	37.27	14.68	14.67	2.30	5.22	4.00	5.79	61.07	15.12	1.70	0.55
	101.50	88.13	102.78	5.37	44.17	16.15	14.98	1.93	5.32	4.10	5.61	61.54	15.04	1.73	0.54
	98.91	97.73	120.93	5.42	34.07	13.59	10.83	1.77	7.27	4.01	6.00	73.24	15.85	2.11	0.68
	101.90	90.94	106.65	5.61	41.76	16.61	15.22	2.06	5.79	4.58	5.76	63.77	16.46	1.85	0.54
	102.85	89.05	109.96	5.57	39.69	15.15	12.78	1.93	6.29	4.17	5.91	69.08	15.95	1.96	0.63
	126.30	123.28	177.20	6.67	40.74	16.12	12.26	2.26	7.30	4.61	7.27	79.75	16.75	2.35	0.73
	129.75	188.51	497.37	6.46	50.90	17.42	22.21	1.74	6.13	11.00	6.76	82.97	22.77	2.29	0.56
	140.54	147.81	457.23	8.16	61.34	22.85	19.32	3.41	9.23	14.70	9.44	102.25	24.61	3.18	0.72
	14.97	15.78	28.12	2.49	9.50	11.37	1.02	6.16	1.91	0.98	1.91	20.76	6.24	0.58	0.16

Contd.

Well no.	Cr (ppm)	Zn (ppm)	V (ppm)	Co (ppm)	Ni (ppm)	Cu (ppm)	Mo (ppm)	Pb (ppm)	Th (ppm)	U (ppm)	Sc (ppm)	Zr (ppm)	Y (ppm)	Hf (ppm)	Ta (ppm)
Well 16	54.28	71.68	125.16	4.83	24.14	14.88	1.89		3.00	1.91	3.76	40.05	9.44	1.84	0.40
	86.72	65.47	141.26	4.87	28.98	15.66	1.55	3.45	3.34	2.00	5.08	55.09	11.51	2.08	0.47
	78.66	66.45	135.12	4.93	26.43	14.46	1.60	3.77	3.20	2.07	4.84	53.58	11.08	2.17	0.44
	77.00	70.07	141.76	5.33	26.24	14.57	2.35	3.42	3.53	2.48	5.29	60.09	12.60	2.12	0.47
	84.31	70.95	132.71	4.57	24.61	12.67	1.37	3.52	3.44	2.21	5.15	53.37	12.33	2.08	0.40
	76.32	99.26	339.97	6.68	36.90	13.86	15.79	2.57	5.57	3.48	6.62	75.87	12.77	2.59	0.70
	70.88	86.85	327.49	6.39	35.43	13.86	14.79	3.22	5.30	3.52	6.46	73.09	12.43	2.36	0.66
	68.99	108.39	327.89	6.51	37.21	13.87	14.05	2.70	5.19	3.29	6.48	71.31	11.87	2.45	0.66
	71.18	93.12	407.48	7.77	40.83	22.01	25.48	3.97	6.05	4.39	7.18	72.89	13.04	2.51	0.66
	70.36	87.50	355.56	7.79	42.60	23.02	21.06	3.71	6.18	4.15	7.31	74.70	12.76	2.42	0.69
	71.16	92.52	418.64	8.77	44.70	23.39	29.10	3.54	6.30	5.35	7.99	78.03	13.02	2.63	0.72
	73.69	91.81	390.47	7.47	37.38	18.33	21.27	3.75	5.00	4.28	6.49	67.82	11.63	2.34	0.58
	55.46	85.46	365.82	7.22	38.25	20.88	22.32	3.52	3.72	4.28	5.36	54.01	10.13	1.94	0.42
	63.41	115.07	456.77	7.78	48.47	23.83	28.07	3.58	4.43	5.39	5.90	59.71	11.26	2.11	0.48
	71.70	92.50	446.91	8.12	54.16	22.75	27.95	2.84	5.42	5.60	6.57	72.31	15.49	2.42	0.58
	66.32	94.02	450.03	7.66	40.74	14.78	25.00	3.90	5.49	5.50	6.25	72.75	13.82	2.48	0.61
	66.37	97.01	356.36	6.92	38.20	15.76	20.17	3.67	5.14	4.54	6.35	69.76	12.47	2.41	0.58
	68.04	111.98	422.47	7.39	54.38	23.39	33.64	2.89	4.43	6.54	5.47	60.87	12.10	2.09	0.51
	75.43	136.33	452.45	7.66	63.23	25.84	44.87	2.03	4.15	7.52	5.20	58.93	12.06	2.09	0.50
	64.98	116.92	380.81	6.73	60.66	29.33	37.71	1.92	3.82	6.09	4.76	54.54	11.47	2.00	0.44
	65.67	110.24	337.35	6.48	51.78	26.94	32.99	3.14	4.15	5.20	4.62	58.65	11.79	2.09	0.46
	58.68	83.67	265.21	5.41	45.15	23.65	27.01	1.87	3.79	5.00	4.02	52.67	11.08	1.90	0.41
	53.71	115.89	421.66	7.22	57.39	26.64	36.43	2.40	4.11	7.03	4.42	63.44	11.48	2.09	0.48
	62.68	136.13	492.69	8.24	56.99	17.60	43.95	2.32	4.41	8.30	4.84	64.33	12.31	2.19	0.51
	62.46	153.29	553.46	9.19	76.56	25.87	53.44	2.54	4.18	9.84	4.95	57.34	11.87	2.09	0.52
	64.57	131.09	508.19	7.88	56.94	20.04	43.91	2.58	4.51	8.06	5.16	66.99	11.86	2.33	0.54
	60.30	138.90	507.68	8.22	62.05	22.65	46.64	2.47	4.49	8.53	5.11	70.87	13.84	2.33	0.61
	77.12	121.95	415.83	8.24	48.70	17.81	37.91	2.74	5.58	7.33	5.88	75.14	13.40	2.53	0.73
	78.47	97.49	151.62	6.08	39.07	16.52	21.09	2.64	6.97	5.36	5.37	91.70	15.56	3.11	0.70
	70.54	93.51	195.99	5.72	42.88	15.35	21.79	1.49	4.44	5.33	4.87	59.01	13.12	2.09	0.46
	68.79	81.39	169.53	5.35	40.44	17.04	17.87	2.12	4.29	5.00	4.84	59.99	13.10	2.13	0.42
	79.60	91.62	143.77	5.78	37.59	16.36	15.77	2.44	6.43	5.47	5.76	76.72	16.69	2.57	0.63
	75.15	87.95	158.46	5.20	37.99	16.76	19.83	2.35	4.85	4.74	5.03	61.38	14.40	2.19	0.52
	99.82	97.82	159.87	5.32	40.74	19.62	20.54	2.58	5.72	4.69	5.67	67.26	15.55	2.30	0.59
	81.93	78.18	123.75	4.98	38.64	19.14	15.11	2.59	5.21	4.16	4.76	59.84	14.95	2.16	0.52
	99.56	93.84	139.55	5.53	41.12	17.74	17.01	2.32	5.75	4.55	5.69	65.33	15.94	2.33	0.60
	109.05	105.82	209.87	6.29	45.10	20.88	22.97	3.06	5.75	4.88	6.34	72.52	15.68	2.49	0.65

Contd.

Well no.	Cr (ppm)	Zn (ppm)	V (ppm)	Co (ppm)	Ni (ppm)	Cu (ppm)	Mo (ppm)	Pb (ppm)	Th (ppm)	U (ppm)	Sc (ppm)	Zr (ppm)	Y (ppm)	Hf (ppm)	Ta (ppm)
	125.65	127.60	232.91	6.86	43.36	15.99	16.38	2.49	6.90	5.84	6.83	89.97	20.65	3.02	0.73
	155.28	160.89	358.78	7.13	43.90	14.78	16.58	2.14	6.73	8.68	7.16	91.98	23.69	3.05	0.68
	145.51	151.33	310.39	6.69	40.78	15.63	17.14	2.45	6.66	7.54	6.54	83.68	21.30	2.83	0.70
	94.75	113.22	284.83	5.84	41.96	12.97	20.00	1.82	5.77	7.40	6.04	70.44	16.51	2.50	0.59
	107.02	148.66	482.03	7.12	49.58	20.08	23.68	2.48	7.78	7.74	8.49	82.80	17.95	2.71	0.67
	129.32	140.24	690.49	6.95	56.36	19.15	29.23	2.33	6.87	11.11	7.77	76.38	18.63	2.67	0.61
	114.25	138.18	569.06	6.33	47.41	18.30	26.39	2.46	6.95	8.98	8.07	81.13	18.24	2.90	0.60
	97.15	113.63	507.99	8.14	49.31	20.19	26.58	2.74	7.81	6.37	8.80	84.53	16.89	2.94	0.72
	97.93	129.55	453.96	7.95	51.55	22.00	27.33	2.94	7.49	7.48	8.65	84.02	18.34	2.88	0.72
	14.92	20.69	30.46	2.81	7.60	8.58	0.87	6.60	2.10	0.96	2.20	24.56	7.39	1.26	0.17
	17.39	27.44	35.96	3.63	9.61	8.17	0.43	4.56	2.66	0.83	3.12	28.15	9.54	1.43	0.22
	18.51	27.60	41.54	4.22	11.73	8.65	0.80	6.25	3.40	1.12	3.06	32.65	9.68	1.63	0.27
	24.06	31.15	55.54	5.28	16.10	10.60	1.67	5.22	3.78	1.41	4.01	35.87	11.21	1.59	0.30
	18.78	28.21	40.58	4.33	11.13	10.05	0.52	5.75	3.45	0.99	3.56	42.18	10.65	1.80	0.26
	22.07	31.61	47.27	9.43	15.07	9.51	0.70	5.47	3.95	1.16	3.95	42.54	11.80	1.75	0.31
Well 17	74.62	97.49	359.23	7.77	49.67	33.98	20.96	10.14	6.34	4.01	7.44	77.81	13.24	2.01	0.72
	62.70	87.11	288.50	6.49	43.66	28.57	17.60	9.43	6.22	3.46	6.29	69.55	12.05	1.94	0.63
	68.22	88.50	352.37	7.61	50.55	33.72	21.93	10.46	6.18	3.88	6.95	73.05	12.40	1.99	0.71
	87.89	107.81	303.37	7.63	51.48	34.29	22.57	6.82	6.62	3.73	7.68	79.94	14.04	2.16	0.80
	75.46	98.18	256.77	6.84	48.81	35.00	22.01	5.56	5.43	4.92	6.50	68.89	15.81	1.76	0.59
	80.82	134.05	377.75	7.87	63.23	36.70	29.89	4.55	5.29	5.75	6.53	67.50	13.72	1.79	0.55
	92.21	104.98	243.04	6.87	55.47	34.48	22.61	4.43	5.85	5.39	6.66	76.14	14.73	1.94	0.61
	81.59	91.34	200.92	5.79	51.66	35.06	25.52	3.74	4.33	5.52	5.43	60.25	13.50	1.52	0.45
	79.91	92.41	224.74	5.81	53.89	36.11	25.69	7.75	4.14	4.81	5.23	59.71	13.79	1.45	0.46
	75.40	110.23	178.14	5.10	50.83	34.54	27.10	6.92	3.91	4.24	4.33	56.27	11.88	1.43	0.41
	79.79	102.23	271.23	6.48	61.58	37.25	31.22	6.12	4.27	5.24	5.04	57.72	13.11	1.44	0.48
	77.75	152.92	537.62	9.56	93.93	47.74	53.69	5.57	4.66	8.77	5.69	64.30	13.36	1.69	0.56
	80.88	100.45	256.77	6.86	61.39	42.86	26.64	4.66	4.87	5.07	5.75	63.64	13.85	1.65	0.54
	88.90	126.68	173.25	6.81	58.65	38.53	22.37	4.81	5.46	5.22	6.19	72.09	15.52	1.92	0.60
	87.67	100.91	207.68	6.92	60.81	39.99	22.65	4.52	5.35	5.20	6.09	70.02	15.19	1.84	0.56
	94.53	106.70	154.74	7.76	59.61	41.13	16.54	5.84	7.58	5.27	7.49	79.57	20.34	2.35	0.77
	107.21	132.03	189.16	7.60	58.05	33.60	19.26	5.29	7.00	5.11	7.03	79.07	17.49	2.20	0.70
	121.31	131.53	218.71	7.30	43.01	24.90	13.84	3.70	6.64	5.46	7.23	81.97	19.58	2.29	0.68
	90.74	124.77	304.52	6.83	70.63	41.03	22.37	7.18	5.14	6.90	5.64	67.75	16.31	1.85	0.53
	109.43	125.77	438.39	8.89	72.89	42.70	28.69	9.74	7.18	9.51	8.69	81.11	19.37	2.32	0.70

Contd.

Well no.	Cr (ppm)	Zn (ppm)	V (ppm)	Co (ppm)	Ni (ppm)	Cu (ppm)	Mo (ppm)	Pb (ppm)	Th (ppm)	U (ppm)	Sc (ppm)	Zr (ppm)	Y (ppm)	Hf (ppm)	Ta (ppm)
Well 19	55.96	56.89	213.67	4.09	40.58	21.44	4.68	6.40	2.59	2.64	3.80	37.13	8.64	1.06	0.33
	75.32	74.81	257.48	4.97	47.19	26.14	4.71	9.41	3.21	3.10	4.85	48.78	10.35	1.22	0.42
	73.81	56.82	146.62	10.18	40.00	22.36	2.77	6.85	7.27	2.65	7.97	114.95	16.81	3.03	0.87
	49.22	84.97	298.17	7.04	54.60	30.59	15.08	4.60	5.59	4.53	6.74	69.59	12.67	2.04	0.55
	82.49	92.98	216.79	8.32	49.91	28.75	10.05	5.89	7.55	3.56	8.99	97.75	16.95	2.71	0.83
	82.69	88.83	224.06	8.28	46.81	27.97	10.25	4.93	7.25	3.51	8.78	97.01	17.05	2.72	0.83
	97.70	87.99	237.45	8.39	49.31	28.43	8.91	5.02	7.64	3.56	9.09	102.11	17.38	2.83	0.85
	97.40	218.99	249.80	7.70	44.95	27.29	13.40	7.51	7.12	3.38	8.60	85.56	16.25	2.34	0.78
	93.56	72.62	243.67	8.33	51.56	27.66	13.43	6.05	7.09	3.30	8.54	93.77	15.92	2.60	0.79
	90.56	61.93	243.78	8.26	49.54	29.36	11.96	7.30	7.07	3.31	8.47	85.98	15.49	2.40	0.79
	97.73	68.35	266.41	7.93	47.92	28.08	13.96	7.32	7.62	3.32	9.13	90.72	16.63	2.54	0.85
	101.03	177.40	263.50	8.20	50.45	29.81	15.41	6.59	7.38	3.50	9.09	89.43	16.38	2.49	0.82
	100.37	60.74	253.02	8.14	49.59	25.76	16.27	7.26	7.80	3.29	9.03	84.18	15.15	2.42	0.87
	105.17	52.37	204.75	8.88	48.45	24.66	14.71	7.32	8.00	3.03	9.53	92.07	14.95	2.63	0.95
	93.36	60.95	253.74	8.81	50.77	30.28	17.34	7.92	7.93	3.33	8.92	85.61	15.62	2.50	0.85
	95.81	63.93	253.85	8.21	49.25	25.74	16.69	9.66	7.83	3.33	9.21	86.14	15.78	2.51	0.88
	98.27	69.24	248.66	8.31	48.97	28.46	16.26	8.26	8.22	3.23	9.62	88.78	15.74	2.53	0.90
	99.17	59.44	254.26	8.03	48.21	28.35	16.08	9.76	8.02	3.19	9.34	90.50	15.42	2.55	0.90
	102.92	161.35	243.47	9.13	50.85	32.67	17.33	7.58	8.48	3.23	9.65	94.42	15.77	2.72	0.98
	89.59	68.91	243.47	7.56	47.77	27.19	13.46	5.53	7.15	3.23	8.42	83.90	14.95	2.42	0.80
	102.93	58.78	237.34	8.35	44.98	28.39	13.63	5.56	8.41	3.09	9.94	93.48	16.15	2.72	0.98
	108.30	196.45	242.74	8.58	48.92	29.26	15.33	6.31	8.66	3.27	10.00	96.71	16.34	2.81	1.00
	104.47	54.36	235.89	8.12	46.12	27.64	15.14	6.07	8.52	3.19	9.61	102.42	16.22	2.76	0.97
	103.55	79.30	242.84	8.99	49.58	30.11	17.13	6.77	8.89	3.28	10.04	102.30	16.61	2.78	1.00
	85.89	56.09	258.10	9.56	51.58	26.76	17.81	8.29	7.72	3.54	9.31	87.08	14.27	2.38	0.89
	112.08	77.51	235.06	10.06	51.36	31.39	15.75	8.71	10.54	3.54	11.78	111.88	18.45	3.17	1.12
	102.41	70.95	283.02	9.78	50.37	37.46	19.99	10.36	10.84	4.29	10.92	104.38	17.01	3.14	1.10
	123.55	79.14	230.70	9.44	43.13	25.96	14.51	6.88	10.13	3.81	11.57	111.67	18.66	3.16	1.13
	118.25	74.73	321.12	9.62	52.94	31.63	21.59	7.23	9.85	4.30	11.62	105.25	18.51	3.01	1.05
	107.46	93.97	228.93	9.50	51.93	28.85	18.11	6.21	9.06	3.41	10.82	101.93	16.96	2.84	1.03
	121.71	193.36	255.72	10.31	56.81	29.91	17.74	4.40	10.17	3.97	11.53	112.09	18.27	3.18	1.16
	129.82	66.37	235.16	10.08	57.06	30.77	15.56	4.31	9.98	4.25	11.58	112.83	20.82	3.05	1.10
	133.71	85.63	229.04	10.64	59.28	31.78	14.35	5.45	10.23	4.42	11.90	120.87	20.91	3.24	1.17
	137.61	71.78	233.40	11.73	63.54	33.39	16.11	4.27	9.97	4.27	11.95	115.48	20.38	3.12	1.12
	154.05	74.74	205.68	10.90	64.48	35.91	14.59	5.32	10.80	5.41	12.37	120.76	21.83	3.41	1.15
	144.53	71.87	244.09	9.93	63.92	34.87	15.81	3.77	9.50	5.73	10.76	107.26	21.69	3.09	1.00
	147.56	87.59	238.69	9.49	70.88	36.81	20.91	3.34	7.99	7.92	9.78	100.80	24.48	2.75	0.83

Contd.

Well no.	Cr (ppm)	Zn (ppm)	V (ppm)	Co (ppm)	Ni (ppm)	Cu (ppm)	Mo (ppm)	Pb (ppm)	Th (ppm)	U (ppm)	Sc (ppm)	Zr (ppm)	Y (ppm)	Hf (ppm)	Ta (ppm)
	119.22	185.28	207.65	10.00	60.91	35.91	17.62	8.74	8.02	6.05	9.61	94.55	19.00	2.70	0.83
	127.01	76.93	201.22	8.66	61.29	32.46	18.08	4.32	7.96	6.60	9.28	95.27	20.33	2.65	0.82
	118.90	85.27	145.99	7.87	61.50	35.02	16.69	4.22	6.96	5.79	8.29	79.69	19.07	2.21	0.71
	134.04	310.92	193.95	8.46	70.12	38.61	21.80	3.43	6.22	5.47	8.13	76.81	18.99	2.11	0.67
	114.46	91.95	186.68	7.77	65.83	36.79	22.78	2.73	6.69	5.10	8.00	79.66	17.35	2.26	0.72
	122.25	109.99	161.04	7.26	64.85	35.01	17.30	2.88	6.28	4.58	7.50	83.59	18.98	2.04	0.69
	132.09	131.03	312.91	8.41	72.68	36.11	28.32	3.57	6.38	5.63	7.60	81.96	16.96	2.21	0.73
	127.12	108.30	174.33	7.32	61.75	32.21	19.58	2.94	6.97	4.48	7.39	89.25	17.08	2.50	0.74
	119.98	106.30	172.67	6.61	55.32	24.28	16.61	3.15	6.75	4.30	7.08	83.43	16.25	2.23	0.71
	113.81	128.24	235.68	7.77	60.69	32.68	17.82	3.16	6.81	4.79	7.57	85.43	16.72	2.33	0.74
	121.49	127.25	330.67	8.29	73.10	36.77	24.93	3.14	6.55	6.12	7.49	81.46	17.35	2.22	0.70
	120.09	121.96	164.37	9.58	65.16	33.11	10.30	4.91	7.71	5.13	8.87	96.06	20.56	2.71	0.83
	116.63	114.08	152.64	9.07	58.17	28.41	9.73	3.64	8.63	5.30	9.11	94.44	20.41	2.81	0.88
	129.71	115.98	158.97	9.70	64.54	32.43	11.02	4.44	8.69	5.26	9.03	91.64	21.19	2.62	0.86
	147.56	160.75	282.91	10.50	72.01	25.44	18.76	4.73	7.62	6.87	8.59	100.04	24.54	2.82	0.77
	153.29	201.53	461.77	10.29	99.53	46.47	27.40	2.53	6.99	9.38	8.65	101.04	25.26	2.58	0.69
	114.46	99.82	212.53	8.18	59.61	21.79	17.19	2.54	7.23	4.73	8.38	90.07	17.84	2.58	0.79
	117.06	104.61	226.13	8.45	67.17	36.51	16.38	3.77	7.41	5.19	8.35	86.68	17.93	2.43	0.76
	133.82	133.23	401.88	9.79	82.17	36.37	25.36	3.22	8.86	8.17	9.23	99.92	19.13	3.05	0.79
	131.12	134.62	285.72	9.78	68.43	30.46	18.51	3.85	8.43	7.74	9.02	94.68	18.90	2.80	0.80
	123.22	125.95	225.20	9.60	66.22	29.82	15.05	4.31	8.83	6.50	8.72	94.09	20.01	2.74	0.84
	147.99	122.76	239.83	9.82	74.38	34.15	14.92	3.39	8.89	5.79	8.70	89.95	20.26	2.67	0.84
	140.31	133.53	267.86	9.44	63.91	31.39	16.59	5.88	8.14	6.14	9.10	97.70	20.08	2.75	0.79
	132.20	126.05	234.54	9.31	68.22	35.00	18.64	4.04	7.89	6.34	8.66	89.40	18.90	2.49	0.79
	108.41	103.61	227.17	8.06	55.16	27.22	17.32	8.42	6.62	5.33	7.81	77.83	16.03	2.11	0.63
Well 20	63.87	55.56	124.23	9.26	32.79	22.93	2.39	4.01	5.98	2.20	7.39	101.35	15.21	2.64	0.76
	76.48	56.75	179.98	8.50	44.86	27.72	7.89	2.17	6.06	3.79	7.50	99.14	15.85	2.55	0.75
	62.43	71.68	219.17	7.90	48.84	27.94	11.43	2.47	5.78	3.92	7.01	85.66	14.50	2.24	0.65
	59.34	75.84	287.57	7.06	53.62	32.49	14.71	2.20	5.55	4.27	6.64	76.68	13.51	2.03	0.57
	59.94	152.34	308.78	7.20	55.97	30.44	15.45	2.23	5.54	4.54	7.20	75.97	13.40	2.00	0.57
	76.23	94.27	284.29	7.23	55.33	29.86	10.51	2.58	5.94	3.81	7.50	84.52	14.68	2.19	0.66
	124.22	112.77	270.54	8.71	42.57	23.60	6.95	3.45	6.66	3.67	8.42	103.76	17.89	2.66	0.84
	90.72	114.32	214.12	8.62	50.06	30.97	11.08	2.95	7.81	4.03	9.78	113.40	18.71	2.91	0.97
	92.54	55.24	213.13	8.07	47.73	27.77	13.54	3.37	7.12	3.10	8.94	96.23	15.99	2.45	0.86
	89.27	70.69	198.38	8.22	45.42	29.98	11.70	3.73	7.11	3.13	9.10	103.46	16.09	2.57	0.90
	96.51	75.16	221.99	7.67	48.18	27.97	12.11	3.25	6.96	3.01	8.92	93.15	15.51	2.36	0.84

Contd.

Well no.	Cr (ppm)	Zn (ppm)	V (ppm)	Co (ppm)	Ni (ppm)	Cu (ppm)	Mo (ppm)	Pb (ppm)	Th (ppm)	U (ppm)	Sc (ppm)	Zr (ppm)	Y (ppm)	Hf (ppm)	Ta (ppm)
98.30	67.79	219.44	8.06	45.64	31.07	12.85	3.80	7.66	3.17	9.44	99.34	16.67	2.57	0.88	
104.14	61.29	215.34	7.98	44.94	31.00	12.14	4.09	7.60	2.99	9.86	101.75	16.51	2.57	0.92	
116.02	60.71	225.32	8.04	46.82	29.92	13.10	3.40	7.36	3.06	9.11	99.24	16.34	2.48	0.87	
103.76	77.28	228.98	8.25	47.44	29.34	16.17	4.01	7.44	2.97	9.45	94.61	16.16	2.34	0.87	
93.62	61.71	205.37	7.44	43.28	26.46	13.10	5.23	6.85	2.68	8.46	89.66	14.48	2.24	0.80	
109.70	52.26	226.32	8.37	45.22	29.20	14.57	5.05	8.05	2.87	10.08	101.65	15.78	2.56	1.00	
113.66	59.29	206.92	7.98	42.28	29.54	11.94	4.14	8.08	2.84	10.49	103.56	16.52	2.61	1.02	
106.40	66.29	193.73	8.46	47.86	28.71	12.63	4.09	8.01	2.90	10.12	103.26	16.45	2.58	0.98	
116.21	56.89	214.34	7.90	44.27	29.49	13.67	4.23	8.40	2.99	10.57	106.27	17.02	2.69	1.05	
112.34	79.71	219.67	8.01	47.69	27.88	14.00	2.75	7.69	3.05	9.93	100.64	16.59	2.55	0.95	
108.29	60.16	204.37	7.96	44.83	23.23	13.49	2.34	7.53	2.88	9.89	101.45	16.14	2.51	0.92	
104.33	76.97	213.90	8.15	44.86	35.75	13.18	4.04	7.74	2.97	10.21	105.06	16.70	2.62	0.89	
22.15	86.43	48.68	4.16	8.51	37.60	6.37	30.75	19.73	6.66	6.28	222.42	27.25	6.50	1.51	
94.14	41.96	377.44	4.65	29.27	5.33	24.72	3.30	7.69	4.03	9.56	113.97	19.27	2.59	1.01	
109.94	163.07	345.61	9.76	59.21	35.45	21.60	4.43	8.39	4.89	11.25	103.34	16.22	2.71	1.05	
119.19	75.38	212.63	9.80	44.52	29.97	11.85	4.56	10.01	3.12	12.81	128.97	19.82	3.37	1.29	
112.17	84.25	194.38	9.06	39.43	23.98	10.86	5.35	10.17	3.44	11.99	134.49	17.98	3.38	1.26	
115.53	93.28	204.73	10.87	44.78	28.20	14.80	6.30	11.42	3.95	14.06	132.40	22.12	3.51	1.23	
157.50	72.99	297.43	10.60	46.70	35.04	14.26	5.81	11.64	3.81	14.09	137.61	20.09	3.73	1.31	
145.51	65.67	245.23	12.22	55.69	36.71	15.29	5.00	10.29	3.20	12.72	138.97	18.39	3.42	1.39	
114.61	81.80	176.90	10.65	51.57	27.15	14.63	5.71	9.79	3.59	12.56	123.65	20.41	3.19	1.21	
188.90	86.46	310.56	12.46	55.29	42.31	21.93	6.05	13.13	4.13	15.87	149.39	19.61	3.81	1.38	
133.31	65.49	266.71	10.90	53.96	44.20	29.40	6.27	10.93	3.88	13.40	124.70	14.57	3.30	1.32	
86.40	34.24	297.65	8.38	54.97	31.48	22.61	5.37	6.87	4.42	10.45	84.46	14.42	2.13	0.82	
161.16	154.10	249.91	12.11	54.23	34.30	14.10	6.44	12.78	4.87	14.76	152.93	23.87	3.79	1.53	
172.54	77.89	259.70	12.28	71.16	41.38	22.52	4.18	11.42	3.17	13.49	144.70	14.26	3.53	1.44	
129.65	61.15	417.28	11.34	65.49	38.90	30.98	4.29	10.51	6.04	13.39	133.24	14.23	3.42	1.46	
190.32	59.00	302.10	13.11	71.58	48.91	35.81	3.14	9.85	5.14	13.86	118.65	14.19	3.04	1.09	
173.35	97.76	178.46	9.89	61.06	41.01	4.91	3.00	10.62	4.24	12.81	140.32	18.47	3.60	1.29	
128.54	57.76	278.84	9.73	58.26	30.56	15.81	2.96	8.12	4.59	12.29	118.55	14.19	2.96	1.21	
145.71	1344.70	235.00	5.52	25.84	9.30	85.99	0.85	6.79	4.79	10.61	95.53	12.82	2.34	0.73	
206.78	126.16	202.06	9.22	72.78	41.36	18.24	1.37	8.19	7.63	11.69	128.76	35.91	2.80	0.86	
132.30	79.37	363.64	7.90	103.62	232.36	30.02	23.96	8.28	9.22	8.04	95.05	15.14	2.36	0.75	
181.18	94.92	296.42	12.95	57.53	42.59	22.87	7.28	13.00	3.66	15.06	149.07	17.26	3.70	1.34	
154.58	124.08	181.42	8.53	62.50	35.28	19.20	1.61	6.85	4.59	9.22	94.11	19.43	2.37	0.79	
124.78	87.21	205.28	10.82	55.41	66.91	19.92	3.73	9.05	4.44	11.62	115.74	17.06	2.94	1.07	
144.29	128.54	130.50	8.97	69.76	40.15	12.03	1.47	6.32	6.13	8.61	94.26	21.99	2.20	0.67	

Contd.

Well no.	Cr (ppm)	Zn (ppm)	V (ppm)	Co (ppm)	Ni (ppm)	Cu (ppm)	Mo (ppm)	Pb (ppm)	Th (ppm)	U (ppm)	Sc (ppm)	Zr (ppm)	Y (ppm)	Hf (ppm)	Ta (ppm)
	144.29	128.54	130.50	8.97	69.76	40.15	12.03	1.47	6.32	6.13	8.61	94.26	21.99	2.20	0.67
	142.33	115.96	180.98	8.94	56.34	29.05	15.77	1.87	7.72	4.64	10.06	101.85	19.99	2.54	0.88
	138.60	141.00	138.18	9.04	71.62	36.89	16.03	1.94	8.25	10.32	9.02	103.13	19.53	2.76	0.80
	115.22	153.27	135.95	8.40	64.35	44.42	14.47	1.71	9.21	9.90	10.83	103.34	24.07	2.84	0.89
	123.35	108.84	108.35	8.52	70.24	40.52	13.52	1.15	5.55	4.74	7.75	77.38	20.44	1.79	0.59
	130.97	129.27	129.94	8.28	68.58	42.27	20.18	1.29	5.89	4.26	8.10	87.01	16.68	2.13	0.61
	299.67	192.66	452.56	13.88	101.69	73.15	58.69	3.22	11.18	5.39	9.75	144.07	15.48	4.37	1.05
	230.16	168.75	392.02	11.40	84.97	62.81	45.81	3.05	9.11	5.62	11.29	123.76	18.14	3.41	0.93
	138.09	120.84	121.15	7.72	68.34	44.85	22.62	1.20	6.08	4.08	7.82	92.21	18.90	2.18	0.69
	148.35	126.43	216.08	9.20	80.70	46.32	27.62	1.28	6.01	6.88	9.47	88.45	23.09	2.11	0.67
	217.25	176.54	225.65	8.77	82.52	58.24	35.27	3.97	7.65	4.80	10.28	101.11	15.98	2.50	0.97
	114.41	120.93	131.17	7.87	58.83	39.04	8.18	2.44	7.93	4.00	8.22	109.59	16.78	2.92	0.81
	147.51	142.41	259.46	8.04	61.51	36.54	19.80	1.31	7.35	5.01	8.45	97.94	19.29	2.46	0.79
	121.42	130.37	135.28	7.63	55.25	37.82	9.43	2.65	6.11	4.02	7.78	93.99	15.43	2.12	0.72
	116.65	156.48	184.03	10.61	66.04	41.51	8.57	2.31	7.21	5.07	8.82	101.44	17.25	2.54	0.77
	97.61	106.74	162.22	8.62	59.55	29.88	3.44	2.89	5.66	3.18	7.74	84.01	16.04	2.05	0.67
	124.47	133.67	158.32	11.88	68.44	35.21	2.83	3.13	7.91	3.79	10.47	106.15	21.42	2.57	0.91
	216.64	233.15	359.97	10.40	90.40	55.24	37.70	3.01	9.44	8.80	9.71	130.74	22.18	3.14	0.99
	103.43	105.45	116.37	10.81	67.23	33.23	3.47	2.43	7.71	4.91	9.38	92.71	19.02	2.35	0.80
	122.54	154.83	133.50	12.71	69.72	33.00	4.55	2.65	10.06	4.12	10.86	117.72	16.72	3.16	1.11
	147.34	137.88	130.28	11.29	79.05	37.25	7.97	1.69	7.56	5.90	9.27	99.53	24.20	2.42	0.80
	156.48	144.02	157.99	10.75	69.11	38.24	5.30	2.23	7.71	5.06	10.35	94.99	20.98	2.48	0.86
	132.19	189.27	134.17	9.37	61.88	36.40	6.37	2.52	5.68	4.05	8.90	85.26	24.39	2.22	0.67
	102.83	123.41	194.27	13.69	51.53	34.48	5.21	9.78	25.22	4.05	10.42	136.47	10.09	4.16	1.38
	134.73	322.01	238.11	10.39	61.69	48.67	13.99	3.12	7.08	8.97	9.99	110.94	36.24	2.79	0.68
	127.32	197.42	1017.70	4.35	113.07	56.08	41.28	0.49	2.66	11.19	5.46	54.33	12.95	1.17	0.24
	30.98	63.31	172.34	7.85	37.62	21.36	7.20	1.00	2.89	5.75	5.32	49.46	11.13	1.20	0.28
	209.53	147.59	669.11	11.76	81.87	37.62	18.03	2.29	6.33	15.33	8.86	108.44	19.76	2.94	0.62
Well 24	72.48	46.69	136.03	9.80	40.25	38.32	2.93	6.99	4.72	2.42	10.18	69.25	13.93	2.01	0.75
	75.92	64.98	180.44	9.28	41.24	28.79	2.19	8.47	9.32	2.52	11.11	120.40	19.54	3.36	1.32
	76.90	74.15	179.50	10.05	43.62	27.72	3.35	8.99	9.14	2.53	10.97	122.26	19.64	3.40	1.29
	134.73	110.62	205.87	11.55	66.19	35.42	8.58	5.11	10.14	5.41	11.58	110.76	22.00	3.47	1.19
	56.76	44.70	113.83	5.35	28.09	18.82	4.05	7.15	4.79	2.98	5.26	56.15	12.84	1.66	0.45
	45.83	46.33	85.02	7.26	26.36	16.06	1.12	10.49	5.97	1.77	6.47	62.13	14.50	1.92	0.56
	45.47	37.23	86.03	7.37	25.36	15.77	0.98	10.39	5.73	1.69	6.18	59.56	14.29	1.83	0.51
	32.60	34.59	66.29	8.18	25.97	13.26	0.94	7.78	2.38	2.28	2.71	32.83	8.46	0.90	0.24

Table 6: Ti/Zr ratios in seven volcanic ash beds and ~300 whole rock samples from seven subsurface cores of EF black shales.

	DEPTH	Ti (wt%)	Zr(ppm)	Ti/Zr
2N	14067.75-14067.95	0.23	87.00	26.52
7L	13701.40-13701-60	0.28	84.00	33.68
11H	13090.45-13091.35	0.15	177.00	8.74
1F	13814.4	0.29	91.00	31.55
3L	13399.95-13400.15	0.26	206.00	12.86
15R	13916.25-13916.85	0.59	120.00	49.29
14R	13914.75-13914.90	0.43	303.00	14.14
Well 3		0.23	52.58	43.31
Well 12		0.25	63.00	39.96
Well 16		0.26	64.48	40.90
Well 17		0.20	70.32	28.98
Well 20		0.26	108.15	23.83
Well 24		0.25	79.17	31.80
Well 19		0.42	92.91	45.16

Table 7: Re-Os isotope systematics of EF Shale. Notice the high Re concentration. The $^{187}\text{Os}/^{188}\text{Os}$ indicates continental crustal origin.

Samples	Os (ppt)	^{188}Os (ppt)	$1/^{188}\text{Os}$	$^{187}\text{Os}/^{188}\text{Os}$	2s	$^{187}\text{Re}/^{188}\text{Os}$	Re (ppt)	Re(ppb)	$^{187}\text{Os}/^{188}\text{Os}$ initial @t=93*10 ⁶
H13	462.6	61.2	0.0163	3.8306	0.0048	243.1	15564	15.564	3.4536
H15	548.6	72.6	0.0138	3.957	0.0055	214.3	16096	16.096	3.6247
H26	173.3	22.9	0.0436	5.2411	0.0066	619.6	13228	13.228	4.2802
H29	224.4	29.7	0.0337	4.7323	0.0042	492.7	14181	14.181	3.9682
H32	534.7	70.8	0.0141	3.8761	0.0037	211.5	15590	15.59	3.5481
H33	650.9	86.2	0.0116	3.8991	0.0032	185.2	16590	16.59	3.6119
H39	932.1	123.4	0.0081	5.3529	0.0023	155.5	17701	17.701	5.1118

Table 8: Raman Band Separation (RBS/G-D), Total Organic Carbon (TOC), RockEval Pyrolysis (T_{max}) and vitrinite reflectance (Ro%) plotted against the depth of the 300 ft long Well 8 core.

Depths	G-D	TOC%	Tmax	Vro	Depths	G-D	TOC%	Tmax	Vro
13095.17766	252.52	0.833	462	1.156	13255.83756	247.23	2.5	474	1.372
13099.74619	254.25	1.88	462	1.156	13261.92893	251.75	3.59	476	1.408
13119.54315	262.09	1.17	448	0.904	13269.54315	249.64	1.99	474	1.372
13131.72589	251.29	2.62	461	1.138	13272.58883	245.64	4.19	472	1.336
13141.62437	251.82	3.05	457	1.066	13281.72589	243.82	2.59	472	1.336
13167.51269	241.01	3.33	464	1.192	13296.19289	254.45	4.21	464	1.192
13168.27411	254.90	0.685	446	0.868	13302.28426	258.30	4.67	468	1.264
13169.03553	247.73	3.5	463	1.174	13329.69543	257.91	5.49	472	1.336
13178.17259	253.23	4.34	464	1.192	13347.96954	243.41	6.1	472	1.336
13186.54822	247.19	3.86	469	1.282	13349.49239	254.73	4.22	467	1.246
13195.68528	259.18	4.92	462	1.156	13359.39086	246.65	0.517	0	0
13204.06091	254.43	4.14	470	1.3	13373.85787	243.25	0.392	0	0
13210.15228	256.08	0.668	454	1.012	13379.18782	256.68	0.392	0	0
13216.24365	246.12	5.35	465	1.21	13389.08629	251.31	0.205	0	0
13220.05076	251.62	5.33	464	1.192					
13221.5736	264.53	2.76	449	0.922					
13229.94924	248.00	5.19	466	1.228					
13234.51777	257.66	4.34	473	1.354					
13246.70051	260.22	2.63	474	1.372					

Table 9: Raman shift spectra analysis of 34 billets of EF black shale.

Depth	G position	D1 Position	G-D1	G/D ratio	(D1/G)area	FWHM (D)	FWHM (G)	FWHM D/FWHM G	%Vro (G-D)
13096	1602.4	1349.79	252.63	1.19	1.17				1.01
13100	1597.5	1343.08	254.38	1.19	1.89	220.9	58.99	3.74	1.06
13120	1602.4	1340.15	262.27	1.2	1.64	145.7	55.43	2.63	1.29
13132	1601.7	1350.29	251.36	1.19	1.59	191.71	56.88	3.37	0.97
13143	1600.3	1348.37	251.91	1.19	1.2	152.85	55.99	2.73	0.98
13167	1599.9	1358.82	241.1	1.18	1.3	176.88	59.51	2.97	0.67
13169	1599.7	1344.63	255.06	1.19	2.04	227.33	59.05	3.85	1.08
13170	1604.4	1356.46	247.89	1.18	1.98	223.43	61.84	3.61	0.87
13179	1600.2	1346.79	253.37	1.19	1.87	215.57	58.87	3.66	1.03
13187	1598	1350.77	247.27	1.18	2.01	235.23	67.91	3.46	0.85
13196	1600.2	1340.77	259.39	1.19	1.27	158.43	53.19	2.98	1.2
13205	1600.5	1345.93	254.56	1.19	1.95	238.16	69.29	3.44	1.06
13211	1602.3	1346.07	256.24	1.19	1.66	201.65	53.79	3.75	1.11
13217	1599.9	1353.64	246.29	1.18	1.85	223.26	61.8	3.61	0.82
13221	1599.7	1347.9	251.84	1.19	1.86	220.41	58.64	3.76	0.98
13223	1599.1	1334.41	264.68	1.2	1.17	277.59	60.37	4.6	1.36
13230	1599.4	1351.19	248.16	1.18	1.37	176.52	58.61	3.01	0.88
13236	1597.2	1339.46	257.77	1.19	1.36	162.27	54.77	2.96	1.15
13247	1602.4	1342.08	260.35	1.19	2.04	241.37	66	3.66	1.23
13256	1595.8	1348.46	247.37	1.18	1.97	216.67	76.11	2.85	0.85

contd.

Depth	G position	D1 Position	G-D1	G/D ratio	(D1/G)area	FWHM (D)	FWHM (G)	FWHM D/FWHM G	%Vro (G-D)
13263	1600	1348.13	251.88	1.19	1.88	216.85	58.64	3.7	0.98
13269	1600.4	1350.67	249.71	1.18	1.63	204.49	58.62	3.49	0.92
13273	1599.6	1353.73	245.85	1.18	1.86	225.15	63.79	3.53	0.81
13282	1594.6	1350.57	244	1.18	1.83	200.55	83.47	2.4	0.76
13297	1596.2	1341.6	254.62	1.19	1.89	212.61	58.36	3.64	1.06
13303	1606.3	1347.86	258.42	1.19	2.04	232.62	65.34	3.56	1.17
13330	1596.8	1338.78	258.06	1.19	1.53	179.18	55.4	3.23	1.16
13349	1599.7	1356.17	243.5	1.18	2	236.67	64.34	3.68	0.74
13350	1600.5	1345.53	254.97	1.19	0.73	103.6	50.68	2.04	1.07
13360	1606.3	1359.43	246.84	1.18	1.3	83.84	52.4	1.6	0.84
13373	1599.7	1356.17	243.5	1.18	2	236.67	64.34	3.68	0.74
13380	1601.6	1344.7	256.94	1.19	1.68	184.11	50.62	3.64	1.13
13389	1600.1	1348.54	251.56	1.19	1.37	166.97	57.48	2.9	0.97

Table 10: U-Pb zircon data of 10 acid volcanic rocks from five complexes within the DT determined from LA-ICP-MS.

Samples	U (ppm)	²⁰⁶ Pb/ ²⁰⁴ Pb	U/Th	Isotope ratios							Apparent ages (Ma)								
				²⁰⁶ Pb*/ ²⁰⁷ Pb*	± (%)	²⁰⁷ Pb*/ ²³⁵ U*	± (%)	²⁰⁶ Pb*/ ²³⁸ U	± (%)	error corr.	²⁰⁶ Pb*/ ²³⁸ U*	± (Ma)	²⁰⁷ Pb*/ ²³⁵ U	± (Ma)	²⁰⁶ Pb*/ ²⁰⁷ Pb*	± (Ma)	Best age (Ma)	± (Ma)	
G8	Spot 1	141	1130	1.7	24.7994	2.7	0.0555	3.6	0.0100	2.3	0.64	64.1	1.4	54.9	1.9	NA	NA	64.1	1.4
	Spot 2	108	864	1.8	31.2477	9.0	0.0444	9.4	0.0101	2.4	0.26	64.6	1.6	44.1	4.0	NA	NA	64.6	1.6
	Spot 3	94	819	1.2	33.0309	11.6	0.0424	12.0	0.0102	3.2	0.26	65.2	2.1	42.2	5.0	NA	NA	65.2	2.1
	Spot 4	117	134197	1.6	17.2094	2.7	0.0819	3.6	0.0102	2.3	0.65	65.6	1.5	79.9	2.7	533.8	59.1	65.6	1.5
	Spot 5	87	135231	1.5	20.1937	3.3	0.0702	4.1	0.0103	2.4	0.58	66.0	1.6	68.9	2.7	172.5	77.7	66.0	1.6
	Spot 6	82	7355	1.4	19.8363	3.7	0.0716	4.5	0.0103	2.6	0.58	66.1	1.7	70.2	3.1	214.1	85.6	66.1	1.7
	Spot 7	101	3263	1.4	22.5351	5.0	0.0632	5.7	0.0103	2.7	0.48	66.2	1.8	62.2	3.4	NA	NA	66.2	1.8
	Spot 8	125	1331	1.3	26.0521	2.9	0.0547	3.8	0.0103	2.5	0.66	66.3	1.6	54.1	2.0	NA	NA	66.3	1.6
	Spot 9	112	1057	1.8	31.4756	21.2	0.0453	21.3	0.0104	2.3	0.11	66.4	1.5	45.0	9.4	NA	NA	66.4	1.5
	Spot 10	89	2622	1.3	24.4246	4.3	0.0586	5.4	0.0104	3.2	0.59	66.6	2.1	57.8	3.0	NA	NA	66.6	2.1
	Spot 11	92	1315	1.4	25.2296	3.5	0.0567	4.3	0.0104	2.5	0.58	66.6	1.6	56.0	2.3	NA	NA	66.6	1.6
	Spot 12	71	2058	1.6	22.7377	4.7	0.0631	5.8	0.0104	3.3	0.58	66.8	2.2	62.2	3.5	NA	NA	66.8	2.2
	Spot 13	95	5606	1.8	21.8077	2.6	0.0672	3.4	0.0106	2.1	0.63	68.2	1.4	66.1	2.1	NA	NA	68.2	1.4
	Spot 14	146	19361	1.3	17.6585	2.9	0.0843	3.9	0.0108	2.6	0.67	69.2	1.8	82.2	3.1	477.1	63.7	69.2	1.8
	Spot 15	103	1973	1.2	24.7653	8.8	0.0619	9.2	0.0111	2.9	0.31	71.3	2.0	61.0	5.5	NA	NA	71.3	2.0
	Spot 16	75	813	1.1	6.3539	18.8	0.2573	20.0	0.0119	6.8	0.34	76.0	5.1	232.5	41.6	2427.7	321.9	76.0	5.1
	Spot 17	85	5384	1.7	18.6570	3.3	0.1013	9.4	0.0137	8.8	0.94	87.8	7.7	98.0	8.8	354.2	75.3	87.8	7.7
	Spot 18	72	2148	1.4	20.3103	3.9	0.1023	6.0	0.0151	4.6	0.77	96.4	4.4	98.9	5.7	159.1	90.1	96.4	4.4
	Spot 19	90	9325	1.5	16.2112	2.9	0.2082	8.2	0.0245	7.7	0.93	155.9	11.8	192.0	14.4	663.2	62.8	155.9	11.8
	Spot 20	101	16972	2.0	17.5083	2.1	0.2078	6.5	0.0264	6.1	0.94	168.0	10.2	191.7	11.3	496.0	47.4	168.0	10.2
	Spot 21	965	36935	1.3	16.0149	0.8	0.2922	8.1	0.0340	8.1	1.00	215.2	17.1	260.3	18.6	689.3	16.7	215.2	17.1
	Spot 22	104	8595	1.6	14.9048	1.4	0.3172	4.3	0.0343	4.0	0.94	217.4	8.6	279.8	10.4	840.6	30.1	217.4	8.6
	Spot 23	145	4974	1.5	18.1224	4.3	0.2876	10.4	0.0378	9.5	0.91	239.3	22.3	256.6	23.6	419.5	95.9	239.3	22.3
	Spot 24	150	14004	1.8	16.9984	2.3	0.3820	7.7	0.0471	7.4	0.95	296.8	21.4	328.5	21.7	560.8	50.6	296.8	21.4
	Spot 25	97	38036	2.7	15.7045	2.5	0.5039	3.7	0.0574	2.8	0.74	359.9	9.7	414.3	12.7	730.9	53.0	359.9	9.7
	Spot 26	211	27685	1.4	15.6760	2.9	0.8428	6.5	0.0959	5.8	0.89	590.1	32.9	620.7	30.3	734.7	61.7	590.1	32.9
	Spot 27	243	247429	2.8	16.1953	1.1	0.8480	2.3	0.0996	2.0	0.87	612.3	11.6	623.5	10.5	665.4	23.5	612.3	11.6
G9	Spot 1	232	2237	1.5	23.0935	8.0	0.0596	8.1	0.0100	1.8	0.22	64.0	1.1	58.7	4.7	NA	NA	64.0	1.1
	Spot 2	460	2391	1.1	23.3647	1.2	0.0602	2.1	0.0102	1.7	0.83	65.5	1.1	59.4	1.2	NA	NA	65.5	1.1
	Spot 3	384	14070	1.4	20.9456	1.4	0.0674	2.8	0.0102	2.4	0.86	65.7	1.6	66.2	1.8	86.6	33.4	65.7	1.6
	Spot 4	257	4873	1.4	21.7494	2.1	0.0652	2.9	0.0103	2.0	0.70	65.9	1.3	64.1	1.8	NA	NA	65.9	1.3
	Spot 5	467	20254	1.0	20.6373	1.0	0.0691	2.3	0.0103	2.0	0.89	66.4	1.3	67.9	1.5	121.6	24.7	66.4	1.3
	Spot 6	208	1261	1.0	26.8470	2.2	0.0533	3.6	0.0104	2.8	0.80	66.6	1.9	52.7	1.8	NA	NA	66.6	1.9
	Spot 7	621	310762	1.2	20.4271	1.6	0.0702	2.4	0.0104	1.8	0.75	66.7	1.2	68.9	1.6	145.7	37.4	66.7	1.2
	Spot 8	426	6752	1.2	21.1630	1.8	0.0678	3.1	0.0104	2.5	0.81	66.8	1.7	66.6	2.0	62.0	43.5	66.8	1.7

contd.

Samples	U (ppm)	²⁰⁶ Pb/ ²⁰⁴ Pb	U/Th	Isotope ratios							Apparent ages (Ma)							
				²⁰⁶ Pb*/ ²⁰⁷ Pb*	±	²⁰⁷ Pb*/ ²³⁵ U*	±	²⁰⁶ Pb*/ ²³⁸ U	±	error corr.	²⁰⁶ Pb*/ ²³⁸ U*	±	²⁰⁷ Pb*/ ²³⁵ U	±	²⁰⁶ Pb*/ ²⁰⁷ Pb*	±	Best age (Ma)	± (Ma)
Spot 9	218	3041	1.1	21.9336	4.3	0.0655	5.2	0.0104	2.9	0.55	66.8	1.9	64.4	3.2	NA	NA	66.8	1.9
Spot 10	568	9630	1.1	20.9791	1.3	0.0685	2.6	0.0104	2.2	0.86	66.9	1.5	67.3	1.7	82.7	31.5	66.9	1.5
Spot 11	376	17591	1.5	21.1986	1.4	0.0681	2.2	0.0105	1.8	0.80	67.2	1.2	66.9	1.4	58.0	32.3	67.2	1.2
Spot 12	170	989	0.9	29.8440	6.0	0.0487	6.6	0.0106	2.9	0.43	67.7	1.9	48.3	3.1	NA	NA	67.7	1.9
Spot 13	192	3526	1.5	20.7624	2.7	0.0701	4.2	0.0106	3.3	0.78	67.8	2.2	68.8	2.8	107.4	62.6	67.8	2.2
Spot 14	220	5669	1.5	21.4868	3.2	0.0678	4.3	0.0106	2.9	0.67	67.8	1.9	66.6	2.8	25.7	77.3	67.8	1.9
Spot 15	149	688	1.9	23.4573	5.0	0.0622	5.5	0.0106	2.2	0.40	67.9	1.5	61.3	3.2	NA	NA	67.9	1.5
Spot 16	186	5470	1.2	22.0827	2.2	0.0670	3.0	0.0107	2.0	0.68	68.8	1.4	65.8	1.9	NA	NA	68.8	1.4
Spot 17	206	6006	1.6	21.6758	2.7	0.0688	4.1	0.0108	3.1	0.76	69.3	2.1	67.5	2.7	4.7	64.1	69.3	2.1
Spot 18	207	16800	1.5	19.2340	2.6	0.0779	3.5	0.0109	2.3	0.67	69.7	1.6	76.1	2.5	285.0	59.0	69.7	1.6
Spot 19	107	3584	1.4	16.6171	5.8	0.0910	6.7	0.0110	3.2	0.49	70.4	2.3	88.5	5.7	610.0	126.3	70.4	2.3
Spot 20	551	30679	4.7	17.7542	1.7	0.1621	5.8	0.0209	5.5	0.95	133.2	7.3	152.6	8.2	465.2	38.7	133.2	7.3
Spot 21	156	9799	1.9	17.1102	2.0	0.2804	3.3	0.0348	2.7	0.81	220.6	5.9	251.0	7.4	546.5	42.6	220.6	5.9
Spot 22	947	36327	4.0	17.0404	1.2	0.3316	5.8	0.0410	5.7	0.98	259.1	14.5	290.8	14.8	555.4	26.3	259.1	14.5
Spot 23	208	17503	2.6	16.7364	2.1	0.6370	7.3	0.0774	6.9	0.96	480.3	32.1	500.5	28.7	594.5	46.3	480.3	32.1
Spot 24	138	33967	1.9	16.9101	1.2	0.6755	2.2	0.0829	1.9	0.85	513.3	9.3	524.0	9.0	572.1	25.1	513.3	9.3
Spot 25	94	136042	3.8	16.3561	1.0	0.8387	2.6	0.0995	2.4	0.92	611.7	14.2	618.4	12.3	644.2	22.2	611.7	14.2
Spot 1	1011	19970	0.8	20.8300	1.2	0.0672	2.3	0.0102	2.0	0.86	65.1	1.3	66.0	1.5	99.6	28.6	65.1	1.3
Spot 2	842	12631	0.9	20.7526	1.2	0.0675	2.5	0.0102	2.2	0.88	65.2	1.4	66.3	1.6	108.4	27.7	65.2	1.4
Spot 3	807	32401	1.0	20.5037	1.4	0.0685	3.2	0.0102	2.9	0.90	65.3	1.9	67.2	2.1	136.9	31.9	65.3	1.9
Spot 4	2874	22429	0.5	19.7718	1.2	0.0714	2.6	0.0102	2.3	0.88	65.7	1.5	70.0	1.8	221.6	28.3	65.7	1.5
Spot 5	951	26717	1.0	20.5956	1.2	0.0686	2.7	0.0103	2.4	0.89	65.8	1.6	67.4	1.8	126.4	29.1	65.8	1.6
Spot 6	1225	16191	0.8	21.0793	1.2	0.0671	2.5	0.0103	2.2	0.88	65.8	1.4	65.9	1.6	71.4	27.5	65.8	1.4
Spot 7	696	24688	0.3	20.6347	1.2	0.0687	2.2	0.0103	1.9	0.85	66.0	1.3	67.5	1.5	121.9	27.8	66.0	1.3
Spot 8	166	2533	0.1	21.1742	3.8	0.0672	4.5	0.0103	2.3	0.51	66.2	1.5	66.1	2.9	60.7	91.5	66.2	1.5
Spot 9	2317	20643	0.6	20.8572	1.1	0.0683	1.9	0.0103	1.6	0.82	66.3	1.1	67.1	1.3	96.6	25.9	66.3	1.1
Spot 10	963	10848	0.5	21.3043	1.4	0.0669	2.5	0.0103	2.0	0.82	66.3	1.3	65.8	1.6	46.1	33.4	66.3	1.3
Spot 11	743	17757	0.1	20.9925	1.5	0.0680	2.6	0.0104	2.1	0.82	66.4	1.4	66.8	1.7	81.2	35.0	66.4	1.4
Spot 12	944	10194	0.4	21.2016	1.2	0.0674	2.4	0.0104	2.1	0.87	66.5	1.4	66.2	1.5	57.6	28.1	66.5	1.4
Spot 13	866	30069	0.3	20.6270	1.2	0.0693	2.3	0.0104	1.9	0.84	66.5	1.3	68.0	1.5	122.7	28.7	66.5	1.3
Spot 14	1599	24033	0.7	20.5469	1.4	0.0696	2.3	0.0104	1.9	0.81	66.5	1.2	68.3	1.5	131.9	32.2	66.5	1.2
Spot 15	1524	2632	0.4	17.5899	5.6	0.0814	5.9	0.0104	2.1	0.35	66.6	1.4	79.5	4.5	485.8	122.9	66.6	1.4
Spot 16	943	19920	0.8	20.7229	1.1	0.0691	2.4	0.0104	2.1	0.89	66.7	1.4	67.9	1.6	111.8	26.4	66.7	1.4
Spot 17	1559	12600	0.6	21.1555	1.2	0.0678	2.2	0.0104	1.9	0.86	66.7	1.3	66.6	1.4	62.8	27.6	66.7	1.3
Spot 18	1232	14781	0.6	19.1542	1.2	0.0749	2.6	0.0104	2.3	0.88	66.7	1.5	73.3	1.9	294.5	28.2	66.7	1.5
Spot 19	915	24109	0.9	19.1503	1.8	0.0750	2.9	0.0104	2.3	0.79	66.8	1.5	73.4	2.1	295.0	41.1	66.8	1.5
Spot 20	1155	39852	0.7	19.5616	1.3	0.0734	2.9	0.0104	2.6	0.90	66.8	1.7	71.9	2.0	246.3	29.3	66.8	1.7
Spot 21	1477	766064	0.5	20.6453	0.9	0.0698	1.8	0.0104	1.6	0.88	67.0	1.0	68.5	1.2	120.7	20.4	67.0	1.0
Spot 22	847	60620	1.0	19.2216	2.2	0.0750	2.9	0.0105	2.0	0.67	67.1	1.3	73.4	2.1	286.5	50.0	67.1	1.3

A7

contd.

Samples	U (ppm)	²⁰⁶ Pb/ ²⁰⁴ Pb	U/Th	²⁰⁶ Pb* ²⁰⁷ Pb*	Isotope ratios						Apparent ages (Ma)							
					±	²⁰⁷ Pb*/ ²³⁵ U*	±	²⁰⁶ Pb*/ ²³⁸ U	±	error corr.	²⁰⁶ Pb*/ ²³⁸ U*	±	²⁰⁷ Pb*/ ²³⁵ U	±	²⁰⁶ Pb*/ ²⁰⁷ Pb*	±	Best age (Ma)	±
Spot 23	1146	1306	0.7	13.1568	7.0	0.1098	7.6	0.0105	3.1	0.41	67.2	2.1	105.8	7.7	1095.3	139.6	67.2	2.1
Spot 24	435	6336	0.3	21.1270	1.6	0.0685	3.1	0.0105	2.7	0.86	67.3	1.8	67.3	2.0	66.1	37.7	67.3	1.8
Spot 25	685	3794	0.8	19.6068	3.2	0.0739	4.0	0.0105	2.4	0.61	67.4	1.6	72.4	2.8	241.0	73.8	67.4	1.6
Spot 26	1312	2410	0.8	15.5799	6.4	0.0934	6.8	0.0106	2.2	0.33	67.7	1.5	90.7	5.9	747.7	135.4	67.7	1.5
Spot 27	995	40816	0.8	17.9352	3.0	0.0816	3.7	0.0106	2.2	0.58	68.1	1.5	79.6	2.8	442.7	67.1	68.1	1.5
Spot 28	521	1313	0.8	11.7425	10.0	0.1246	10.6	0.0106	3.5	0.33	68.1	2.4	119.2	11.9	1319.2	194.5	68.1	2.4
Spot 29	598	8486	0.6	21.2783	1.7	0.0691	3.0	0.0107	2.5	0.82	68.4	1.7	67.8	2.0	49.0	41.1	68.4	1.7
Spot 30	925	1873	0.8	11.1462	9.3	0.1321	9.6	0.0107	2.1	0.22	68.5	1.5	126.0	11.3	1419.5	178.7	68.5	1.5
Spot 31	449	12515	0.4	20.4515	1.6	0.0723	2.6	0.0107	2.1	0.79	68.8	1.4	70.9	1.8	142.9	38.0	68.8	1.4
Spot 32	343	4478	1.2	14.5657	4.5	0.1020	5.4	0.0108	3.0	0.56	69.1	2.1	98.7	5.1	888.4	92.5	69.1	2.1
Spot 33	128	3552	0.2	13.8703	2.8	0.1104	3.9	0.0111	2.7	0.70	71.3	1.9	106.4	3.9	988.7	56.2	71.3	1.9
Spot 34	889	534	1.0	8.2960	8.0	0.1927	9.3	0.0116	4.7	0.51	74.3	3.5	178.9	15.3	1964.2	143.6	74.3	3.5
Spot 1	98	574	0.8	40.5280	5.6	0.0332	6.4	0.0098	3.1	0.48	62.6	1.9	33.2	2.1	NA	NA	62.6	1.9
Spot 2	88	902	1.7	29.1647	4.3	0.0480	5.4	0.0102	3.3	0.61	65.1	2.1	47.6	2.5	NA	NA	65.1	2.1
Spot 3	86	6362	0.6	20.3300	2.8	0.0691	3.7	0.0102	2.4	0.65	65.3	1.6	67.8	2.4	156.8	65.7	65.3	1.6
Spot 4	95	2995	1.4	23.4115	6.4	0.0605	7.0	0.0103	2.9	0.42	65.9	1.9	59.6	4.1	NA	NA	65.9	1.9
Spot 5	108	1449	1.5	25.0003	4.3	0.0572	5.2	0.0104	2.9	0.56	66.6	1.9	56.5	2.9	NA	NA	66.6	1.9
Spot 6	102	1662	1.5	24.6894	4.5	0.0580	5.1	0.0104	2.4	0.47	66.6	1.6	57.2	2.8	NA	NA	66.6	1.6
Spot 7	198	5252	1.1	20.1571	2.7	0.0711	3.6	0.0104	2.5	0.68	66.7	1.6	69.8	2.4	176.8	62.0	66.7	1.6
Spot 8	205	4922	1.3	21.4203	2.1	0.0671	3.9	0.0104	3.2	0.84	66.9	2.2	65.9	2.5	33.1	50.4	66.9	2.2
Spot 9	127	1637	1.3	23.6496	3.1	0.0609	4.3	0.0105	3.0	0.69	67.0	2.0	60.0	2.5	NA	NA	67.0	2.0
Spot 10	136	1230	1.0	26.7967	7.9	0.0539	8.4	0.0105	2.9	0.35	67.2	1.9	53.3	4.4	NA	NA	67.2	1.9
Spot 11	153	2011	1.3	23.7748	2.4	0.0609	3.4	0.0105	2.4	0.70	67.3	1.6	60.0	2.0	NA	NA	67.3	1.6
Spot 12	234	36503	0.9	20.5987	1.7	0.0702	2.9	0.0105	2.4	0.80	67.3	1.6	68.9	2.0	126.0	41.1	67.3	1.6
Spot 13	81	16231	1.5	20.1912	3.0	0.0719	4.0	0.0105	2.7	0.67	67.6	1.8	70.5	2.7	172.8	69.9	67.6	1.8
Spot 14	202	4563	1.0	21.5448	2.3	0.0677	3.4	0.0106	2.5	0.73	67.9	1.7	66.5	2.2	19.3	55.4	67.9	1.7
Spot 15	105	4754	1.1	21.7297	3.0	0.0675	3.5	0.0106	1.9	0.54	68.3	1.3	66.3	2.3	NA	NA	68.3	1.3
Spot 16	94	16296	1.6	16.9632	2.2	0.2275	3.7	0.0280	3.0	0.81	178.1	5.3	208.2	7.1	565.3	48.3	178.1	5.3
Spot 17	281	11065	5.5	17.5448	1.2	0.2886	4.9	0.0367	4.8	0.97	232.6	10.9	257.4	11.2	491.4	27.5	232.6	10.9
Spot 18	150	5227508	2.7	16.8490	1.2	0.3060	2.7	0.0374	2.4	0.90	236.8	5.7	271.1	6.5	580.0	25.4	236.8	5.7
Spot 19	92	6207	1.3	17.8603	1.6	0.2959	2.7	0.0383	2.2	0.81	242.6	5.2	263.2	6.3	452.0	35.5	242.6	5.2
Spot 20	84	4835	1.1	17.8763	3.7	0.3477	8.0	0.0451	7.1	0.89	284.4	19.8	303.0	21.1	450.0	82.7	284.4	19.8
Spot 21	128	21763	2.1	16.1670	1.4	0.5448	2.5	0.0639	2.1	0.84	399.3	8.2	441.6	9.0	669.1	29.3	399.3	8.2
Spot 22	295	22701	12.1	17.3530	1.0	0.6212	2.3	0.0782	2.1	0.90	485.5	9.7	490.6	9.0	515.6	22.3	485.5	9.7
Spot 23	394	28092	1.6	16.9189	1.1	0.6769	3.0	0.0831	2.7	0.93	514.6	13.6	524.9	12.1	571.0	23.4	514.6	13.6
Spot 24	389	108177	1.6	16.7686	0.9	0.7079	2.4	0.0861	2.2	0.92	532.6	11.1	543.5	10.0	590.4	20.3	532.6	11.1
Spot 25	389	61873	1.6	16.8242	1.2	0.7225	2.8	0.0882	2.6	0.91	544.9	13.5	552.2	12.1	583.2	25.7	544.9	13.5

G1

contd.

Samples	U (ppm)	²⁰⁶ Pb/ ²⁰⁴ Pb	U/Th	Isotope ratios							Apparent ages (Ma)								
				²⁰⁶ Pb*/ ²⁰⁷ Pb*	± (%)	²⁰⁷ Pb*/ ²³⁵ U*	± (%)	²⁰⁶ Pb*/ ²³⁸ U	± (%)	error corr.	²⁰⁶ Pb*/ ²³⁸ U*	± (Ma)	²⁰⁷ Pb*/ ²³⁵ U	± (Ma)	²⁰⁶ Pb*/ ²⁰⁷ Pb*	± (Ma)	Best age (Ma)	± (Ma)	
B5	Spot 1	722	1162	0.3	13.4545	6.2	0.0966	8.1	0.0094	5.1	0.64	60.5	3.1	93.7	7.2	1050.3	125.3	60.5	3.1
	Spot 2	633	19198	0.6	20.6046	1.3	0.0670	2.8	0.0100	2.5	0.88	64.3	1.6	65.9	1.8	125.3	31.3	64.3	1.6
	Spot 3	4267	53581	0.6	21.1216	1.0	0.0660	2.1	0.0101	1.9	0.89	64.9	1.2	64.9	1.3	66.7	22.9	64.9	1.2
	Spot 4	830	8608	0.9	21.6880	1.5	0.0645	2.4	0.0101	1.9	0.78	65.1	1.2	63.5	1.5	3.3	37.0	65.1	1.2
	Spot 5	572	16856	0.6	20.9446	1.3	0.0669	3.0	0.0102	2.7	0.90	65.2	1.8	65.7	1.9	86.7	30.8	65.2	1.8
	Spot 6	2921	7360	0.5	19.1077	3.2	0.0735	3.6	0.0102	1.7	0.48	65.4	1.1	72.0	2.5	300.1	72.7	65.4	1.1
	Spot 7	516	7413	0.5	21.4654	2.2	0.0656	3.3	0.0102	2.5	0.74	65.5	1.6	64.5	2.1	28.1	53.8	65.5	1.6
	Spot 8	593	8193	0.6	20.7683	1.5	0.0681	3.4	0.0103	3.0	0.89	65.8	2.0	66.9	2.2	106.7	36.4	65.8	2.0
	Spot 9	2314	20931	2.4	21.3422	1.2	0.0664	2.6	0.0103	2.3	0.88	66.0	1.5	65.3	1.6	41.9	29.7	66.0	1.5
	Spot 10	613	11993	0.6	21.7749	1.6	0.0656	2.9	0.0104	2.5	0.85	66.5	1.6	64.5	1.8	NA	NA	66.5	1.6
	Spot 11	943	8634	0.3	20.7159	1.3	0.0693	2.7	0.0104	2.3	0.87	66.8	1.6	68.0	1.8	112.6	31.2	66.8	1.6
	Spot 12	297	6629	0.3	21.8668	1.6	0.0657	3.0	0.0104	2.5	0.83	66.9	1.6	64.6	1.9	NA	NA	66.9	1.6
	Spot 13	186	801	0.7	18.9581	9.4	0.0759	9.9	0.0104	2.9	0.29	67.0	1.9	74.3	7.1	317.9	215.1	67.0	1.9
	Spot 14	367	3880	0.6	23.0954	1.5	0.0626	2.9	0.0105	2.5	0.85	67.3	1.7	61.7	1.7	NA	NA	67.3	1.7
	Spot 15	350	4161	0.6	21.0237	3.3	0.0689	4.1	0.0105	2.4	0.60	67.4	1.6	67.7	2.7	77.7	78.4	67.4	1.6
	Spot 16	348	21649	0.4	20.6730	2.4	0.0701	3.9	0.0105	3.1	0.79	67.5	2.1	68.8	2.6	117.5	56.3	67.5	2.1
	Spot 17	564	4033	0.4	23.1000	1.7	0.0630	2.7	0.0106	2.1	0.79	67.7	1.4	62.0	1.6	NA	NA	67.7	1.4
	Spot 18	1145	5063	0.5	16.2020	3.2	0.0899	3.7	0.0106	1.8	0.49	67.7	1.2	87.4	3.1	664.5	68.6	67.7	1.2
	Spot 19	310	2716	0.6	23.7325	2.9	0.0618	3.8	0.0106	2.5	0.65	68.3	1.7	60.9	2.3	NA	NA	68.3	1.7
	Spot 20	554	235	0.5	4.1686	9.8	0.4480	11.7	0.0136	6.3	0.54	86.8	5.4	375.9	36.6	3119.2	156.9	86.8	5.4
	Spot 21	573	247	0.6	3.8864	3.7	0.5051	6.0	0.0142	4.8	0.79	91.2	4.3	415.1	20.6	3230.3	58.8	91.2	4.3
	Spot 22	320	89867	2.4	13.3318	0.8	1.9292	2.1	0.1866	1.9	0.93	1103.0	19.4	1091.3	13.8	1068.8	15.4	1068.8	15.4
	Spot 23	370	139376	2.3	13.2934	1.1	1.9626	3.0	0.1893	2.8	0.93	1117.6	28.3	1102.8	19.9	1074.6	21.3	1074.6	21.3
	Spot 24	255	34335	2.4	13.2449	0.8	1.9370	2.4	0.1862	2.3	0.94	1100.5	23.3	1094.0	16.3	1081.9	16.0	1081.9	16.0
B2	Spot 1	564	6725	0.7	19.1836	2.1	0.0723	3.5	0.0101	2.8	0.79	64.5	1.8	70.9	2.4	291.0	48.7	64.5	1.8
	Spot 2	714	40701	0.4	19.5667	1.9	0.0716	2.8	0.0102	2.1	0.74	65.2	1.4	70.2	1.9	245.7	43.4	65.2	1.4
	Spot 3	1014	3454	0.4	22.7443	1.5	0.0617	2.6	0.0102	2.1	0.82	65.3	1.4	60.8	1.5	NA	NA	65.3	1.4
	Spot 4	856	14301	0.6	21.5025	1.7	0.0656	2.8	0.0102	2.2	0.78	65.6	1.4	64.5	1.7	23.9	41.9	65.6	1.4
	Spot 5	1703	57796	0.3	20.8371	0.9	0.0680	2.2	0.0103	2.0	0.92	65.9	1.3	66.8	1.4	98.9	21.1	65.9	1.3
	Spot 6	651	7318	0.7	21.8757	1.4	0.0648	2.6	0.0103	2.2	0.84	66.0	1.5	63.8	1.6	NA	NA	66.0	1.5
	Spot 7	1113	15787	0.3	17.7781	3.0	0.0799	4.0	0.0103	2.6	0.66	66.1	1.7	78.0	3.0	462.2	67.3	66.1	1.7
	Spot 8	713	25328	0.7	20.7268	1.9	0.0687	3.1	0.0103	2.4	0.78	66.3	1.6	67.5	2.0	111.4	46.0	66.3	1.6
	Spot 9	572	3285	0.3	22.7190	1.7	0.0627	2.9	0.0103	2.3	0.81	66.3	1.5	61.8	1.7	NA	NA	66.3	1.5
	Spot 10	636	35346	0.3	20.9955	1.7	0.0684	3.1	0.0104	2.6	0.83	66.8	1.7	67.2	2.0	80.9	40.8	66.8	1.7
	Spot 11	1411	7550	0.4	21.6319	1.4	0.0664	2.8	0.0104	2.4	0.87	66.8	1.6	65.3	1.8	9.5	33.0	66.8	1.6
	Spot 12	1735	2193	0.3	16.8833	5.5	0.0852	6.4	0.0104	3.2	0.50	67.0	2.1	83.1	5.1	575.6	120.4	67.0	2.1
	Spot 13	823	7730	0.4	21.6698	2.2	0.0665	3.2	0.0105	2.3	0.71	67.0	1.5	65.4	2.0	5.3	54.0	67.0	1.5
	Spot 14	1161	27948	0.4	21.1482	1.0	0.0683	2.6	0.0105	2.3	0.91	67.2	1.6	67.1	1.7	63.6	24.7	67.2	1.6
	Spot 15	550	37979	0.7	20.7190	1.8	0.0699	3.0	0.0105	2.4	0.80	67.4	1.6	68.6	2.0	112.3	42.3	67.4	1.6

contd.

Samples	U (ppm)	²⁰⁶ Pb/ ²⁰⁴ Pb	U/Th	Isotope ratios							Apparent ages (Ma)							
				²⁰⁶ Pb*/ ²⁰⁷ Pb*	± (%)	²⁰⁷ Pb*/ ²³⁵ U*	± (%)	²⁰⁶ Pb*/ ²³⁸ U	± (%)	error corr.	²⁰⁶ Pb*/ ²³⁸ U*	± (Ma)	²⁰⁷ Pb*/ ²³⁵ U	± (Ma)	²⁰⁶ Pb*/ ²⁰⁷ Pb*	± (Ma)	Best age (Ma)	± (Ma)
Spot 16	738	1479	0.4	14.2117	3.2	0.1020	4.2	0.0105	2.6	0.63	67.4	1.7	98.6	3.9	939.0	66.3	67.4	1.7
Spot 17	381	5814	0.5	21.8405	1.8	0.0664	3.4	0.0105	2.8	0.84	67.5	1.9	65.3	2.1	NA	NA	67.5	1.9
Spot 18	520	10877	0.3	18.9493	1.9	0.0768	3.7	0.0106	3.1	0.86	67.7	2.1	75.1	2.7	319.0	43.1	67.7	2.1
Spot 19	1566	1495	0.3	13.6424	4.9	0.1067	5.4	0.0106	2.2	0.41	67.7	1.5	102.9	5.3	1022.3	100.1	67.7	1.5
Spot 20	1172	1163	0.3	13.0899	8.0	0.1116	8.5	0.0106	2.9	0.34	68.0	2.0	107.4	8.6	1105.5	159.2	68.0	2.0
Spot 21	448	1743	0.5	15.4412	2.9	0.0946	4.2	0.0106	3.0	0.73	68.0	2.1	91.8	3.7	766.6	60.1	68.0	2.1
Spot 22	811	2140	0.2	15.9541	5.7	0.0920	6.2	0.0107	2.3	0.38	68.3	1.6	89.4	5.3	697.4	122.2	68.3	1.6
Spot 23	731	599	0.2	9.7015	6.0	0.1549	6.6	0.0109	2.8	0.42	69.9	1.9	146.3	9.0	1680.2	110.8	69.9	1.9
Spot 24	156	1403	1.2	17.5628	6.1	0.0867	6.8	0.0110	3.0	0.45	70.8	2.1	84.4	5.5	489.2	134.6	70.8	2.1
Spot 25	560	853	0.5	11.5731	4.8	0.1330	5.5	0.0112	2.8	0.51	71.6	2.0	126.8	6.6	1347.3	92.0	71.6	2.0
Spot 26	631	780	0.8	10.3862	8.6	0.1501	9.2	0.0113	3.2	0.35	72.5	2.3	142.0	12.1	1553.3	161.4	72.5	2.3
Spot 27	1288	384	0.7	6.0959	5.5	0.2809	6.4	0.0124	3.1	0.49	79.6	2.5	251.4	14.1	2497.8	93.1	79.6	2.5
Spot 28	2305	276	0.7	4.7698	3.0	0.3786	4.1	0.0131	2.8	0.68	83.9	2.3	326.0	11.3	2902.9	48.4	83.9	2.3
Spot 1	96	354	1.7	121.1092	21.1	0.0114	21.3	0.0100	3.3	0.15	64.1	2.1	11.5	2.4	NA	NA	64.1	2.1
Spot 2	293	3436	0.9	21.9044	5.0	0.0632	5.4	0.0100	2.1	0.39	64.4	1.3	62.2	3.3	NA	NA	64.4	1.3
Spot 3	317	2235	1.2	22.1847	2.9	0.0628	3.9	0.0101	2.6	0.68	64.8	1.7	61.8	2.3	NA	NA	64.8	1.7
Spot 4	271	2019	1.1	19.7905	7.6	0.0710	8.0	0.0102	2.3	0.29	65.4	1.5	69.6	5.4	219.4	176.5	65.4	1.5
Spot 5	206	756	1.2	23.6868	4.8	0.0599	5.3	0.0103	2.3	0.43	66.0	1.5	59.0	3.1	NA	NA	66.0	1.5
Spot 6	180	3123	1.4	16.7485	5.4	0.0848	6.3	0.0103	3.3	0.53	66.1	2.2	82.6	5.0	592.9	116.5	66.1	2.2
Spot 7	759	3737	0.8	19.9980	1.4	0.0710	2.5	0.0103	2.0	0.82	66.1	1.3	69.7	1.7	195.3	33.1	66.1	1.3
Spot 8	601	4212	1.1	20.0846	4.0	0.0709	4.6	0.0103	2.3	0.50	66.3	1.5	69.6	3.1	185.2	92.4	66.3	1.5
Spot 9	218	6040	1.2	20.7250	2.3	0.0690	2.9	0.0104	1.9	0.64	66.6	1.3	67.8	1.9	111.6	53.4	66.6	1.3
Spot 10	206	15683	1.4	20.0202	2.7	0.0717	3.8	0.0104	2.7	0.71	66.8	1.8	70.3	2.6	192.7	62.4	66.8	1.8
Spot 11	251	3118	1.0	21.6354	2.5	0.0666	3.1	0.0105	1.8	0.60	67.1	1.2	65.5	1.9	9.1	59.0	67.1	1.2
Spot 12	1070	4723	1.2	16.8783	3.8	0.0855	4.6	0.0105	2.6	0.56	67.2	1.7	83.3	3.7	576.2	83.1	67.2	1.7
Spot 13	135	3823	1.4	15.9564	2.6	0.0907	3.6	0.0105	2.4	0.68	67.3	1.6	88.2	3.0	697.1	55.9	67.3	1.6
Spot 14	423	2604	1.0	20.7379	2.4	0.0698	3.2	0.0105	2.1	0.65	67.4	1.4	68.6	2.1	110.1	56.6	67.4	1.4
Spot 15	213	2822	1.2	23.0621	2.8	0.0633	3.4	0.0106	2.0	0.57	67.9	1.3	62.3	2.1	NA	NA	67.9	1.3
Spot 16	198	6937	0.9	17.5645	2.1	0.0834	3.1	0.0106	2.3	0.74	68.1	1.5	81.3	2.4	488.9	46.3	68.1	1.5
Spot 17	1345	3507	1.0	16.4574	1.7	0.0901	2.2	0.0108	1.3	0.59	69.0	0.9	87.6	1.8	630.9	37.7	69.0	0.9
Spot 18	1593	4260	3.9	13.0992	4.5	0.1139	5.2	0.0108	2.6	0.50	69.4	1.8	109.5	5.4	1104.0	90.0	69.4	1.8
Spot 19	186	1733	1.1	17.6438	4.7	0.0846	5.4	0.0108	2.7	0.51	69.5	1.9	82.5	4.3	479.0	102.8	69.5	1.9
Spot 20	462	2532	3.6	16.1203	4.2	0.0930	5.3	0.0109	3.2	0.60	69.7	2.2	90.3	4.5	675.3	89.9	69.7	2.2
Spot 21	169	4287	1.3	11.5755	4.2	0.1301	4.8	0.0109	2.2	0.47	70.1	1.6	124.2	5.6	1346.9	81.4	70.1	1.6
Spot 22	171	1735	1.3	10.7852	7.3	0.1411	7.9	0.0110	3.2	0.40	70.8	2.2	134.0	10.0	1482.2	138.3	70.8	2.2
Spot 23	246	1633	1.2	12.3254	6.0	0.1237	6.5	0.0111	2.7	0.41	70.9	1.9	118.4	7.3	1224.7	117.4	70.9	1.9
Spot 24	474	2928	1.3	22.5463	2.6	0.0692	3.3	0.0113	2.0	0.61	72.6	1.5	68.0	2.2	NA	NA	72.6	1.5
Spot 25	229	1363	1.5	11.5132	3.6	0.1403	4.3	0.0117	2.3	0.54	75.1	1.7	133.3	5.3	1357.3	69.2	75.1	1.7

contd.

Samples	U (ppm)	²⁰⁶ Pb/ ²⁰⁴ Pb	U/Th	Isotope ratios							Apparent ages (Ma)								
				²⁰⁶ Pb*/ ²⁰⁷ Pb*	± (%)	²⁰⁷ Pb*/ ²³⁵ U*	± (%)	²⁰⁶ Pb*/ ²³⁸ U	± (%)	error corr.	²⁰⁶ Pb*/ ²³⁸ U*	± (Ma)	²⁰⁷ Pb*/ ²³⁵ U	± (Ma)	²⁰⁶ Pb*/ ²⁰⁷ Pb*	± (Ma)	Best age (Ma)	± (Ma)	
Spot 26	490	470	1.7	6.7987	2.1	0.2418	3.9	0.0119	3.3	0.85	76.4	2.5	219.9	7.7	2312.3	35.7	76.4	2.5	
Spot 27	352	7909	2.8	16.4638	2.6	0.1016	4.9	0.0121	4.1	0.85	77.7	3.2	98.2	4.6	630.0	55.7	77.7	3.2	
Spot 28	899	440	1.2	6.2747	20.6	0.2750	20.8	0.0125	2.8	0.13	80.2	2.2	246.7	45.6	2449.0	352.6	80.2	2.2	
Spot 29	372	343	1.6	5.1753	12.1	0.3367	12.9	0.0126	4.5	0.34	81.0	3.6	294.7	33.1	2769.8	200.0	81.0	3.6	
Spot 30	239	5391	0.7	14.4873	4.6	0.1204	5.1	0.0127	2.4	0.46	81.1	1.9	115.4	5.6	899.5	94.3	81.1	1.9	
Spot 31	368	6275	1.2	13.4492	3.2	0.1345	3.8	0.0131	2.0	0.53	84.1	1.7	128.2	4.6	1051.1	65.1	84.1	1.7	
Spot 32	238	235	0.4	3.8611	13.1	0.5221	14.0	0.0146	4.7	0.34	93.6	4.4	426.5	48.6	3240.6	208.1	93.6	4.4	
Spot 1	176	545	0.2	8.5643	1.4	0.1867	3.1	0.0116	2.7	0.88	74.3	2.0	173.8	4.9	1907.3	26.0	74.3	2.0	
Spot 2	178	783	0.2	7.4492	1.5	0.2151	2.9	0.0116	2.5	0.86	74.5	1.9	197.8	5.3	2154.2	26.2	74.5	1.9	
Spot 3	12	301	0.1	6.3045	6.9	0.2612	7.9	0.0119	3.8	0.48	76.6	2.9	235.6	16.6	2441.0	117.2	76.6	2.9	
Spot 4	23	639	0.1	4.7285	6.2	0.3738	7.7	0.0128	4.5	0.58	82.2	3.6	322.5	21.2	2916.9	101.1	82.2	3.6	
Spot 5	19	831	0.1	4.2887	3.0	0.4389	4.8	0.0137	3.8	0.78	87.5	3.3	369.5	15.0	3073.9	48.5	87.5	3.3	
Spot 6	21	495	0.1	3.0848	1.1	0.6781	3.4	0.0152	3.2	0.94	97.1	3.1	525.6	13.9	3589.7	17.1	97.1	3.1	
Spot 7	25	386	0.1	2.7788	1.3	0.7981	3.7	0.0161	3.5	0.94	102.9	3.5	595.7	16.6	3749.3	19.4	102.9	3.5	
Spot 8	24	248	0.1	2.1401	3.8	1.3498	14.4	0.0210	13.9	0.96	133.7	18.4	867.5	84.2	NA	NA	133.7	18.4	
Spot 9	10	91	0.2	2.4586	0.0	2.4288	16.8	0.0433	16.8	1.00	273.4	44.9	1251.2	121.2	NA	NA	273.4	44.9	
Spot 1	110	982	0.8	20.6584	3.3	0.0652	4.4	0.0098	2.9	0.66	62.7	1.8	64.1	2.8	119.2	78.4	62.7	1.8	
Spot 2	860	4497	0.3	21.9544	2.7	0.0631	3.4	0.0101	2.1	0.62	64.5	1.4	62.2	2.0	NA	NA	64.5	1.4	
Spot 3	1449	9808	0.8	21.3347	1.9	0.0651	3.6	0.0101	3.0	0.84	64.7	1.9	64.1	2.2	42.7	46.4	64.7	1.9	
Spot 4	510	58306	0.4	20.9651	1.8	0.0665	3.4	0.0101	2.9	0.85	64.9	1.8	65.4	2.1	84.3	41.9	64.9	1.8	
Spot 5	855	18776	0.2	19.2514	1.4	0.0728	2.5	0.0102	2.0	0.83	65.2	1.3	71.3	1.7	283.0	31.4	65.2	1.3	
Spot 6	432	6605	0.7	21.5494	1.6	0.0651	3.9	0.0102	3.5	0.92	65.3	2.3	64.1	2.4	18.7	37.3	65.3	2.3	
Spot 7	290	1035	0.9	29.2626	2.7	0.0483	3.7	0.0103	2.6	0.70	65.8	1.7	47.9	1.8	NA	NA	65.8	1.7	
Spot 8	1387	18726	0.7	21.5251	1.2	0.0657	2.7	0.0103	2.4	0.89	65.8	1.6	64.6	1.7	21.4	29.5	65.8	1.6	
Spot 9	778	10764	0.3	20.7889	1.6	0.0681	3.6	0.0103	3.2	0.89	65.9	2.1	66.9	2.4	104.3	39.0	65.9	2.1	
Spot 10	156	807	0.6	32.0406	5.2	0.0445	6.1	0.0103	3.1	0.52	66.3	2.1	44.2	2.6	NA	NA	66.3	2.1	
Spot 11	67	3415	0.7	21.9696	4.4	0.0649	5.0	0.0103	2.4	0.49	66.3	1.6	63.8	3.1	NA	NA	66.3	1.6	
Spot 12	751	5545	0.3	21.9157	2.5	0.0653	3.7	0.0104	2.7	0.73	66.6	1.8	64.2	2.3	NA	NA	66.6	1.8	
Spot 13	1942	11808	0.7	21.6949	1.2	0.0661	2.6	0.0104	2.3	0.89	66.7	1.5	65.0	1.6	2.5	28.6	66.7	1.5	
Spot 14	751	43137	0.1	16.8216	2.7	0.0854	3.6	0.0104	2.4	0.66	66.8	1.6	83.2	2.9	583.5	59.3	66.8	1.6	
Spot 15	953	2283	0.3	15.3083	5.2	0.0941	5.8	0.0105	2.5	0.43	67.0	1.6	91.3	5.0	784.8	109.6	67.0	1.6	
Spot 16	340	4680	0.8	22.1239	2.3	0.0652	4.4	0.0105	3.8	0.86	67.1	2.5	64.1	2.8	NA	NA	67.1	2.5	
Spot 17	131	1664	0.5	25.0384	4.4	0.0576	5.1	0.0105	2.4	0.48	67.2	1.6	56.9	2.8	NA	NA	67.2	1.6	
Spot 18	845	19864	0.3	20.9188	1.3	0.0692	2.7	0.0105	2.3	0.88	67.4	1.6	68.0	1.7	89.6	30.3	67.4	1.6	
Spot 19	455	6933	0.9	21.7500	2.0	0.0667	3.1	0.0105	2.4	0.77	67.5	1.6	65.6	2.0	NA	NA	67.5	1.6	
Spot 20	620	37256	0.4	21.0535	1.5	0.0691	3.0	0.0106	2.6	0.87	67.7	1.8	67.8	2.0	74.3	35.5	67.7	1.8	
Spot 21	384	5838	0.5	21.2891	3.1	0.0688	4.3	0.0106	3.0	0.69	68.1	2.0	67.5	2.8	47.8	75.0	68.1	2.0	

contd.

Samples	U (ppm)	²⁰⁶ Pb/ ²⁰⁴ Pb	U/Th	Isotope ratios						Apparent ages (Ma)									
				²⁰⁶ Pb*/ ²⁰⁷ Pb*	± (%)	²⁰⁷ Pb*/ ²³⁵ U*	± (%)	²⁰⁶ Pb*/ ²³⁸ U	± (%)	error corr.	²⁰⁶ Pb*/ ²³⁸ U*	± (Ma)	²⁰⁷ Pb*/ ²³⁵ U	± (Ma)	²⁰⁶ Pb*/ ²⁰⁷ Pb*	± (Ma)	Best age (Ma)	± (Ma)	
Spot 22	157	4748	0.6	19.9799	3.5	0.0733	4.3	0.0106	2.5	0.58	68.1	1.7	71.8	3.0	197.3	81.8	68.1	1.7	
Spot 23	108	10342	0.7	21.0300	3.0	0.0702	4.4	0.0107	3.2	0.73	68.6	2.2	68.9	2.9	77.0	71.5	68.6	2.2	
Spot 24	149	2625	0.7	20.0844	3.1	0.0747	4.5	0.0109	3.3	0.73	69.8	2.3	73.2	3.2	185.2	71.7	69.8	2.3	
Spot 25	191	39520	0.5	20.4333	2.3	0.0736	3.6	0.0109	2.8	0.77	69.9	1.9	72.1	2.5	144.9	53.6	69.9	1.9	
Spot 26	75	8009	0.8	20.6393	3.6	0.0744	4.6	0.0111	2.8	0.61	71.4	2.0	72.9	3.2	121.3	85.8	71.4	2.0	
R7	Spot 1	478	2425	1.6	19.7524	2.2	0.0715	3.3	0.0103	2.5	0.75	65.8	1.6	70.2	2.2	223.9	50.3	65.8	1.6
	Spot 2	200	2738	1.2	22.9707	3.4	0.0626	4.1	0.0104	2.3	0.57	66.9	1.5	61.7	2.4	NA	NA	66.9	1.5
	Spot 3	204	1482	1.2	25.9087	6.7	0.0555	7.2	0.0104	2.6	0.36	67.0	1.8	54.9	3.9	NA	NA	67.0	1.8
	Spot 4	266	3905	1.0	18.2000	4.5	0.0799	5.2	0.0106	2.5	0.49	67.7	1.7	78.1	3.9	410.0	100.7	67.7	1.7
	Spot 5	147	1053	1.2	26.7768	11.2	0.0551	11.5	0.0107	2.6	0.23	68.7	1.8	54.5	6.1	NA	NA	68.7	1.8
	Spot 6	248	29678	1.2	19.4410	2.0	0.0761	3.6	0.0107	2.9	0.82	68.8	2.0	74.4	2.6	260.5	47.0	68.8	2.0
	Spot 7	227	2294	1.2	16.7016	4.9	0.0890	5.6	0.0108	2.6	0.47	69.2	1.8	86.6	4.6	599.0	106.4	69.2	1.8
	Spot 8	258	6654	1.0	21.1696	2.4	0.0705	3.8	0.0108	3.0	0.78	69.4	2.1	69.1	2.5	61.3	56.4	69.4	2.1
	Spot 9	360	2850	1.0	13.2543	7.4	0.1134	8.0	0.0109	3.0	0.38	69.9	2.1	109.1	8.3	1080.5	148.8	69.9	2.1
	Spot 10	163	26657	1.1	12.3262	8.7	0.1236	9.2	0.0111	2.9	0.32	70.9	2.1	118.4	10.3	1224.5	171.7	70.9	2.1

1. Analyses with >10% uncertainty (1-sigma) in ²⁰⁶Pb/²³⁸U age are not included.
2. Analyses with >10% uncertainty (1-sigma) in ²⁰⁶Pb/²⁰⁷Pb age are not included, unless ²⁰⁶Pb/²³⁸U age is <400 Ma.
3. Best age is determined from ²⁰⁶Pb/²³⁸U age for analyses with ²⁰⁶Pb/²³⁸U age <900 Ma and from ²⁰⁶Pb/²⁰⁷Pb age for analyses with ²⁰⁶Pb/²³⁸U age >900 Ma.
4. Concordance is based on ²⁰⁶Pb/²³⁸U age / ²⁰⁶Pb/²⁰⁷Pb age. Value is not reported for ²⁰⁶Pb/²³⁸U ages <400 Ma because of large uncertainty in ²⁰⁶Pb/²⁰⁷Pb age.
5. Analyses with ²⁰⁶Pb/²³⁸U age >400 Ma and with >20% discordance (<80% concordance) are not included.
6. Analyses with ²⁰⁶Pb/²³⁸U age >400 Ma and with >5% reverse discordance (<105% concordance) are not included.
7. All uncertainties are reported at the 1-sigma level, and include only measurement errors.
8. Systematic errors are as follows (at 2-sigma level): [sample 1: xxx% (²⁰⁶Pb/²³⁸U) & xxx% (²⁰⁶Pb/²⁰⁷Pb)] These values are reported on cells U1 and W1 of E2agecalc.
9. Analyses conducted by LA-ICPMS, as described by Gehrels et al. (2008) and Gehrels and Pecha (2014).
10. U concentration and U/Th are calibrated relative to FC-1 zircon standard and are accurate to ~20%.
11. Common Pb correction is from measured ²⁰⁴Pb with common Pb composition interpreted from Stacey and Kramers (1975).
12. Common Pb composition assigned uncertainties of 1.5 for ²⁰⁶Pb/²⁰⁴Pb, 0.3 for ²⁰⁷Pb/²⁰⁴Pb, and 2.0 for ²⁰⁸Pb/²⁰⁴Pb.
13. U/Pb and ²⁰⁶Pb/²⁰⁷Pb fractionation is calibrated relative to fragments of large Sri Lanka zircons and individual crystals of FC-1, and R33.
14. U decay constants and composition as follows: ²³⁸U = 9.8485 x 10⁻¹⁰, ²³⁵U = 1.55125 x 10⁻¹⁰, ²³⁸U/²³⁵U = 137.88.

Table 11: U-Pb zircon data of samples A7 (Alech) and B6 (Barda) determined using CA-ID-TIMS

Fraction	Composition				Isotopic Ratios								Dates (Ma) *							
	Pb _c (pg) ^a	Pb ^a / Pb _c ^b	mass U (ng)	Th/ U ^c	²⁰⁶ Pb/ ²⁰⁴ Pb §	²⁰⁶ Pb/ ²⁰⁶ Pb †	²⁰⁶ Pb/ ²³⁸ U †	±2σ %	²⁰⁷ Pb/ ²³⁵ U †	±2σ %	Corr. coef.	²⁰⁷ Pb/ ²⁰⁶ Pb †	±2σ %	²⁰⁶ Pb/ ²³⁸ U ‡	±2σ abs	²⁰⁷ Pb/ ²³⁵ U ‡	±2σ abs	²⁰⁷ Pb/ ²⁰⁶ Pb ‡	±2σ abs	% disc
A7 zircon																				
z1	0.26	90	1.9	1.04	4712	0.331	0.0102408	0.055	0.06695	0.30	0.381	0.04744	0.28	65.749	0.038	65.80	0.19	70.3	6.8	6.6
z2	0.26	102	2.0	1.48	4824	0.470	0.0102404	0.055	0.06708	0.30	0.306	0.04753	0.28	65.729	0.041	65.92	0.19	74.8	6.7	12.2
z3	0.28	16	0.34	1.51	783	0.481	0.010247	0.14	0.0679	1.7	0.338	0.04806	1.6	65.772	0.093	66.7	1.1	101	39	35.1
z4	0.23	33	0.57	1.50	1568	0.477	0.0102456	0.090	0.06748	0.88	0.316	0.04779	0.86	65.762	0.062	66.31	0.57	88	20	25.3
z5	0.30	28	0.67	1.10	1431	0.349	0.0102386	0.086	0.06731	0.92	0.333	0.04770	0.89	65.732	0.058	66.14	0.59	83	21	21.2
z6	0.33	32	0.80	1.36	1572	0.434	0.0102448	0.087	0.06706	0.87	0.347	0.04749	0.84	65.762	0.060	65.90	0.55	73	20	10.0
z7	0.35	41	1.1	1.37	2009	0.436	0.0102480	0.070	0.06721	0.66	0.341	0.04758	0.64	65.782	0.050	66.04	0.42	78	15	15.3
B6 zircon																				
z1	0.27	80	1.7	1.14	4068	0.364	0.0102365	0.073	0.06698	0.40	0.481	0.04747	0.37	65.717	0.050	65.83	0.26	72.1	8.9	8.9
z2	0.27	190	4.2	1.10	9768	0.351	0.0102352	0.054	0.06695	0.17	0.565	0.047462	0.14	65.711	0.038	65.80	0.11	71.5	3.5	8.1
z3	0.35	101	2.1	2.69	3830	0.856	0.0102447	0.055	0.06713	0.35	0.384	0.04755	0.34	65.710	0.051	65.98	0.23	75.8	8.0	13.3
z4	0.37	70	2.2	1.04	3662	0.331	0.0102395	0.059	0.06708	0.39	0.342	0.04754	0.37	65.741	0.041	65.93	0.25	75.1	8.8	12.6
z5	0.54	21	0.85	1.43	1020	0.457	0.010237	0.11	0.06743	1.3	0.340	0.04780	1.2	65.708	0.075	66.26	0.82	88	29	25.5
z6	0.45	50	1.8	1.25	2504	0.398	0.0102438	0.068	0.06703	0.54	0.347	0.04748	0.52	65.760	0.048	65.88	0.34	72	12	9.3
z7	0.31	42	0.85	2.25	1731	0.716	0.0102429	0.080	0.06723	0.77	0.363	0.04763	0.74	65.715	0.061	66.07	0.49	80	18	17.5
z8	0.29	97	1.6	2.88	3547	0.918	0.0102478	0.057	0.06716	0.38	0.364	0.04755	0.36	65.722	0.055	66.00	0.24	76.1	8.7	13.6

^a Total mass of common Pb.

^b Ratio of radiogenic Pb (including ²⁰⁶Pb) to common Pb.

^c Th contents calculated from radiogenic ²⁰⁶Pb and ²³⁰Th-corrected ²⁰⁶Pb/²³⁸U date of the sample, assuming concordance between U-Pb Th-Pb systems.

§ Measured ratio corrected for fractionation and spike contribution only.

† Measured ratios corrected for fractionation ($\alpha = 0.18 \pm 0.02$ ‰/amu), tracer (ET-535; Condon et al., 2015), and the MIT laboratory blank composition.

‡ Corrected for initial Th/U disequilibrium using radiogenic ²⁰⁹Pb and Th/U[magma] = 2.8.

* Isotopic dates calculated using $\lambda_{238} = 1.55125 \text{E-}10$ (Jaffey et al. 1971) and $\lambda_{235} = 9.8485 \text{E-}10$ (Jaffey et al. 1971).

% discordance = $100 - (100 * (^{206}\text{Pb}/^{238}\text{U date}) / (^{207}\text{Pb}/^{206}\text{Pb date}))$

Table 12: Lu-Hf isotope data of zircons from seven acid volcanic rocks from four complexes within the DT determined by LA-ICP-MS.

Sample	$(^{176}\text{Yb} + ^{176}\text{Lu}) / ^{176}\text{Hf}$ (%)	Volts Hf	$^{176}\text{Hf}/^{177}\text{Hf}$	$\pm (1\sigma)$	$^{176}\text{Lu}/^{177}\text{Hf}$	$^{176}\text{Hf}/^{177}\text{Hf}$ (T)	ϵ_{Hf} (0)	$\epsilon_{\text{Hf}}(0) \pm (1\sigma)$	$\epsilon_{\text{Hf}}(T)$	Age (Ma)
B5	164.2	2.4	0.282672	0.000049	0.009851	0.282660	-4.0	1.7	-3.0	64
	162.6	2.0	0.282815	0.000041	0.006642	0.282807	1.1	1.4	2.2	65
	99.3	2.1	0.282879	0.000032	0.004122	0.282874	3.3	1.1	4.6	65
	196.0	1.6	0.282877	0.000048	0.008017	0.282867	3.3	1.7	4.4	65
	152.7	1.8	0.282932	0.000053	0.006824	0.282924	5.2	1.9	6.4	67
	179.0	2.0	0.282900	0.000041	0.007779	0.282890	4.1	1.4	5.2	67
	56.4	2.5	0.282926	0.000023	0.002874	0.282923	5.0	0.8	6.4	67
	128.7	2.1	0.282899	0.000040	0.005696	0.282891	4.0	1.4	5.3	68
	117.1	2.3	0.282821	0.000030	0.005716	0.282813	1.3	1.1	2.5	68
	184.3	2.1	0.282827	0.000058	0.009558	0.282812	1.5	2.1	2.9	86
PM 4 - 24	18.4	1.6	0.282254	0.000031	0.001051	0.282253	-18.8	1.1	-17.4	64
	28.5	1.7	0.282365	0.000027	0.001410	0.282363	-14.9	1.0	-13.5	64
	31.9	2.0	0.282334	0.000022	0.001862	0.282332	-15.9	0.8	-14.6	65
	41.7	2.7	0.282302	0.000025	0.002812	0.282298	-17.1	0.9	-15.7	66
	27.8	2.0	0.282246	0.000026	0.001518	0.282244	-19.0	0.9	-17.6	67
	75.9	2.8	0.282309	0.000027	0.005138	0.282303	-16.8	1.0	-15.5	69
	16.8	2.7	0.282316	0.000025	0.000936	0.282315	-16.6	0.9	-15.1	70
	38.0	1.8	0.282377	0.000027	0.002563	0.282372	-14.4	1.0	-12.7	84
B6	25.0	2.6	0.282795	0.000022	0.001310	0.282794	0.4	0.8	1.7	63
	218.8	2.2	0.283020	0.000048	0.009459	0.283009	8.3	1.7	9.4	65
	64.9	2.8	0.282787	0.000019	0.002922	0.282783	0.1	0.7	1.4	65
	71.3	2.2	0.282891	0.000027	0.003640	0.282887	3.8	1.0	5.0	65

contd.

Sample	$(^{176}\text{Yb} + ^{176}\text{Lu}) / ^{176}\text{Hf} (\%)$	Volts Hf	$^{176}\text{Hf}/^{177}\text{Hf}$	$\pm (1\sigma)$	$^{176}\text{Lu}/^{177}\text{Hf}$	$^{176}\text{Hf}/^{177}\text{Hf}$ (T)	ϵ_{Hf} (0)	$\epsilon_{\text{Hf}}(0) \pm$ (1 σ)	ϵ_{Hf} (T)	Age (Ma)
	47.0	2.5	0.282939	0.000029	0.002476	0.282935	5.4	1.0	6.8	66
	175.5	2.9	0.282796	0.000041	0.007909	0.282786	0.4	1.5	1.5	67
	439.0	2.6	0.283056	0.000077	0.022999	0.283027	9.6	2.7	10.0	67
	143.1	2.5	0.282840	0.000032	0.006848	0.282831	1.9	1.1	3.1	67
	140.6	1.3	0.282900	0.000043	0.007719	0.282890	4.1	1.5	5.2	68
	106.3	2.7	0.282974	0.000037	0.004440	0.282969	6.7	1.3	8.0	68
	26.1	2.6	0.282893	0.000019	0.001357	0.282891	3.8	0.7	5.3	68
	63.5	2.5	0.282834	0.000029	0.003229	0.282830	1.7	1.0	3.0	65
	199.2	2.5	0.282882	0.000032	0.009108	0.282870	3.4	1.1	4.5	66
	86.6	2.6	0.282968	0.000035	0.004029	0.282963	6.5	1.2	7.7	66
	261.1	2.4	0.282867	0.000058	0.010582	0.282853	2.9	2.0	3.9	67
B2	221.9	2.7	0.282851	0.000045	0.010092	0.282839	2.3	1.6	3.4	67
	93.8	2.4	0.282934	0.000032	0.004342	0.282929	5.3	1.1	6.6	67
	246.7	2.2	0.282904	0.000057	0.010843	0.282891	4.2	2.0	5.2	67
	162.6	2.6	0.283046	0.000045	0.007996	0.283036	9.2	1.6	10.4	68
	444.6	2.2	0.283138	0.000114	0.023237	0.283109	12.5	4.0	13.0	68
	135.5	1.8	0.282922	0.000048	0.006610	0.282912	4.8	1.7	6.3	80
	16.2	2.0	0.282777	0.000034	0.000796	0.282776	-0.3	1.2	1.1	64
	17.0	2.2	0.282559	0.000022	0.001057	0.282558	-8.0	0.8	-6.6	65
G8	13.9	1.9	0.282396	0.000023	0.000741	0.282395	-13.7	0.8	-12.3	66
	20.6	2.1	0.282689	0.000026	0.000957	0.282687	-3.4	0.9	-2.0	66
	12.3	2.0	0.282274	0.000029	0.000747	0.282273	-18.1	1.0	-16.6	66
	12.8	2.0	0.282532	0.000024	0.000729	0.282531	-8.9	0.8	-7.5	67

contd.

Sample	$(^{176}\text{Yb} + ^{176}\text{Lu}) / ^{176}\text{Hf} (\%)$	Volts Hf	$^{176}\text{Hf}/^{177}\text{Hf}$	$\pm (1\sigma)$	$^{176}\text{Lu}/^{177}\text{Hf}$	$^{176}\text{Hf}/^{177}\text{Hf}$ (T)	$\epsilon_{\text{Hf}}(0)$	$\epsilon_{\text{Hf}}(0) \pm (1\sigma)$	$\epsilon_{\text{Hf}}(T)$	Age (Ma)
	19.7	1.8	0.282767	0.000031	0.001030	0.282765	-0.7	1.1	0.8	69
	16.3	1.8	0.282350	0.000035	0.000860	0.282349	-15.4	1.2	-13.8	71
	11.8	2.0	0.282073	0.000031	0.000611	0.282072	-25.2	1.1	-23.3	88
G9	19.7	2.1	0.282783	0.000022	0.000935	0.282782	-0.1	0.8	1.4	66
	18.0	2.0	0.282497	0.000024	0.000951	0.282496	-10.2	0.9	-8.7	66
	40.2	1.7	0.282772	0.000039	0.001760	0.282770	-0.5	1.4	0.9	67
	24.2	1.5	0.282712	0.000033	0.001271	0.282710	-2.6	1.2	-1.2	67
	15.9	2.4	0.282618	0.000028	0.000817	0.282617	-5.9	1.0	-4.4	67
	18.2	2.1	0.282536	0.000018	0.000955	0.282535	-8.8	0.6	-7.3	68
R7	18.1	2.1	0.282096	0.000035	0.001185	0.282094	-24.4	1.2	-22.9	67
	22.8	2.3	0.282203	0.000026	0.001583	0.282201	-20.6	0.9	-19.2	67
	20.4	2.3	0.282111	0.000021	0.001096	0.282109	-23.8	0.7	-22.4	68
	14.8	2.2	0.281975	0.000023	0.000749	0.281974	-28.6	0.8	-27.2	69
	20.8	2.2	0.282054	0.000023	0.001128	0.282053	-25.8	0.8	-24.4	69
	27.2	2.1	0.282141	0.000028	0.001333	0.282139	-22.8	1.0	-21.3	70
	14.7	2.4	0.281996	0.000019	0.000756	0.281995	-27.9	0.7	-26.4	71

Table 13: Lu-Hf isotope data of zircons from samples A7 (Alech) and B6 (Barda) determined using Solution-MC-ICP-MS

Sample	Fraction	$^{176}\text{Hf}/^{177}\text{Hf}_m$ (* $\pm 2s$ int.†) $\pm 2s$ tot. (§)	$^{176}\text{Lu}/^{177}\text{Hf}$ (#)	Age (Ma)	$^{176}\text{Hf}/^{177}\text{Hf}_m$ ** $\pm 2s$ (††)	ϵHf (t) $\pm 2s$	Total Hf (V)
B6	z1	0.282871 ± 7 ± 11	0.0037	65.7	0.282867 ± 11	4.34 ± 0.39	17.9
B6	z2	0.282871 ± 7 ± 10	0.0057	65.7	0.282864 ± 10	4.26 ± 0.37	23.2
B6	z3	0.282869 ± 5 ± 10	0.0048	65.7	0.282863 ± 10	4.22 ± 0.35	21.1
B6	z4	0.282880 ± 6 ± 10	0.0055	65.7	0.282873 ± 10	4.57 ± 0.37	12.6
B6	z5	0.282865 ± 7 ± 11	0.0026	65.7	0.282862 ± 11	4.19 ± 0.39	13.8
B6	z6	0.282890 ± 9 ± 12	0.0075	65.7	0.282881 ± 12	4.84 ± 0.44	7.9
B6	z7	0.282880 ± 8 ± 11	0.0049	65.7	0.282875 ± 11	4.62 ± 0.40	12.0
B6	z8	0.282867 ± 7 ± 11	0.0070	65.7	0.282858 ± 11	4.06 ± 0.39	16.7
		B6		Weighted Mean	0.282867	4.37	
		n=8		$\pm 2\sigma$	0.000004	0.14	
				MSWD	1.7		
A7	z1	0.282896 ± 13 ± 15	0.0101	65.7	0.282884 ± 15	4.94 ± 0.54	6.1
A7	z2	0.282908 ± 11 ± 14	0.0083	65.7	0.282897 ± 14	5.43 ± 0.50	4.7
A7	z3	0.282921 ± 21 ± 23	0.0023	65.7	0.282918 ± 23	6.17 ± 0.81	2.6
A7	z4‡	0.283027 ± 33 ± 34	0.0134	65.7	0.283011 ± 34	9.45 ± 1.21	1.0
A7	z5‡	0.282939 ± 24 ± 25	0.0089	65.7	0.282928 ± 25	6.52 ± 0.89	1.8
A7	z6	0.282893 ± 11 ± 14	0.0044	65.7	0.282887 ± 14	5.08 ± 0.50	4.5
A7	z7	0.282904 ± 12 ± 15	0.0083	65.7	0.282894 ± 15	5.31 ± 0.52	3.1
		A7		Weighted Mean	0.282893	5.29	
		n=5		$\pm 2\sigma$	0.000007	0.25	
				MSWD	1.9		

* Modern $^{176}\text{Hf}/^{177}\text{Hf}$ measured by MC-ICP-MS on purified Hf aliquots. See supplementary file with analytical methods for details

† Internal uncertainties (2 SE) estimated for each individual run based on counting statistics

§ Total analysis uncertainty (2 SE) estimated from the propagation of individual internal uncertainties and 2 SD external reproducibility of bracketing 25 ppb JMC-475 Hf standards used for correction. See supplementary file with analytical methods for details

Compositions estimated from elemental Lu/Hf ratios measured on 'trace element' aliquots and assuming $^{175}\text{Lu}/^{176}\text{Lu} = 0.02655$ from Vervoort et al. (2004). See supplementary file with analytical methods for details

** Initial $^{176}\text{Hf}/^{177}\text{Hf}$ ratios corrected for radiogenic ingrowth using the calculated $^{176}\text{Lu}/^{177}\text{Hf}$ composition and U-Pb date of each zircon and the decay constant of Söderlund et al. (2004); $\lambda_{176}\text{Lu} = 1.867 \times 10^{-11} \text{ a}^{-1}$

†† Uncertainty on the initial $^{176}\text{Hf}/^{177}\text{Hf}$ ratio assumed as the total uncertainty of the modern $^{176}\text{Hf}/^{177}\text{Hf}$ ratio. No uncertainties on the estimated $^{176}\text{Lu}/^{177}\text{Hf}$ or $\lambda_{176}\text{Lu}$ were propagated

‡ Fractions not considered towards weighted mean calculations due to low total Hf beam (i.e., <2 V)

Table 14: Major oxides of whole rock samples and their crystallization temperatures from Rhyolite-MELTS and olivine liquidus temperatures from PRIMELT3 at 2kbar.

Samples	Rock Type	SiO ₂	TiO ₂	Al ₂ O ₃	Total Fe ₂ O ₃	Fe ₂ O ₃	FeO	MnO	MgO	CaO	Na ₂ O	K ₂ O	P ₂ O ₅	Sum of all oxides	LOI	Crystallization temp. from Rhyolite-MELTS (°C) at 2kbar	Olivine liquidus temp. from PRIMELT3 (°C) at 2kbar	Mantle Potential Temp. (°C)
R3	rhyolite	71.42	0.20	13.02	2.56	0.26	2.31	0.01	0.06	0.39	3.60	5.01	0.08	96.34	3.66	863		
A8	rhyolite	71.25	0.35	14.23	1.57	0.16	1.42	0.01	0.02	0.18	4.73	4.94	0.08	97.35	2.65	884		
P8	rhyolite	71.86	0.26	12.30	3.05	0.30	2.74	0.08	0.01	0.71	3.65	5.04	0.08	97.03	2.97	893		
A1	granophyre	72.43	0.28	11.98	3.08	0.31	2.77	0.05	0.01	0.74	3.65	4.01	0.17	96.40	3.60	903		
G10	granophyre	73.63	0.18	11.89	2.24	0.22	2.01	0.03	0.02	0.70	2.25	5.39	0.08	96.40	3.60	916		
P6	rhyolite	70.29	0.34	13.06	3.59	0.36	3.23	0.08	0.04	0.60	3.87	5.08	0.08	97.05	2.95	926		
P1	rhyolite	59.93	0.56	11.95	5.37	0.54	4.83	0.10	0.01	7.43	2.96	4.59	0.13	93.04	6.96	926		
PH24	dolerite	70.16	0.36	13.46	3.53	0.35	3.18	0.05	0.19	0.68	3.30	5.83	0.08	97.65	2.35	945		
B6	granophyre	71.29	0.37	11.83	4.95	0.50	4.46	0.10	0.07	1.56	4.44	3.63	0.08	98.31	1.69	953		
A6	granophyre	73.52	0.30	12.61	4.73	0.47	4.26	0.08	0.03	1.83	2.76	4.52	0.08	100.45	-0.45	963		
B2	granophyre	73.35	0.28	12.14	3.42	0.34	3.08	0.05	0.13	0.34	4.28	4.31	0.08	98.39	1.61	965		
G9	diorite	75.97	0.15	11.99	1.99	0.20	1.79	0.03	0.04	0.35	2.53	5.46	0.08	98.58	1.42	967		
PH47	granophyre	77.12	0.09	11.17	1.64	0.16	1.47	0.02	0.08	0.54	2.90	4.62	0.03	98.22	1.78	978		
G8	diorite	69.43	0.69	12.13	5.56	0.56	5.00	0.08	0.67	2.03	2.79	3.71	0.13	97.21	2.79	989		
G1	granophyre	70.86	0.60	12.20	4.93	0.49	4.44	0.07	0.56	1.66	2.74	4.35	0.12	98.09	1.91	995		
R5	rhyolite	68.95	0.41	13.01	4.04	0.40	3.63	0.04	0.22	0.37	1.19	8.39	0.08	96.71	3.29	997		
O1	rhyolite	71.59	0.19	12.88	2.48	0.25	2.23	0.02	0.01	0.50	2.13	7.31	0.08	97.20	2.80	1009		
B5	granodiorite	71.21	0.57	12.19	5.85	0.58	5.26	0.12	0.01	1.57	4.26	3.61	0.08	99.46	0.54	1010		
PH46	augen gneiss	65.83	0.69	14.08	6.22	0.62	5.59	0.12	0.94	2.43	3.59	4.63	0.20	98.72	1.28	1044		
B4	granodiorite	62.02	0.90	11.99	12.67	1.27	11.40	0.18	0.17	2.51	4.12	2.82	0.17	97.55	2.45	1066		
R8	basalt	43.87	1.63	11.18	11.81	1.18	10.63	0.15	3.02	6.64	2.13	0.54	0.17	81.14	18.86		1090	1139
P3	basalt	48.05	2.77	15.95	12.27	1.23	11.05	0.19	3.89	8.58	3.05	1.69	0.41	96.86	3.14		1101	1139
PH49	tinguaite	52.41	2.56	13.96	13.93	1.39	12.53	0.18	4.64	8.89	1.94	1.15	0.27	99.93	0.07		1113	1157
B3	basalt	46.74	1.35	14.15	13.31	1.33	11.97	0.19	6.37	8.71	3.00	0.14	0.25	94.20	5.80		1186	1216
O5	basalt	48.36	1.52	14.91	13.24	1.32	11.92	0.19	7.02	9.86	2.39	0.90	0.25	98.63	1.37		1189	1226
G7	nepheline syenite	48.37	0.43	15.23	7.59	0.76	6.83	0.12	10.31	16.58	1.21	0.08	0.02	99.93	0.07		1217	1313

contd.

Samples	Rock Type	SiO ₂	TiO ₂	Al ₂ O ₃	Total Fe ₂ O ₃	Fe ₂ O ₃	FeO	MnO	MgO	CaO	Na ₂ O	K ₂ O	P ₂ O ₅	Sum of all oxides	LOI	Crystallization temp. from Rhyolite-MELTS (°C) at 2kbar	Olivine liquidus temp. from PRIMELT3 (°C) at 2kbar	Mantle Potential Temp. (°C)
PH45	basalt	48.30	0.37	11.93	10.41	1.04	9.37	0.17	14.70	13.79	1.00	0.23	0.08	100.99	-0.99		1345	1454
G11	basalt	48.60	0.81	17.12	9.46	0.95	8.51	0.14	7.13	10.86	2.48	0.31	0.11	97.03	2.97		1390	1492
G3	basalt	49.72	1.83	17.65	9.20	0.92	8.28	0.15	3.73	8.19	3.91	3.14	0.44	97.96	2.04		1443	1519
G2	basalt	50.76	0.98	17.42	10.07	1.01	9.06	0.16	5.66	12.27	2.52	0.15	0.13	100.13	-0.13		1462	1523
PH50	nepheline syenite	49.34	1.23	18.32	9.58	0.96	8.63	0.15	3.68	9.85	3.04	1.93	0.32	97.45	2.55		1464	1584
P5	dolerite	46.02	2.41	11.88	12.32	1.23	11.08	0.17	12.51	9.41	1.79	0.78	0.27	97.56	2.44		1474	1612
P4	trap	45.72	2.40	12.98	13.23	1.32	11.91	0.17	7.63	12.33	1.84	0.55	0.26	97.12	2.88		1480	1624
A2	basalt	49.18	0.92	16.51	11.51	1.15	10.36	0.18	6.26	11.98	2.17	0.28	0.22	99.21	0.79		1483	1440
R4	dolerite	49.03	1.15	15.77	11.09	1.11	9.98	0.1420	5.50	9.80	2.16	0.82	0.13	95.57	4.43		1514	1660
PH4	basalt	46.70	1.82	15.92	13.46	1.35	12.11	0.22	3.98	9.07	4.03	2.57	0.81	98.58	1.42		1519	1628

- a. FeO is estimated as 90% of total Fe₂O₃.
- b. H₂O estimated based on LOI (Loss on Ignition).

Table 15: Sm-Nd and Rb-Sr systematics of acidic rocks and associated basalts of the five complexes within DT.

Samples	Rock Type	Rb (ppm)	Sr (ppm)	$^{87}\text{Rb}/^{86}\text{Sr}$	$^{87}\text{Sr}/^{86}\text{Sr}$ - measured	$^{87}\text{Sr}/^{86}\text{Sr}$ - initial	Sm (ppm)	Nd (ppm)	$^{147}\text{Sm}/^{144}\text{Nd}$	$^{143}\text{Nd}/^{144}\text{Nd}$ measured	$^{143}\text{Nd}/^{144}\text{Nd}$ - initial	ϵ_{Nd} initial at 66Ma
A1	granophyre	109.5	58.6	5.27	0.712549	0.707609	9.1	42.2	0.14	0.512470	0.512411	-1.4
A2	basalt	5.2	184.0	0.08	0.710595	0.707934	2.4	9.1	0.16	0.512380	0.512310	-3.4
A3	felsite	69.4	69.0	2.84	0.714023	0.711361	8.4	40.0	0.51	0.512440	0.512008	-9.3
A4	breccia	7.8	5.6	3.9	0.711035	0.707353	6.6	1.5	2.84	0.512440	0.511216	-24.7
A5	rhyolite	29.1	19.6	4.18	0.712227	0.708304	4.2	19.2	0.14	0.511780	0.511720	-14.9
A7	granophyre	126.9	26.6	13.4	0.718175	0.705570	9.3	43.0	0.14	0.512600	0.512541	1.1
B2	granophyre	141.2	48.0	8.3	0.714752	0.706969	11.6	53.5	0.14	0.512474	0.512381	-2.0
B3	basalt	4.6	570.2	0.02	0.709990	0.709969	3.0	11.7	0.16	0.512580	0.512510	0.5
B4	granodiorite	81.8	134.0	1.72	0.708136	0.706521	8.2	35.9	0.14	0.512050	0.511988	-9.7
B5	granophyre	110.8	95.6	3.27	0.748725	0.745658	11.4	48.5	0.15	0.512200	0.512136	-6.8
B6	granophyre	102.5	73.2	3.9	0.710094	0.706392	10.4	47.0	0.14	0.512440	0.512380	-2.0
G1	granophyre	136.0	34.0	11.29	0.737759	0.727167	6.2	31.3	0.12	0.512520	0.512466	-2.4
G10	rhyolite	291.6	40.9	20.09	0.748835	0.729991	1.6	5.6	0.17	0.512440	0.512364	-2.4
G11	basalt	4.0	221.0	0.05	0.708723	0.708675	2.5	9.0	0.18	0.512440	0.512008	-2.3
G2	diorite	4.2	220.6	0.05	0.704844	0.704793	5.0	28.1	0.11	0.512428	0.512352	-2.6
G3	dolerite	71.1	555.1	0.36	0.707599	0.707260	3.4	22.7	0.09	0.511630	0.511198	-25.1
G4	neph. Syenite	310.3	13.3	65.65	0.764012	0.702439	0.6	1.6	0.25	0.512000	0.511450	-20.2
G6	neph. Syenite	359.5	751.4	1.3	0.708827	0.707562	13.8	82.7	0.11	0.512060	0.511981	-9.8
G8	Granophyre	160.7	114.9	3.94	0.705959	0.705418	4.2	18.6	0.14	0.511487	0.511426	-20.6
PH46	granophyre	194.9	165.8	3.32	0.750322	0.747211	6.2	28.8	0.14	0.511085	0.510653	-35.7
PH49	basalt	33.4	355.9	0.26	0.712621	0.712373	12.0	48.9	0.15	0.512279	0.511847	-12.4
PH50	tinguaite	35.7	327.9	0.31	0.718706	0.718418	11.99	48.88	0.15	0.511635	0.511203	-25.0
R1	basalt	206.9	68.7	8.49	0.733840	0.725874	8.5	44.3	0.12	0.512171	0.511739	-14.5
R3	rhyolite	166.4	24.2	19.36	0.727140	0.708982	18.3	116.6	0.10	0.510712	0.510678	-35.2
R7	trachyte	130.1	300.4	1.2	0.762078	0.760932	135.0	23.4	3.63	0.511111	0.511077	-27.4

- a. The reported $^{87}\text{Sr}/^{86}\text{Sr}$ isotope ratios given herein correspond to average SRM 987 Sr standard measured during analysis of 0.710291 with .000005 error.
- b. The reported $^{143}\text{Nd}/^{144}\text{Nd}$ isotope ratios given herein correspond to measured average La Jolla Nd standard of 0.511880 with 0.000006 error.

BIOGRAPHY

Puloma Chakrabarty was born and brought up in the city of Kolkata, West Bengal, India. She graduated from Presidency College (presently Presidency University), Kolkata with a Bachelor of Science in Geology with Physics and Mathematics in 2009. In 2012, she graduated with Masters in Science and Technology in Applied Geology from Indian School of Mines, Dhanbad (presently Indian Institute of Technology, Dhanbad), India. She was the Vice-President of SEG ISM Chapter.

After receiving her Masters, she started working with an Australian company, HDR|Salva where she was involved in exploration, resource estimation and recovery of lithium in pegmatites in Liden, Sweden. She later joined Geovale Services Pvt. Ltd and worked in exploration of Fe, Au and Cu before she joined the PhD program.

In Fall 2014, Puloma was admitted to the Department of Earth and Environmental Sciences at the University of Texas at Arlington, Texas for her PhD in Isotope Geochemistry. Puloma has been a member of GSA, AGU and GS. She is the Treasurer of the AAPG Section in the EES Department at UT Arlington. She has presented papers in national and international meetings, including, AGU, GSA and Goldschmidt. She has 8 conference proceedings and 1 co-authored publication in Micropaleontology journal. She has 4 on-going manuscripts in preparation.

Puloma aims to be a professional in the industry upon finishing her PhD. She calls herself a “sassy geochemist with a penchant for trying new methods to achieve her goals”.

Puloma Chakrabarty
May, 2019